THE FLUID MECHANICS OF THE AABERG EXHAUST HOOD

Gary Richard Hunt

Submitted in accordance with the requirements for

the degree of Doctor of Philosophy

The University of Leeds

Department of Applied Mathematical Studies

I confirm that the work submitted is my own and that appropriate credit has been given where reference has been made to the work of others.

July 1994

Abstract

In this thesis an investigation of the fluid mechanics of the Aaberg exhaust hood is presented. The Aaberg exhaust hood is unique in its design as the speed of the air flow towards the exhaust inlet is enhanced by the entrainment of fluid into the hood's jet flow. The complex air flow pattern of the hood is governed by the Navier-Stokes equations. However, in this thesis modelling techniques have been developed in order to reduce the complexity of determining the fundamental air flow pattern. The modelling procedure adopted considers the hood's overall air flow to be composed of three component flows, namely, (i) the flow in the jet region, (ii) the jet-induced flow and (iii) the suction flow. In practice the fluid flow pattern generated by the hood is such that the Reynolds number is very large, and hence the suction and jet-induced flows are modelled as potential flows with the boundary conditions governing the jet-induced flow coming from the solution of the shear-layer equations. This solution procedure enables the parameters which govern the hood's air flow to be identified and their effect on the flow produced by the hood may then be determined. Both two-dimensional and three-dimensional axisymmetric exhaust designs have been examined and for the latter case a new numerical model for the axisymmetric radial flow of a fluid from the space between two identical concentric discs, for laminar and turbulent flows, has been developed. Agreement between the turbulent radial jet model developed and the results of numerous other established theoretical and experimental investigations is very good. The inviscid models for the overall air flow have been developed in terms of the stream function

and, except for in the simplest case considered where an analytical solution is possible, the equations of motion which govern the fluid flow in the region of interest have been solved numerically using finite-difference techniques. The models developed illustrate all of the flow phenomena observed experimentally and comparisons made between the predictions of both the two-dimensional and three-dimensional axisymmetric mathematical models and (i) the available experimental data and (ii) the commercially available CFD code FLUENT, which solves the full turbulent Navier-Stokes equations, show good agreement, thereby confirming the credibility of the cost-effective modelling approach adopted in this thesis.

Acknowledgements

I am truly grateful to Professor D. B. Ingham for allowing me the opportunity to study at the University of Leeds and for his enthusiastic supervision and encouragement throughout the course of my studies for a Ph.D. Furthermore, I would like to thank Dr.X.Wen for all his assistance during my studies and Dr.B.Fletcher and Dr.L.G.Pedersen for providing the experimental data used in this thesis. I would also like to thank Dr.S.J.Dunnett for the interest she has shown in this project and Miss.S.Lawton for proof-reading the thesis. Finally, I gratefully acknowledge the Scientific and Engineering Research Council and the Health and Safety Executive for their financial support of this research project.

At the time of submission much of the work contained in this thesis has been published. The analytical model for the fluid mechanics of the Aaberg exhaust hood developed in chapter 3 of this thesis has been published in the Annals of Occupational Hygiene (Hunt and Ingham (1992)). The first section of chapter 4 has been presented at the 1992 European Aerosol Conference, 6-11 September, Oxford, U.K., and the 1993 IChemE Research Event, 2-4 January, Birmingham University, U.K., whilst the second section was presented at ROOMVENT'92, the 3rd International Conference on Air Distribution in Rooms, 2-4 September, Aalborg, Denmark. The contents of chapter 6 have been presented at the 1993 European Aerosol Conference, 4-8 October, Duisburg, Germany. The model of the Aaberg slot exhaust developed in chapter 7 has been published in the Journal of Mathematical Engineering in Industry (Hunt and Ingham (1993)) and has been presented at the 7th Annual Conference of the Aerosol Society, 29-30 June 1993, Bristol, U.K..

Contents

	Page
Abstract	i
Acknowledgements	iii
Contents	iv
Nomenclature	ix
List of Figures	xv
List of Tables	xx
CHAPTER ONE General Introduction and Literature Review	1
1.1 INTRODUCTION	2
1.1.1 Traditional Exhaust Hoods	3
1.1.2 The Aaberg Principle	5
1.2 A REVIEW OF THE EXISTING LITERATURE	9
1.3 CONCLUSIONS	26
CHAPTER TWO Mathematical Modelling: Tools, Techniques and Terminology	28
2.1 INTRODUCTION	29
2.2 FORMULATION	30
2.2.1 The Flow in the Jet	31
2.2.2 The Jet-induced Flow	43
2.2.3 The Exhaust Flow	47
2.3 METHODS OF SOLUTION	48
2.4 TERMINOLOGY	49
2.4.1 The Capture Speed	50
2.4.2 The Effective Capture Region	51
2.4.3 The Effective Working Range	51

2.5 CONCLUSIONS ——— 52

CHAPTER THREE A Simple Two-dimensional Analytical Model for the Fluid Mechanics of the Aaberg Exhaust Hood 53

3.1 INTRODUCTION ——— 54

3.2 THE MATHEMATICAL MODEL ——— 55

3.2.1 The Stream Function due to the Sink ——— 56

3.2.2 The Two-dimensional Laminar Plane Jet ——— 57

3.2.3 The Two-dimensional Turbulent Plane Jet ——— 60

3.2.4 The Flow Induced by a Two-dimensional Jet ——— 62

3.3 A TWO-DIMENSIONAL MODEL OF THE AABERG EXHAUST HOOD'S FLUID FLOW ——— 63

3.4 RESULTS AND DISCUSSION ——— 66

3.4.1 The Laminar Model ——— 68

3.4.2 The Turbulent Model ——— 74

3.5 THE REYNOLDS NUMBER OF THE JET ——— 78

3.6 CONCLUSIONS ——— 80

CHAPTER FOUR The Effect of the Exhaust Inlet Size on the Effective Capture Area of an Aaberg Exhaust Hood and the Deflection of the Air Flow into the Hood which is caused by the Floor of the Workplace ——— 81

4.1 INTRODUCTION ——— 82

4.2 FORMULATION ——— 83

4.3 THE EFFECT OF THE EXHAUST INLET SIZE ——— 84

4.3.1 The Equations of Motion and the Boundary Conditions 84

4.3.2 The Finite-difference Scheme ——— 87

4.3.3 Results and Discussion ——— 89

4.4 CONCLUSIONS OF THE EFFECTS OF THE EXHAUST INLET SIZE —— 93

4.5 THE EFFECT OF THE FLOOR ON THE AIR FLOW INTO AN AABERG EXHAUST HOOD —— 94

4.5.1 The Equations of Motion and the Boundary Conditions 95

4.5.2 The Finite-difference Scheme —— 98

4.5.3 Results and Discussion —— 100

4.5.3.1 Air Speeds along the Floor Surface of the Workplace —— 104

4.5.3.2 Air Speeds along the Centre-line of the Ventilator —— 106

4.5.3.3 The Effective Capture Area —— 108

4.6 CONCLUSIONS OF THE EFFECT OF THE FLOOR ON THE AIR FLOW INTO AN AABERG EXHAUST HOOD —— 109

CHAPTER FIVE A Three-dimensional Axisymmetric Model for the Radial Jet Issuing from the Aaberg Exhaust Hood —— 112

5.1 INTRODUCTION —— 113

5.2 FORMULATION —— 113

5.3 THE GOVERNING EQUATIONS OF MOTION AND THE BOUNDARY CONDITIONS —— 115

5.4 THE INITIAL BEHAVIOUR OF THE RADIAL FREE JET —— 117

5.4.1 The Laminar Radial Jet —— 118

5.4.2 The Turbulent Radial Jet —— 119

5.5 THE ASYMPTOTIC BEHAVIOUR OF THE RADIAL FREE JET —— 122

5.5.1 The Laminar Radial Jet —— 123

5.5.2 The Turbulent Radial Jet —— 124

5.6 SOLUTION OF THE EQUATIONS OF MOTION GOVERNING THE FLOW IN A RADIAL FREE JET FOR $0 < x^* < \infty$ —— 127

5.6.1 The Laminar Radial Jet ——— 128

5.6.2 The Turbulent Radial Jet ——— 129

5.7 NUMERICAL SOLUTION OF THE NON-LINEAR PARABOLIC PARTIAL DIFFERENTIAL EQUATION ——— 133

5.8 RESULTS AND DISCUSSION ——— 139

5.8.1 The Laminar Radial Jet ——— 141

5.8.2 The Turbulent Radial Jet ——— 142

5.9 CONCLUSIONS ——— 146

CHAPTER SIX A Three-dimensional Axisymmetric Model of the Fluid Flow Pattern Created by an Aaberg Exhaust Hood 147

6.1 INTRODUCTION ——— 148

6.2 THE MATHEMATICAL MODEL ——— 149

6.2.1 The Axisymmetric Radial Jet Flow ——— 150

6.2.2 The Jet-induced Flow ——— 150

6.2.3 The Exhaust Flow ——— 151

6.2.4 The Upstream Boundary Condition ——— 152

6.3 THE FINITE-DIFFERENCE SCHEME ——— 155

6.4 THE OPERATING PARAMETERS ——— 156

6.5 RESULTS AND DISCUSSION ——— 158

6.6 CONCLUSIONS ——— 166

CHAPTER SEVEN Application of the Aaberg Principle to the Slot Exhaust Hood ——— 167

7.1 INTRODUCTION ——— 168

7.2 THE MATHEMATICAL MODEL ——— 169

7.2.1 The Two-dimensional Turbulent Wall Jet ——— 170

7.2.2 The Two-dimensional Turbulent Free Jet ——— 173

7.3 THE OPERATING PARAMETERS ——— 175

7.4 RESULTS AND DISCUSSION ——— 177

7.4.1 The HI-Experiments ——— 177

7.4.2 The HHY-Experiments ——— 188

7.5 CONCLUSIONS ——— 188

CHAPTER EIGHT The Use of FLUENT - A Full Turbulence Model — 191

8.1 INTRODUCTION ——— 192

8.2 THE FULL TURBULENCE MODEL ——— 193

8.2.1 The k-ε Model ——— 193

8.2.2 The Boundary Conditions ——— 194

8.3 THE NUMERICAL METHOD ——— 197

8.3.1 An Outline of the SIMPLEC Algorithm ——— 201

8.3.2 Solution of the Algebraic Equations and Convergence Criterion ——— 201

8.3.3 The Computational Grid ——— 203

8.4 RESULTS AND DISCUSSION ——— 204

8.4.1 The Axisymmetric Aaberg Exhaust Hood ——— 204

8.4.2 The Aaberg Slot Exhaust Hood ——— 211

8.5 CONCLUSIONS ——— 219

CHAPTER NINE General Conclusions ——— 221

REFERENCES ——— 227

Nomenclature

a	width/radius of the exhaust flange in two-dimensional/axisymmetric cases, respectively
b	width of the jet, as a function of x*
b_s	width of the jet at a characteristic distance s from the jet orifice
$b_{1/2}$	width of the shear-layer when $u = \tilde{u}/2$; $b_{1/2} = 0.881\ b$
$b(0)$	width of the jet nozzle
C_e	concentration of tracer gas in the exhaust
C_{bc}	background concentration of tracer gas
C_r	reference concentration of tracer gas
C_R	constraint ratio, $= 2a/b(0)$
C_o, C_∞	non-dimensional parameters: $C_o = 0.0144\ K^{1/2}$, $C_\infty = 0.0260\ K^{1/2}$
C_1, C_2, C_μ	empirical constants: $C_1 = 1.44$, $C_2 = 1.92$, $C_\mu = 0.09$
d	diameter of the exhaust inlet, $d = 2s$
E	wall roughness parameter, $= 9.8$
$f, \bar{f}, \hat{f}$	non-dimensional stream functions
f_∞	parameter, $= \begin{cases} (9k\nu/2)^{1/3} & \text{for laminar flow} \\ (3k/\sigma_o)^{1/2}/2 & \text{for turbulent flow} \end{cases}$
G_F, G_W	non-dimensional operating parameters for two-dimensional turbulent free jet and wall jet flows, respectively
G_L, G_T	non-dimensional operating parameters for two-dimensional laminar and turbulent free jet flows, respectively
G_{Axi}	non-dimensional parameter for turbulent axisymmetric radial jet flow
h	step length in the lateral direction across the radial jet shear-layer: $\eta = jh$

h	height of the ventilator unit above the floor
H	non-dimensional height of the ventilator unit above the floor, = h/a
h_s	distance between the bench surface and the centre of the exhaust inlet
H_s	non-dimensional distance between the bench surface and the centre of the exhaust inlet, = h_s/p
I	ratio of the momentum flux of the jet flow to the momentum flux of the exhaust flow, = $m_j u(0)/m\ u_{in}$
I_∞	upstream turbulent intensity
j	momentum flux of the free jet
k	kinematic momentum flux of the free jet, = j/ρ; in chapter 8, k is used to denote the turbulent kinetic energy
K	non-dimensional kinematic momentum flux of the free jet
m	volumetric flow rate of the exhaust
m_j	volumetric flow rate of the jet
n	number of iterations
p	height of the jet nozzle above the bench surface, = $a + h_s$
P	ratio of pressure to density, = p/ρ
p	fluid pressure
p'	pressure correction
p^*	guessed pressure
q	resultant air speed
Q	non-dimensional resultant air speed
q_b	resultant bifurcation speed
Q_b	non-dimensional resultant bifurcation speed
q_c	resultant capture speed
Q_c	non-dimensional resultant capture speed

q_1, q_2	dependent variables: $q_1 = q(X^*, Y)$, $q_2 = q(X^*+\delta X^*, Y)$
(r_α, α)	dimensional coordinate system
(R_α, α)	non-dimensional coordinate system, $R_\alpha = r_\alpha/a$
(r_γ, γ)	dimensional coordinate system
(R_γ, γ)	non-dimensional coordinate system, $R_\gamma = r_\gamma/a$
(r, θ)	dimensional coordinate system
(R, θ)	non-dimensional coordinate system, $R = r/a$
(r, θ, ϕ)	dimensional spherical polar coordinate system
R_e	Reynolds number of the jet, $= u(0)b(0)/\nu$
R_h	hydraulic radius
R_{in}	Reynolds number of the exhaust flow, $= u_{in}a/\beta_o$
$R_j(x^*)$	Reynolds number of the jet as a function of x^*, $= \tilde{u}\, x^*/\nu$
R_{mass}	mass residual
R_∞	radial position of outer artificial boundary
s	width/radius of the exhaust inlet for two-dimensional/axisymmetric cases, respectively
S	non-dimensional width/radius of the exhaust inlet for two-dimensional/axisymmetric cases, respectively
S_ϕ	source term
u	velocity vector, $= ui + vj + wk$
u(0)	jet exit speed
u_{in}	fluid speed at the face of the exhaust inlet
$\tilde{u}$	maximum fluid speed in the jet
$\tilde{u}_s$	centre-line velocity of the jet at a characteristic distance s from the jet orifice
u^+	shear speed, $= \sqrt{\tau_w/\rho}$
U_∞	speed upstream of the exhaust hood
u, v	velocity components in the x and y directions, respectively

U, V	non-dimensional velocity components in the x and y directions, respectively
u', v'	velocity corrections
u^*, v^*	velocity based on the guessed pressure p^*
u_r, u_θ	radial and tangential velocity components, respectively
U_r, U_θ	non-dimensional radial and tangential velocity components, respectively
u_r, u_ϕ	radial and tangential velocity components, respectively
U_r, U_ϕ	non-dimensional radial and tangential velocity components, respectively
x^*	distance along the jet axis measured from the jet orifice
X_∞	position of outer artificial boundary
(x, y)	dimensional cartesian coordinate system
(X, Y)	non-dimensional cartesian coordinate system
(x, θ, y)	dimensional cylindrical polar coordinate system
y	lateral distance measured perpendicular to the jet axis
y^+	dimensionless friction length, $= yu^+/\nu$

Greek

α	constant of integration
α_{cap}	capture efficiency
β	kinematic viscosity, $= \begin{cases} \nu & \text{for laminar flow} \\ \varepsilon & \text{for turbulent flow} \end{cases}$
β_o	scaling factor for β, $= \begin{cases} \nu & \text{for laminar flow} \\ \varepsilon_o & \text{for turbulent flow} \end{cases}$
γ_e	empirical constant
Γ	general diffusion coefficient
δR	radial step length: $R = i\delta R$

δx step length in the X direction: $X = i\delta x$

δX^* step length in the Crank-Nicolson scheme

$\delta\theta$ step length in the tangential direction: $\theta = i\delta\theta$

$\delta\xi$ step length, $= \ln(1+\delta R)$

$\delta\phi$ step length in the tangential direction: $\phi = i\delta\phi$

$\Delta x, \Delta y$ x and y direction widths of the control volume

$\Delta\psi$ the volume flux of fluid between adjacent streamlines

ε apparent kinematic viscosity; in chapter 8, ε is used to denote turbulent energy dissipation and the apparent kinematic viscosity is then denoted ν_t

ε_s apparent kinematic viscosity at a characteristic distance s from the jet orifice

ε_o 'initial' apparent kinematic viscosity, $= u(0)b(0)$

ε_1 tolerance in the Newton iteration procedure

ε_2 tolerance between successive solutions in radial direction

$\eta, \bar{\eta}, \hat{\eta}$ shear-layer variables which measure the distance normal to the centre-line of the jet

κ the von Karman constant, $= 0.42$

λ parameter, $= \begin{cases} 1/3 & \text{for the laminar plane jet} \\ 1/2 & \text{for the turbulent plane jet} \end{cases}$

λ_i dimensionless function of X^*, $i = 1,2,3,4$

μ viscosity of the fluid

ν kinematic viscosity of the fluid

ν_e effective kinematic viscosity of the fluid, $= \nu + \varepsilon$

ξ radial coordinate, $= \ln(R)$

ρ density of the fluid

$\sigma_k, \sigma_\varepsilon$ empirical constants: $\sigma_k = 1.0$, $\sigma_\varepsilon = 1.3$

σ_o, σ_∞ constants which characterize the spreading rate of the turbulent jet. For the plane jet $b = \sigma_o^{-1} x^*$, for the axisymmetric radial jet: $b = \begin{cases} \sigma_o^{-1} x^* & \text{at } x^* = 0 \\ \sigma^{-1} x^* & \text{as } x^* \longrightarrow \infty \end{cases}$

τ shear stress, $= \mu \, \partial u / \partial y$

τ_w shear stress on the wall

τ_{ij} truncation error

Φ production of turbulent kinetic energy

χ empirical constant

ψ stream function

Ψ dimensionless stream function

Ψ_∞ stream function value at the edge of the shear-layer

ω relaxation parameter

Subscripts

e, n, s, w	control volume faces (Fig. 8.1)
E, N, P, S, W	grid points
nb	neighbouring grid point

Abbreviations

ASE	Aaberg slot exhaust
CFD	Computational fluid dynamics
CLV	Centre-line velocity
CPU	Central processing unit
LEV	Local exhaust ventilation
LVA	Low velocity flow analyser
REEXS	Reinforced exhaust system
SIMPLEC	Semi-Implicit Method for Pressure Linked Equations (Consistent)
S.O.R.	Successive over relaxation

List of Figures

Page

Fig.1.1(a) The non-directional flow of a traditional LEV hood ——— 5

Fig.1.1(b) Air speed profiles of a traditional flanged LEV hood, Greenough (1988) ——— 5

Fig.1.2 A schematic representation of the Aaberg principle — 6

Fig.1.3 Capture of tracer gas released at 5d from an exhaust hood of dimensions: a ≃ 0.15m, s = 0.037m, b(0) = 8.0mm; courtesy of the Health and Safety Executive, Research Division, Sheffield, England. (a) Suction alone, u_{in} = 12.7ms^{-1}, I = 0.0. (b) Combined suction and injection, u_{in} = 12.7ms^{-1} and u(0) = 7.71ms^{-1}, I ≃ 0.65 — 8

Fig.1.4 An Aaberg exhaust hood with a back wall ——— 11

Fig.1.5 The Aaberg ventilator unit suspended 3.5d above the floor. Smoke is released on the floor beneath the ventilator ——— 13

Fig.1.6 Contours of constant air speed for an Aaberg exhaust hood as obtained by Høgsted (1987) ——— 14

Fig.1.7 The efficient and recycled flow regions of an Aaberg exhaust hood proposed by Høgsted (1987). The shading illustrates the efficient flow region ——— 16

Fig.1.8 The deflection of the Aaberg flow pattern. The shading illustrates the efficient flow region ——— 16

Fig.1.9. (a) Contours of constant air speed and (b) contours of constant capture efficiency, as obtained by Fletcher and Saunders (1991), for an exhaust hood of dimensions: a ≃ 0.15m, s = 0.037m, b(0) = 7.5mm and operating with u_{in} = 15.5ms^{-1} and u(0) = 7.7ms^{-1} ——— 21

Fig.1.10 Cross-section through the Aaberg slot exhaust hood — 24

Fig.2.1 The three flow regions of the model, (i) the jet flow regions, (ii) the jet-induced flow regions and (iii) the exhaust flow region ——— 31

Fig.2.2 Schematic diagram of the jet illustrating the coordinate system and notation ——— 34

Fig.2.3(a) The flow induced by a two-dimensional plane jet which discharges perpendicular to a straight wall as observed by Lippisch (1958) ——— 45

Fig.2.3(b) The flow induced by a two-dimensional turbulent wall jet issuing parallel to a straight wall as observed by Sigalla (1958a). The arrow indicates the position of the orifice of the jet ——— 45

Fig.3.1 The geometry and coordinate system used for the sink flow ——— 57

Fig.3.2 The geometry and coordinate systems used for the induced flow ——— 64

Fig.3.3 Streamlines modelling the Aaberg flow for a laminar injection of fluid, $\lambda = 1/3$, (a) $G_L = 0.05$, (b) $G_L = 0.5$ and (c) $G_L = 5$ ——— 71

Fig.3.4 Lines of constant speed in front of the hood for a laminar injection of fluid, $\lambda = 1/3$, (a) $G_L = 0.05$, (b) $G_L = 0.5$ and (c) $G_L = 5$ ——— 72

Fig.3.5 Variation in the centre-line velocity with distance from the inlet for laminar injections of fluid, $G_L = 0.05$, 0.5 and 5 ——— 74

Fig.3.6 Streamlines modelling the Aaberg flow for a turbulent injection of fluid, $\lambda = 1/2$, (a) $G_T = 0.2$, (b) $G_T = 2$ and (c) $G_T = 20$ ——— 76

Fig.3.7 Lines of constant speed in front of the hood for a turbulent injection of fluid, $\lambda = 1/2$, (a) $G_T = 0.2$, (b) $G_T = 2$ and (c) $G_T = 20$ ——— 77

Fig.3.8 Variation in the centre-line velocity with distance from the inlet for turbulent injections of fluid, $G_T = 0.2$, 2 and 20 ——— 78

Fig.4.1 The geometry and coordinate system used to model the effect of the exhaust inlet size ——— 85

Fig.4.2 Lines of constant speed modelling the air flow created by an Aaberg exhaust hood operating with $G_T = 2$, (a) $S = 1/8$, (b) $S = 1/4$ and (c) $S = 1/2$ ——— 91

Fig.4.3 Streamlines modelling the air flow created by an Aaberg exhaust hood operating with $G_T = 2$, (a) $S = 1/8$, (b) $S = 1/4$ and (c) $S = 1/2$ ——— 91

Fig.4.4 Variation in the resultant air speed along the centre-line of the Aaberg exhaust hood as a function of the distance, Y, from the inlet ——— 93

Fig.4.5 The geometry and coordinate system used for the ventilator unit ——— 96

Fig.4.6 Streamlines modelling the flow of the ventilator unit, H = 8, for **(a)** G = 0, **(b)** G = 2 and **(c)** G = 4 ——— 102

Fig.4.7 Lines of constant speed in the workplace induced by a ventilator unit, H = 8, for **(a)** G = 0, **(b)** G = 2 and (c) G = 4 ——— 103

Fig.4.8 Variation in the resultant air speed along the floor surface as a function of the ventilator height, H, for **(a)** G = 0, **(b)** G = 2 and **(c)** G = 4 ——— 105

Fig.4.9 Variation in the resultant air speed along the centre-line of the ventilator as a function of the ventilator height, H, for **(a)** G = 0, **(b)** G = 2 and (c) G = 4 ——— 107

Fig.5.1 The geometry and coordinate system used for the radial free jet ——— 115

Fig.5.2 The stream function at the edge of the laminar radial jet as a function of X^* for $K = 10^8$ ——— 141

Fig.5.3 The stream function at the edge of the turbulent radial jet as a function of X^* for K = 10, (i) $\varepsilon/\varepsilon_o$ as given by equation (5.6.22a), (ii) $\varepsilon/\varepsilon_o$ as given by equation (5.6.22b), (iii) Tuve (1953), (iv) Squire (1955) and Heskestad (1966), (v) Patel (1979), (vi) Poreh and Cermak (1959) and Witze and Dwyer (1976) ——— 144

Fig.6.1 The geometry and coordinate system for the axisymmetric Aaberg exhaust hood ——— 149

Fig.6.2 The solution domain and the boundary conditions used to model the axisymmetric Aaberg exhaust hood ——— 154

Fig.6.3(a) Lines of constant air speed in front of an axisymmetric flanged exhaust hood operating under suction alone, a = 0.1515m, s = 0.037m, $u_{in} = 15.5 ms^{-1}$, Fletcher and Saunders (1993) ——— 159

Fig.6.3(b) Lines of constant air speed deduced from the model for an axisymmetric flanged exhaust hood operating under suction alone, K = 0, S = 0.244, R_{in} = 138132 ——— 159

Fig.6.4(a) Lines of constant air speed in front of an axisymmetric flanged exhaust hood reinforced by a radial jet flow, a = 0.1515m, s = 0.037m, u_{in} = 15.5ms^{-1}, b(0) = 0.0075m, u(0) = 7.7ms^{-1}, Fletcher and Saunders (1993) ——— 162

Fig.6.4(b) Lines of constant air speed deduced from the model for an axisymmetric flanged exhaust hood reinforced by a turbulent radial jet, K = 10.1, S = 0.244, R_{in} = 40.7 —— 162

Fig.6.5 Variation in the centre-line air speed, u/u_{in}, as a function of the distance, y/a, along the hood's centre-line for (a) I = 0.0, (b) I = 0.5, (c) I = 0.9 and (d) I = 1.95. ■ Pedersen (1993), —— Model ——— 164

Fig.7.1 A schematic diagram of the Aaberg slot exhaust hood – 171

Fig.7.2 The geometry and coordinate system of the ASE model – 171

Fig.7.3 The variation in the dimensionless resultant air speed, Q, as a function of Y along X = 0.174, (a) I = 0.0, (b) I = 0.5, (c) I = 0.9 and (d) I = 2.5 —— 179

Fig.7.4 The variation in the dimensionless resultant air speed, Q, as a function of X from Y = 5.22, (a) I = 0.9 and (b) I = 1.5 ——— 183

Fig.7.5 Sets of streamlines modelling the ASE flow pattern predicted by the wall jet model, (a) G_W = 0.00, (b) G_W = 14.9, (c) G_W = 20.0 and (d) G_W = 33.4. The shaded area represents the predicted effective capture region ——— 185

Fig.7.6 Cross-section through the Aaberg slot exhaust – illustrating the back wall design modification ——— 189

Fig.8.1 A two-dimensional rectangular control volume ——— 199

Fig.8.2 The streamlines for the flow around an axisymmetric Aaberg exhaust hood, the volume flux of air between adjacent streamlines is denoted by $\Delta\psi$, (a) I = 0.0, $\Delta\psi \propto 2.5\text{x}10^{-3}\text{m}^3\text{s}^{-1}$, (b) I = 0.5, $\Delta\psi \propto 1\text{x}10^{-2}\text{m}^3\text{s}^{-1}$, (c) I = 0.9, $\Delta\psi \propto 1\text{x}10^{-2}\text{m}^3\text{s}^{-1}$ and (d) I = 1.95, $\Delta\psi \propto 1\text{x}10^{-2}\text{m}^3\text{s}^{-1}$ ——— 206

Fig.8.3 The variation in the resultant air speed, u/u_{in}, along the centre-line of the axisymmetric exhaust hood, showing the present CFD results (– – –), the model (——) and the experimental results of Pedersen (1993) (■), for (a) I = 0.0, (b) I = 0.5, (c) I = 0.9 and (d) I = 1.95 —— 208

Fig.8.4 Streamlines for the flow around the ASE unit operating at I = 0.0, (a) the CFD model, the volume flux of air between adjacent streamlines $\Delta\psi \propto 8.75\times10^{-3}m^3s^{-1}$ per metre length of the slot, (b) the simple mathematical ASE model, see chapter 7 —— 212

Fig.8.5 Streamlines for the flow around the ASE unit operating at I = 0.5, (a) the CFD model, the volume flux of air between adjacent streamlines $\Delta\psi \propto 3.5\times10^{-2}m^3s^{-1}$ per metre length of the slot, (b) the simple mathematical ASE model, see chapter 7 —— 213

Fig.8.6 Streamlines for the flow around the ASE unit operating at I = 0.9, (a) the CFD model, the volume flux of air between adjacent streamlines $\Delta\psi \propto 3.5\times10^{-2}m^3s^{-1}$ per metre length of the slot, (b) the simple mathematical ASE model, see chapter 7 —— 214

Fig.8.7 Streamlines for the flow around the ASE unit operating at I = 2.5, (a) the CFD model, the volume flux of air between adjacent streamlines $\Delta\psi \propto 3.5\times10^{-2}m^3s^{-1}$ per metre length of the slot, (b) the simple mathematical ASE model, see chapter 7 —— 215

Fig.8.8 The variation in the resultant air speed, q/(m/p), at a height of x/a = 0.174 above the bench surface, showing the present CFD results (– – –), the ASE model (——) and the experimental results of Pedersen (1993) (■), for (a) I = 0.0, (b) I = 0.5, (c) I = 0.9 and (d) I = 2.5 —— 217

List of Tables

Table 5.1 Experimentally determined values of the spreading constant, σ_∞, for the turbulent radial free jet ——— 127

Table 5.2 The coefficients, γ_e, of equation (5.8.6) ——— 143

Table 6.1 The characteristic dimensions of the axisymmetric Aaberg exhaust hoods of Fletcher and Saunders (1993) and Pedersen and Nielsen (1991) and the resulting model operating parameter values ——— 158

CHAPTER ONE

GENERAL INTRODUCTION AND LITERATURE REVIEW

1.1 INTRODUCTION

Production processes may be accompanied by the emission of noxious gases, vapours, dust or heat, which affect the composition and state of the air, and may harm the health and well-being of the workpeople, create distressing working conditions and reduce productivity. To combat these problems and to maintain a prescribed condition and cleanliness of the air which meets the requirements of hygiene some form of ventilation system is needed in the workplace. This ventilation process removes the contaminated air from the building (extract ventilation) and replaces it with clean air (inflow ventilation). Ventilation methods can be classed as local or general. Local extract ventilation is intended for removing polluted air at source to prevent the dispersal of impurities throughout the building. The incoming air replaces the air removed by the local exhaust. General ventilation is required whenever it is impossible or impractical to use local exhaust hoods, for example where the exhaust hood might severely hinder the technological process. Here the role of the incoming air is to dilute the impurity at least to the maximum allowable concentration.

Local exhaust ventilation (LEV) systems are used in many industries for the removal of all types of impurity, both particulate and gaseous or vapour. These impurities are caught at source and so prevented from contaminating the general atmosphere in the workplace and as a consequence the necessary air change is kept to a minimum. Impurities may be removed by being blown towards the outlets by suitably arranged air currents; they may be removed directly by exhaustion or by a combination of air currents and

exhaustion.

A local exhaust ventilation system consists of a collection hood for the capture of the contaminated air and an exhaust duct system along which the contaminated air is transported and discharged into the atmosphere, either directly or through cleaning equipment. The main requirement of the collection hood is that it should capture the maximum amount of impurity with the minimum amount of air consumed and without interfering with the technological process. A well-functioning local exhaust hood is therefore characterized by a high concentration of pollutant in the exhaust air, by a low volume of ventilation air, and by a low consumption of energy. The factors under the control of the designer in meeting these requirements are the geometry of the hood, its location with respect to the source and the exhaust volumetric flow rate. The geometry of the hood is chosen to suit the particular application, with the hood as close to the source of the contaminant as possible without hindering the technological process. The volumetric flow rates for each hood are determined by the designer and are based on the nature of the process to be controlled and the type of hood selected. The volumetric flow rates must also be capable of overcoming crosscurrents and other background air disturbances which could deflect the stream of impurity from the hood and hence a range of volumetric flow rates are usually recommended for each hood.

1.1.1 Traditional Exhaust Hoods

Although having many inherent weaknesses, the local exhaust ventilation systems used in many of today's industries remain

virtually unchanged in their methods of operation when compared with those introduced in the 1930's. The weaknesses of these LEV systems are as a result of the air flow pattern which characterizes the traditional hood. The traditional hood's air flow pattern is non-directional, as air is exhausted from all directions, and this results in the second characteristic and weakness, namely that the air speed developed in front of the hood decreases almost inversely with the square of the distance from the hood. The capture efficiency of the traditional hood is therefore highly dependent on and influenced by the level of background air disturbances. The variation of the air speed with distance from the hood is of prime importance in the design of a LEV system and a number of empirical formulae for the variation of the centre-line air speed of unflanged hoods have been proposed, see Fletcher (1977). The non-directionality of the air flow pattern further adds to the hood's inefficiency as quantities of clean air, which in many circumstances may have been drawn from behind the hood, are continually being exhausted. A typical air flow pattern developed by the traditional exhaust hood is shown schematically in Fig.1.1(a). Minor improvements have been made by introducing a flange to the exhaust which limits the directions from which the exhaust can draw air, see for example Fletcher (1978). However, the high rate of decrease of the air velocity in front of the hood remains. Typical profiles of constant air speed and streamlines for a traditional flanged hood with a circular exhaust opening, of diameter d, are shown in Fig.1.1(b), where the speed of each profile is labelled as a percentage of the air speed at the face of the exhaust opening. As a result of these drawbacks traditional suction devices, for example

hoses, are often very difficult to fit into working conditions as they have to be installed close to the technological processes and often interfere with the work or are pushed aside by the workers.

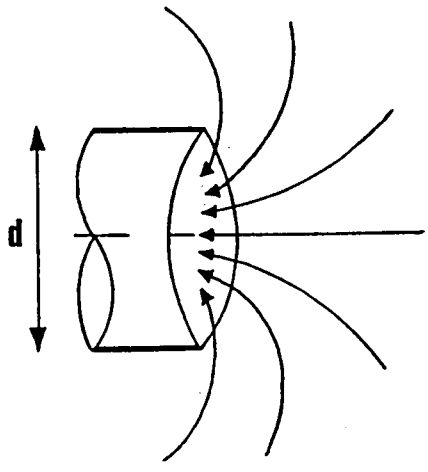

Fig.1.1(a) The non-directional flow of a traditional LEV hood.

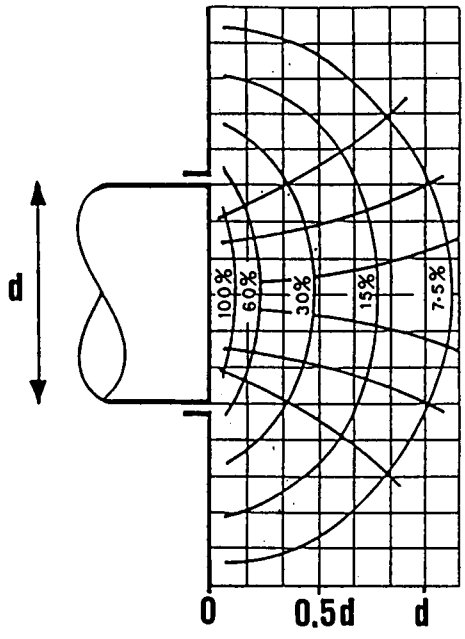

Fig.1.1(b) Air speed profiles of a traditional flanged LEV hood, Greenough (1988).

1.1.2 The Aaberg Principle

In 1965 a new reinforced exhaust system (REEXS) was introduced by the Danish manufacturer C.P. Aaberg. By combining two well-known flows used in ventilation technology, namely injection and exhaustion, Aaberg demonstrated that it is possible to enhance the air speeds generated by traditional hoods as well as achieve a directional air flow pattern. Through a balanced combination of the injection and exhaustion flows, known as the Aaberg principle in LEV technology, a movement of air which consists of two well-defined regions can be created towards the exhaust. Air moving in the first

region is drawn directly towards the exhaust inlet whilst air in the second region is led away from the exhaust inlet by the injection flow. In its design the Aaberg exhaust hood is very similar to a traditional flanged hood. However, it is fitted with a flange through which air can be ejected radially from a narrow slot. A cross-section through the Aaberg exhaust hood, illustrating the Aaberg principle, is shown schematically in Fig.1.2.

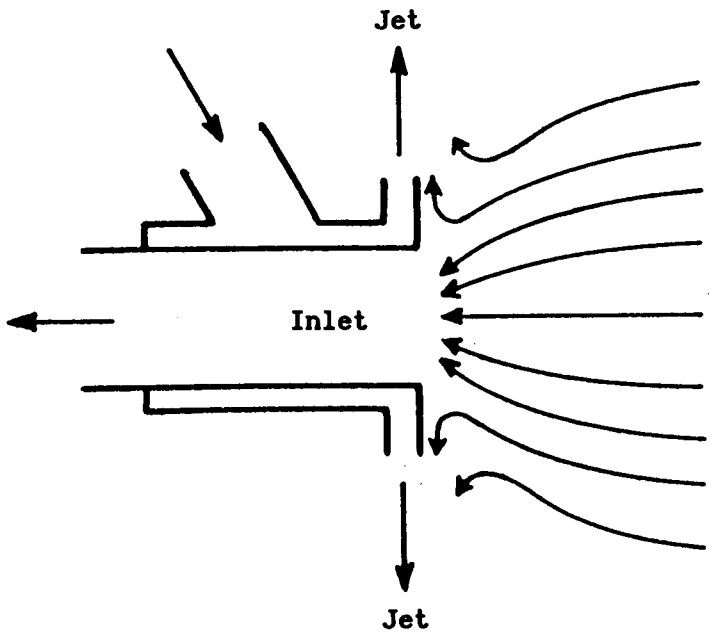

Fig.1.2 A schematic representation of the Aaberg principle.

The dramatic effect which is caused by the blowing jet on the hood's overall air flow can be explained as follows: due to the friction developed at the radial jet/air interface an entrainment flow develops which, under the correct conditions, has the property of removing the clean air from in front of the hood (the recycled flow) as well as enhancing and concentrating the exhaust's suction in a zone along the hood's longitudinal axis (the efficient flow).

This results in quite new profiles of constant air speed in front of the exhaust opening and a directional exhaust capable of creating a flow towards the opening at distances of up to 10 times the exhaust diameter, see Høgsted (1987). Although replacement air should still be supplied the Aaberg exhaust works with significantly smaller quantities of air than traditional exhausts. This, together with a higher concentration of pollutant in the exhaust air, makes the Aaberg process for limiting pollutant emission less expensive and more effective than traditional methods. The performance differences between a conventional LEV system and the Aaberg system are further highlighted in Fig.1.3. Figure 1.3(a) depicts a traditional flanged exhaust hood of inlet radius s = 0.037 m and face velocity of u_{in} = 12.7 ms^{-1}, and clearly shows that operating under suction alone the vast majority of the pollutant enters the environment and that only a few wisps of the contaminant are successfully exhausted. The contaminant is modelled as a continuous release of smoke from a burning pellet located along the hood's longitudinal axis at five inlet diameters from the face of the inlet. In contrast, Fig.1.3(b) depicts a hood operating under the same inlet conditions but which is now reinforced by a radial jet of air. The exhaust flange has a radius of a $\simeq$ 0.15 m and the jet issues through a nozzle of width b(0) = 8.0 mm with an average speed of u(0) = 7.71 ms^{-1}. The volume flux of fluid exhausted is approximately 90% of that injected. The striking effect achieved by the combination of the exhaustion and injection air flows is very clear as now the vast majority of the contaminant is contained in a narrow zone along the hood's longitudinal axis and is drawn directly towards the exhaust inlet.

(a)

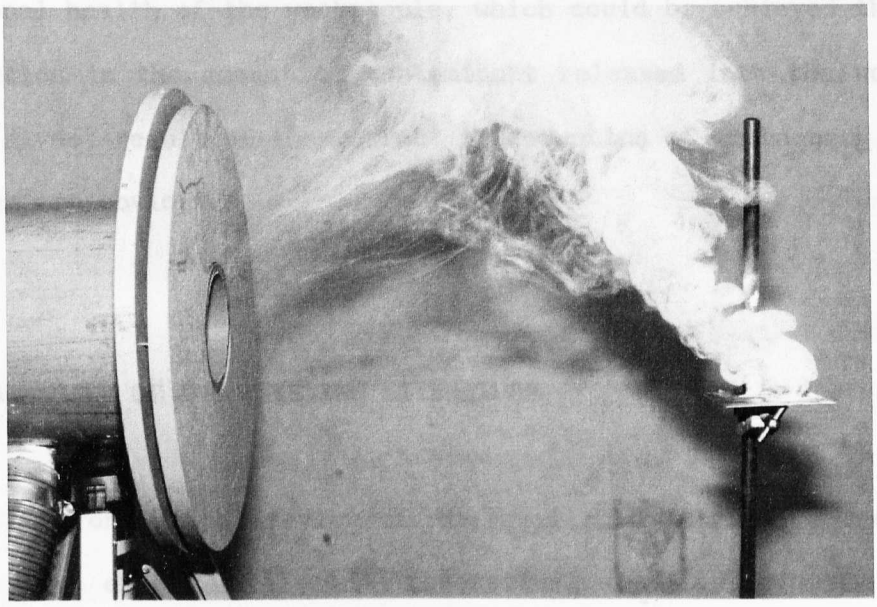

(b)

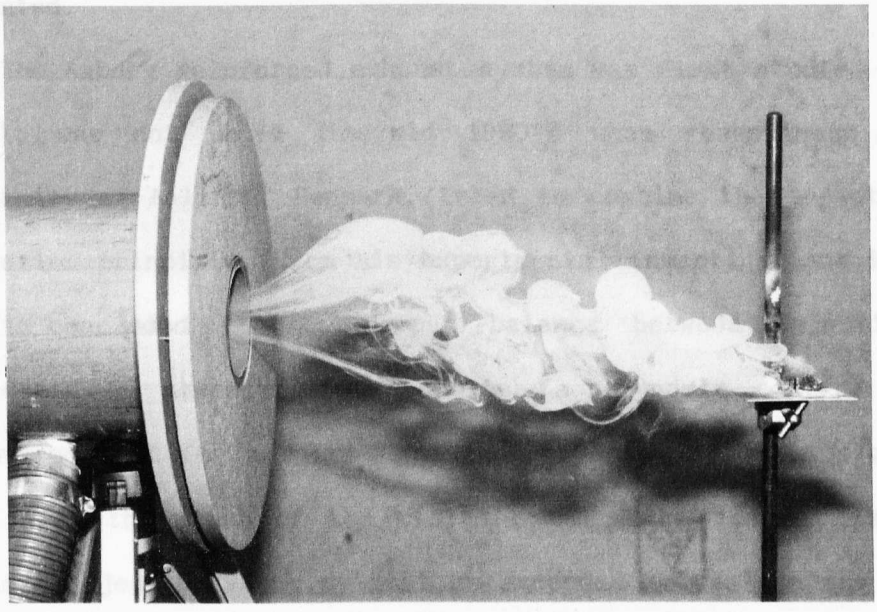

Fig.1.3 Capture of tracer gas released at 5d from an exhaust hood of dimensions: a ≃ 0.15 m, s = 0.037 m, b(0) = 8.0 mm; courtesy of the Health and Safety Executive, Research Division, Sheffield, England. (a) Suction alone, u_{in} = 12.7 ms^{-1}, I = 0.0. (b) Combined suction and injection, u_{in} = 12.7 ms^{-1} and u(0) = 7.71 ms^{-1}, I ≃ 0.65.

The numerous benefits, both to the environment and to the personal health of the workpeople, which could be achieved through a reduction in the amount of contaminant released into the workplace as a direct result of the correct introduction of the Aaberg exhaust system are obvious.

1.2 A REVIEW OF THE EXISTING LITERATURE

A chronological review of the available literature concerning both the experimental and theoretical aspects of the Aaberg principle applied to local exhaust ventilation systems is now presented.

The Aaberg reinforced exhaust system was first studied in 1965 but it was not until the mid 1980's when researchers at the University of Aalborg, Denmark, tried to combine the injection and exhaustion principle. From his experimental investigations Hyldgård (1987) concluded that a proper balance between injection and exhaustion is necessary to establish aerodynamic control and he discovered that for a given hood geometry and injection slot width b(0), i.e. the width of the slot through which the jet issues, a critical injection velocity must be exceeded to realize the desired air flow pattern. Hyldgård (1987) defined the critical injection velocity as the minimum initial velocity of the jet needed to prevent the jet of air being captured by the exhaust opening. Below the critical velocity the hood will be less effective than a conventional hood as the flow will 'short-circuit' as the suction captures the radial jet. His results showed that increasing the

injection velocity above the critical value further increased the air speed in the efficient flow region but reduced its width as the injection entrained more air. Aiming for greater energy efficiency and quieter operation Hyldgård developed and tested a new hood and through a series of experiments sought to reduce the injection velocity to a minimum without destroying the desired effect. He found that the critical injection velocity is dependent upon the direction of the injection flow and demonstrated that the critical injection velocity can be lowered if the exhaust flange is orientated at 105° to the axis of symmetry of the hood. Other experiments conducted by Hyldgård (1987) investigated the effects of the injection slot width on the critical injection velocity. Previously, very small injection slot widths, e.g. b(0) = 0.15 mm, had been used with very high injection velocities, e.g. u(0) = 30 - 50 ms^{-1}, which required high injection pressures and generated high levels of noise. Hyldgård found that the critical injection velocity is directly proportional to the exhaust flow rate and that for a given exhaust flow rate the critical injection velocity can be reduced by increasing the injection slot width. This is because the structure of the flow in the radial jet depends upon its momentum flux and not the initial speed of the air jet. Hyldgård then conducted experiments on the Aaberg exhaust hood for various ratios of the momentum flow in the exhaust to the injection where the momentum ratio, I, is defined as

$$I = \frac{m_j \, u(0)}{m \, u_{in}} \qquad (1.2.1)$$

where m_j is the volume flux of fluid injected with initial speed u(0) and m is the volume flux of fluid exhausted with face speed

u_{in}. With an Aaberg exhaust hood operating at the critical injection velocity Hyldgård (1987) showed that if the width of the injection slot was chosen between b(0) = 2 mm and b(0) = 2.5 mm then the ratio, I, could be minimized, the minimal value being between I = 0.4 and I = 0.5. Taking into account the energy consumption of the injection fan and the generation of noise an injection slot width of b(0) = 2.5 mm was chosen by Hyldgård as the optimum size.

Comparisons made by Hyldgård (1987) between the air speeds created by an Aaberg exhaust hood and those of a conventional exhaust highlighted the superiority of the former in design and function. Hyldgård introduced the notion of a clutch velocity, defining it as the velocity of the air in front of the hood caused by the hood, and operating two Aaberg exhaust hoods, one standard and one with a back wall, see Fig.1.4, he made measurements of it.

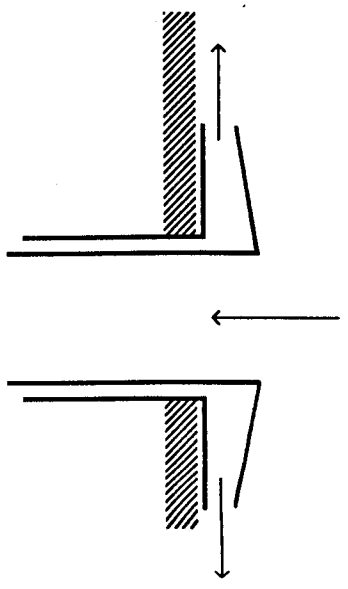

Fig.1.4 An Aaberg exhaust hood with a back wall.

The ratio between the clutch velocity and the velocity of the pollutant is a decisive factor in determining whether or not the exhaust will collect the pollutant. The results he obtained demonstrated the effectiveness of the injection which significantly enhanced the clutch velocities as well as the range over which contaminant capture occurs. Simply by increasing the injection velocity Hyldgård noticed that the clutch velocity along the centre-line increased dramatically and that this effect, together with a narrowing of the efficient flow region, resulted in a more concentrated exhaust over larger distances. Hyldgård also found that incorporating a back wall, although reducing the differences between the clutch velocity in situations with and without injection, as the wall acts as a flange, had the advantage of allowing the critical injection velocity to be significantly reduced. Thus, with a back wall the Aaberg hood can induce a specified clutch velocity, required for the capture of a particular pollutant, at noise and energy levels lower than possible with a standard hood.

Experiments were also performed on the Aaberg principle by Høgsted (1987), who had access to Aaberg exhaust hoods in the form of both a local ventilation system and a ventilator unit, see Fig.1.5. Høgsted gives a detailed description of some experimental work on the aerodynamic control of an Aaberg exhaust hood. Using a ratio of injected to exhausted air quantities which is typically 1:10 he achieved aerodynamic control and described the injection effect as creating a selective hood with no air drawn from behind the hood as in flanged and unflanged traditional hoods. In a comparison with those of traditional hoods, see Fig.1.1(b), Høgsted

Fig.1.5 The Aaberg ventilator unit suspended 3.5d above the floor. Smoke is released on the floor beneath the ventilator.

describes the resulting flow as having quite different air speed profiles in relation to the exhaust opening with the individual contours of constant speed regarded as three-dimensional spherical surfaces with centres at -2d, see Fig.1.6. In Fig.1.6 the speed contours for 0.30 ms^{-1} and 0.40 ms^{-1} are only drawn in the central area as measurements did not cover the shaded area.

In Høgsted (1987), results of laboratory tests performed on a freely suspended Aaberg exhaust hood whose longitudinal axis pointed vertically downwards, as in Fig.1.5, are presented. Measurements were taken using a non-directionally sensitive low velocity flow

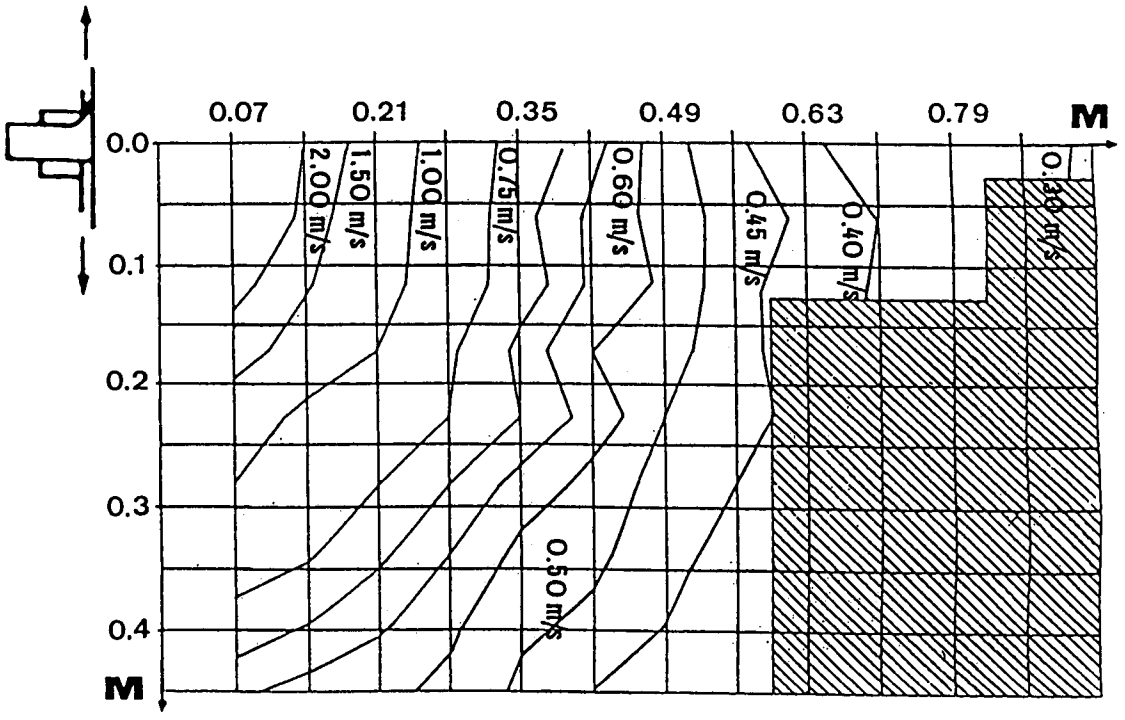

Fig.1.6 Contours of constant air speed for an Aaberg exhaust hood as obtained by Høgsted (1987).

analyser (LVA) and the objective of the investigations were to determine contours of constant speed, streamlines and ultimately the efficient flow region. Experiments to examine the efficient flow region of the suspended Aaberg exhaust hood revealed that not all of the air moving towards the hood is captured by the exhaust inlet but some is drawn away from the inlet in the injection flow. During smoke experiments Høgsted discovered that smoke released close to the hood's centre-line was totally evacuated via the exhaust opening but if released some distance from the centre-line was captured in the injection flow and blown back into the room. This led Høgsted to propose that the region in front of the hood could be theoretically divided into two distinct regions, namely an efficient region and an inefficient (or recycled) region. Capture efficiencies are assumed

to be 100% and 0% in the efficient and recycled regions, respectively, with the two regions being separated by a so-called A-surface, see Fig.1.7. The capture efficiency, α_{cap}, of the exhaust system is measured using tracer gas techniques and is defined as

$$\alpha_{cap} = \frac{C_e - C_{bc}}{C_r} \qquad (1.2.2)$$

where C_e is the concentration of tracer gas in the exhaust, C_{bc} is the mean background concentration and C_r is the reference concentration which is determined by capturing 100% of the tracer gas.

To further investigate the behaviour of the Aaberg flow pattern, obstacles were introduced and the deflection of the flow pattern monitored. Results of these investigations show that the Aaberg REEXS exhibits some quite exceptional and extremely interesting qualities. Experiments by Høgsted (1987) show that smoke burnt from behind a vertical plate placed in front of a local Aaberg REEXS can be exhausted even though the combustion creates a strong thermal influence. Experiments carried out by Høgsted on an Aaberg ventilator unit suspended above the floor surface of the workplace show that smoke released at floor level far from the hood's centre-line is captured. The floor, thought of as the obstacle in the experiment, deflects the flow pattern and the efficient flow region of the hood radially outwards over the floor surface and thereby creates a suction effect over a considerable surface area, see Fig.1.8. In fact, Høgsted reports that the efficient region of a ventilator unit suspended 3.5d above the floor is deflected over the floor surface to a radial distance from the centre-line of up to 5 or 6d.

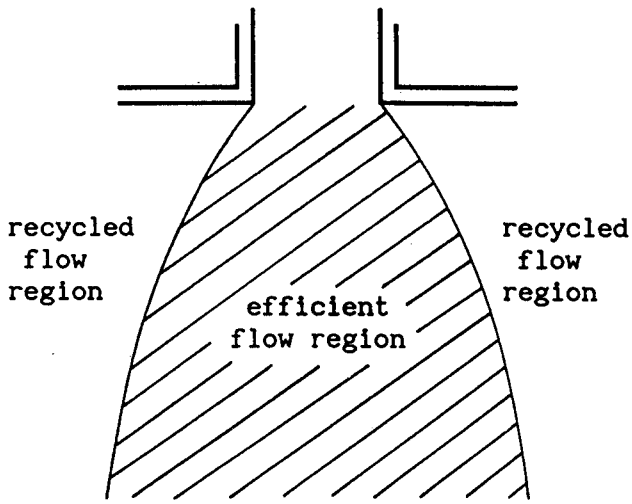

Fig. 1.7 The efficient and recycled flow regions of an Aaberg exhaust hood proposed by Høgsted (1987). The shading illustrates the efficient flow region.

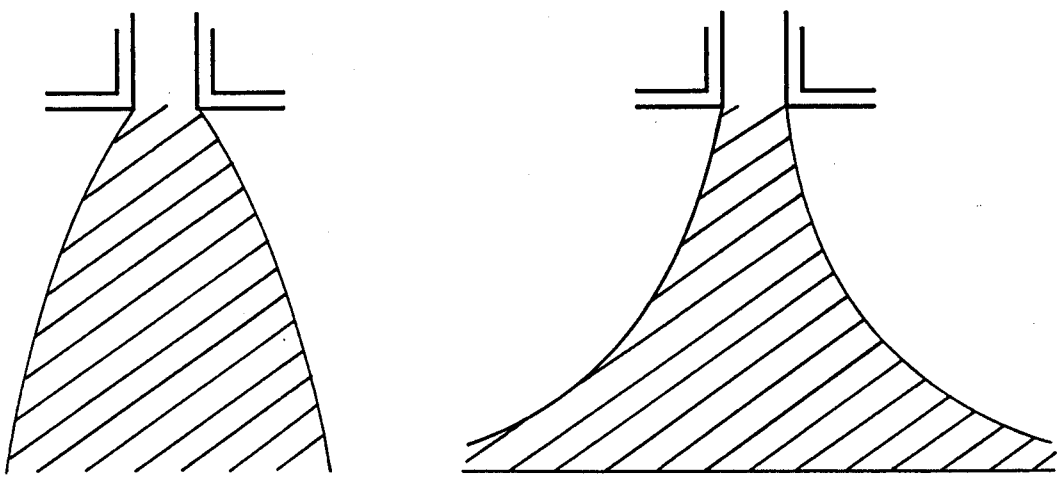

a) Undeflected flow.

b) Deflected flow.

Fig. 1.8 The deflection of the Aaberg flow pattern. The shading illustrates the efficient flow region.

Høgsted is cautious when suggesting possible applications of the Aaberg principle and explains that although a trial of the system exists in practice it is not yet applicable to industry as it requires careful adjustment to each operating situation and that far from all the flow influencing parameters have been determined. In order to avoid incorrect application and consequently disappointing results Høgsted (1987) underlines the necessity to understand how the system works and lists some basic rules to follow regarding the application of an Aaberg REEXS. These include recommendations for the correct installation of the hood and particularly for the freedom of the injection flow to spread unhindered thereby avoiding undesirable flow patterns.

More recently, Pedersen and Nielsen (1991) have described how the capture efficiency is determined by the ratio of momentum flows in the exhaust and injection, I, see equation (1.2.1). They also discovered that the exhaust velocity, c.f. Hyldgård's (1987) clutch velocity, depends on the momentum ratio, I, and found that the lowest possible ratio to avoid a 'short-circuit' is $I \simeq 0.1$. In a comparison made between the Aaberg REEXS and traditional exhaust systems Pedersen and Nielsen (1991) comment on the superiority of the Aaberg REEXS and state that in order to induce air speeds at 6d from the exhaust inlet which are comparable with a hood operating at $I = 0.1$ the volume flow rate of the suction of a traditional hood ($I = 0.0$) would have to be increased by a factor of between 4 and 11. In other experiments Pedersen and Nielsen measure the centre-line velocity of three types of Aaberg flow, namely, axisymmetric, three-dimensional and three-dimensional wall jet flow

for various values of the momentum ratio, I. By attaching an exhaust hood to the edge of a bench with its centre-line parallel to the bench surface Pedersen and Nielsen (1991) were able to change the flow from an axisymmetric flow to a three-dimensional flow. A three-dimensional wall jet flow was achieved by supplying the injection air along a plane surface.

The results obtained by Pedersen and Nielsen (1991) do not agree exactly with the theoretical capture regions proposed by Høgsted (1987). Indeed, contrary to the postulated 100% capture efficiency inside the A-surface, see Høgsted (1987), Pedersen and Nielsen (1991) found that the capture efficiency decreased with increasing distance from the centre-line and a 100% to 0% discontinuity in the efficiency at the A-surface was not observed. Pedersen and Nielsen (1991) argue that due to the fluid flow circling around the longitudinal axis to the exhaust opening and to the turbulence of the flow, the capture efficiency close to the A-surface is reduced. The rotation of the flow towards the exhaust inlet observed by Pedersen and Nielsen (1991) is induced by a swirling radial jet. Pedersen and Nielsen state that due to the high exhaust velocity induced, the Aaberg REEXS is able to maintain a high capture efficiency in disturbed surroundings where the capture efficiency of a traditional hood would be approximately zero. They advise that a low value of the ratio I should be chosen for maximum capture efficiency (as the efficient flow region is then broad) whilst making sure that the exhaust velocity necessary to capture the particular contaminant is sufficient. They conclude that the momentum ratio determines the induced velocity and the region of high capture efficiency. Pedersen and Nielsen's capture efficiency

results represent the maximum theoretical capture efficiency for the given pollutant source. In practice, background disturbances, e.g. cross draughts, temperature gradients, etc., would have to be taken into consideration when calculating the capture efficiency.

Experimental research into the Aaberg principle has also been undertaken by Fletcher and Saunders (1991,1993) and they have explored two main factors involved in the hood's operation, namely induced velocities and capture efficiencies. Velocity measurements taken using a DANTEC low velocity flow analyser with an omni-directional probe were used to produce contours of equal air speed. Fletcher and Saunders (1991) regarded air speeds above 0.25 ms^{-1} to be those induced by the hood and those below 0.25 ms^{-1} to be due to background air disturbances. With an Aaberg exhaust hood operating under combined suction and injection Fletcher and Saunders (1991) noticed that at the edge of the exhaust flange air was either drawn into the exhaust inlet or caught in the injection flow, i.e. a dividing surface between the two flows exists. They found that by operating an Aaberg exhaust hood of dimensions: $a \simeq 0.15$ m, $s = 0.037$ m and $b(0) = 7.5$ mm at the ratio of $I \simeq 0.4$, i.e. with $u_{in} = 15.5$ ms^{-1} and $u(0) = 7.7$ ms^{-1}, it was possible to achieve controlled air movements towards the hood of over 0.25 ms^{-1}, and hence overcome the level of background air disturbances, at distances of up to 9d away from the hood along the centre-line, see Fig.1.9(a). This result compares favourably with the length of the controlled air flow pattern, of 10d, obtained by Høgsted (1987).

Capture efficiencies of an Aaberg exhaust hood were measured by Fletcher and Saunders (1991) using a tracer gas technique. The

tracer gas used was a neutrally-buoyant mixture of 15% sulphur hexafluoride with helium and a MIRAN 1A-CVF infra-red gas analyser was used to measure tracer gas concentrations. To obtain better estimates of the capture efficiency, allowances were made for the amounts of tracer gas re-entering the atmosphere via the injection flow and creating a different background concentration at each measurement point. The experimental results obtained by Fletcher and Saunders (1991) suggest that contaminants located outside the capture region normally associated with a conventional hood will be carried towards the Aaberg exhaust hood mainly by the jet-induced flow. Once inside this capture region the contaminant will be drawn into the exhaust inlet by the suction. Profiles of capture efficiencies were found to be similar to the contours of equal air speed but the boundaries were in terms of percentage captures as opposed to air speeds, see Fig.1.9(b). Fletcher and Saunders (1991) showed that in areas where the induced air speeds are comparable to the level of background air movements low captures are obtained. Background disturbances in the laboratory gave the low capture envelopes, below 50%, ill-defined boundaries so only those above 50% were plotted. The main result they obtained was that inside the A-surface the capture efficiency is not constant but decreases with increasing distance along the centre-line from the exhaust inlet. This result is in agreement with the observations of Pedersen and Nielsen (1991). Fletcher and Saunders (1991) found that the size of the capture region created by a controlled Aaberg hood, operating at $I \propto 0.4$, was very encouraging. The 100% capture boundary enclosed a significant area and intersected the centre-line at a distance of approximately 4d from the exhaust inlet, although the width of the

(a)

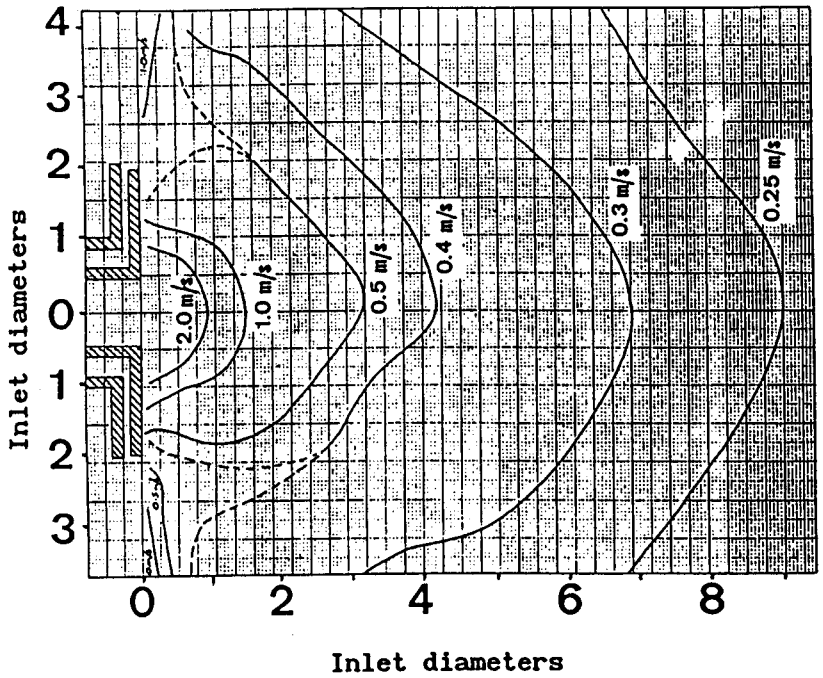

(b)

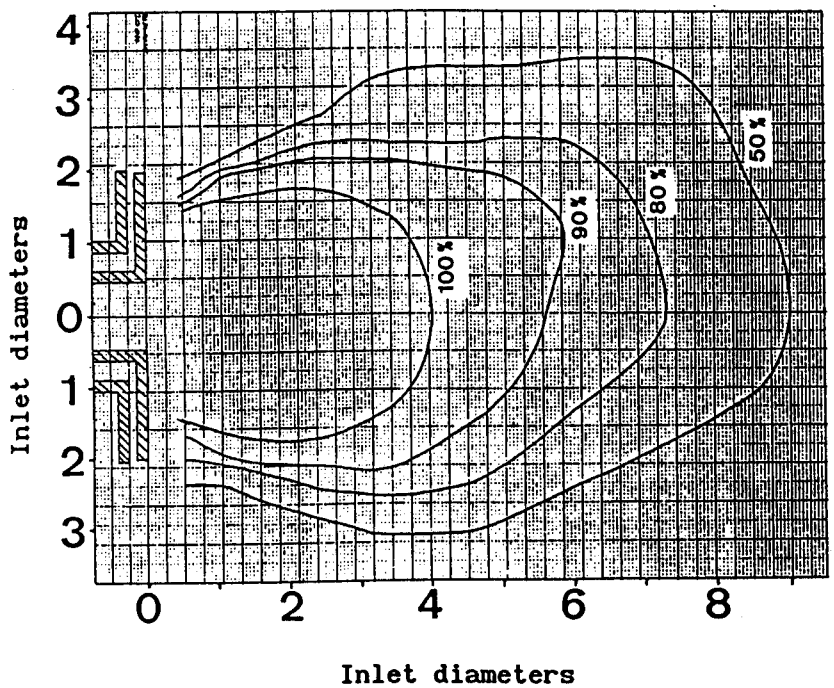

Fig.1.9 (a) Contours of constant air speed and (b) contours of constant capture efficiency, as obtained by Fletcher and Saunders (1991), for an exhaust hood of dimensions: a ≃ 0.15 m, s = 0.037 m, b(0) = 7.5 mm and operating with u_{in} = 15.5 ms^{-1} and u(0) = 7.7 ms^{-1}.

boundary appeared to be limited to the diameter of the flange, see Fig.1.9(b). The 50% capture line, see Fig.1.9(b), was found to cut the centre-line at approximately 9d from the face of the exhaust inlet and compared well with the 0.25 ms^{-1} air speed boundary. The significance of this result is that even though the hood induces adequate clutch velocities to overcome the background air disturbances, the capture of contaminant from this range is not complete due to the diffusion of the contaminant into the surrounding air. By reducing the volume flow of the suction, to $I \propto 0.6$, capture envelopes intersecting the centre-line at similar distances were produced. However, the width of the capture envelopes close to the hood face appeared to be narrower. In accordance with the results of Pedersen and Nielsen (1991), Fletcher and Saunders (1991) found that the momentum ratio of the injection to exhaustion flows affects the size and profile of the capture region. By reducing the injection velocity, and hence I, they found it was possible to augment the overall size of the capture region. However, a large proportion of the capture region was then in regions of low air speed and therefore in an industrial environment, as opposed to under laboratory conditions, capture from this region would be highly dependent on the level of background air disturbances. Thus, the true capture region would be much smaller than the apparent capture region observed experimentally. In practical situations, decreasing the injection will therefore not necessarily increase the hood's capture range as the results of Fletcher and Saunders (1991) might imply.

Fletcher and Saunders (1991) also observed that the largest capture region was produced by a hood operating under suction alone,

contradicting the findings deduced from the air speed contours. However, the contours of equal air speed obtained by Fletcher and Saunders (1991) show that when operating under suction alone the majority of the capture region has been induced from regions where the air speeds are at a background level. This result may be explained as follows: under laboratory conditions a hood operating under suction alone does not create any 'negative' disturbances in the room and air is drawn slowly towards the exhaust and hence capture occurs at large distances. However, when the radial jet is employed, disturbances in the ambient air are produced and the tracer gas, modelling the contaminant, is more easily dispersed. Large capture velocities are then required to overcome the increasing level of air disturbance, thus reducing (narrowing) the overall capture region.

In conclusion, Fletcher and Saunders (1991) emphasize the need for experiments to be carried out in conditions more representative of normal working environments so that more realistic performance differences between conventional local exhaust systems and the Aaberg system can be established. They suggest that experiments should be conducted under laboratory conditions where controlled levels of background air movements for suction and injection can be maintained.

Originally inducing a three-dimensional axisymmetric flow the Aaberg principle has been implemented in a bench hood design with a slot exhaust, rather than a circular exhaust, to produce an approximately two-dimensional flow, see Fig.1.10. The flow pattern created by the hood design, termed a bench exhaust hood or an Aaberg

slot exhaust (ASE) hood, has been studied by Pedersen (1991a). Pedersen (1991a) conducted various experiments on the ASE, operating both as a conventional exhaust and as a REEXS, under different simulated external influences which in practice affect the capture efficiency of an exhaust system. With a slot exhaust in a cross flow of between 0.0 ms^{-1} and 0.6 ms^{-1} Pedersen (1991a) has demonstrated that the average capture efficiency can be increased almost three-fold, from 27% to 71%, owing to the application of the REEXS principle. Two-dimensional slot exhausts are commonly used as welding exhausts and in connection with the welding process the location of an Aaberg slot exhaust compared with the orientation of the contaminants has been optimized by Pedersen (1991a). He found that a vertical distance between the exhaust slot and the surface of the bench of h_s = 0.4 m, see Fig.1.10, and a momentum ratio of approximately I = 0.6, provided the most efficient solution in disturbed surroundings. Pedersen (1991a) also gives general guidelines for the use of the ASE system in other applications.

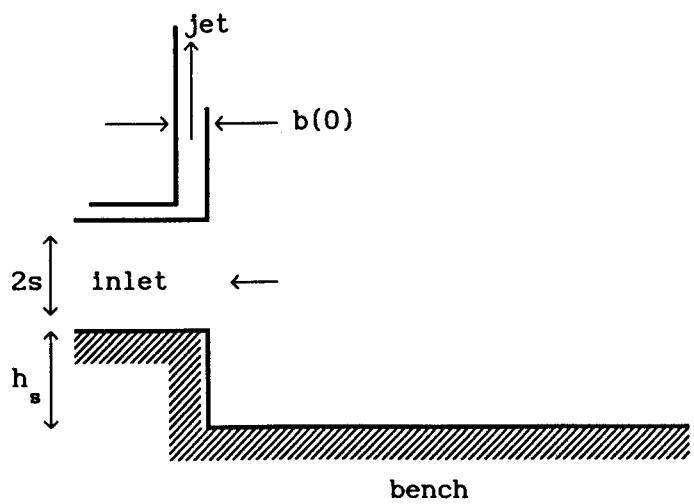

Fig.1.10 Cross-section through the Aaberg slot exhaust hood.

The most recent publication which examines the Aaberg principle is that of Fletcher and Saunders (1993) who describe the results of experiments examining the efficiency of axisymmetric hoods of two different sizes. Fletcher and Saunders (1993) examine the percentage capture of contaminant on the hood's centre-line for different volume flow rates of air ejected for a fixed quantity of inlet air exhausted. They demonstrate that when operating with suction alone the capture efficiency drops off rapidly for distances greater than two inlet diameters from the hood; whilst the capture distance rapidly increases to a maximum, achieved when $I \simeq 0.6$, and then slowly falls as the volume of the ejected air is further increased, i.e. for $I > 0.6$. By examining the distance along the centre-line to the position of 90% capture efficiency as a function of the momentum ratio, I, with the injection slot width, b(0), used as the parameter in the experiment, Fletcher and Saunders (1993) also show that the flow is independent of the injection slot width, thus contradicting the findings of Hyldgård (1987). The range of injection slot widths examined in the experiments was between $b(0) = 1$ mm and $b(0) = 7.5$ mm. The two hoods studied, although of slightly different design, were found to perform very similarly and only very small differences in the distance to 90% capture were observed. Fletcher and Saunders (1993) attribute the fall in the distance to 90% capture, observed for $I > 0.6$, to the amount of contaminated air being drawn towards the inlet, by the jet-induced flow, exceeding the amount of air being exhausted by the suction opening and thus causing a 'build up' of contaminant. In conclusion Fletcher and Saunders (1993) state that capture can be effected at much larger distances by a LEV hood with a blowing jet than by an unassisted

hood and that a value of I = 0.6 gives a large capture distance whilst being clear of the range of values of I where rapid changes in the distance to 90% capture occur.

1.3 CONCLUSIONS

Experimental studies have explored two main factors involved in the hood's operation, namely induced velocities and capture efficiencies and as a result of these studies the Aaberg exhaust hood has been described as providing the only effective means of removing airborne contaminants from the breathing zone of an operator, as being far superior to conventional suction and involving lower investment and operating costs. However, although trials of the Aaberg REEXS have been carried out in practice it is not yet applicable to industry as it requires careful adjustment to each operating situation. The most important conclusion drawn from these experimental results is that the flow of the Aaberg exhaust hood is characterized by the ratio of the momentum flows in the exhaust to the injection and that the induced flow travelling towards the exhaust hood is divided into two well-defined regions in which the capture efficiencies are close to 100% and 0%, respectively. The desired air flow pattern has been achieved over a wide range of momentum ratios from I = 0.1 to I = 2.5.

Although the advantages of the Aaberg REEXS over traditional exhaust systems have been demonstrated experimentally, its design and operating conditions have been developed purely on an ad-hoc basis. The cost of laboratory research and equipment involved in the

experimental attempts to maximize the efficiency of an Aaberg exhaust hood is considerable. These costs may be further increased by experimentalists conducting trials in parameter ranges and on hood designs which are unlikely to optimize the flow pattern. A full understanding of the flow characteristics of the REEXS can best be achieved by solving the mathematical equations which describe the underlying fluid mechanics under realistic flow conditions. The aim of the relatively inexpensive fluid dynamics modelling to be presented in the following chapters is to help avoid unnecessary expenditure by accurately modelling the operating conditions and to use the resulting model to make confident predictions as to the typical parameter ranges and design modifications likely to prove beneficial in the hood's operation. In this way the fluid dynamics modelling conducted interactively with experimental research promises to provide a most effective means of developing a full understanding of the Aaberg flow pattern and of how it may be optimized to suit individual operating situations; a necessary step to be taken before the Aaberg exhaust hood can be correctly introduced to industrial applications. It is extremely important to design the REEXS so that the exhaust removes the maximum amount of contaminant, in concentrated form, from the breathing zone of the worker. It may be thought that simply increasing the suction and blowing velocities will reduce the level of contaminant in the room. However, the ratio of these two fluid flows must be carefully adjusted and will depend on both the location and nature of the contaminant. Ideally one would wish to design a hood which collects all of the contaminant with the use of a minimal amount of energy.

CHAPTER TWO

MATHEMATICAL MODELLING : TOOLS, TECHNIQUES AND TERMINOLOGY

2.1 INTRODUCTION

The experimental studies undertaken by Hyldgård (1987), Høgsted (1987), Pedersen and Nielsen (1991) and Fletcher and Saunders (1991,1993) have all concluded that under correctly chosen operating conditions an Aaberg exhaust hood is far superior in its ability to capture airborne contaminants than traditional unassisted exhaust designs. To optimize the efficiency of the Aaberg exhaust hood by experimentation alone is time-consuming and complicated as the operation of the hood depends upon a number of geometric and flow parameters. In the following chapters two-dimensional and three-dimensional axisymmetric models of the Aaberg exhaust hood's air flow pattern will be developed in order to predict what effect different parameters have on the air flow. The aim of this chapter is to assemble the mathematical tools and techniques which will allow us to simplify the problem of modelling the relatively complex air flow pattern induced by the Aaberg exhaust hood and thus assess the effects of the various parameters that control the air flow. In order to obtain a simple mathematical model for the air flow, numerous simplifying assumptions therefore have to be made and the reasons for making them are now described. Also introduced in this chapter are the terms; 'capture speed', 'effective capture region' and 'effective working range'. These terms will allow us to use the models to predict the regions of the air flow from which we expect a high capture efficiency.

2.2 FORMULATION

In this thesis we are primarily interested in determining the fundamental air flow pattern generated by the Aaberg exhaust hood and therefore only the fully developed, steady air flow pattern induced by the hood will be investigated. For the purpose of determining the efficient and recycled flow regions, the contaminant will be assumed to be neutrally-buoyant and spread throughout the entire fluid flow domain and the effects of diffusion will be neglected. Thus the contaminant modelled will follow the streamlines of the air flow. In practice, the fluid flow pattern generated by the Aaberg exhaust hood is such that the Reynolds number is very large and hence an inviscid model is developed for the fluid flow in the region of interest but with the boundary conditions coming from shear-layer solutions. The fluid modelled is air at room temperature, i.e. at about 20°C, and it is assumed to be of constant density, i.e. an incompressible fluid. The equations of motion governing the flow of an incompressible, viscous fluid are then the Navier-Stokes equations, namely the continuity equation and the momentum equation, i.e.

$$\nabla . \mathbf{u} = 0 \qquad (2.2.1a)$$

$$(\mathbf{u}.\nabla)\mathbf{u} = - \nabla P + \nabla^2(\nu_e \mathbf{u}) \; . \qquad (2.2.1b)$$

where $\mathbf{u}$, ρ, $P = p/\rho$ and ν_e are the velocity, pressure and the effective kinematic viscosity of the fluid, respectively. The effective kinematic viscosity, ν_e, consists of the sum of the physical viscosity, ν, and the turbulent viscosity, ε, i.e. $\nu_e = \nu + \varepsilon$. The turbulent viscosity, in contrast to the physical viscosity, is not a property of the fluid but depends strongly on

the state of turbulence and may vary significantly from one point in the flow to another and also from flow to flow. The overall air flow pattern induced by the Aaberg exhaust hood may be considered to be composed of three distinct regions, namely (i) the flow in the jet, (ii) the jet-induced flow and (iii) the exhaust flow, see Fig.2.1. The fluid behaviour in each of the three flow regions is now discussed and the mathematical tools and techniques required to model each flow are presented.

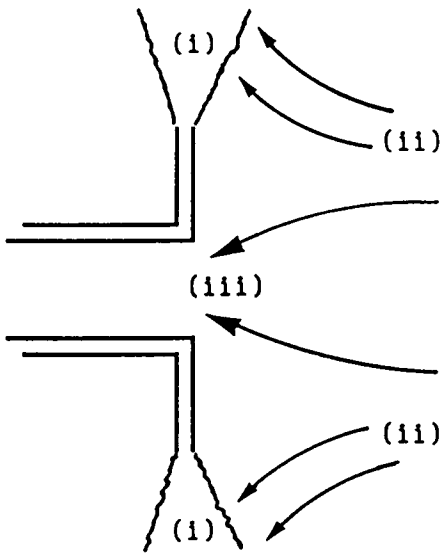

Fig.2.1 The three flow regions of the model, (i) the jet flow regions, (ii) the jet-induced flow regions and (iii) the exhaust flow region.

2.2.1 The Flow in the Jet

Accurately modelling the flow in the jet is very important as the flow conditions at the edge of the jet shear-layer govern the induced inviscid fluid flow which occurs in the majority of the region of interest. In the following chapters two-dimensional and three-dimensional axisymmetric models of the air flow pattern created by the Aaberg exhaust hood will be developed and hence

two-dimensional plane jets and three-dimensional axisymmetric radial jets, for both laminar and turbulent flows, will be investigated. Furthermore, the two-dimensional turbulent wall jet flow which occurs in the Aaberg slot exhaust, see Pedersen (1991a), will also be investigated later.

The two-dimensional plane jet has received a great deal of attention in the literature and there exists numerous theoretical and experimental publications on the subject. A review of the literature concerning the two-dimensional plane jet is given by Schneider (1983), who examines both laminar and turbulent jets and their induced flows. In this study the plane jet solutions used are analogous to the Görtler (1942) solution, where for the turbulent jet the Prandtl constant momentum transfer expression for the eddy viscosity has been adopted, see Schlichting (1968). Comparisons, illustrated in Schlichting (1968), made between the theoretical Görtler (1942) plane jet solution and the results of experiments carried out by Reichardt, see Schlichting (1968), on a two-dimensional plane jet show excellent agreement and for this reason more complicated turbulence models, for example the k-ε turbulence model, requiring a more sophisticated numerical treatment have not been adopted in the present work. A full numerical treatment of the plane turbulent jet is described by Bergstrom (1992).

In contrast, the radial free jet appears to have received very little attention in the literature and a short review of some of the available radial jet literature is now presented. Witze and Dwyer (1976) presented a concise review of the literature concerning the radial jet. They state that the earliest theoretical treatment of

the radial jet was given by Rumer (1949), who performed a mixing length analysis analogous to the Tollmein (1926) plane jet solution. Taliyev (1954) and Abramovich (1963) presented integral solutions of the boundary-layer equations derived from assumed velocity profiles. The publication of Squire (1955) is unusual as he solved the complete Navier-Stokes equations, in spherical polar coordinates, rather than the usual boundary-layer equations. Poreh and Cermak (1959) used a simple eddy viscosity model and derived a solution similar to the Görtler (1942) plane jet results. Rodi (1972) presented results of a numerical technique that used a turbulent kinematic energy/shear stress model. The turbulent radial jet has also been studied by Wood and Chen (1985) who described results of a numerical investigation in which comparisons were made between three different turbulence models and the experimental results of Heskestad (1966). More recently, Rubel (1985) and Malin (1988) have examined the applicability of various k-ε turbulence models to the radial jet by comparing the spreading rate of the jet predicted by the models with those determined from experiment.

In addition to the theoretical investigations just described, the flow of a radial jet stream has also been studied experimentally and a brief description of these studies is now given. The earliest experimental investigation on the radial jet was performed by Tuve (1953) who measured the jet's centre-line velocity, $\tilde{u}$, and velocity profiles for two different designs of nozzles which produce radial jets. Two of the most important findings made by Tuve (1953) were that (i) the velocity distribution in the jet can be well-described by the law

$$\left(\frac{y}{b_{1/2}}\right)^2 = 3.3 \ln\left(\frac{\tilde{u}}{u}\right) \qquad (2.2.2a)$$

where $b_{1/2}$ is the value of y where $u = \tilde{u}/2$, i.e. a measure of the typical shear-layer thickness, and that (ii) the profiles of lateral, or cross jet, velocity at various distances from the jet nozzle are similar. Figure 2.2 schematically illustrates the notation and coordinate system of the jet.

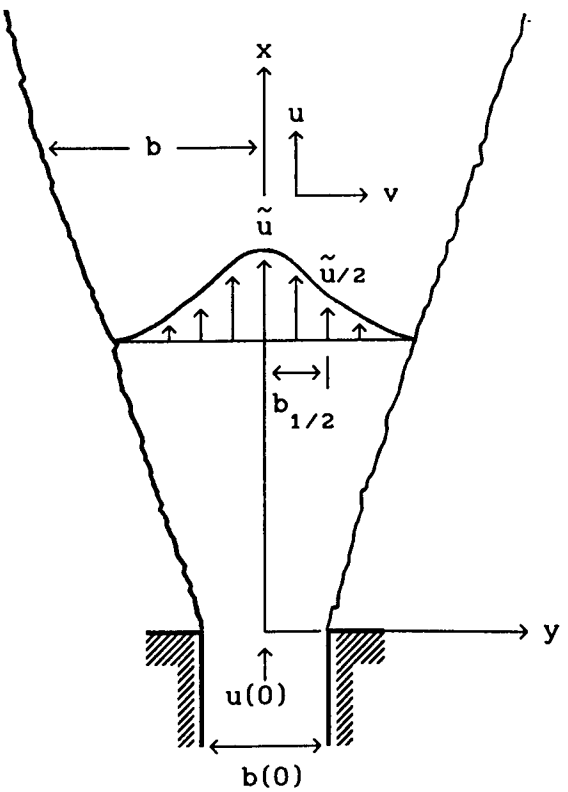

Fig.2.2 Schematic diagram of the jet illustrating the coordinate system and notation.

Heskestad (1966) presented a detailed experimental study of the turbulent radial jet and described hot-wire anemometry measurements of some of the turbulence quantities in the jet, e.g. the lateral distributions of the normal and Reynolds stresses and the

intermittency factor. The experimental results of Heskestad (1966) indicate that the lateral velocity distribution may be well-described by the semi-empirical formula of Squire (1955), namely

$$\frac{\tilde{u}}{u} = \text{sech}^2(7.86\eta) \qquad \eta = y/x \qquad (2.2.2b)$$

where x is the radial distance along the centre-line of the jet measured from the perimeter of the jet nozzle. Experimental investigations have also been reported by Tanaka and Tanaka (1976) who measured the fluctuations in the streamwise velocity and obtained experimental results which are comparable to Heskestad (1966). The most recent extensive experimental study is given by Witze and Dwyer (1976) who distinguished between two classes of radial jets, namely 'constrained' radial jets or 'impinged' radial jets depending upon the ratio between the width of the nozzle through which the jet issues and the radius of the jet flange. Witze and Dwyer (1976) measured lateral velocity distributions, centre-line velocities and turbulence intensities and their results illustrate the similarity behaviour of the lateral velocity profiles which compare favourably with the velocity profile reported by Poreh and Cermak (1959), namely

$$\frac{u}{u(0)} = \text{sech}^2\left(\frac{0.881y}{b_{1/2}} \right) \quad \text{for} \quad y/b_{1/2} < 1. \qquad (2.2.2c)$$

The empirical formula (2.2.2a) of Tuve (1953) shows a good agreement with his own experimental results for $y/b_{1/2} \leq 2$, i.e. it provides better agreement close to the edge of the jet shear-layer than the expression (2.2.2c) of Poreh and Cermak. Patel (1979) extended the results of Witze and Dwyer (1976) by measuring the growth and the centre-line velocities of the radial jet up to a value of

$x/b(0) = 72$. His results suggested that for radial free jets having small separation distances, $b(0)$, the rate of growth is 0.115, i.e. $b_{1/2} = 0.115\ x$, and he found that the mathematical function

$$\frac{u}{u(0)} = \exp\left\{-0.693\left(\frac{y}{b_{1/2}}\right)^2\right\} \qquad (2.2.2d)$$

fitted his results very well.

A mathematical description of the fluid flow in a jet is now given and the equations of motion and boundary conditions which govern the flow in the shear-layers of both the two-dimensional plane and the three-dimensional axisymmetric radial jet are presented.

Fluid of low viscosity is discharged from the narrow nozzle, width $b(0)$, of the Aaberg exhaust hood at a relatively high initial speed, $u(0)$, into an initially stagnant surrounding fluid of the same density and viscosity. Due to the friction developed at its boundary, the emerging jet of fluid carries with it some of the surrounding fluid which was originally at rest so that the mass flow in the jet increases along its length. As a consequence the jet spreads out and its centre-line velocity, i.e. the velocity along $y = 0$, decreases as the distance x along the jet increases. However, the total momentum of the jet remains constant. The streamwise component of the velocity in the jet, u, is a maximum along the jet's centre-line and decreases to zero at the edge of the shear-layer, whilst the y direction component of the velocity, v, is zero along the centre-line. These physical flow characteristics of the jet lead to the following boundary conditions:

$$\frac{\partial u}{\partial y} = 0,\ v = 0 \quad \text{on} \quad y = 0 \qquad 0 < x < \infty \qquad (2.2.3a,b)$$

$$u \longrightarrow 0 \quad \text{as} \quad y \longrightarrow \infty \qquad 0 < x < \infty\ . \qquad (2.2.3c)$$

For large values of the Reynolds number, R_e, where

$$R_e = \frac{u(0)b(0)}{\nu} \qquad (2.2.4)$$

the thickness of the jet is very small. Inside this very thin shear-layer the velocity gradient normal to the direction of flow, i.e. $\partial u/\partial y$, is very large as the u component of the velocity in the jet decreases from a maximum value of $\tilde{u}$ along the centre-line of the jet to zero at the edge of the shear-layer. Therefore, even with a very small viscosity, μ, the frictional shearing stress, i.e. $\tau = \mu\, \partial u/\partial y$, in the shear-layer is considerable because of the large velocity gradient across the flow. In the remaining fluid flow regions such large velocity gradients do not occur and the effect of viscosity in these regions may be neglected.

Shear-layers may be laminar or turbulent, depending on the distance from the orifice, the fluid viscosity and velocity, i.e. the Reynolds number of the jet. While the flow in the jet is laminar, the thickness of the jet decreases as the Reynolds number increases. However, as the Reynolds number tends to infinity, and the jet becomes turbulent, the thickness of the jet does not vanish but is approximately independent of the jet Reynolds number. Andrade (1939) states that a two-dimensional plane jet remains laminar for R_e less than approximately 30. However, an estimate of the equivalent critical Reynolds number for an axisymmetric radial jet has not been found in the literature. The equations of motion governing the flow in both laminar and turbulent shear-layers are now examined.

(a) Laminar shear-layers

The Navier-Stokes equations (2.2.1) are difficult to solve because of the non-linearity which is introduced by the presence of the convection term and no general analytical methods for their integration are available. However, the physical characteristics of the shear-layer at large Reynolds numbers allow us to reduce the Navier-Stokes equations to a simpler form, although the non-linearity is still present.

By assuming that the shear-layer thickness, b, is very small compared with a typical distance along the jet, l, and that the variation of the u component of the velocity across the shear-layer is of the same order of magnitude as the centre-line velocity, $\tilde{u}$, then the order of magnitude of each term in the governing equations can be estimated. The desired simplification can then be achieved by neglecting lower-order terms. Following this approach it can be demonstrated that the pressure in the direction normal to the shear-layer is approximately constant, i.e. $\partial P/\partial y \sim O(b)$. The pressure gradient in the x direction, i.e. the term dP/dx, has been set identically zero in the equations of motion because to a first approximation the fluid is stationary outside the shear-layer and hence the pressure is constant everywhere in the jet. As a consequence, the momentum flux, j, of the jet is constant and independent of the distance, x, along the jet. The Navier-Stokes equations then reduce to the Prandtl boundary-layer equations, which for incompressible laminar flow in (i) a two-dimensional plane jet and (ii) an axisymmetric radial jet are given by:

(i) for the two-dimensional laminar plane jet, in cartesian coordinate form, we have

$$u \frac{\partial u}{\partial x} + v \frac{\partial u}{\partial y} = \nu \frac{\partial^2 u}{\partial y^2} \qquad (2.2.5a)$$

$$\frac{\partial u}{\partial x} + \frac{\partial v}{\partial y} = 0 \qquad (2.2.5b)$$

where

$$j = 2\rho \int_0^\infty u^2 \, dy \qquad (2.2.6)$$

and (ii) for the axisymmetric laminar radial jet, in cylindrical polar coordinate form, we have

$$u \frac{\partial u}{\partial x} + v \frac{\partial u}{\partial y} = \nu \frac{\partial^2 u}{\partial y^2} \qquad (2.2.7a)$$

$$\frac{\partial}{\partial x}(xu) + \frac{\partial}{\partial y}(xv) = 0 \qquad (2.2.7b)$$

where

$$j = 4\pi\rho \int_0^\infty xu^2 \, dy \; . \qquad (2.2.8)$$

(b) Turbulent shear-layers

At sufficiently high values of the Reynolds number it is found that after a very short distance from the point of discharge of the jet the flow becomes turbulent. It is well-known that the components of the mean velocity of turbulent flows satisfy the same equations as those satisfied by the laminar flows, except that the laminar stresses must be increased by additional stresses known as the apparent or virtual stresses of the turbulent flow. In free turbulent flows, such as in turbulent plane and radial jet flows, the components of viscous, or normal, stresses are negligible in comparison with the apparent stresses and consequently it is reasonable to neglect the viscous components. Thus, the time-averaged equations of motion on the boundary-layer approximation for incompressible, turbulent flow in (i) a

two-dimensional plane jet and (ii) an axisymmetric radial jet are the Prandtl boundary-layer equations, namely:

(i) for the two-dimensional turbulent plane jet, in cartesian coordinate form, we have

$$u \frac{\partial u}{\partial x} + v \frac{\partial u}{\partial y} = \frac{\partial}{\partial y}\left(\varepsilon \frac{\partial u}{\partial y}\right) \qquad (2.2.9a)$$

$$\frac{\partial u}{\partial x} + \frac{\partial v}{\partial y} = 0 \qquad (2.2.9b)$$

and (ii) for the axisymmetric turbulent radial jet, in cylindrical polar coordinate form, we have

$$u \frac{\partial u}{\partial x} + v \frac{\partial u}{\partial y} = \frac{\partial}{\partial y}\left(\varepsilon \frac{\partial u}{\partial y}\right) \qquad (2.2.10a)$$

$$\frac{\partial}{\partial x}(xu) + \frac{\partial}{\partial y}(xv) = 0 \qquad (2.2.10b)$$

where ε is the apparent or eddy viscosity. When dealing with problems of turbulent jets it is usually assumed that the mixing length, i.e. the distance a fluid element is carried in the transverse direction, is proportional to the width of the jet, b, because in this way we are led to useful results. Prandtl's constant momentum transfer model for the eddy viscosity uses this assumption and by assuming that the fluid particles momentum is conserved in the transverse direction expresses ε in the form

$$\varepsilon = \chi \, b \, \tilde{u} \qquad (2.2.11)$$

where χ is a dimensionless empirical constant. In this way the apparent kinematic viscosity remains constant over the whole width of every cross-section of the jet, i.e. independent of y.

Solutions of the shear-layer equations

The solution of the shear-layer equations, subject to the boundary conditions (2.2.3) and to the conservation of momentum,

will give us a complete description of the flow in the jet. Numerical solutions of the shear-layer equations are not straightforward because of the non-linearity in the equations. However, the nature of the flow observed in the shear-layer, i.e. the similarity of the lateral velocity profiles along the developing jet, indicates the form that their solution should take.

Early experimental observations, e.g. Förthmann (1936), demonstrated that the lateral distributions of the mean velocity in the x direction of the plane turbulent free jet, i.e. the variation of u with y at different x locations, all have the same geometrical shape. At every x location, u decreases from a maximum value of $\tilde{u}$ on the axis of the jet to zero at some distance from the axis. By scaling the velocity u and the y coordinate with respect to $\tilde{u}$ and $b_{1/2}$, respectively, at that x location, Förthmann plotted $u/\tilde{u}$ as a function of $y/b_{1/2}$ and found that the velocity distributions at different x locations fall on a universal curve. Förthmann, and other experimentalists, have shown that a very large number of flows in the field of fluid jets, including the radial jet, see Tuve (1953), exhibit this property of similarity. Similar solutions are defined as those for which the component u of the velocity has the property that two velocity profiles u(x,y) located at different coordinates x differ by only a scale factor in u and y, i.e. where

$$\frac{u(\, x_1, y/b(x_1)\,)}{u(x_1)} = \frac{u(\, x_2, y/b(x_2)\,)}{u(x_2)} \,. \qquad (2.2.12)$$

Hence we may assume that the velocity u is a function of y/b and that $b \sim x^q$. Accordingly, we may write the stream function in the form

$$\psi = Ax^p \, f(\eta) \quad , \quad \eta = y/Bx^q \qquad (2.2.13)$$

where the constants A and B and the exponents p and q can be determined from the shear-layer assumptions, namely that (a) the inertial and viscous terms are of the same order of magnitude in the jet and (b) the total flux of momentum at any location x is constant and independent of x.

In cases where similar solutions exist it is possible, as we shall see in more detail later, to reduce the systems of partial differential equations to ones involving ordinary differential equations which constitutes a considerable mathematical simplification of the problem. Analytical similarity solutions of the shear-layer equations are possible for both laminar and turbulent two-dimensional plane and three-dimensional axisymmetric radial jet flows. However, the similarity solutions of the shear-layer equations may be regarded only as asymptotic solutions for two reasons, namely, (i) the jet is assumed to emerge from a singular point and (ii) the shear-layer equations are only valid for very large values of the Reynolds number.

The asymptotic solution of the two-dimensional plane jet equations of motion provides us with an adequate representation of the flow in a plane jet, though the model is really an ideal flow due to the fact that the fluid issues from an orifice of infinitesimal width with an infinite initial velocity. However, the solution of the equations of motion governing the flow in an axisymmetric radial jet provides only the behaviour of the radial jet flow as $x \longrightarrow \infty$, as the radial jet is then modelled as though it issues radially from a point source. In practice, the radial jet of the Aaberg exhaust hood issues from the perimeter of the exhaust flange, i.e. from a circular disc of a finite radius, and therefore

the development of the Aaberg's radial jet flow from its initial to its asymptotic behaviour must be modelled. A solution of the governing shear-layer equations of motion, i.e. equations (2.2.7) and (2.2.10), must therefore be sought in the general form

$$\psi \sim g(x)\, f(\eta^*, x) \qquad (2.2.14)$$

where the function g(x) and the variable η^* must be chosen so as to exhibit the correct initial behaviour of the radial jet for small x and its asymptotic behaviour as $x \longrightarrow \infty$. A detailed analysis of the equations governing the flow in the radial jet will be presented in chapter 5.

Once the solution of the shear-layer equations has been determined then the stream function at the edge of the jet, given by the value of ψ in the limit as $y \longrightarrow \infty$, can be deduced. The value of the stream function at the edge of the jet shear-layer represents the volume flux of fluid drawn into the developing jet. For a powerful injection of fluid the jet will be very thin and may be considered to be confined to the x axis, i.e. assumed to be of zero thickness. Thus the value of the stream function at the outer edge of the shear-layer may be regarded as the value of the stream function at y = 0. Therefore, in two dimensions, with respect to the induced flow the jet acts as a line sink whose local strength is given the rate of change of the mass flux in the jet.

2.2.2 The Jet-induced Flow

Entrainment into a jet gives rise to a flow of the ambient fluid known as the jet-induced flow and it is this flow that distinguishes the flow of the Aaberg exhaust hood from the flows generated by traditional designs. The jet-induced flow is free from

any large changes in the velocity gradient and hence for large Reynolds numbers the effects of viscous forces are negligible compared with the inertial forces, i.e. the fluid may be assumed to be inviscid in this region of the flow. Although such a fluid cannot exist in nature, under certain conditions it may give valuable information about how a real viscous fluid behaves.

It is a common assumption that the flow which is induced by a thin, i.e. high Reynolds number, jet is an inviscid potential flow, i.e. it satisfies the conditions of incompressibility and irrotationality, see for example Schneider (1981,1983). The influence of a jet on a flow field has been investigated by a number of experimentalists using flow visualization techniques. The flow induced by a two-dimensional plane jet of fluid which discharges perpendicular to a straight wall was observed by Lippisch (1958) and is illustrated in Fig.2.3(a). The flow induced by a two-dimensional turbulent wall jet of fluid was investigated by Sigalla (1958a) and is illustrated in Fig.2.3(b). The smoke filaments released into the flows clearly illustrate their laminar nature.

One limitation of the potential flow model for the jet-induced flow is that a slip condition exists between the fluid and the flange of the exhaust. The flow induced by the jet will produce a boundary-layer flow along the exhaust flange but this is of a lower-order than the jet-induced flow and therefore has been neglected in this work as it only plays a passive role. The equations of motion governing the inviscid potential flow in both two-dimensional polar coordinate and three-dimensional axisymmetric spherical polar coordinate form are now presented.

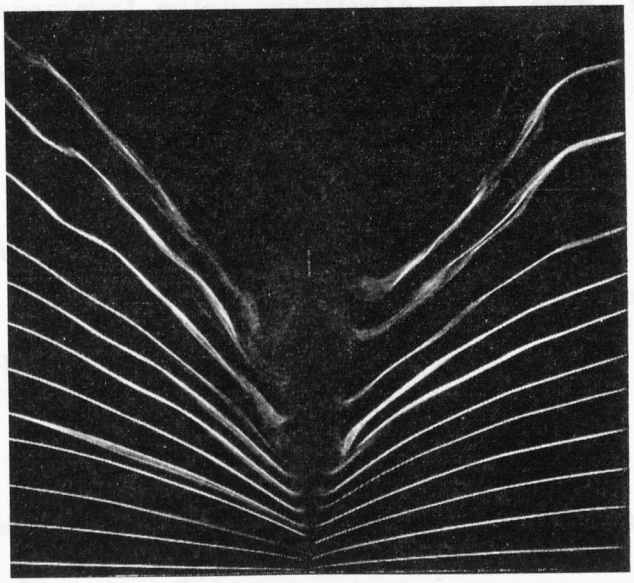

Fig.2.3(a) The flow induced by a two-dimensional plane jet which discharges perpendicular to a straight wall as observed by Lippisch (1958).

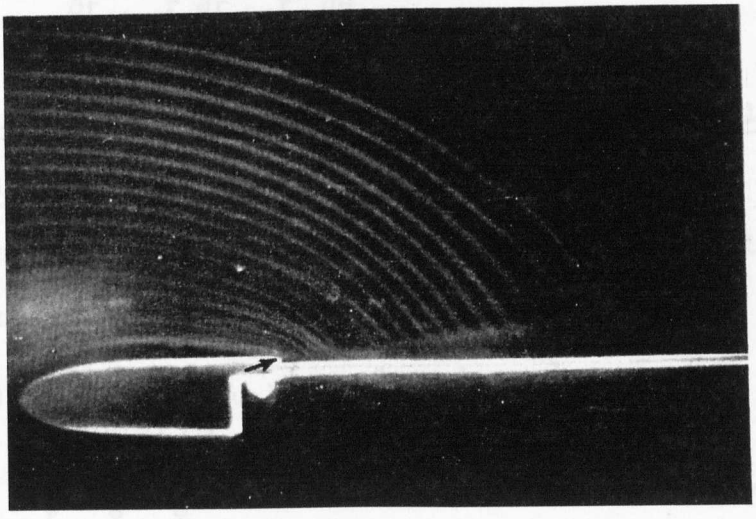

Fig.2.3(b) The flow induced by a two-dimensional turbulent wall jet issuing parallel to a straight wall as observed by Sigalla (1958a). The arrow indicates the position of the orifice of the jet.

(a) The potential flow equations for the two-dimensional model

In two-dimensional polar coordinate (r,θ) form, the continuity equation may be written

$$\frac{\partial}{\partial r}(ru_r) + \frac{\partial}{\partial \theta}(u_\theta) = 0 \qquad (2.2.15)$$

where u_r and u_θ denote the components of the velocity in the radial and tangential directions respectively. We now introduce the stream function $\psi(r,\theta)$ in order to satisfy the equation (2.2.15), i.e.

$$u_r = \frac{1}{r}\frac{\partial \psi}{\partial \theta}\ ,\ u_\theta = -\frac{\partial \psi}{\partial r}\ . \qquad (2.2.16a,b)$$

For irrotationality we insist that $\nabla \times \mathbf{u} = 0$ which implies that

$$\frac{\partial}{\partial r}(ru_\theta) - \frac{\partial}{\partial \theta}(u_r) = 0\ . \qquad (2.2.17)$$

On substitution of equations (2.2.16) into equation (2.2.17) we obtain the equation of motion which governs the potential flow, namely the Laplace equation:

$$\frac{\partial^2 \psi}{\partial r^2} + \frac{1}{r}\frac{\partial \psi}{\partial r} + \frac{1}{r^2}\frac{\partial^2 \psi}{\partial \theta^2} = 0\ . \qquad (2.2.18)$$

(b) The potential flow equations for the three-dimensional axisymmetric model

In spherical polar coordinates (r,θ,ϕ) the continuity equation may be written

$$\frac{1}{r^2}\frac{\partial}{\partial r}(r^2u_r) + \frac{1}{r\sin(\phi)}\frac{\partial}{\partial \theta}(u_\theta) + \frac{1}{r\sin(\phi)}\frac{\partial}{\partial \phi}(u_\phi \sin(\phi)) = 0 \qquad (2.2.19)$$

where $\mathbf{u} = (u_r, u_\theta, u_\phi)$. If we assume axial symmetry so that $\mathbf{u} = (u_r, 0, u_\phi)$, where u_r and u_ϕ denote the velocity components in the radial and tangential directions, respectively, then the continuity equation (2.2.19) reduces to

$$\frac{1}{r^2}\frac{\partial}{\partial r}(r^2u_r) + \frac{1}{r\sin(\phi)}\frac{\partial}{\partial \phi}(u_\phi \sin(\phi)) = 0 \qquad (2.2.20)$$

which may be satisfied by introducing the Stokes stream function $\psi(r,\phi)$ such that

$$u_r = -\frac{1}{r^2\sin(\phi)}\frac{\partial\psi}{\partial\phi} \quad , \quad u_\phi = \frac{1}{r\sin(\phi)}\frac{\partial\psi}{\partial r} \; . \qquad (2.2.21a,b)$$

For irrotationality we require that

$$\frac{\partial}{\partial r}(ru_\phi) - \frac{\partial}{\partial\phi}(u_r) = 0 \qquad (2.2.22)$$

and on substituting equation (2.2.21) into the above equation we obtain the equation of motion governing the inviscid potential flow of the Aaberg exhaust hood, namely

$$\frac{\partial^2\psi}{\partial r^2} - \frac{\cot\phi}{r^2}\frac{\partial\psi}{\partial\phi} + \frac{1}{r^2}\frac{\partial^2\psi}{\partial\phi^2} = 0 \; . \qquad (2.2.23)$$

2.2.3 The Exhaust Flow

In practice, experimentalists have observed that when operating under suction alone the fluid flow induced by the exhaust is laminar and hence, as for the jet-induced flow, since the Reynolds number is large, the effects of viscosity in the exhaust flow may be neglected. In two dimensions, a very simple representation of the flow into an exhaust inlet can be obtained by modelling the exhaust as a line sink of fluid. Although providing a good overall model of the flow field induced by an exhaust, very near to the exhaust inlet the line sink model of the exhaust flow is unrepresentative of the actual flow which is observed in practice. This is due to the infinitesimal width of the sink's inlet which results in an infinite fluid velocity into the sink. A far more realistic representation of an exhaust flow is achieved by modelling the exhaust inlet as a slot of a finite width in two dimensions and as a circular orifice in three dimensions and by assuming that the velocity distribution

across the face of the inlet is constant. In practice the velocity distribution is observed to be constant at only a very short distance down the inlet but for simplicity, in the mathematical models presented in this thesis, it is reasonable to enforce the condition of a constant velocity across the face of the inlet.

2.3 METHODS OF SOLUTION

Under the simplifying assumptions made, and for the reasons given in the preceding sections, the overall air flow pattern developed by the Aaberg exhaust hood, that is the combination of the jet-induced and the exhaust flows, may be considered to be an inviscid potential flow. We shall see in the following chapters that apart from in the simplest cases an analytical solution of the governing inviscid potential flow equations is not possible. In the more realistic models of the air flow pattern then, numerical techniques provide the only way of determining the air flow pattern.

Before the solution of the governing elliptic equation of motion can be determined using numerical methods a boundary condition which models the flow field as $r \longrightarrow \infty$ is required. In the numerical models to be presented in the following chapters this upstream boundary condition has been taken to be the superposition of the upstream component of the overall flow produced by (i) the suction, which as $r \longrightarrow \infty$ is a purely radial flow, and (ii) the injection, which as $r \longrightarrow \infty$ is determined from the asymptotic solution of the governing potential equation.

Finite-difference techniques were considered to be the most

convenient means of solving the equations of motion due to the fact that the solution domain is free from any curved geometry and other methods, for example the finite element method and the boundary element method, were not considered to have any advantages over the finite-difference method. The finite-difference method consists of placing a mesh over the entire solution domain and replacing all derivatives of the governing equation of motion by their central-difference approximations. The resulting finite-difference equations are then written in their classical five point form at each mesh point and the resulting system of linear, algebraic equations solved using matrix methods. The Gauss-Seidel iterative procedure was chosen to solve the system of equations and the successive over-relaxation (S.O.R.) method was used in order to accelerate the rate of convergence.

As the flow field generated by an Aaberg exhaust hood is symmetrical about the hood's centre-line then the computational domain can be halved in size. All the results presented in this thesis are such that they are independent of the mesh size and the position of the upstream boundary condition. Sets of streamlines and lines of constant speed deduced from the model can then be used to examine the hood's air flow pattern and to illustrate the effect of the governing parameters on the air flow.

2.4 TERMINOLOGY

In chapter 1 the notion of a clutch velocity, i.e. the air velocity in front of the hood caused by the hood, was introduced and

Hyldgård (1987) stated that the ratio between the clutch velocity and the velocity of the pollutant is a decisive factor in determining whether or not the exhaust will collect the pollutant. However, the ratio described is not a sufficient condition for contaminant capture to take place, indeed, for the typical air flow pattern induced by the Aaberg exhaust hood, contaminated air may be drawn initially towards the hood but then led away from the exhaust inlet as it moves in the jet-induced flow.

At this stage it is convenient to introduce further terminology that will allow us to theoretically describe the region in front of an exhaust hood from which we expect the air flow to be drawn successfully into the exhaust inlet and hence the region from which capture of contaminant is assumed to occur. The terms 'capture speed', 'effective capture region' and 'effective working range' which will be referred to frequently in the following chapters are now defined.

2.4.1 The Capture Speed

Due to the nature of the contaminant and to the background air movements, in an industrial environment successful contaminant capture will only occur from a region of the workplace where the air speed in the efficient flow, i.e. the flow which leads directly towards the exhaust inlet, exceeds a minimum speed, known as the capture speed, q_c. Under normal practical conditions, and for a neutrally-buoyant contaminant, the capture speed is typically of the order of 0.25 ms^{-1}, see Høgsted (1987) and Fletcher and Saunders (1991,1993).

2.4.2 The Effective Capture Region

The region of the efficient flow where the air speed induced by the hood exceeds the capture speed is hereafter referred to as the effective capture region. The effective capture region therefore describes the region of the workplace where contaminant capture is assumed to be successful. In the models to be presented in the following chapters the effective capture region predicted represents the maximum theoretical size of the region from which sampling can be expected to occur in an industrial environment. This is due to the fact that the most simple model for a contaminant is assumed and buoyancy and diffusion effects are neglected. In two dimensions the effective capture region is referred to as the effective capture area.

2.4.3 The Effective Working Range

The effective working range of the hood refers to the distance upstream from the hood to the region in the flow where the air speed is equal to the capture speed, i.e. it is the length which the effective capture region extends upstream. In the case of the ventilator unit, see Fig.1.5, the effective working range is taken to be the distance which the effective capture region extends upstream along the floor surface from the centre-line of the unit. It is very important to consider the effective working range of an Aaberg exhaust hood as it has been demonstrated that the very small effective working range of the traditional exhaust hood results in serious problems relating to its installation.

2.5 CONCLUSIONS

Mathematical techniques have been used to reduce the complexity of modelling the Aaberg exhaust hood's air flow pattern. The simplifying assumptions have allowed the Navier-Stokes equations to be reduced to more tractable forms, namely, to the shear-layer equations in the jet flow region, where the effects of viscosity are important, and to the potential flow equations in the remaining flow region where the effects of viscosity are negligible and inertia dominates.

Now that the background and framework of the mathematical model have been developed and the governing equations of motion set up we proceed to examine in detail the boundary conditions for both the two-dimensional and three-dimensional axisymmetric models of the Aaberg exhaust hood's air flow pattern. In this way we will establish the governing operating parameters and their effect on the air flow.

CHAPTER THREE

A SIMPLE TWO-DIMENSIONAL ANALYTICAL MODEL FOR THE FLUID MECHANICS OF THE AABERG EXHAUST HOOD

3.1 INTRODUCTION

Originally the Aaberg exhaust hood was three-dimensional axisymmetric in design, see Høgsted (1987), but a two-dimensional version was studied by Pedersen (1991a). The principles of operation for the two- and three-dimensional hoods are the same and hence, for simplicity we begin by examining a two-dimensional hood. The aim of this chapter is to obtain an analytical solution for a simple mathematical model of the hood's air flow pattern for both laminar and turbulent injections of fluid, using the mathematical modelling approach described in chapter 2. A description of the fluid flow in each region is given together with the equations of motion and boundary conditions. The shear-layer equations which govern the flow of the two-dimensional plane jet, for both laminar and turbulent flows, are solved analytically for the stream function following the method given by Schlichting (1968). In turbulent flow the Prandtl constant momentum transfer model for the eddy viscosity has been adopted. The two-dimensional jet-induced flow is then determined by solving the governing potential equation, subject to the appropriate boundary conditions, by the method of separation of variables. By modelling the exhaust flow as a line sink of fluid then, the stream functions for the jet-induced flow and the exhaust flow are combined to give a simple model of the Aaberg exhaust hood's air flow. A full description of this simple two-dimensional model is now presented.

3.2 THE MATHEMATICAL MODEL

We have seen in chapter 2 that in order to model the fluid flow which is generated by the Aaberg exhaust hood it is necessary to make a number of simplifying assumptions. For clarity these assumptions will be reiterated during the development of the two-dimensional model. The fluid is assumed to be incompressible and the flow to be steady. The solution technique is divided into three parts:

(i) To model the exhaust flow.

The exhaust flow is modelled as a line sink of fluid at the centre of a plane, the plane representing the flange of the exhaust.

(ii) To model the injection flow.

The injection flow is modelled as a two-dimensional plane jet which issues from the ends of the exhaust flange. Both laminar and turbulent plane jets are examined and the solution in the form of a stream function has been determined from boundary-layer theory, see Schlichting (1968). From the stream function the boundary condition at the edge of the jet shear-layer is derived.

(iii) To model the fluid flow induced by the injection.

Due to the friction which is developed at its boundary the emerging jet carries with it some of the surrounding fluid, which was originally at rest. The stream function for the jet-induced flow is found by assuming that the flow induced by the slender, i.e. high Reynolds number, jet is an inviscid potential flow. Hence, the stream function for this flow must satisfy the Laplace equation with the value of the stream function, as found in (ii), as one of the boundary conditions. The stream function for the jet-induced flow is

determined analytically by solving the Laplace equation (2.2.18) using the method of separation of variables.

Stream functions for the sink and the induced flow are then combined to give a stream function for the total flow created by the two-dimensional Aaberg exhaust hood.

3.2.1 The Stream Function due to the Sink

To calculate the stream function for a sink of strength m at the centre of a vertical flange we use the polar coordinates (r,θ) and the velocity components in the radial and tangential directions are denoted by u_r and u_θ, respectively. The flux of fluid drawn into the sink is given by:

$$-\pi\, r\, u_r = m \qquad (3.2.1)$$

and hence

$$u_r = -\frac{m}{\pi\, r} \quad . \qquad (3.2.2)$$

The line perpendicular to the exhaust flange, passing through the sink, about which the problem is symmetric, hereafter referred to as the centre-line, represents a streamline of the flow and we take $\psi = 0$ along this line. Hence, from the radial and tangential components of velocity, given by expressions (2.2.16), we obtain

$$\psi = -\frac{m}{\pi}\,\theta \qquad (3.2.3)$$

which in terms of the angle γ, see Fig.3.1, may be written

$$\psi = -\frac{m}{\pi}\left(\gamma - \frac{\pi}{2}\right) \quad . \qquad (3.2.4)$$

The boundary conditions satisfied by the sink flow along the hood's centre-line and the exhaust flange are therefore

$$\psi = 0 \qquad \text{on} \quad \gamma = \pi/2 \qquad (3.2.5a)$$

and

$$\psi = m/2 \qquad \text{on} \quad \gamma = 0 \ , \qquad (3.2.5b)$$

respectively.

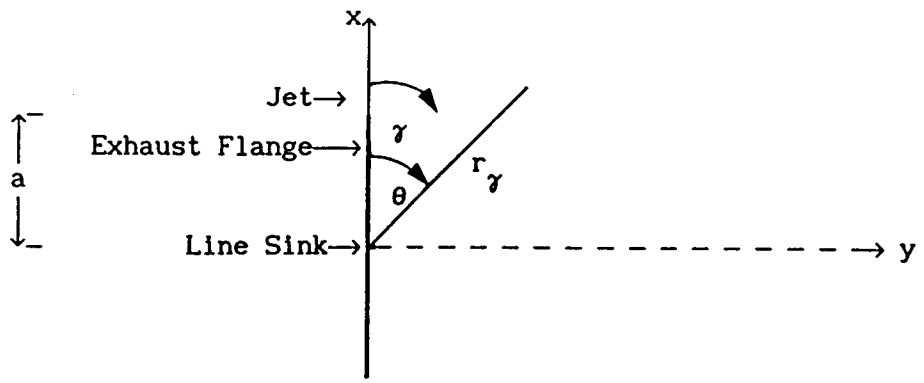

Fig. 3.1 The geometry and coordinate system used for the sink flow.

3.2.2 The Two-dimensional Laminar Plane Jet

The equations of motion of a two-dimensional incompressible, laminar and steady flow in the plane jet are the shear-layer equations (2.2.5). In this chapter, for convenience, the cartesian coordinate system (x,y) is adopted with its origin at the centre of the exhaust flange, so that the y axis is along the centre-line of the hood and the x axis perpendicular to the centre-line, see Fig. 3.1. A new coordinate system (x^*,y), whose origin is located at the orifice of the jet with the x^* axis along the axis of the jet, is now introduced such that

$$x^* = x - a \qquad (3.2.6)$$

where the quantity, a, denotes the width of the exhaust flange. Equations (2.2.5) now become

$$u \frac{\partial u}{\partial x^*} + v \frac{\partial u}{\partial y} = \nu \frac{\partial^2 u}{\partial y^2} \qquad (3.2.7a)$$

$$\frac{\partial u}{\partial x^*} + \frac{\partial v}{\partial y} = 0 \qquad (3.2.7b)$$

and have to be solved subject to the boundary conditions (2.2.3) and to conservation of momentum which is given by expression (2.2.6).

The continuity equation (3.2.7b) implies the existence of a stream function ψ where:

$$u = \frac{\partial \psi}{\partial y} \quad \text{and} \quad v = -\frac{\partial \psi}{\partial x^*} \quad . \tag{3.2.8a,b}$$

In order to determine the form of the stream function in the jet we shall assume that the lateral velocity profiles in the jet are similar and hence we seek a solution of equations (3.2.7) of the form given by expression (2.2.13), i.e.

$$\psi = A(x^*)^p \, f(\eta) \quad , \quad \eta = y/Bx^{*q}. \tag{3.2.9}$$

Using the shear-layer assumptions, namely that (a) the inertial and viscous terms are of the same order of magnitude in the jet and (b) the total flux of momentum at any position x^* is constant, results in

$$p = \frac{1}{3} \quad \text{and} \quad q = \frac{2}{3} \, . \tag{3.2.10}$$

Using condition (a) we can choose, for convenience,

$$A = \nu^{1/2} \quad , \quad B = 3\nu^{1/2} \tag{3.2.11}$$

and hence

$$\psi = \nu^{1/2} \, (x^*)^{1/3} \, f(\eta) \quad ; \quad \eta = \frac{y}{3 \, \nu^{1/2} (x^*)^{2/3}} \tag{3.2.12}$$

where $f(\eta)$ satisfies the ordinary differential equation

$$f''' + ff'' + (f')^2 = 0 \, . \tag{3.2.13}$$

The prime denotes differentiation with respect to η. This equation has to be solved subject to the boundary conditions

$$f'' = 0 \, , \; f = 0 \quad \text{on} \quad \eta = 0 \tag{3.2.14a,b}$$

and

$$f' \longrightarrow 0 \quad \text{as} \quad \eta \longrightarrow \infty \, . \tag{3.2.14c}$$

Integrating equation (3.2.13) once gives

$$f'' + ff' = \text{constant} \, . \tag{3.2.15}$$

To satisfy the boundary conditions (3.2.14a,b) the constant must be

set to zero and therefore

$$f''' + ff'' = 0 \ . \qquad (3.2.16)$$

This second-order differential equation could be integrated directly if the second term contained a factor of two, therefore we make the following transformation:

$$\xi = \eta \quad , \quad f = 2\,F(\xi) \ . \qquad (3.2.17)$$

Hence equation (3.2.16) becomes

$$F''' + 2\,FF'' = 0 \quad \text{where} \quad F' = \frac{dF}{d\xi} \qquad (3.2.18)$$

and the boundary conditions (3.2.14b,c) reduce to

$$F = 0 \ , \ \xi = 0 \qquad (3.2.19a)$$

and

$$F' \longrightarrow 0 \ \text{ as } \ \xi \longrightarrow \infty \ . \qquad (3.2.19b)$$

Integrating equation (3.2.18) gives

$$F'' + F^2 = \alpha^2 \qquad (3.2.20)$$

where α^2 is an unknown constant. Rearranging equation (3.2.20) gives

$$\frac{dF}{d\xi} = \alpha^2 - F^2 \qquad (3.2.21)$$

and integrating we have

$$\xi = \frac{1}{\alpha} \tanh^{-1}\left(\frac{F}{\alpha} \right) \qquad (3.2.22)$$

hence

$$F = \alpha \tanh(\xi\alpha) \ . \qquad (3.2.23)$$

Condition (b) gives us an expression for the momentum flux, j, namely

$$j = \frac{16}{9} \rho \alpha^3 \nu^{1/2} \qquad (3.2.24)$$

and hence if we assume that the flux of momentum, j, for the jet is a known quantity, then the constant α is given by

$$\alpha = \left(\frac{9\,k}{16\,\nu^{1/2}} \right)^{1/3} \qquad (3.2.25)$$

where $k = j/\rho$ is the kinematic momentum flux. The stream function for the two-dimensional laminar jet issuing from the coordinate

origin is then given by:

$$\psi = 2\,\alpha\,\nu^{1/2}\,(x^*)^{1/3}\,\tanh(\eta\alpha)\ . \qquad (3.2.26)$$

If we let $y \longrightarrow \infty$ in the above expression then the stream function is given by

$$\psi \longrightarrow 2\,\alpha\,\nu^{1/2}\,(x^*)^{1/3} \qquad x^* > 0 \qquad (3.2.27)$$

and this is the boundary condition at the edge of the shear-layer that we have imposed when solving for the flow induced by a two-dimensional plane laminar jet.

3.2.3 The Two-dimensional Turbulent Plane Jet

In reality the emerging jet, originally a laminar flow, passes through a transitional chaotic stage and soon becomes fully turbulent. Following Schlichting (1968) we shall assume that the width of the jet, b, is proportional to x^*, i.e. $b \sim x^*$. The relationship between the centre-line velocity, $\tilde{u}$, and x^* can then be obtained from the momentum conservation equation (2.2.6), from which we obtain

$$j = \text{constant}\ \tilde{u}^2\ b \qquad (3.2.28)$$

and hence

$$\tilde{u} = \text{constant}\ (x^*)^{-1/2} j^{1/2}\ . \qquad (3.2.29)$$

Thus the rate of decrease in the centre-line velocity $\tilde{u} \sim (x^*)^{-1/2}$. Prandtl's expression (2.2.11) for ε simplifies the differential equation (2.2.9a) and thus the equations of motion governing the flow in a two-dimensional plane turbulent jet, i.e. equations (2.2.9), then reduce to:

$$u \frac{\partial u}{\partial x^*} + v \frac{\partial u}{\partial y} = \varepsilon \frac{\partial^2 u}{\partial y^2} \qquad (3.2.30a)$$

$$\frac{\partial u}{\partial x^*} + \frac{\partial v}{\partial y} = 0 \qquad (3.2.30b)$$

and the boundary conditions are given by equations (2.2.3). Equation (3.2.30a) is formally identical with that for the laminar jet case except the kinematic viscosity, ν, of the laminar flow has been replaced by the apparent kinematic viscosity, ε, of the turbulent flow. Denoting the centre-line velocity and the width of the jet at a fixed characteristic distance, s, from the orifice by $\tilde{u}_s$ and b_s, respectively, we may write

$$\tilde{u} = \tilde{u}_s \left(\frac{x^*}{s} \right)^{-1/2} \quad ; \quad b = b_s \left(\frac{x^*}{s} \right) \qquad (3.2.31a)$$

and hence

$$\varepsilon = \varepsilon_s \left(\frac{x^*}{s} \right)^{1/2} \quad ; \quad \varepsilon_s = \chi \, b_s \, \tilde{u}_s \, . \qquad (3.2.31b)$$

The stream function is again introduced and assumed to take the form

$$\psi = \sigma_o^{-1} \, \tilde{u}_s s^{1/2} \, (x^*)^{1/2} F(\eta) \quad , \quad \eta = \sigma_o y / x^* \qquad (3.2.32)$$

where the function σ_o denotes a free constant. Substituting expression (3.2.32) into Prandtl's shear-layer equation (3.2.30a) we obtain the following differential equation for $F(\eta)$:

$$\frac{1}{2} (F')^2 + \frac{1}{2} F'' F + (\varepsilon_s \sigma_o^2 / \tilde{u}_s s) \, F''' = 0 \qquad (3.2.33)$$

where the prime now denotes differentiation with respect to η, where $\eta = \sigma_o y / x^*$. The boundary conditions (2.2.3) now become

$$F = 0 \, , \; F' = 1 \quad \text{on} \quad \eta = 0 \qquad (3.2.34a,b)$$

and

$$F' \longrightarrow 0 \quad \text{as} \quad \eta \longrightarrow \infty \, . \qquad (3.2.34c)$$

Since ε_s contains the free constant χ, we write

$$\sigma_o = \frac{1}{2} \left(\frac{\tilde{u}_s s}{\varepsilon_s} \right)^{1/2} . \qquad (3.2.35)$$

This substitution simplifies the preceding differential equation which can now be integrated twice to give

$$F' + F^2 = 1 \ . \qquad (3.2.36)$$

This is similar to the equation for the two-dimensional plane laminar jet and the solution is given by

$$F = \tanh \eta \ . \qquad (3.2.37)$$

The characteristic velocity, $\tilde{u}_s$, can now be expressed in terms of the constant momentum flux per unit length, using the momentum equation we have

$$j = \frac{4}{3} \rho \, \tilde{u}_s^2 \, \frac{s}{\sigma_o} \qquad (3.2.38a)$$

hence

$$\tilde{u}_s^2 s = \frac{3}{4} k \, \sigma_o \qquad (3.2.38b)$$

where $k = j/\rho$. The final form of the stream function for the two-dimensional turbulent jet is therefore given by:

$$\psi = \frac{1}{2} \left(\frac{3k}{\sigma_o} \right)^{1/2} (x^*)^{1/2} \tanh \eta \ . \qquad (3.2.39)$$

The constant σ_o was determined experimentally by H. Reichardt, see Schlichting (1968), and found to be $\sigma_o = 7.67$. If we let $y \longrightarrow \infty$ in the above then the stream function is given by

$$\psi \longrightarrow \frac{1}{2} \left(\frac{3k}{\sigma_o} \right)^{1/2} (x^*)^{1/2} \qquad x^* > 0 \qquad (3.2.40)$$

and this is the boundary condition at the edge of the shear-layer that we have imposed when solving Laplace's equation for the flow induced by a two-dimensional plane turbulent jet.

3.2.4 The Flow Induced by a Two-dimensional Jet

The effect which the two-dimensional jets of fluid have on the entrainment of the surrounding fluid is now investigated under the assumption that an inviscid potential flow is induced. If we let

$y \longrightarrow \infty$ in equations (3.2.26) and (3.2.39), then the condition for ψ at the edge of the shear-layer is of the form

$$\psi(x^*,\infty) = f_\infty (x^*)^\lambda \qquad x^* > 0 \qquad (3.2.41a)$$

where

$$f_\infty = \left(\frac{9k\nu}{2} \right)^{1/3}, \quad \lambda = 1/3 \qquad (3.2.41b)$$

for the laminar jet and

$$f_\infty = \frac{1}{2} \left(\frac{3k}{\sigma_o} \right)^{1/2}, \quad \lambda = 1/2 \qquad (3.2.41c)$$

for the turbulent jet. For simplicity the slender jet is assumed to have zero thickness so that the boundary condition is enforced along the x axis. The solution of the Laplace equation (2.2.18) subject to the following boundary conditions

$$\psi = f_\infty (x^*)^\lambda \qquad \text{on} \quad \theta = 0 \qquad (3.2.42a)$$

$$\psi = 0 \qquad \text{on} \quad \theta = \pi \qquad (3.2.42b)$$

$$\psi = 0 \ , \quad r = r_\alpha \qquad \text{on} \quad \theta = \pi - \alpha \qquad (3.2.42c)$$

will give a complete description of the flow induced by the jet. The geometry and coordinate systems used for the induced flow are illustrated in Fig.3.2. Using the method of separation of variables we find the solution in the form:

$$\psi = f_\infty (\sin(\lambda\pi))^{-1} \left[r^\lambda \sin[\, \lambda(\pi-\theta) \,] - r_\alpha^\lambda \sin(\lambda\alpha) \right] . \qquad (3.2.43)$$

3.3 A TWO-DIMENSIONAL MODEL OF THE AABERG EXHAUST HOOD'S FLUID FLOW

In this study we are interested in determining the fundamental air flow pattern created by the Aaberg exhaust hood and we therefore assume that the contaminant is spread throughout the fluid and is

neutrally-buoyant, i.e. has the same density as air, and diffusion effects have been ignored. The stream function for the two-dimensional flow pattern which models that created by the Aaberg exhaust hood can then be written in the form

$$\psi = -\frac{m}{\pi}\left(\gamma - \frac{\pi}{2}\right) + f_{\infty}(\sin(\lambda\pi))^{-1}\left[\, r^{\lambda}\sin\left[\, \lambda(\pi-\theta)\,\right] - r_{\alpha}^{\lambda}\,\sin\lambda\alpha\,\right] . \qquad (3.3.1)$$

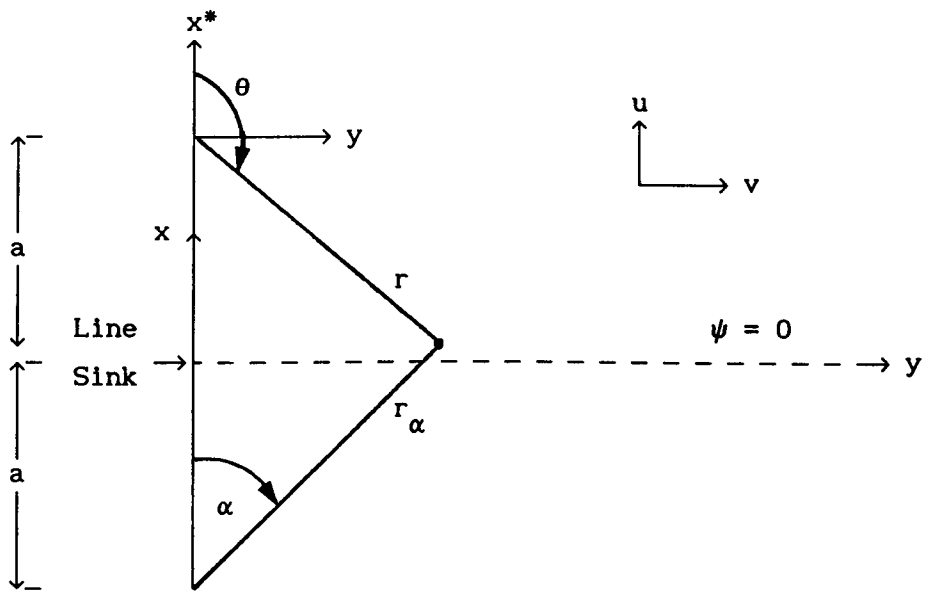

Fig.3.2 The geometry and coordinate systems used for the induced flow.

Although we have made these assumptions it is easy to adapt the model to include the effects of having a neutrally-buoyant emission of contaminant, modelling it as a line source of fluid which can be placed anywhere in space in front of the hood. Also, solid particles, representing contaminants can be easily introduced into the flow at various positions and their individual particle paths

calculated for different hood operating conditions. However, modelling the effects of a continuously emitted, non-neutrally-buoyant contaminant is more complicated and leads to a two-phase problem.

The above expression for the stream function is now expressed in dimensionless form by referring all lengths to the width of the exhaust flange, a, and the stream function with respect to the volume flux, m, into the exhaust inlet. Thus introducing the dimensionless quantities

$$R = r/a \ , \ R_\alpha = r_\alpha/a \ , \ R_\gamma = r_\gamma/a \ , \ \Psi = \psi/m \qquad (3.3.2)$$

expression (3.3.1) becomes

$$\Psi = -\left(\frac{1}{\pi}\left(\gamma - \frac{\pi}{2}\right) - G\left[R^\lambda \sin\left[\lambda(\pi-\theta) \right] - R_\alpha^\lambda \sin\lambda\alpha \right] \right) \qquad (3.3.3)$$

where $G = a^\lambda f_\infty / m\sin(\lambda\pi)$ is an important dimensionless quantity, referred to hereafter as the operating parameter. The operating parameter, G, will be denoted by G_L when the flow in the jet is laminar and G_T when the flow in the jet is turbulent. The dimensionless resultant speed, Q, of the flow is given by

$$Q = \sqrt{U^2 + V^2} \qquad (3.3.4)$$

where U and V are the dimensionless cartesian components of velocity in the $X = x/a$ and $Y = y/a$ directions, respectively, such that $U = u/(m/a)$ and $V = v/(m/a)$. Hence

$$U = -\left(\frac{\cos\gamma}{\pi R_\gamma} + \lambda G\left(R^{\lambda-1}\cos A + R_\alpha^{\lambda-1}\cos B \right) \right) \qquad (3.3.5a)$$

and

$$V = -\left(\frac{\sin\gamma}{\pi R_\gamma} + \lambda G\left(R^{\lambda-1}\sin A + R_\alpha^{\lambda-1}\sin B \right) \right) \qquad (3.3.5b)$$

where

$$A = \lambda\pi + \theta(1-\lambda) \quad , \quad B = \alpha(1-\lambda) \; . \qquad (3.3.6a,b)$$

From a knowledge of these components the velocity directly in front of the exhaust hood along its centre-line can be determined. Along the centre-line

$$U = 0 \; , \; \gamma = \frac{\pi}{2} \; , \; R_{\gamma} = Y \; , \; \alpha + \theta = \pi \; , \; R = R_{\alpha} \qquad (3.3.7)$$

and hence the dimensionless centre-line velocity (CLV), is given by

$$CLV = - \left(\frac{1}{\pi Y} + \lambda G R^{\lambda-1} \left(\sin A + \sin B \right) \right) \qquad (3.3.8)$$

where

$$\theta = \frac{\pi}{2} + \tan^{-1}\left(\frac{1}{Y}\right) \; , \; \alpha = \tan^{-1} Y \; , \; R^2 = 1 + Y^2 . \qquad (3.3.9)$$

3.4 RESULTS AND DISCUSSION

The mathematical model presented in this chapter represents a very simple analytical model for the air flow pattern which is created by a two-dimensional exhaust hood assisted by a jet flow following the principles of operation suggested by Aaberg. However, an exhaust hood of the same design as that modelled does not exist in practice and therefore there are no appropriate operating conditions and experimental data on which to base the validity of the model. However, for the purposes of illustrating the qualitative behaviour of the two-dimensional air flow pattern predicted by the model we obtain appropriate values of the dimensionless operating parameter G from the operating conditions of a three-dimensional Aaberg exhaust hood as supplied by Fletcher and Saunders (1991) of

the Health and Safety Executive, Sheffield, England. These conditions lead to the following approximate values of the physical quantities:

$$m \simeq 0.05\ m^3 s^{-1}, \quad k \simeq 0.50\ m^4 s^{-2}, \quad a \simeq 0.15\ m. \qquad (3.4.1)$$

The fluid used was air at about 20°C, and therefore the kinematic viscosity, ν, is approximately equal to 1.7×10^{-5} Pa s. These parameters result in a value of $G_L \simeq 0.5$ for the laminar jet and $G_T \simeq 2.0$ for the turbulent jet. The value of the operating parameter G may be varied and its effect on the flow pattern examined. Increasing the value of the parameter G by a factor F may be regarded as equivalent to one of the following:

Laminar Jet Case ($\lambda = 1/3$)

$$G_L = \frac{1}{m}\left(\frac{9ak\nu}{2}\right)^{1/3} \qquad (3.4.2)$$

(a) Increasing k by a factor of F^3

(b) Decreasing m by a factor of F

(c) Increasing a by a factor of F^3,

i.e. decreasing the sink strength by a factor of F is equivalent to increasing the kinematic momentum flux by a factor of F^3.

Turbulent Jet Case ($\lambda = 1/2$)

$$G_T = \frac{1}{2m}\left(\frac{3ka}{\sigma_o}\right)^{1/2} \qquad (3.4.3)$$

(a) Increasing k by a factor of F^2

(b) Decreasing m by a factor of F

(c) Increasing a by a factor of F^2

From equations (3.4.2) and (3.4.3) the following relationship between the laminar and turbulent operating parameters, G_L and G_T, can be derived:

$$G_T = G_L \left(\frac{ak}{12\nu^2\sigma_o^3} \right)^{1/6} . \qquad (3.4.4)$$

On substitution of the physical quantities given in expressions (3.4.1), equation (3.4.4) simplifies to the approximate relationship

$$G_T \simeq 4\, G_L . \qquad (3.4.5)$$

Once the laminar operating parameters are known then their equivalent turbulent parameters can be calculated from equation (3.4.5). In this chapter the flow patterns corresponding to the laminar operating conditions $G_L = 0.05$, 0.5 and 5 and their turbulent equivalents $G_T = 0.2$, 2 and 20 are investigated. The conditions $G_L = 0.05$ and $G_L = 5$ represent one tenth and ten times the value of the laminar operating condition deduced from the Health and Safety Executive data, respectively.

It should be noted that the operating condition G = 0 is equivalent to one of a traditional flanged hood, i.e. it models a hood operating under suction alone.

3.4.1 The Laminar Model

The sets of streamlines describing the flow created by the Aaberg exhaust hood deduced from expression (3.3.3) with $\lambda = 1/3$ are shown in Figs.3.3(a)-(c) when the flow in the jet is assumed to be laminar for the parameters $G_L = 0.05$, 0.5 and 5, respectively. It can clearly be seen that increasing the value of the dimensionless operating parameter G_L forces the dividing streamline, $\psi = 1/2$, which divides the flow travelling towards the inlet from that travelling towards the ejector flow, towards the centre-line of the hood, resulting in the streamlines becoming more compact in the region in front of the inlet. The width of the efficient flow region

decreases, implying an increased fluid velocity towards the inlet.

With $G_L = 0.05$ the sink dominates the flow and fluid is drawn into the inlet from all directions in front of the hood. The injection effect is very small and the width of the efficient flow region is reduced only very slightly over the case when G = 0. The fluid velocities towards the inlet are only slightly enhanced, and under these conditions the Aaberg exhaust hood would perform in much the same way as a traditional exhaust hood. For $G_L = 5$ we reach the other extreme, the injection totally dominates the flow and the jet entrains large amounts of fluid. Velocities towards the inlet are substantially increased, although the penalty is an efficient flow region so narrow that the exhaust would be rendered almost useless for the capture of contaminants. Under the operating condition $G_L = 0.5$ there is a good balance between the suction and the injection. In this case the velocity towards the inlet is substantially increased over the case when G = 0 while the efficient flow region remains broad for the effective capture of contaminants.

These three values of the operating parameter G_L illustrate the necessity to obtain a good balance between injection and exhaustion in order to achieve near optimum contaminant control from the Aaberg exhaust hood.

From expression (3.4.2) we can deduce that a hood operating with parameter $G_L = 0.05$ and a laminar injection of fluid can be modified into one operating more effectively by either:

(a) increasing k by a factor of 1000

or (b) decreasing m by a factor of 10

or (c) increasing a by a factor of 1000.

The modification (a) would require a very high supply pressure for

the injection, create much noise and require a large increase in energy, and (c) would almost certainly prove impractical, so that it would seem most reasonable to choose modification (b). However, care must be taken as decreasing m by a factor of 10 will decrease the air speeds in the efficient flow, which for the exhaust to operate effectively must at least exceed the capture speed.

The effect of G_L on the flow is again illustrated in Figs.3.4(a)-(c); these show lines of constant speed in front of the hood, deduced from expressions (3.3.5), with a laminar injection of fluid for $G_L = 0.05$, 0.5 and 5, respectively. As G_L increases the fluid velocity in front of the inlet, in both the efficient and the recycled flow regions, increases. Under normal practical conditions the capture speed is typically of the order of $0.25\ ms^{-1}$, see Høgsted (1987) and Fletcher and Saunders (1991,1993). A capture speed of $0.25\ ms^{-1}$ corresponds to a non-dimensional speed of $Q_c = 0.75$ for the operating conditions given in expressions (3.4.1). Thus, in this model, we can define the effective capture area, from which the air will be drawn into the exhaust inlet and successfully removed from the workplace, as the area bounded by the line of constant speed $Q_c = 0.75$ and the dividing streamline $\psi = 1/2$.

We can see from Figs.3.3 and 3.4 how the shape of this area changes as G_L changes. On increasing the value of G_L from $G_L = 0.5$ to $G_L = 5$ we see that the width of the effective capture area decreases but its length increases. Thus increasing the value of G_L also increases the effective working range of the hood which can then be placed at greater distances from the source of the contaminant whilst still achieving the same results.

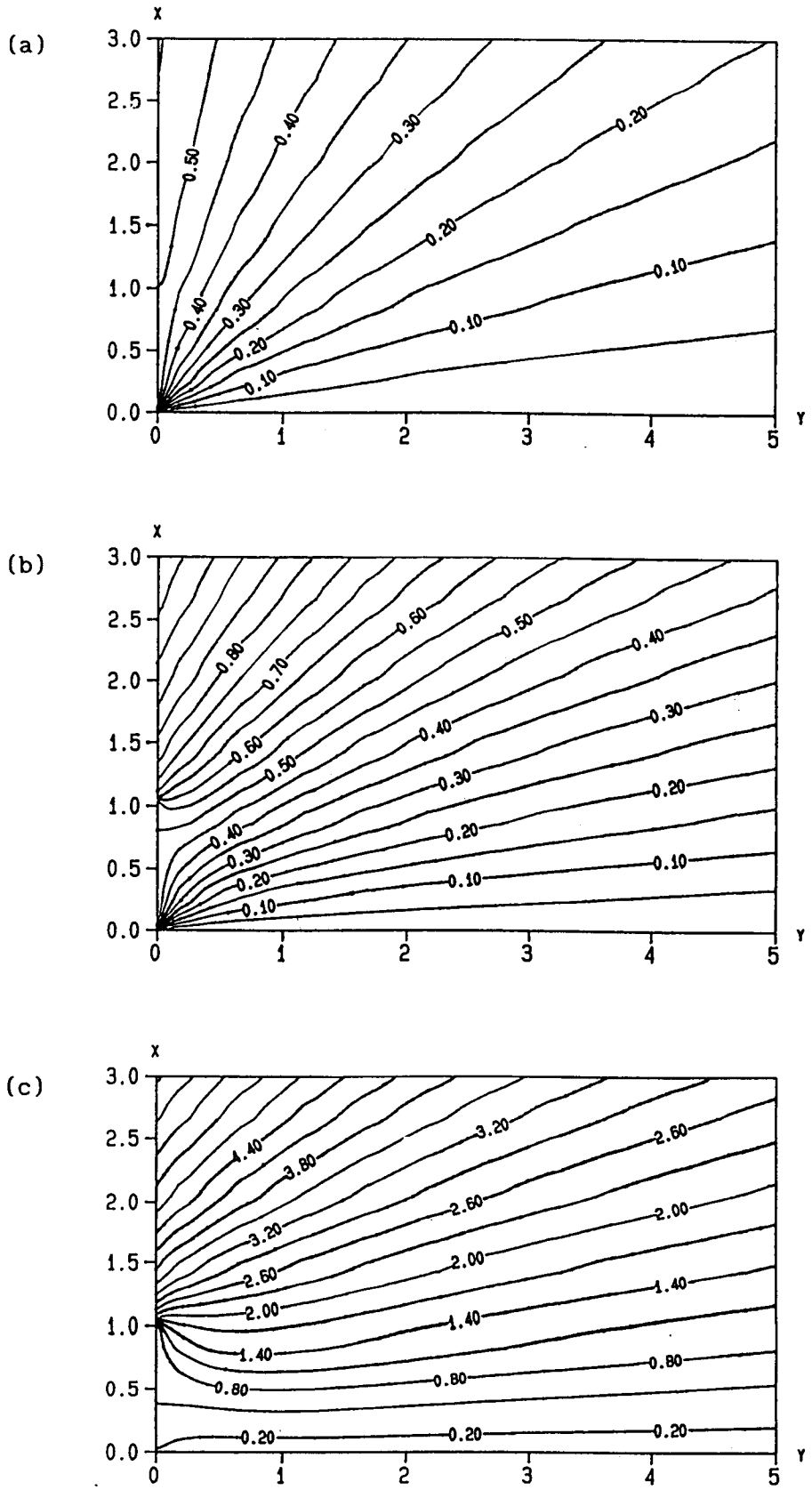

Fig.3.3 Streamlines modelling the Aaberg flow for a laminar injection of fluid, $\lambda = 1/3$. (a) $G_L = 0.05$, (b) $G_L = 0.5$, (c) $G_L = 5$.

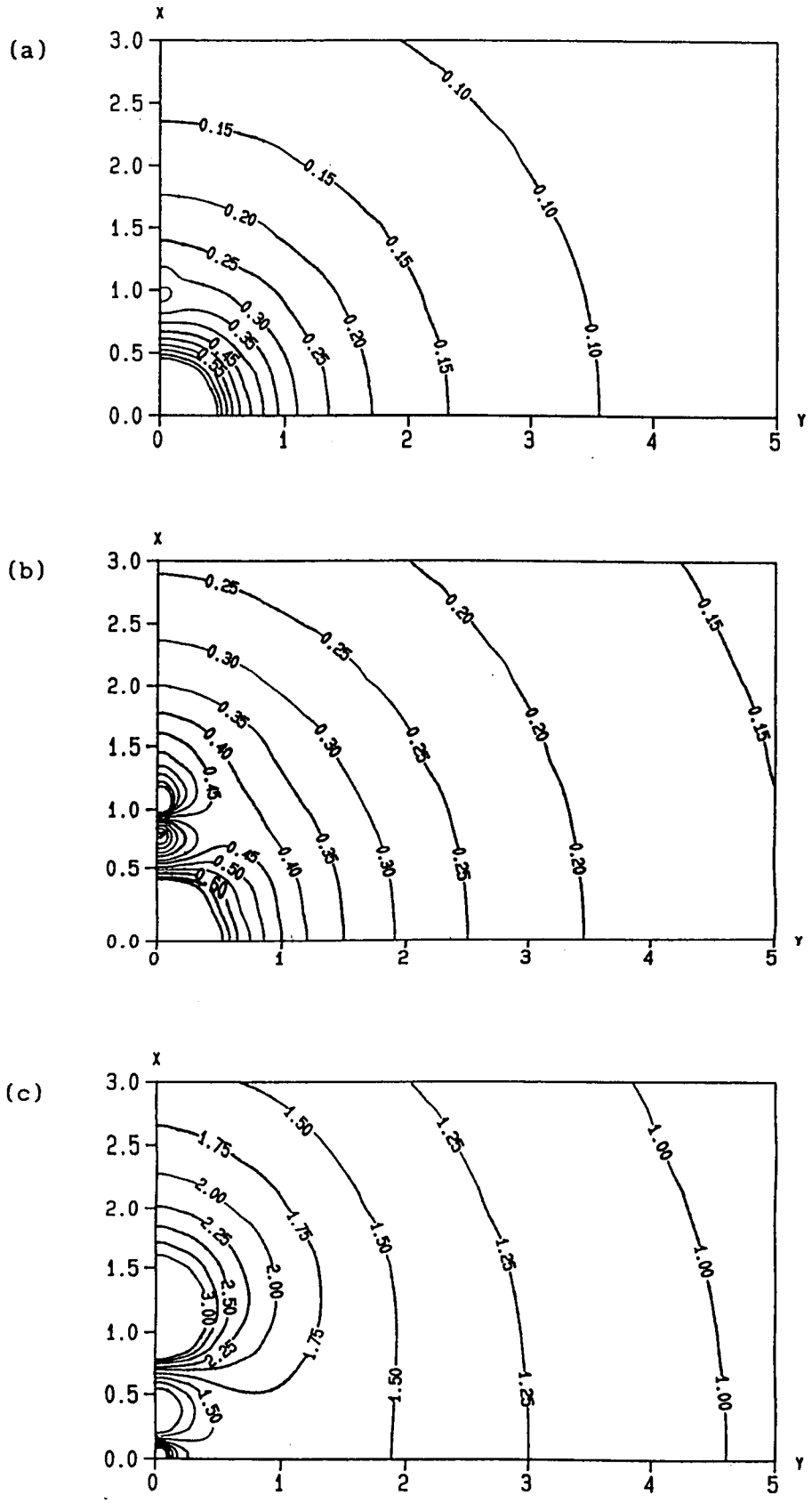

Fig.3.4 Lines of constant speed in front of the hood for a laminar injection of fluid, $\lambda = 1/3$. (a) $G_L = 0.05$, (b) $G_L = 0.5$, (c) $G_L = 5$.

Further examination of Fig.3.4(b), which shows the lines of constant speed in front of a hood operating with $G_L = 0.5$, suggests that a line of constant speed Q_b, between the lines $Q = 0.4$ and $Q = 0.45$, bifurcates, the fluid here being either captured by the suction or caught in the injection flow. This phenomena was also observed experimentally by Fletcher and Saunders (1991,1993). The form of the lines of constant speed is in qualitative agreement with the three-dimensional experimental results obtained by Høgsted (1987) and Fletcher and Saunders (1991,1993). The reason why the agreement between the model and the experimental results is only qualitative is because the flow in the theory is two-dimensional whereas the experiments were carried out on a three-dimensional hood.

An idea of the pressure distribution developed by the Aaberg exhaust hood can be gained from Fig.3.4 which shows lines of constant speed in front of the hood. As a result of the Bernoulli equation for steady flow, i.e.

$$P + \frac{1}{2} q^2 = \text{constant}, \qquad (3.4.6)$$

the lines of constant speed are also representative of the lines of constant pressure, with the areas of high fluid speed corresponding to areas of low fluid pressure.

Figure 3.5, which is derived from expression (3.3.8), shows the dramatic variation in the CLV as a function of the distance, Y, from the inlet of the exhaust hood when the flow in the jet is assumed to be laminar and for $G_L = 0.05$, 0.5 and 5. With $G_L = 0.05$ and $G_L = 0.5$ the injection effect is minimal and the CLV falls sharply as we move away from the inlet. As G_L is increased to 5 the CLV again falls until, at a distance of the order of 0.5a from the inlet, the effect

of the injection of the fluid begins to influence the flow, raising the fluid velocity until a local maximum is reached at a distance of the order of 1a from the inlet. Moving further away from the inlet the fluid velocity decreases, although it remains considerably higher than was predicted for $G_L = 0.05$ and $G_L = 0.5$. Quantitatively, the theory predicts that a hood operating with $G_L = 5$ has an effective working range of over 5a compared with one of less than 0.5a for one operating with $G_L = 0.05$.

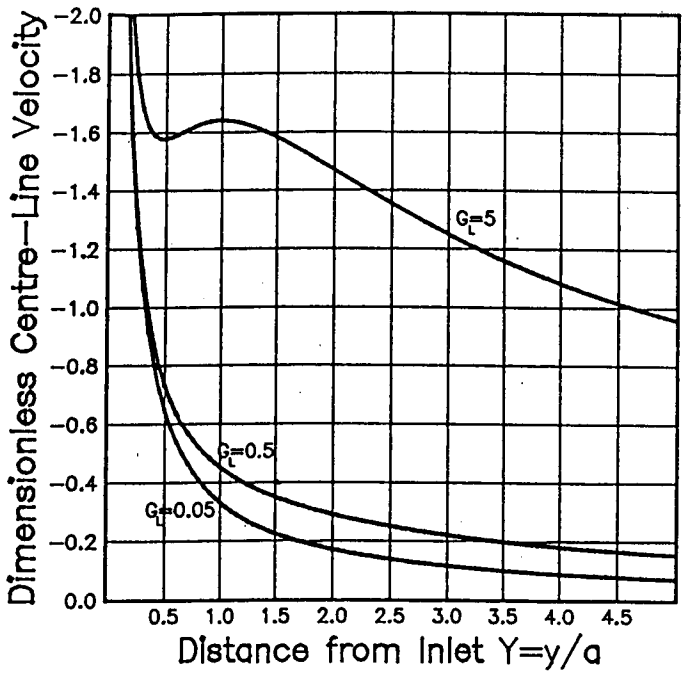

Fig.3.5 Variation in the centre-line velocity with distance from the inlet for laminar injections of fluid, $G_L = 0.05$, 0.5 and 5.

3.4.2 The Turbulent Model

The sets of streamlines, obtained from expression (3.3.3) with $\lambda = 1/2$, describing the flow created by the Aaberg exhaust hood with a turbulent injection of fluid are shown in Figs.3.6(a)-(c) for the parameters $G_T = 0.2$, 2 and 20, respectively. The effect of increasing

the value of G_T is the same as that observed for the laminar case and again results in increased velocities in the efficient flow region of the hood.

Figures 3.7(a)-(c) show the lines of constant speed in front of the Aaberg hood with a turbulent injection of fluid, derived from expressions (3.3.5) for G_T= 0.2, 2 and 20, respectively. Once more it can clearly be seen that as G_T increases the fluid velocity in front of the inlet increases. Figures 3.6 and 3.7 also illustrate that, as in the laminar model, the shape of the effective capture area changes with G_T, becoming narrower and longer as the value of the operating parameter increases. With a turbulent injection of fluid, the effective working range of the hood is greater than for the corresponding laminar case as the turbulent jets entrain more fluid for an equivalent value of the operating parameter (see also Fig.3.3(b) and 3.6(b)). Again, as a direct result of the Bernoulli equation (3.4.6) the lines of constant speed in front of the hood indicate the form of the lines of constant pressure.

Figure 3.8 illustrates how the CLV varies as a function of the distance Y from the inlet with a turbulent injection of fluid for the parameters G_T= 0.2, 2 and 20. With G_T= 0.2 and G_T= 2 the effect due to the injection is minimal with the CLV falling very sharply before levelling off, but increasing G_T by a further factor of 10 to G_T= 20 has a marked effect on the CLV. With G_T= 20 the CLV again falls sharply as we move away from the inlet until a local minimum velocity is reached at a distance of the order of a/4 from the inlet. At this distance from the inlet the Aaberg injection is then able to fully influence the flow, raising its velocity until a local maximum is reached at a distance of the order of 3a/2 from the

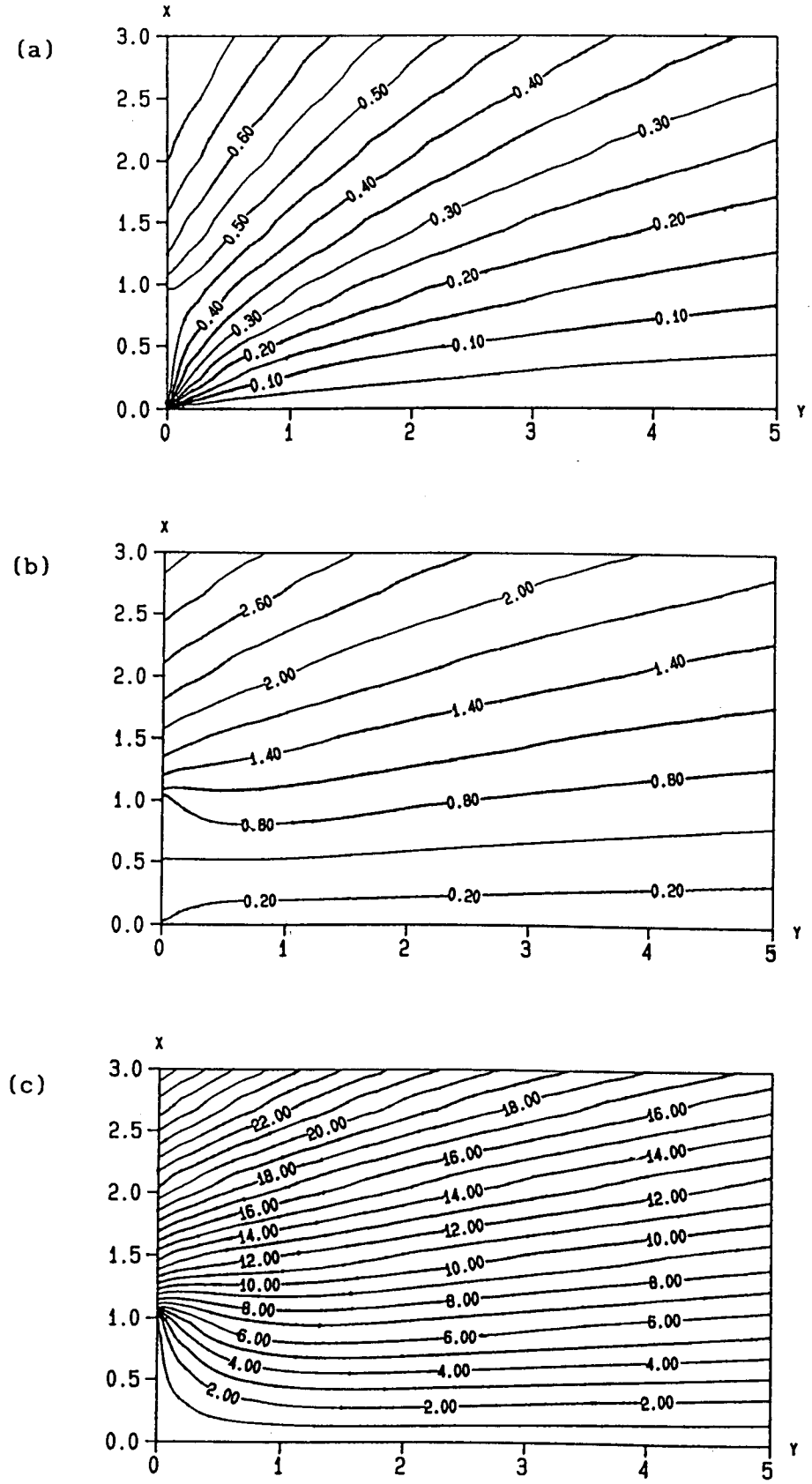

Fig.3.6 Streamlines modelling the Aaberg flow for a turbulent injection of fluid, $\lambda = 1/2$. (a) $G_T = 0.2$, (b) $G_T = 2$, (c) $G_T = 20$.

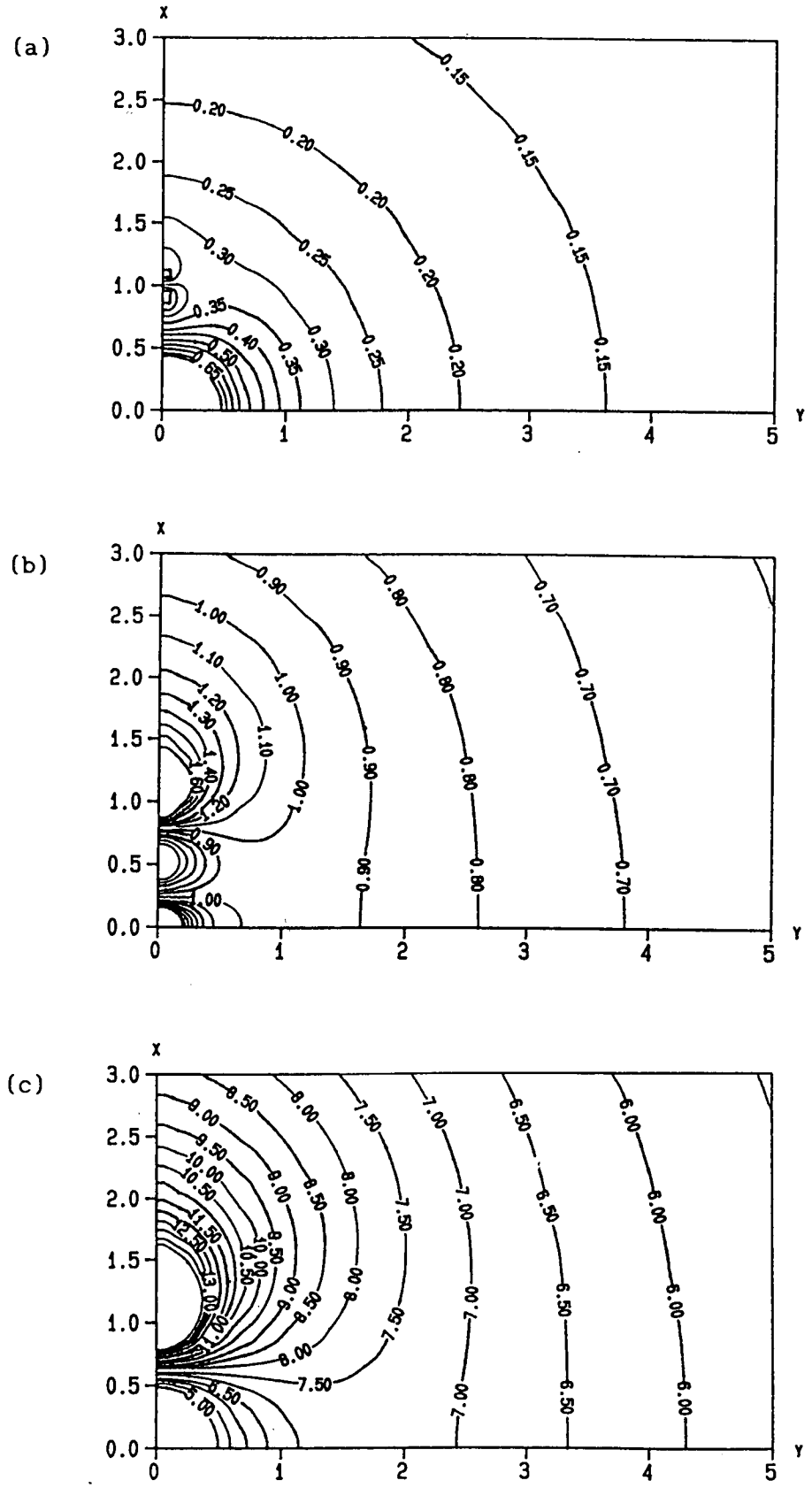

Fig.3.7 Lines of constant speed in front of the hood for a turbulent injection of fluid, $\lambda = 1/2$. (a) $G_T = 0.2$, (b) $G_T = 2$, (c) $G_T = 20$.

inlet. On moving further away from the inlet the CLV steadily decreases although it remains much higher than that predicted for the other values of G_T which were investigated. Quantitatively, Fig.3.8 shows that increasing the magnitude of the parameter G_T from G_T= 0.2 to G_T= 2 increases the effective working range of the hood by approximately a factor of 7. A further increase to G_T= 20 substantially increases this range.

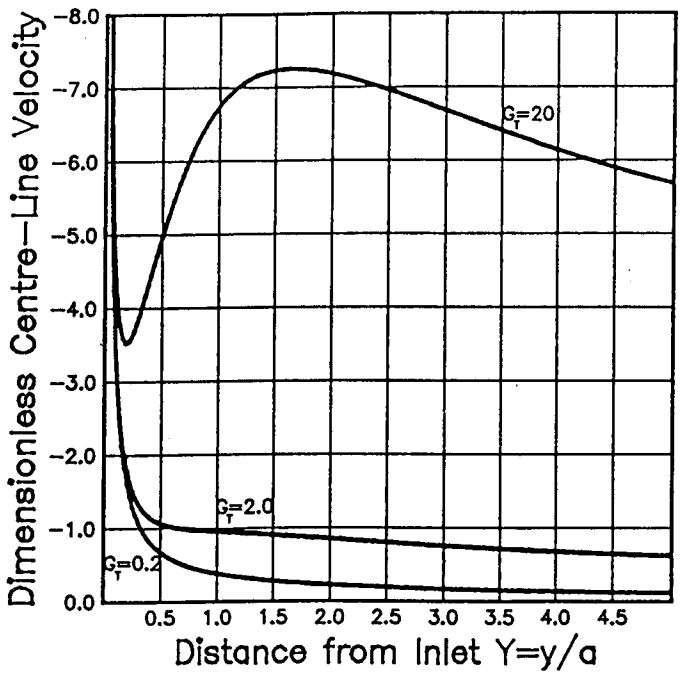

Fig.3.8 Variation in the centre-line velocity with distance from the inlet for turbulent injections of fluid, G = 0.2, 2 and 20.

3.5 THE REYNOLDS NUMBER OF THE JET

In the two-dimensional mathematical model of the jet, the orifice is infinitesimally small and therefore the Reynolds number of the jet cannot be defined in terms of the velocity at the face of

the orifice and the orifice width. Hence, we define the Reynolds number in the jet as

$$R_j(x^*) = \frac{\tilde{u}\, x^*}{\nu} \quad . \tag{3.5.1}$$

The velocity, $\tilde{u}$, along the centre-line of the jet is given by

$$\tilde{u}(x^*) = \frac{2}{3}\,\alpha^2\,(x^*)^{-1/3} \tag{3.5.2}$$

and we therefore obtain the following expression for the jet Reynolds number

$$R_j(X^*) = \frac{2}{3}\left(\frac{9kaX^*}{16\nu^2}\right)^{2/3} \tag{3.5.3}$$

where $X^* = x^*/a$ is the dimensionless distance along the jet axis. On substituting the values of the quantities k and a into the above expression we find that, for air at 20°C,

$$R_j(X^*) \simeq 0.185 \times 10^6\,(X^*)^{2/3}. \tag{3.5.4}$$

It is important to indicate which of the two models, namely the laminar or the turbulent jet, most appropriately models the flow created by the two-dimensional Aaberg exhaust hood. Arriving at a definite critical value of the Reynolds number at which the laminar flow in the jet breaks down to give turbulence is not easy. According to measurements by Andrade (1939) the two-dimensional jet remains laminar up to a critical Reynolds number of approximately $R_e = 30$, where the Reynolds number, R_e, given by equation (2.2.4), relates to the efflux velocity, u(0), and to the width of the slit, b(0), through which the fluid issues. Denoting the flux of fluid issuing from the jet orifice as m_j we have, in two dimensions

$$R_e = m_j/\nu \tag{3.5.5}$$

and the critical Reynolds number of 30 leads to a critical flux, in air, of 5 $cm^2 s^{-1}$. Therefore according to Andrade's observations we would expect the flow in the jet to become turbulent for

$m_j > 5\ cm^2s^{-1}$. This leads us to conclude that the flow in the jet of the two-dimensional Aaberg hood is almost certainly turbulent.

3.6 CONCLUSIONS

A simple, analytical mathematical model for the fluid mechanics of the two-dimensional Aaberg exhaust hood has been developed and the parameter, G, which characterizes this flow has been identified. The parameter G is similar to the experimentalists momentum ratio, I, and models a ratio of the volume flow in the jet to that in the inlet. The analysis presented shows how G is related to the other flow parameters included in the model, i.e. $G_L = G_L(a,k,\nu,m)$ and $G_T = G_T(a,k,m)$. Thus, once the effect which G has on the air flow pattern has been determined then the effect of the individual parameters can also be deduced. This simple model allows us to predict the area of the workplace from which contaminated air can be removed as a function of the parameter G. Although two-dimensional Aaberg hoods exist in practice, see Pedersen (1991a), no experimental data is available for the hood modelled in this chapter and therefore the results obtained in this chapter have been compared with the available three-dimensional axisymmetric hood data. It is found that the lines of constant speed, the shape of the effective capture area and the streamlines are in good qualitative agreement with the limited available data, see Høgsted (1987), Hyldgård (1987), Pedersen and Nielsen (1991) and Fletcher and Saunders (1991,1993).

CHAPTER FOUR

THE EFFECT OF THE EXHAUST INLET SIZE ON THE EFFECTIVE CAPTURE AREA OF AN AABERG EXHAUST HOOD

AND

THE DEFLECTION OF THE AIR FLOW INTO THE HOOD WHICH IS CAUSED BY THE FLOOR OF THE WORKPLACE

4.1 INTRODUCTION

The simple analytical model for the air flow pattern created by a two-dimensional Aaberg exhaust hood which has been presented in chapter 3 predicts that the inviscid fluid flow generated by the hood is governed by the operating parameters G_L and G_T, for laminar and turbulent injections of fluid, respectively. The effect which the parameters G_L and G_T have on the air flow into the hood has now been determined and consequently the effects of the numerous geometrical and flow parameters which arise in the model, e.g. a, k and m, are also known. We now wish to extend the model presented in chapter 3 in order to consider the effect of another geometrical parameter, namely $S = s/a$, where s is the width of the exhaust inlet and a is the width of the exhaust flange. By examining the size and profile of the hood's effective capture area as a function of the inlet size the effect of the parameter S can be established. The model presented in chapter 3 clearly illustrates the advantages of the Aaberg principle over the traditional mode of operation when the air flow induced by the exhaust hood is allowed to develop and spread unhindered. However, does the Aaberg system retain its advantages over traditional systems when the air flow into the hood is obstructed? Also presented in this chapter is an examination of the effect of the floor surface of the workplace on the air flow pattern into an Aaberg exhaust hood when the hood is suspended vertically above and facing the floor. In the field of ventilation engineering an exhaust hood orientated in this manner, see for example Fig.1.5, is usually referred to as a ventilator or ventilator unit. Mathematical modelling techniques are used to

predict the air flow pattern induced by both a traditional ventilator and a ventilator which employs the Aaberg mode of operation. The resulting air flows can then be used to compare the effectiveness of the two different modes of operation. The effect which a variation in the height of the ventilator above the floor surface has on the air flow into the hood is also examined. This effect is predicted by modelling the variation in the air speed induced along the floor surface and centre-line of the ventilator as a function of the height, h, at which it is suspended.

4.2 FORMULATION

When considering the influence of the exhaust inlet size and the presence of the floor on the hood's air flow pattern the only modifications which have to be made to the model which was developed in chapter 3 are to replace the line sink of fluid, which models the exhaust inlet, with an opening of finite width and to introduce an exterior boundary. The introduction of a finite-sized opening means that it is no longer possible to obtain an analytical solution of the equations of motion, and the governing equations have to be solved using numerical techniques for which the finite-difference method has been employed.

The solution procedure is as follows: initially the jet solution is determined and the condition for ψ at the outer edge of the jet shear-layer, which governs the jet-induced flow, deduced. When examining the effects of both the exhaust inlet size and the presence of a floor, the injection flow of the hood is modelled as a

plane turbulent jet of fluid. The upstream boundary condition and the boundary condition across the exhaust inlet are then determined; the remaining boundary conditions, including the modified jet boundary condition, can then be deduced.

For convenience all lengths in the model are non-dimensionalised with respect to the width, a, of the exhaust flange and the stream function with respect to the volume flux, m, into the exhaust inlet. We therefore introduce the dimensionless quantities :

$$S = \frac{s}{a}, \quad H = \frac{h}{a}, \quad R = \frac{r}{a}, \quad X = \frac{x}{a}, \quad Y = \frac{y}{a}, \quad \Psi = \frac{\psi}{m} . \qquad (4.2.1)$$

4.3 THE EFFECT OF THE EXHAUST INLET SIZE

In order to model the effect of the exhaust inlet size on the air flow pattern into the hood it is most convenient to use the polar coordinate system (r,θ). The geometry and coordinate system used to model the two-dimensional Aaberg exhaust hood with a finite-sized exhaust inlet are shown in Fig.4.1. Using the symmetry of the problem, the equations of fluid motion have only to be solved in the region for which $0 \leq \theta \leq \pi/2$ and $r \geq 0$.

4.3.1 The Equations of Motion and the Boundary Conditions

In terms of the dimensionless quantities (4.2.1) the boundary condition at the edge of the turbulent free jet, i.e. equation (3.2.40), may be written

$$\Psi \longrightarrow G_T(R-1)^{1/2} \qquad R > 1 \qquad (4.3.1)$$

where the operating parameter G_T is defined in equation (3.4.3). For

simplicity the slender jet is assumed to have zero thickness so that the boundary condition (4.3.1) is imposed along $\theta = 0$ for $R > 1$.

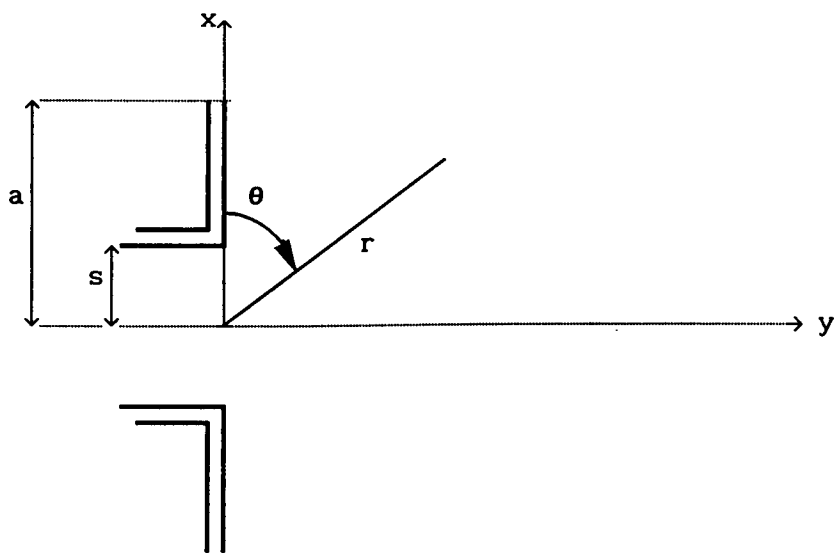

Fig.4.1 The geometry and coordinate system used to model the effect of the exhaust inlet size.

In order to determine numerically the solution of the governing elliptic partial differential equation, i.e. the dimensionless form of equation (2.2.18), namely

$$\frac{\partial^2\Psi}{\partial R^2} + \frac{1}{R}\frac{\partial\Psi}{\partial R} + \frac{1}{R^2}\frac{\partial^2\Psi}{\partial\theta^2} = 0 \ , \qquad (4.3.2)$$

one further boundary condition is required. In this model the boundary condition at large distances upstream from the Aaberg exhaust hood is enforced on $R = R_\infty$ for $0 \leq \theta \leq \pi/2$ where $R_\infty \gg 1$. This boundary condition is taken to be the asymptotic solution of equation (4.3.2) subject to the boundary condition for the jet-induced flow on $\theta = 0$, i.e equation (4.3.1), and subject to

$$\Psi(R,\pi/2) = 0 \qquad (4.3.3)$$

plus the upstream radial flow contribution which results from the flow into the exhaust inlet. To a first-order approximation

$$\Psi = G_T R^{\lambda} \quad \text{on} \quad \theta = 0 \tag{4.3.4}$$

where $\lambda = 1/2$ and following the method of separation of variables we therefore seek a solution of equation (4.3.2) in the form $\Psi = R^{\lambda}\,\theta_1(\theta)$, where θ_1 is a function of θ only. The resulting first-order solution, satisfying boundary conditions (4.3.3) and (4.3.4), is then found to take the form

$$\Psi = G_T \frac{R^{\lambda}}{\sin\lambda\frac{\pi}{2}} \sin\left[\lambda\left(\frac{\pi}{2} - \theta\right)\right] . \tag{4.3.5}$$

To a second-order approximation $\Psi = G_T R^{\lambda} - G_T \lambda R^{\lambda-1}$ on $\theta = 0$ and hence we seek a solution of equation (4.3.2) in the form

$$\Psi = G_T \frac{R^{\lambda}}{\sin\lambda\frac{\pi}{2}} \sin\left[\lambda\left(\frac{\pi}{2} - \theta\right)\right] + R^{\lambda-1}\,\theta_2(\theta) \tag{4.3.6}$$

where θ_2 is a function of θ only, to give the second-order solution

$$\Psi = G_T \frac{R^{\lambda}}{\sin\lambda\frac{\pi}{2}} \sin\left[\lambda\left(\frac{\pi}{2} - \theta\right)\right] - G_T \frac{\lambda R^{\lambda-1}}{\sin(\lambda-1)\frac{\pi}{2}} \sin\left[(\lambda-1)\left(\frac{\pi}{2} - \theta\right)\right] . \tag{4.3.7}$$

Following this process, higher-order approximations to the solution are readily determined. Hence, with the contribution from the exhaust flow we obtain

$$\Psi(R,\theta) = G_T \left\{ \frac{R^{\lambda}}{\sin\lambda\frac{\pi}{2}} \sin\left[\lambda\left(\frac{\pi}{2} - \theta\right)\right] - \frac{\lambda R^{\lambda-1}}{\sin(\lambda-1)\frac{\pi}{2}} \sin\left[(\lambda-1)\left(\frac{\pi}{2} - \theta\right)\right] + \frac{\lambda(\lambda-1)R^{\lambda-2}}{2!\sin(\lambda-2)\frac{\pi}{2}} \sin\left[(\lambda-2)\left(\frac{\pi}{2} - \theta\right)\right] - \ldots \right\} - \left(\frac{1}{\pi R}\right) \tag{4.3.8}$$

on $0 \le \theta \le \pi/2$, $R = R_{\infty} \gg 1$.

The exhaust inlet of the hood is modelled as a rectangular slot of width s into which a flux of fluid, m, is exhausted per unit time. Across the face of the exhaust inlet the fluid velocity is assumed to be constant and hence we obtain the following boundary

condition

$$\psi(r,0) = \frac{mr}{2s} \qquad 0 \leq r \leq s. \qquad (4.3.9)$$

Non-dimensionalising equation (4.3.9) we obtain the boundary condition across the face of the exhaust inlet, namely

$$\Psi(R,0) = \frac{R}{2S} \qquad 0 \leq R \leq S \qquad (4.3.10)$$

and thus the exhaust flange is modelled by the boundary condition

$$\Psi(R,0) = \frac{1}{2} \qquad S < R \leq 1. \qquad (4.3.11)$$

The effect of the exhaust's suction is to modify the boundary condition at the edge of the turbulent jet shear-layer, i.e. equation (4.3.1), which now becomes

$$\Psi(R,0) \longrightarrow 1/2 + G_T(R-1)^{1/2} \qquad R > 1. \qquad (4.3.12)$$

4.3.2 The Finite-difference Scheme

A mesh was placed over the entire solution domain and all derivatives approximated by their usual central-difference approximations. The mesh chosen concentrated the grid points in the area where rapid changes in the solution were expected and was made sufficiently fine so as to ensure the results were mesh independent. A fine mesh was adopted for $0 \leq R \leq 1$ and for $R > 1$ the step length in the radial direction was increased exponentially thus allowing the boundary condition along $R = R_\infty$ for $0 \leq \theta \leq \pi/2$, i.e. equation (4.3.8), to be enforced without demanding excessive computational storage and run times. A detailed description of the finite-difference approximations to the governing equation of fluid motion is now given.

Defining the mesh points in the (R,θ) plane by the points of intersection of the circles $R = i\delta R$ $(i = 1, 2, ..n)$ and the straight lines $\theta = j\delta\theta$ $(j = 1, 2, ..m)$ we may approximate the Laplace

equation (4.3.2) at the point (i,j) using central-difference approximations to all the derivatives, by the finite-difference formula

$$C1\ \Psi_{i-1,j} + C4\ \Psi_{i,j+1} - C3\ \Psi_{i,j} + C2\ \Psi_{i+1,j} + C4\ \Psi_{i,j-1} = 0 \qquad (4.3.13)$$

where the coefficients C1, C2, C3 and C4 are given by

$$C1 = 1 - \frac{1}{2i} \qquad C2 = 1 + \frac{1}{2i} \qquad (4.3.14a,b)$$

$$C3 = 2\left(1 + \frac{1}{(i\delta\theta)^2}\right) \qquad C4 = \frac{1}{(i\delta\theta)^2}\ . \qquad (4.3.14c,d)$$

The finite-difference equation (4.3.13) has a truncation error $\tau_{ij} = O(\delta R^2, \delta\theta^2)$ and using S.O.R. we obtain

$$\Psi_{i,j}^{(n+1)} = \Psi_{i,j}^{(n)} + \frac{\omega}{C3}\left(C1\ \Psi_{i-1,j}^{(n+1)} + C2\ \Psi_{i+1,j}^{(n)} + C4\ \Psi_{i,j-1}^{(n+1)} + C4\ \Psi_{i,j+1}^{(n)} - C3\ \Psi_{i,j}^{(n)}\right) \qquad (4.3.15)$$

where ω is the relaxation parameter and n denotes the number of iterations. The boundary condition for Ψ along the outer curved boundary at $R = R_\infty$ must be imposed where it is realistically met, i.e. for sufficiently large values of R_∞, to ensure that it does not incorrectly influence the flow and so that only a few terms of the series in expression (4.3.8) are needed to approximate the boundary condition to the required accuracy. For this reason an improved mesh is needed and to this end the transformation

$$\xi = \ln R \qquad (4.3.16)$$

is chosen for $R > 1$. The transformation (4.3.16) increases the mesh size in the radial direction exponentially and this enables the condition for Ψ to be imposed for large R whilst demanding less computer storage than with the standard constant mesh. Transforming

the Laplace equation (4.3.2) we obtain

$$\frac{\partial^2\Psi}{\partial\xi^2} + \frac{\partial^2\Psi}{\partial\theta^2} = 0 \qquad (4.3.17)$$

for $R > 1$. Using central-difference approximations for the derivatives, equation (4.3.17) may be approximated at the point (i,j) by the finite-difference formula

$$f1\ \Psi_{i-1,j} + f3\ \Psi_{i,j+1} - f2\ \Psi_{i,j} + f1\ \Psi_{i+1,j} + f3\ \Psi_{i,j-1} = 0 \qquad (4.3.18)$$

where the coefficients f1, f2 and f3 are defined to be

$$f1 = \frac{1}{(\delta\xi)^2}, \quad f2 = 2\left(\frac{1}{(\delta\xi)^2} + \frac{1}{(\delta\theta)^2}\right), \quad f3 = \frac{1}{(\delta\theta)^2}. \qquad (4.3.19a,b,c)$$

The finite-difference equation (4.3.18) has a truncation error $\tau_{ij} = O(\delta\xi^2) + O(\delta\theta^2)$ and in S.O.R. form may be written as

$$\Psi_{i,j}^{(n+1)} = \Psi_{i,j}^{(n)} + \frac{\omega}{f2}\left(f1\ \Psi_{i-1,j}^{(n+1)} + f1\ \Psi_{i+1,j}^{(n)} + f3\ \Psi_{i,j-1}^{(n+1)} + f3\ \Psi_{i,j+1}^{(n)} - f2\ \Psi_{i,j}^{(n)}\right). \qquad (4.3.20)$$

The step length $\delta\xi$ is chosen such that

$$\delta\xi = \ln(1 + \delta R) \qquad (4.3.21)$$

in order to ensure that the meshes match at $R = 1$. Once the approximations to Ψ at the grid points of the mesh have been determined, subject to the appropriate boundary conditions, the dimensionless components of the velocity can be approximated and from them the dimensionless resultant air speed created by the Aaberg exhaust hood, Q, where $Q = q/(m/a)$, may be predicted.

4.3.3 Results and Discussion

The geometry of the Aaberg exhaust hood investigated by Fletcher and Saunders (1991,1993) has an inlet size of $s = 0.037$ m

and this results in a dimensionless inlet size of approximately S = 1/4 for a hood of radius a ≈ 0.15 m. For the purposes of this study the ratio between the momentum flow of the exhaust and that of the injection is kept constant. The momentum ratio chosen corresponds to $G_T \approx 2.0$ and represents the operating conditions at which Fletcher and Saunders (1991) obtained aerodynamic control of their Aaberg exhaust hood. In order to predict what effect varying the inlet size has on the air flow into the hood three different sizes of inlet are considered, namely S = 1/8, 1/4 and 1/2. For each inlet size, streamlines and lines of constant air speed (and hence the effective capture area) deduced from the model are examined for the inlet condition which has a constant volume flux into the inlet.

Lines of constant speed modelling the air flow pattern created by an Aaberg exhaust hood are shown in Figs.4.2(a)-(c) for the inlet sizes of S = 1/8, 1/4 and 1/2, respectively. For the operating conditions given by Fletcher and Saunders (1991), see expressions (3.4.1), the dimensionless resultant capture speed, which corresponds to the level of background air disturbance, is given by $Q_c = 0.75$. From the results shown in Fig.4.2 it is clear that the line of constant speed $Q_c = 0.75$ is not significantly affected by the size of the inlet and in all three cases intersects the centre-line at a distance of approximately 3a from the inlet. Sets of streamlines describing the air flow for the inlet sizes of S = 1/8, 1/4 and 1/2 are shown in Figs.4.3(a)-(c), respectively, and the shaded region illustrates the predicted effective capture area. By comparing Figs.4.3(a)-(c) it is evident that, except very close to the hood, varying the size of the exhaust inlet results in no visible change in the form of the streamlines and hence the

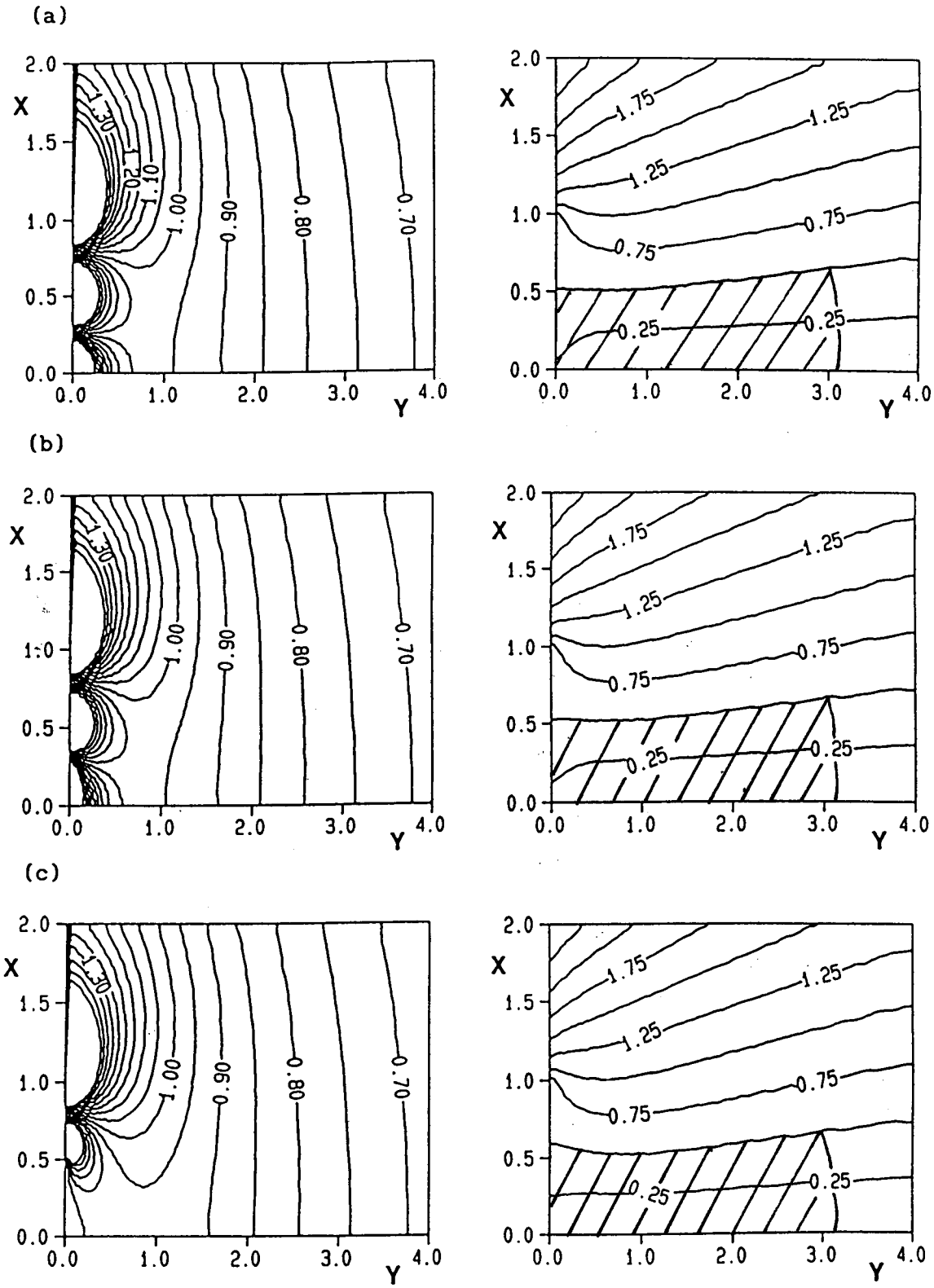

Fig.4.2 Lines of constant speed.

Fig.4.3 Streamlines.

Figs.4.2 and 4.3 The flow pattern created by an Aaberg exhaust hood operating with a constant inlet flux, $G_T = 2$, (a) S = 1/8, (b) S = 1/4 and (c) S = 1/2.

effective capture area may be considered to be virtually independent of S for the inlet sizes considered. Very close to the hood the effective capture area is broadest for the largest inlet size considered and this is most clearly illustrated by comparing Figs.4.3(a) and 4.3(c). The width of the effective capture area predicted by the model for $G_T = 2$ agrees well with the width of the region of 100% capture efficiency observed by Fletcher and Saunders (1991) for the same conditions of exhaustion and injection, see Fig.1.9(b). In both cases the width described is limited to the width of the exhaust flange.

To further investigate the effects of the exhaust inlet size on the induced air flow the air speed along the hood's centre-line deduced from the model was examined for the inlet sizes of S = 1/8, 1/4 and 1/2. Figure 4.4 illustrates the variation in the dimensionless resultant centre-line air speed as a function of the distance, Y = y/a, from the inlet and indicates that although, for small values of Y, the air speed developed by the smaller of the inlet sizes is the greater, the centre-line air speed for each inlet size considered rapidly approaches a common value as Y increases. The common centre-line air speed which is reached after only a very short distance from the inlet, i.e. of the order of 1.5a, confirms that the exhaust's suction has a very limited effect on the movement of air in the workplace. From Fig.4.4 we can also conclude that for $Y > 1.5$ the fluid flow created by the Aaberg exhaust hood is almost totally dominated by the flow induced by the turbulent jet. This result is in agreement with the experimental observations of Fletcher and Saunders (1991,1993) and verifies the conclusions of the plots of the streamlines and air speeds.

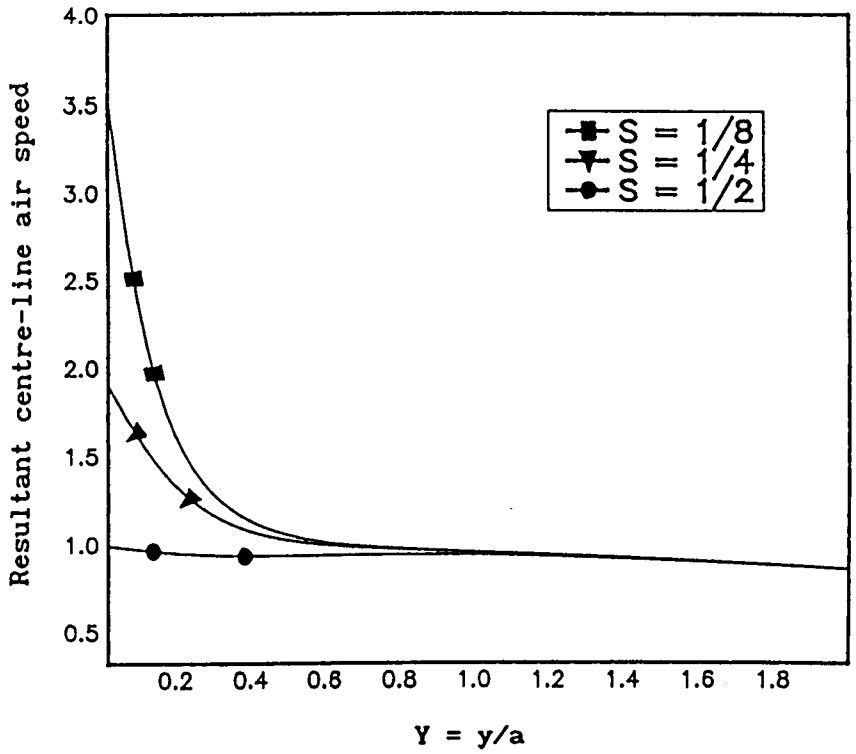

Fig.4.4 Variation in the resultant air speed along the centre-line of the Aaberg exhaust hood as a function of the distance, Y, from the inlet.

4.4 CONCLUSIONS OF THE EFFECTS OF THE EXHAUST INLET SIZE

In this simple mathematical model the fundamental air flow pattern modelling that created by an Aaberg exhaust hood for the case of a neutrally-buoyant contaminant, neglecting the effects of diffusion, has been considered. Under these assumptions the model predicts that varying the size of the exhaust inlet, whilst keeping the exhaust flow rate constant, has no significant effect on the air flow into the hood except in a region very near to the exhaust inlet. In the immediate neighbourhood of the exhaust inlet the model predicts that the width of the effective capture area increases as

the inlet size increases. However, an industrial application of the Aaberg exhaust hood will require the induced air flow to contain and exhaust contaminant which is released in front of and at some distance from the hood. Consequently, the slight increase in the width of the effective capture area at the face of the exhaust which is predicted for an increase in the inlet size will not effect the hood's ability to capture contaminant. The effective capture area of the two-dimensional hood may therefore be regarded as being virtually independent of the exhaust inlet size. In practice, due to the random movement of the contaminant at the edge of the effective capture area, where the air speed is close to the capture speed, we expect the effects of diffusion to dominate the fluid motion. The effective capture area outlined above models that which would be obtained in ideal conditions, i.e. of a neutrally-buoyant contaminant, without the effects of diffusion and where background air disturbances are small.

4.5 THE EFFECT OF THE FLOOR ON THE AIR FLOW INTO AN AABERG EXHAUST HOOD

We now wish to investigate what effect the floor has on the air flow into an Aaberg exhaust hood, see for example Fig.1.5 which depicts a ventilator unit which is placed at a vertical distance of approximately $h = 8a$ above the floor of the workplace. To date, Høgsted (1987) remains the only author to have addressed this problem. Through various experiments Høgsted (1987) observed that, under the correct operating conditions, the presence of the floor

causes the original efficient flow region of the hood, shown schematically in Fig.1.8(a), to be deflected over a wide area of the floor, as illustrated in Fig.1.8(b). The result is an air flow pattern capable of successfully exhausting contaminant which is released far from the centre-line of the hood. Many industrial processes are exothermic and produce buoyant plumes. Such processes, for example reheat furnaces, can be equipped with a ventilator that functions as a hood to receive the hot plume of contaminant. In these, and other processes where it may be beneficial to draw the contaminant vertically upwards, it has been demonstrated experimentally by Høgsted (1987) that a jet-reinforced exhaust system, such as one employing the Aaberg principle, may, under the correct operating conditions prove advantageous over traditional hoods in drawing the contaminant more effectively into the exhaust opening. In the following section a computational mathematical model of the air flow pattern created by a two-dimensional ventilator unit reinforced by a turbulent jet flow, as described by Høgsted (1987), is presented in order to predict the effect of the floor on the hood's effective capture area.

4.5.1 The Equations of Motion and the Boundary Conditions

The ventilator unit is modelled as a two-dimensional flanged opening suspended at a height h above the floor of the workplace. The cartesian coordinate system (x,y) adopted is with the origin at the face of the exhaust inlet, the x axis along the flange of the ventilator and the y axis along its centre-line, see Fig.4.5. The fluid velocities in the x and y directions are denoted by u and v, respectively. The centre-line of the ventilator and the solid floor

surface of the workplace are streamlines of the flow through which the fluid may not cross and along these lines we may take the stream function $\psi = 0$. Owing to the symmetry of the problem about the centre-line the flow need only be determined in the region given by $x \geq 0$, $0 \leq y \leq h$.

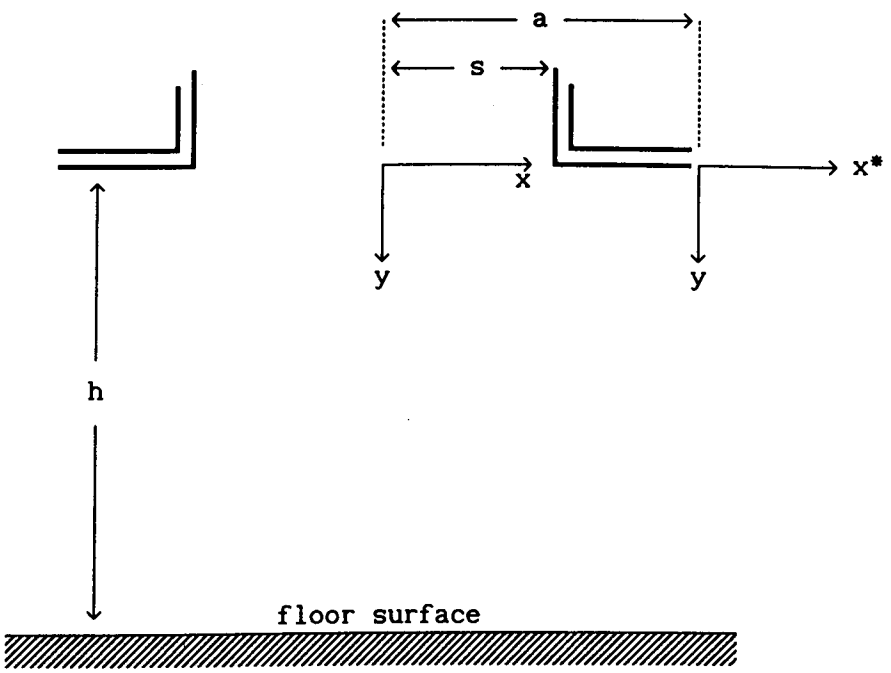

Fig.4.5 The geometry and coordinate system used for the ventilator unit.

The continuity equation, namely

$$\frac{\partial u}{\partial x} + \frac{\partial v}{\partial y} = 0 \qquad (4.5.1)$$

may be satisfied by introducing the stream function ψ such that

$$u = \frac{\partial \psi}{\partial y} \quad \text{and} \quad v = -\frac{\partial \psi}{\partial x} \qquad (4.5.2a,b)$$

and as the exhaust flow is assumed to be inviscid and irrotational then the equation governing the fluid motion is the Laplace equation, which when expressed in terms of the non-dimensional quantities (4.2.1) becomes

$$\frac{\partial^2\Psi}{\partial X^2} + \frac{\partial^2\Psi}{\partial Y^2} = 0 \ . \qquad (4.5.3)$$

In relation to the dimensionless cartesian coordinate system (X,Y) the boundary condition (3.2.40), which models the amount of fluid drawn into the developing turbulent jet, may be written

$$\Psi(X,0) = G_T(X-1)^{1/2} \qquad X > 1. \qquad (4.5.4)$$

Operating under injection alone the plane of the exhaust inlet, the exhaust flange, the centre-line of the hood and the floor all form flow boundaries on which we take $\Psi = 0$. The boundary condition modelling the flow far upstream, i.e. for $X \gg 1$ and $0 \le Y \le H$, which is created by the jet-induced flow is given by the asymptotic solution of equation (4.5.3), subject to the boundary condition (4.5.4) and to $\Psi = 0$ along the floor. The boundary condition which represents the effect of the suction flow far upstream is determined by assuming that the asymptotic flow is purely horizontal with a constant velocity across the depth, $H = h/a$, of the workplace. The constant velocity condition represents only the first-order approximation to the upstream flow which is created by the suction. However, higher-order approximations decay exponentially rather than algebraically, as for the jet flow, and are therefore neglected. Under these assumptions the following upstream boundary condition in the stream function can be derived:

$$\Psi(X,Y) = G_T(X-1)^{1/2}\left(1 - \frac{Y}{H}\right) - \frac{1}{24}G_T(X-1)^{-3/2}\left(2HY - 3Y^2 + \frac{Y^3}{H}\right) -$$

$$\frac{1}{384}G_T(X-1)^{-7/2}\left(8H^3Y - 20HY^3 + 15Y^4 - 3\frac{Y^5}{H}\right) + \ldots. + \frac{1}{2}\left(1 - \frac{Y}{H}\right)$$

for $X \gg 1$, $0 \le Y \le H$. $\qquad (4.5.5)$

The boundary condition which models the flow at the face of the exhaust inlet has already been determined, see section **4.3.1**, and

hence

$$\Psi(X,0) = \frac{X}{2S} \qquad 0 \leq X \leq S. \qquad (4.5.6)$$

The effect of the exhaust's suction is to modify the boundary condition at the edge of the jet shear-layer, i.e. equation (4.5.4), which now becomes

$$\Psi(X,0) \longrightarrow 1/2 + G_T(X-1)^{1/2} \qquad X > 1. \qquad (4.5.7)$$

The centre-line of the ventilator, the floor surface, and the exhaust flange all form flow boundaries and along these we have

$$\Psi(0,Y) = 0 \qquad 0 \leq Y \leq H, \qquad (4.5.8)$$

$$\Psi(X,H) = 0 \qquad X > 0 \qquad (4.5.9)$$

and

$$\Psi(X,0) = 1/2 \qquad S < X \leq 1, \qquad (4.5.10)$$

respectively. The flow of the jet-reinforced ventilator unit is then given by the solution of equation (4.5.3), subject to the boundary conditions (4.5.5)-(4.5.10).

Due to the complexity of the problem an analytical solution is not possible and hence a finite-difference technique has to be used to solve the problem numerically. Although the mathematical model developed above is based on a number of simplifying assumptions some of these may be relaxed in order to examine other aspects of the flow. For instance the model may be adapted to include the effects of different room geometries or hood positions, e.g. a sloping floor surface could be introduced and its effect on the flow pattern investigated.

4.5.2 The Finite-difference Scheme

Finite-difference techniques were chosen to solve the problem with a rectangular mesh in the (X,Y) plane whose grid points are defined by the points of intersection of the perpendicular lines

$X = i\delta x$ $(i = 0, 1, \ldots n)$ and $Y = j\delta x$ $(j = 0, 1, \ldots m)$. By replacing all derivatives by their central-difference approximations the Laplace equation (4.5.3) may be approximated at the point $(i\delta x, j\delta x)$ by the usual five-point formula, namely

$$\Psi_{i-1,j} + \Psi_{i,j+1} - 4\,\Psi_{i,j} + \Psi_{i+1,j} + \Psi_{i,j-1} = 0 \qquad (4.5.11)$$

which in S.O.R. form may be written as

$$\Psi_{i,j}^{(n+1)} = \Psi_{i,j}^{(n)} + \frac{\omega}{4}\left(\Psi_{i-1,j}^{(n+1)} + \Psi_{i,j-1}^{(n+1)} + \Psi_{i+1,j}^{(n)} + \Psi_{i,j+1}^{(n)} - 4\,\Psi_{i,j}^{(n)} \right). \qquad (4.5.12)$$

The upstream boundary condition across the depth of the room, given by equation (4.5.5), must be imposed at a sufficiently large value of X, say for $X = X_\infty$, so as to ensure that it does not incorrectly influence the flow and so that only a few terms of the series approximation in equation (4.5.5) are necessary to give the boundary condition to the level of accuracy of the finite-difference scheme. For this reason the standard rectangular mesh is not suitable and an improved mesh is needed. To this end the transformation $\xi = \ln X$ is chosen for $X > 1$. The mesh length in the Y direction is kept constant, although for large values of H a similar transformation to that used in the X direction could be employed. Using the transformation $\xi = \ln X$ the following finite-difference equations for $X > 1$ may be obtained

$$f1\,\Psi_{i-1,j} + f2\,\Psi_{i,j+1} - f3\,\Psi_{i,j} + f4\,\Psi_{i+1,j} + f2\,\Psi_{i,j-1} = 0 \qquad (4.5.13)$$

and iterating, we obtain

$$\Psi_{i,j}^{(n+1)} = \Psi_{i,j}^{(n)} + \frac{\omega}{f3}\left(f1\,\Psi_{i-1,j}^{(n+1)} + f2\,\Psi_{i,j-1}^{(n+1)} + f4\,\Psi_{i+1,j}^{(n)} + f2\,\Psi_{i,j+1}^{(n)} - f3\,\Psi_{i,j}^{(n)} \right) \qquad (4.5.14)$$

where the coefficients f1, f2, f3 and f4 are now given by

$$f1 = e^{-2\xi}\left(\frac{1}{(\delta\xi)^2} + \frac{1}{2\delta\xi}\right) \qquad f2 = \frac{1}{(\delta x)^2} \qquad (4.5.15a,b)$$

$$f3 = 2\left(\frac{e^{-2\xi}}{(\delta\xi)^2} + \frac{1}{(\delta x)^2}\right) \qquad f4 = e^{-2\xi}\left(\frac{1}{(\delta\xi)^2} - \frac{1}{2\delta\xi}\right) . \qquad (4.5.15c,d)$$

To ensure the meshes match at X = 1 we again must insist that $\delta\xi = \ln(1 + \delta x)$.

4.5.3 Results and Discussion

The operating conditions that Høgsted (1987) employed to run his ventilator unit were not given and so the operating conditions at which Fletcher and Saunders (1991) ran their local Aaberg exhaust hood are used. These operating conditions, see expressions (3.4.1), result in the operating condition which has $G_T \simeq 2$. It should be noted that the operating condition $G_T = 0$ is equivalent to a traditional ventilator, i.e. it models a ventilator operating under suction alone.

Streamlines and lines of constant speed deduced from the model are now used to examine the effect of the turbulent injection of fluid on the air speed induced by a ventilator. Sets of streamlines which describe the air flow pattern created by a ventilator suspended at the height of H = 8 are shown in Figs.4.6(a)-(c) for $G_T = 0$, 2 and 4, respectively. The dimensionless height of H = 8 corresponds approximately to the height at which Høgsted (1987) suspended a ventilator unit when conducting his flow visualization experiments.

From the results shown in Fig.4.6 it is clear that the effect of the injection of fluid on the air flow is to displace the

dividing streamline, $\Psi = 1/2$, towards the floor surface and thereby concentrate the suction in a narrow zone along the floor area of the workplace. The dividing streamline separates the flow travelling towards the inlet from that travelling towards the ejector flow and it is assumed that any contaminant located in the region above the dividing streamline is blown back into the workplace via the jet flow. Figure 4.6(a), which shows sets of streamlines modelling the flow created by a ventilator operating under suction alone, illustrates that under these conditions the ventilator is non-selective, drawing air from all directions towards the exhaust inlet. In Figs.4.6(b) and 4.6(c), which depict sets of streamlines modelling the flow created by a ventilator operating under combined exhaustion and injection, it can be seen that the contaminated air is now selected from an area immediately above the floor surface and drawn towards the inlet. The effect of further increasing the injection, modelled by increasing G_T from $G_T = 2$ to $G_T = 4$, results in the selection of fluid from a very narrow layer immediately above the floor surface. As the injection is further increased the height of the efficient flow region decreases, implying an increased fluid velocity along the floor surface towards the centre-line of the ventilator.

Figures 4.7(a)-(c) show lines of constant air speed in the workplace for a ventilator suspended at the height of $H = 8$ above the floor surface, operating with zero injection ($G_T = 0$) and with combined injection and exhaustion for the parameters $G_T = 2$ and $G_T = 4$, respectively. The effect of the injection of fluid on the lines of constant speed appears quite complicated. However, it can be seen in Fig.4.7 that for the whole area of the workplace the air

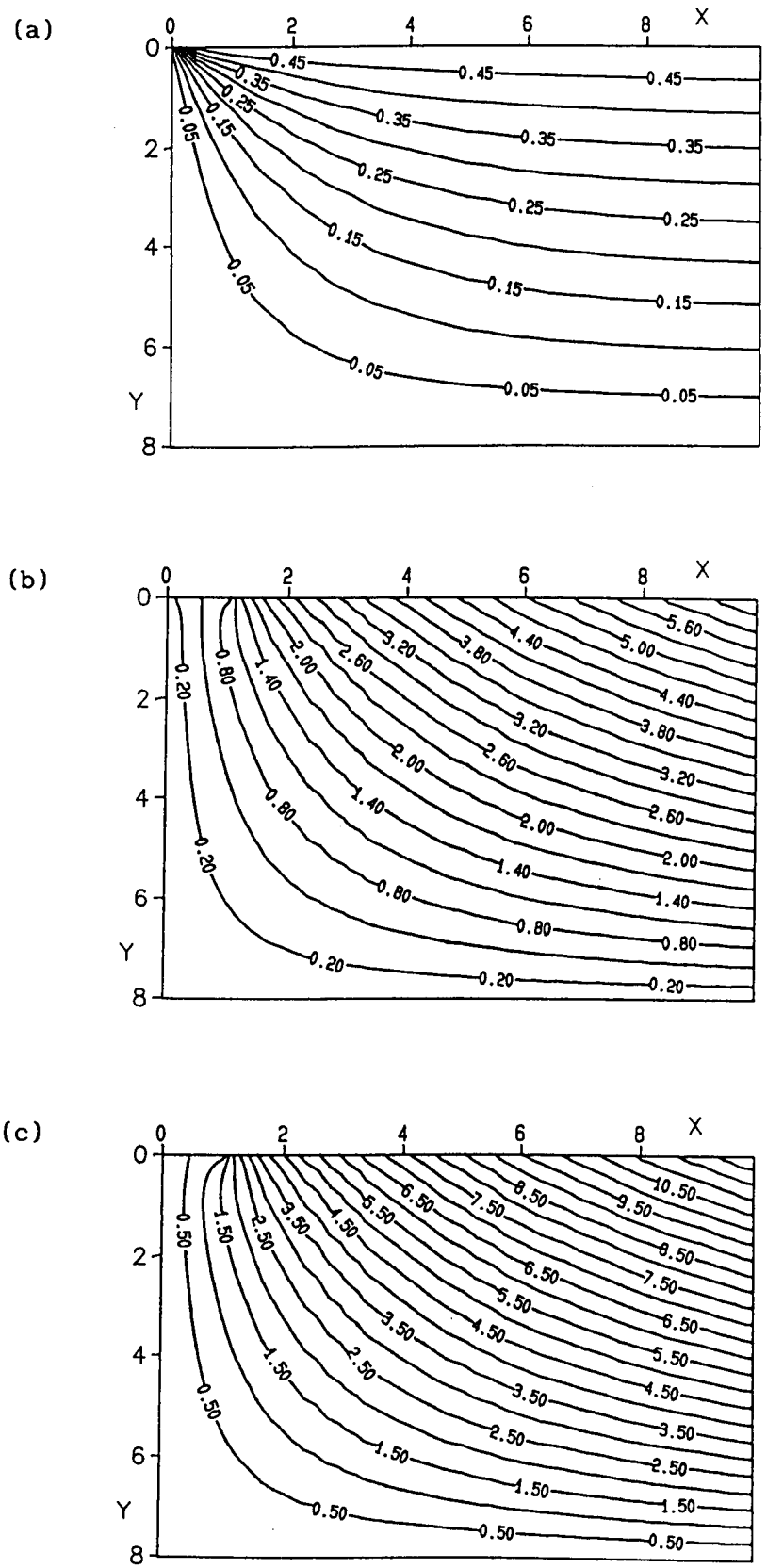

Fig.4.6 Streamlines modelling the flow of the ventilator unit, H = 8, for (a) G = 0, (b) G = 2 and (c) G = 4.

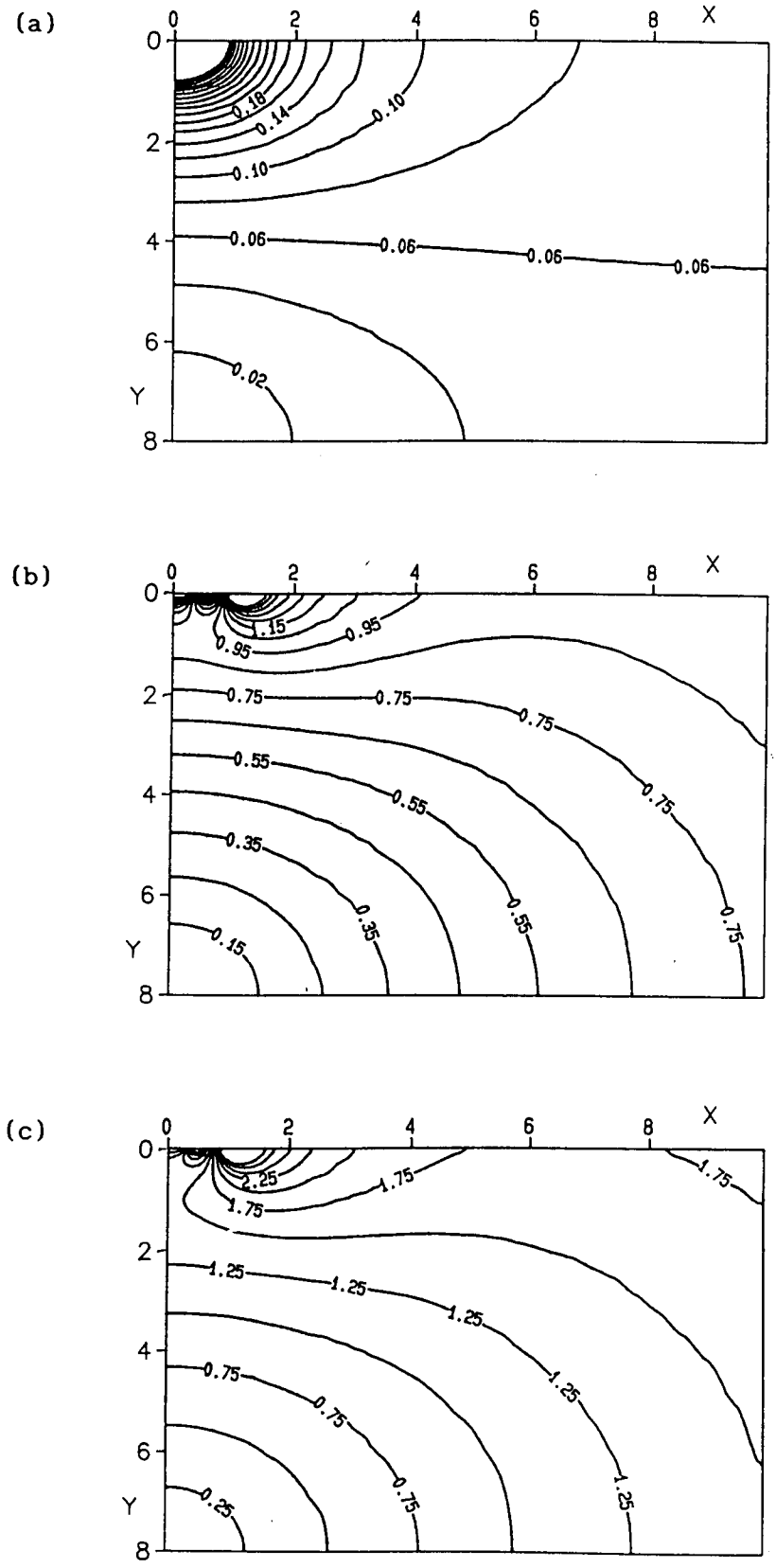

Fig.4.7 Lines of constant speed in the workplace induced by a ventilator unit, H = 8, for (a) G = 0, (b) G = 2 and (c) G = 4.

speeds which are achieved when combining injection and exhaustion are significantly increased over those developed under exhaustion alone ($G_T = 0$), and increasing the parameter G_T further increases the air speeds. The regions where the induced air speeds are most significant for the effective control of the contaminant are along the floor surface and the ventilator's centre-line. The air speeds in these regions are now investigated for a ventilator operating under exhaustion alone and under combined injection and exhaustion.

4.5.3.1 Air Speeds along the Floor Surface of the Workplace

The air speeds along the floor surface of the workplace are of particular interest since once they are known the effective working range of the hood at floor level, for neutrally-buoyant contaminants, may be predicted for various heights of the ventilator above the floor.

Figure 4.8(a) illustrates the variation in the resultant air speed as a function of the distance, X, along the floor surface of the workplace produced by a ventilator operating under exhaustion alone for H = 1, 2, 4 and 8. The figure clearly illustrates how the air speed along the floor surface, created by the exhaustion, falls dramatically as the height of the ventilator above the floor surface is increased.

Figures 4.8(b) and 4.8(c) illustrate how the resultant air speed along the floor surface varies, as a function of X, for a ventilator suspended at heights of H = 1, 2, 4 and 8 when operating with combined exhaustion and injection for the parameters $G_T = 2$ and $G_T = 4$, respectively. By comparing Fig.4.8(a) with Figs.4.8(b) and 4.8(c) the striking effect of the injection of fluid on the air

(a)

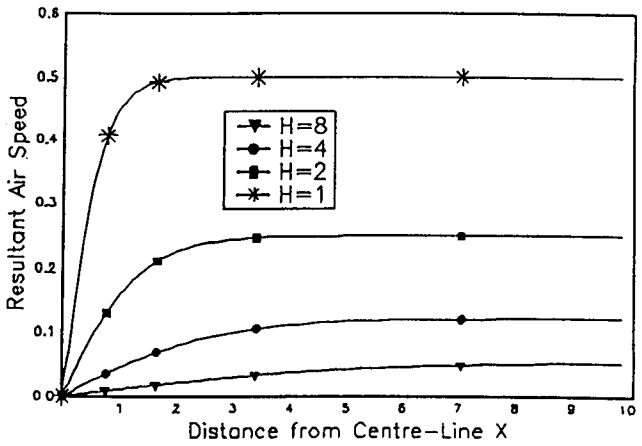

(b)

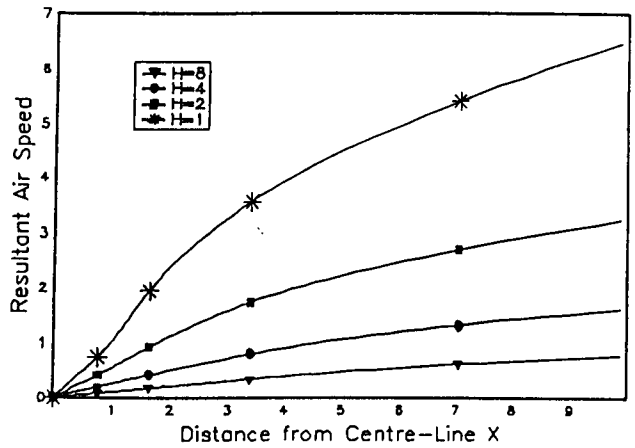

(c)

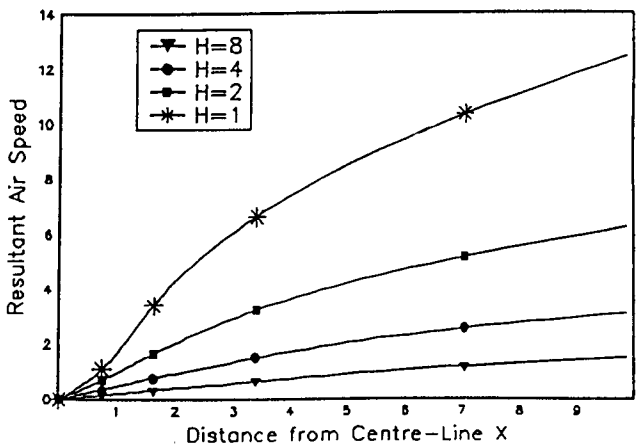

Fig.4.8 Variation in the resultant air speed along the floor surface as a function of the ventilator height, H, for (a) G = 0, (b) G = 2 and (c) G = 4.

speed along the floor surface is clearly visible. The injection significantly enhances the air speed induced along the floor surface for each height, H, considered. Thus, contaminated air from either side of the ventilator's centre-line can be drawn, from a region immediately above the floor surface, towards the centre-line at an increased speed with combined injection and exhaustion than can be achieved with exhaustion alone. The increased air speeds developed when operating at $G_T = 2$ and $G_T = 4$ (over those obtained when $G_T = 0$) also serve to increase the lateral effective working range of the ventilator, allowing contaminated air to be sampled from greater distances either side of the ventilator's centre-line. To summarize, the effect of increasing G_T is to increase the air speed induced along the floor surface towards the centre-line and hence the lateral effective working range of the ventilator.

4.5.3.2 Air Speeds along the Centre-line of the Ventilator

To examine how the turbulent injection of fluid affects the air speed along the ventilator's centre-line, air speeds were calculated for a ventilator operating at $G_T = 0$, $G_T = 2$ and $G_T = 4$ and the results obtained from the three operating situations compared.

The variation in the centre-line air speed, as a function of Y, for a ventilator suspended at the heights of H = 1, 2, 4 and 8 above the floor and operating under exhaustion alone is shown in Fig.4.9(a). This figure illustrates that for each height considered, the air speed along the ventilator's centre-line decays very rapidly with increasing distance from the inlet; from a speed of Q = 2 at the face of the inlet to Q = 0 at the floor surface. Figures 4.9(b) and 4.9(c) depict the variation in the centre-line air speed, as a

(a)

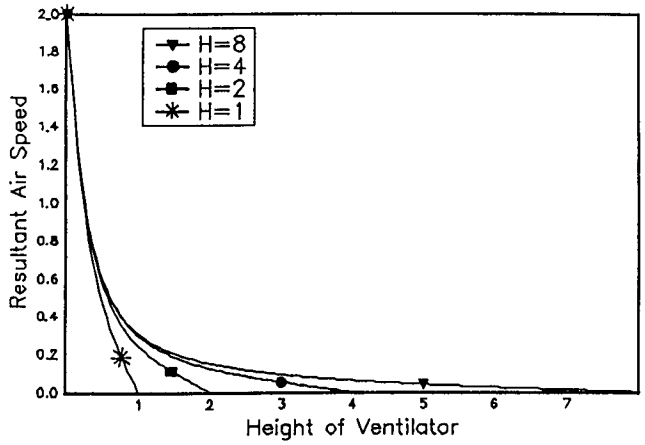

(b)

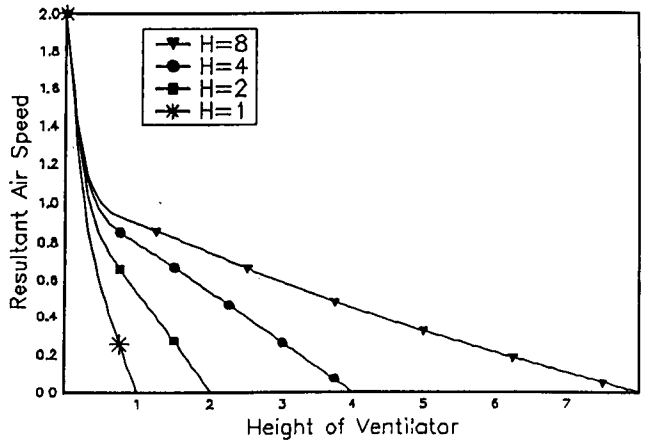

(c)

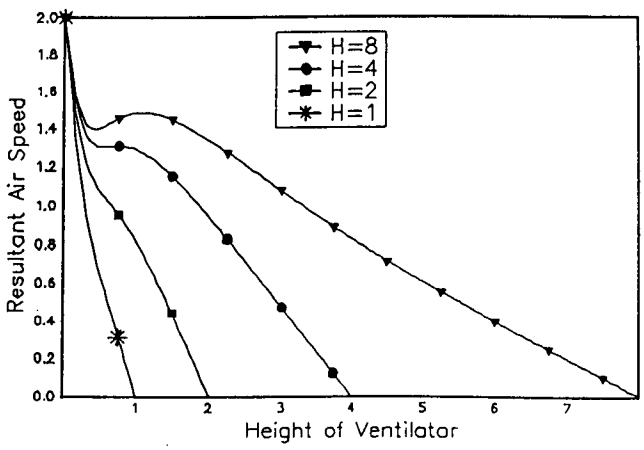

Fig.4.9 Variation in the resultant air speed along the centre-line of the ventilator as a function of the ventilator height, H, for (a) G = 0, (b) G = 2 and (c) G = 4.

function of Y, for a ventilator suspended at the heights of H = 1, 2, 4 and 8 for G_T= 2 and G_T= 4, respectively, and show that initially, as for a ventilator operating under exhaustion alone, the air speeds fall very sharply as one moves away from the hood along its centre-line. However, at only a very small distance from the inlet (of the order of 0.25a) the injection of fluid begins to influence the flow, reducing the sharpness in the decay of the centre-line air speed. This phenomena is observed for each height considered with the only exception being when H = 1.

From Fig.4.9 it can clearly be seen that for a ventilator suspended at the height of H = 1 above the floor surface the injection effect only slightly enhances the centre-line air speed; at this height the suction effect dominates the flow. However, as the ventilator is raised further above the floor surface the effect of the injection of fluid is to significantly enhance the flow into the exhaust opening, with increased air speeds along the centre-line predicted for each height increase considered.

Thus, the model predicts that the effect of the injection on the air flow along the centre-line is only 'felt' after some minimum distance from the inlet has been exceeded and then the injection effect considerably increases the air speeds along the centre-line. The role of the suction is only to draw the contaminated air that distance along the centre-line, towards the inlet, over which the injection of fluid has little effect.

4.5.3.3 The Effective Capture Area

The effective capture area is defined to be the area from which the neutrally-buoyant contaminated air will be drawn into the inlet

and successfully removed from the workplace, see section 2.4.2. In this model the effective capture area is therefore given by the region bounded by the line of constant speed $Q_c = 0.75$ and the dividing streamline $\Psi = 1/2$. From Figs.4.6 and 4.7 we can predict how the shape of this area changes as a function of G_T. On increasing the value of G_T from $G_T = 2$ to $G_T = 4$ we see that the height of the effective capture area above the floor surface decreases and its length increases. Hence increasing the value of G_T implies that the lateral range of the ventilator across the floor area of the workplace increases. Detailed examination of Fig.4.6(c) and 4.7(c) show that for $X > 4$ the contaminant is drawn towards the ventilator's centre-line in a fluid layer immediately above the floor surface and then enters a region where the air speed developed by the hood is less than the capture speed. In this region the contaminated air is free to randomly wander and here diffusion effects will dominate the fluid motion. Contaminated air drawn upwards towards the inlet and which has been successfully contained in the efficient flow region then enters a zone where the air speed is greater than the capture speed and may then be sampled.

4.6 CONCLUSIONS OF THE EFFECT OF THE FLOOR ON THE AIR FLOW INTO AN AABERG EXHAUST HOOD

A simple mathematical model for the fluid mechanics of a two-dimensional ventilator unit reinforced by a turbulent jet of fluid has been developed. This simple model allows us to predict from what area of the floor surface of the workplace the

neutrally-buoyant contaminated air can be successfully removed as a function of the height, H, of the ventilator unit above the floor and the operating parameter G_T. The model predicts, in accordance with the observations of Høgsted (1987), that for a ventilator employing the Aaberg principle the presence of the floor surface results in a lateral deflection of the efficient flow region which may then occupy a substantial region of the floor surface. As a consequence contaminant capture is possible from a significant distance either side of the ventilator's centre-line. Under a correctly balanced ratio of injection and exhaustion the hood will draw contaminated air from a region immediately above the floor surface towards the centre-line and then upwards into the exhaust inlet at greatly enhanced speeds compared to those of a conventional ventilator operating under suction alone.

The other main conclusion which may be drawn from the model highlights the importance which must be placed on the correct installation of the hood. The model predicts that a critical distance between the ventilator and the floor surface exists below which the suction will be the dominant flow. Therefore, in order to obtain the maximum benefit from the addition of the jet of air, the ventilator must be installed above this critical height. In this study the critical height for a two-dimensional ventilator has not been determined although the results obtained in this chapter indicate that, for the chosen operating conditions, the minimum distance of the ventilator from the floor surface should exceed the width of the exhaust flange, a.

The qualitative agreement between the mathematical model for the fluid mechanics of the two-dimensional Aaberg exhaust hood and

the three-dimensional results is encouraging. Hence in the next chapter an axisymmetric, three-dimensional mathematical model will be investigated in order to obtain more quantitative agreement with the experimental data.

CHAPTER FIVE

A THREE-DIMENSIONAL AXISYMMETRIC MODEL FOR THE RADIAL JET ISSUING FROM THE AABERG EXHAUST HOOD

5.1 INTRODUCTION

The simple mathematical models presented in chapters 3 and 4 have given us an understanding of the driving mechanism and operating parameters which govern the fluid flow generated by an Aaberg exhaust hood. The contours of constant speed and the streamlines predicted by the two-dimensional models show good qualitative agreement with the three-dimensional experimental data and flow patterns described by the experimentalists. However, to obtain more detailed information about the air flow pattern generated by the original Aaberg exhaust hood it is necessary to consider the axisymmetric radial free jet flow which is produced by the hood and its effect on the surrounding fluid. In order to determine the flow induced by the axisymmetric radial free jet then the form of the jet must first be determined. The purpose of this chapter is to present a new approach to mathematically model the flow issuing from an axisymmetric radial free jet for both laminar and turbulent flows.

5.2 FORMULATION

The radial free jet produced by the Aaberg exhaust hood may be defined as the axisymmetric flow resulting from a continuous discharge of fluid from the space between two identical, parallel, circular, concentric discs into an infinite region of stagnant fluid of the same density and viscosity. The flow of the radial free jet is one of considerable interest as it occurs in many practical

engineering applications, e.g. in internal combustion engine valves and also in ventilation systems where it is commonly used to provide a ventilating jet. The analogous wall jet flows are encountered in the fields of air cushioning and in vertical take-off and landing (VTOL) aircraft. Although having numerous applications the radial free jet has received little attention in the literature.

By definition, the flow of the radial free jet is axisymmetric and hence, in the cylindrical polar coordinate system (x,θ,y), is independent of the angular coordinate θ, see Fig.5.1. A discussion of the solution procedure to be presented in the following sections is now given.

In the immediate vicinity of the exhaust flange the radial jet of fluid issuing from the annular jet nozzle does not recognize the curvature of the exhaust flange and in this region the flow of fluid from the nozzle is governed by the two-dimensional plane free jet equations. However, at large distances from the exhaust flange the fluid jet appears to issue from a point source and in this region the flow may be modelled as a radial free jet issuing from a point source. The solution of the Prandtl shear-layer equations which govern the fluid motion in both the two-dimensional plane jet and point source radial free jet regions is then determined analytically and expressed in its similarity solution form. In both cases the method followed is analogous to that described by Schlichting (1968) for the two-dimensional plane jet. The two similarity regimes are then combined in a single global regime which exhibits both the properties of the two-dimensional plane jet for $x^* \ll 1$ and of the point source radial free jet for $x^* \gg 1$, where x^* is the distance along the jet axis measured from the jet orifice. Substitution of

the global regime into the governing equation of fluid motion yields a non-linear parabolic partial differential equation whose solution, at each station x*, is determined by marching in the radial direction, away from the initial two-dimensional plane jet solution. The method follows that described by Merkin (1976).

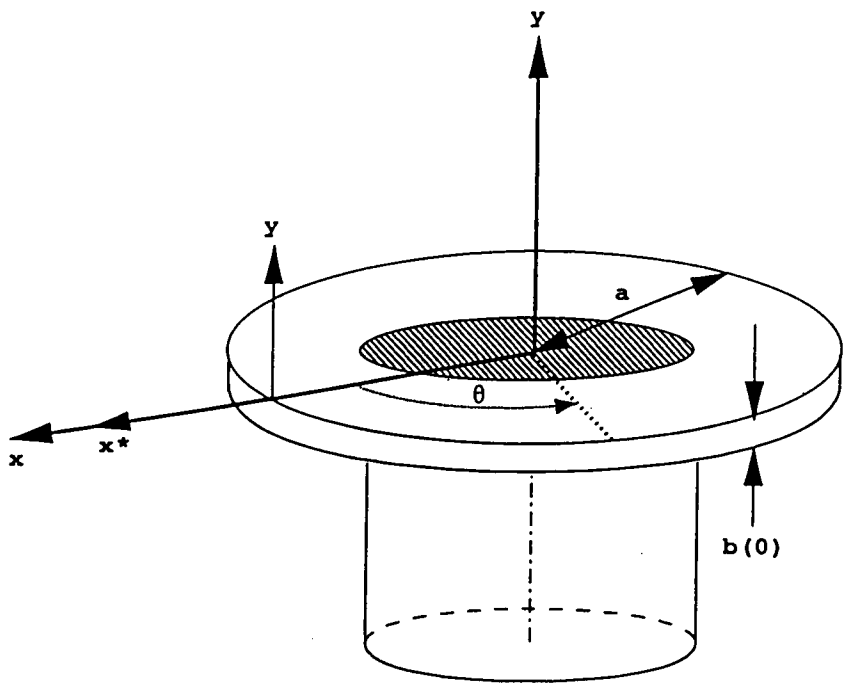

Fig.5.1 The geometry and coordinate system used for the radial free jet.

5.3 THE GOVERNING EQUATIONS OF MOTION AND THE BOUNDARY CONDITIONS

The equations of motion governing the flow of the axisymmetric radial free jet for both laminar and turbulent flows, i.e. equations (2.2.7) and (2.2.10), respectively, may be written in the combined form

$$u \frac{\partial u}{\partial x} + v \frac{\partial u}{\partial y} = \beta \frac{\partial^2 u}{\partial y^2} \qquad (5.3.1a)$$

$$\frac{\partial}{\partial x}(xu) + \frac{\partial}{\partial y}(xv) = 0 \qquad (5.3.1b)$$

where the kinematic viscosity, β, is given by

$$\beta = \begin{cases} \nu & \text{for laminar flow,} \\ \varepsilon & \text{for turbulent flow.} \end{cases}$$

The solution of the differential equations (5.3.1) subject to the boundary conditions (2.2.3) and to the momentum flux condition (2.2.8) will give us a complete description of the flow in a radial free jet which issues radially from a point source. However, in order to model the flow which results from the uniform discharge of fluid from the perimeter of the Aaberg's circular exhaust flange, which has a finite radius, a, it is necessary to define a new coordinate system (x^*,y) whose origin is located at the periphery of the flange, see Fig.5.1. This is achieved by a translation of the radial coordinate x:

$$x^* = x - a \; . \qquad (5.3.2)$$

Equations (5.3.1) then reduce to the following system of equations:

$$u \frac{\partial u}{\partial x^*} + v \frac{\partial u}{\partial y} = \beta \frac{\partial^2 u}{\partial y^2} \qquad (5.3.3a)$$

$$\frac{\partial}{\partial x^*}[(a+x^*)u] + \frac{\partial}{\partial y}[(a+x^*)v] = 0 \qquad (5.3.3b)$$

and expression (2.2.8) for the kinematic momentum flux of the radial free jet in the mainstream direction is now given by

$$k = 4\pi \int_0^\infty (a+x^*)u^2 \, dy = \text{constant.} \qquad (5.3.4)$$

In order to satisfy the continuity equation (5.3.3b) we introduce the Stokes stream function, ψ, such that

$$u = \frac{1}{a+x^*}\frac{\partial \psi}{\partial y} \quad \text{and} \quad v = -\frac{1}{a+x^*}\frac{\partial \psi}{\partial x^*} \; . \qquad (5.3.5a,b)$$

A similarity solution of the equations of motion which govern the flow of the radial free jet produced by the Aaberg exhaust hood, namely a solution of equations (5.3.3), is not possible for $0 < x^* < \infty$ and their solution must be sought in the form of equation (2.2.14). However, before such a solution is sought we must first examine the initial and asymptotic behaviour of the radial free jet for both laminar and turbulent flows. We now investigate the form of the governing equations of fluid motion in these two limiting cases, namely (i) at $x^* = 0$ and (ii) as $x^* \longrightarrow \infty$. The solution of the resulting equations at $x^* = 0$ will give us a complete description of the initial fluid behaviour as it emerges from the narrow space between the exhaust flanges and the solution of the governing equations as $x^* \longrightarrow \infty$ will describe the 'final' or asymptotic behaviour of the radial free jet.

5.4 THE INITIAL BEHAVIOUR OF THE RADIAL FREE JET

In the limit as $x^* \longrightarrow 0$ the governing system of equations (5.3.3) reduce to those for the incompressible flow in a two-dimensional plane jet, namely

$$u\frac{\partial u}{\partial x^*} + v\frac{\partial u}{\partial y} = \beta\frac{\partial^2 u}{\partial y^2} \qquad (5.4.1a)$$

$$\frac{\partial u}{\partial x^*} + \frac{\partial v}{\partial y} = 0 \qquad (5.4.1b)$$

and have to be solved subject to the boundary conditions (2.2.3) and to the momentum conservation equation (5.3.4), which at $x^* = 0$

reduces to

$$k = 4\pi a \int_0^\infty u^2 \, dy = \text{constant.} \qquad (5.4.2)$$

A similarity solution of the equations of motion (5.4.1) which govern the initial development of the radial free jet is now sought for both laminar and turbulent flows.

5.4.1 The Laminar Radial Jet

Following Schlichting (1968) we seek a similarity solution of equations (5.4.1), where $\beta = \nu$, of the form

$$\psi = A(x^*)^p \, \bar{f}(\bar{\eta}) \quad , \quad \bar{\eta} = \frac{y}{B(x^*)^q} \qquad (5.4.3)$$

where the constants A and B, and the exponents p and q are to be determined. At $x^* = 0$ the components of velocity (5.3.5) reduce to

$$u = \frac{1}{a}\frac{\partial \psi}{\partial y} \quad \text{and} \quad v = -\frac{1}{a}\frac{\partial \psi}{\partial x^*} \qquad (5.4.4a,b)$$

and hence we have

$$u = \frac{A}{aB}(x^*)^{p-q} \, \bar{f}' \qquad (5.4.5a)$$

and

$$v = -\frac{A}{a}(x^*)^{p-1} \left(\bar{f}p - q\bar{\eta}\bar{f}' \right) \qquad (5.4.5b)$$

where the prime represents differentiation with respect to $\bar{\eta}$. If we assume that the inertial and viscous terms are of the same order of magnitude in the jet and that the kinematic momentum flux is constant and independent of x^*, then substitution of expressions (5.4.5) for the velocity components into equation (5.4.1a), results in

$$p = \frac{1}{3} \quad , \quad q = \frac{2}{3} \qquad (5.4.6)$$

and

$$AB = \nu a \, . \qquad (5.4.7)$$

For convenience, we may choose

$$A = \nu a^{2/3} \quad , \quad B = a^{1/3} \tag{5.4.8}$$

and hence

$$\psi = \nu a^{2/3} (x^*)^{1/3} \, \bar{f}(\bar{\eta}) \quad , \quad \bar{\eta} = \frac{y}{a^{1/3} (x^*)^{2/3}} \tag{5.4.9}$$

where $\bar{f}(\bar{\eta})$ satisfies the third-order ordinary differential equation

$$\bar{f}''' + \frac{1}{3} \bar{f} \, \bar{f}'' + \frac{1}{3} (\bar{f}')^2 = 0 \tag{5.4.10}$$

which must be solved subject to the boundary conditions

$$\bar{f}'' = 0 \quad , \quad \bar{f} = 0 \quad \text{on} \quad \bar{\eta} = 0 \tag{5.4.11a,b}$$

$$\bar{f}' \longrightarrow 0 \quad \text{as} \quad \bar{\eta} \longrightarrow \infty \, . \tag{5.4.11c}$$

Equation (5.4.10) may be integrated three times to give

$$\bar{f} = 6\alpha \tanh(\alpha \bar{\eta}) \tag{5.4.12}$$

where α is the constant of integration to be determined. From equation (5.4.2) we obtain the required expression for α, namely

$$\alpha = \left(\frac{k}{96\pi\nu^2} \right)^{1/3} \, . \tag{5.4.13}$$

From equations (5.4.5a) and (5.4.9) the initial streamwise component of the velocity and stream function of the laminar radial free jet are then

$$u = 6 \, \alpha^2 \, \nu \, a^{-2/3} (x^*)^{-1/3} \, \mathrm{sech}^2(\alpha \bar{\eta}) \tag{5.4.14}$$

and

$$\psi = 6 \, \alpha \, \nu \, a^{2/3} (x^*)^{1/3} \tanh(\alpha \bar{\eta}) \, , \tag{5.4.15}$$

respectively.

5.4.2 The Turbulent Radial Jet

Following Schlichting (1968) we assume that initially the width of the turbulent radial free jet, b, is proportional to x^*, i.e.

$$b \sim x^* . \tag{5.4.16}$$

The relationship between the centre-line velocity, $\tilde{u}$, in the jet and x^* can then be determined from the momentum conservation equation (5.4.2), from which we obtain

$$k = \text{constant } \tilde{u}^2 \, b \tag{5.4.17}$$

and hence

$$\tilde{u} = \text{constant } x^{*-1/2} \, k^{1/2}. \tag{5.4.18}$$

From the Prandtl expression (2.2.11) for the apparent kinematic viscosity, and in view of equations (5.4.16) and (5.4.18), we have $\varepsilon \sim x^{*1/2}$. Denoting values of the parameters of the flow at a fixed characteristic distance, s, from the jet orifice by the subscript s we may write

$$\tilde{u} = \tilde{u}_s \left(\frac{x^*}{s}\right)^{-1/2}, \quad b = b_s \left(\frac{x^*}{s}\right) \tag{5.4.19a,b}$$

and denoting $\varepsilon_s = \chi \, b_s \tilde{u}_s$ we obtain

$$\varepsilon = \varepsilon_s \left(\frac{x^*}{s}\right)^{1/2}. \tag{5.4.19c}$$

In order to satisfy the equation of continuity (5.4.1b) we now introduce the Stokes stream function, ψ, of the form

$$\psi = \sigma_o^{-1} \, \tilde{u}_s s^{3/2} \, x^{*1/2} \, \bar{f}(\bar{\eta}) \quad , \quad \bar{\eta} = \sigma_o \frac{y}{x^*} \tag{5.4.20}$$

where the constant σ_o denotes the initial spreading rate of the turbulent jet, namely $b = \sigma_o^{-1} x^*$. From equations (5.4.4) the velocity components in the radial free jet are then given by

$$u = \frac{1}{a} \tilde{u}_s s^{3/2} \, x^{*-1/2} \, \bar{f}' \tag{5.4.21}$$

and

$$v = \frac{1}{a} \sigma_o^{-1} \, \tilde{u}_s s^{3/2} \, x^{*-1/2} \left(\bar{\eta}\bar{f}' - \frac{1}{2} \bar{f} \right) \tag{5.4.22}$$

where the prime represents differentiation with respect to $\bar{\eta}$, where $\bar{\eta} = \sigma_o y/x^*$. On substitution of the velocity components into equation (5.4.1a), where $\beta = \varepsilon$, we obtain the following differential equation for $\bar{f}(\bar{\eta})$:

$$\frac{1}{2} \bar{f}'^2 + \frac{1}{2} \bar{f}\bar{f}'' + (\varepsilon_s \sigma_o^2 a \, / \, \tilde{u}_s s^2) \bar{f}''' = 0 \tag{5.4.23}$$

and the boundary conditions (2.2.3) become

$$\bar{f}'' = 0 \quad , \quad \bar{f} = 0 \quad \text{on} \quad \bar{\eta} = 0 \tag{5.4.24a,b}$$

$$\bar{f}' \longrightarrow 0 \quad \text{as} \quad \bar{\eta} \longrightarrow \infty \ . \tag{5.4.24c}$$

The quantity multiplying $\bar{f}'''$ in equation (5.4.23) is dimensionless and as ε_s contains the free constant χ we may choose

$$(\varepsilon_s \sigma_o^2 a \ / \ \tilde{u}_s s^2) = \frac{1}{4} \ . \tag{5.4.25}$$

This substitution simplifies the preceding differential equation which may now be integrated twice to give

$$\bar{f}' + \bar{f}^2 = \frac{a}{s} \tag{5.4.26}$$

and whose solution is given by

$$\bar{f} = \alpha \tanh(\alpha\bar{\eta}) \ , \text{ where } \ \alpha = \left(\frac{a}{s}\right)^{1/2} . \tag{5.4.27}$$

Without loss of generality, the characteristic distance, s, is taken to be the length scale, a, and hence we can express the characteristic velocity, $\tilde{u}_s$, in terms of the kinematic momentum flux, k, which is a known quantity. Thus, from equation (5.4.2), we obtain

$$\tilde{u}_s s^{3/2} = \left(\frac{3ka}{8\pi} \sigma_o \right)^{1/2} . \tag{5.4.28}$$

Using equations (5.4.27) and (5.4.28), the streamwise velocity component (5.4.21) and the stream function (5.4.20) of the turbulent radial free jet, at $x^* = 0$, may then be written as

$$u = \left(\frac{3k}{8\pi a} \sigma_o \right)^{1/2} x^{*-1/2} \operatorname{sech}^2(\bar{\eta}) \tag{5.4.29}$$

and

$$\psi = \left(\frac{3ka}{8\pi\sigma_o} \right)^{1/2} x^{*1/2} \tanh(\bar{\eta}) \ , \tag{5.4.30}$$

respectively.

The apparent kinematic viscosity as $x^* \longrightarrow 0$

It is appropriate at this stage to examine what form the apparent kinematic viscosity, ε, of the turbulent radial free jet assumes as $x^* \longrightarrow 0$, and from equations (5.4.19c), (5.4.25) and

(5.4.28) we obtain

$$\varepsilon = \frac{1}{4}\left(\frac{3k}{8\pi a\sigma_o^3}\right)^{1/2} x^{*1/2}. \qquad (5.4.31)$$

Based on the preceding analysis it seems reasonable to assume that the initial spreading rate of the turbulent radial free jet is identical to that of the two-dimensional turbulent plane jet. The spreading constant, σ_o, has been determined experimentally by Reichardt to be $\sigma_o = 7.67$ for the two-dimensional turbulent plane jet, see Schlichting (1968).

5.5 THE ASYMPTOTIC BEHAVIOUR OF THE RADIAL FREE JET

As $x^* \longrightarrow \infty$ equations (5.3.3) which govern the flow of the radial free jet reduce to

$$u\frac{\partial u}{\partial x^*} + v\frac{\partial u}{\partial y} = \beta\frac{\partial^2 u}{\partial y^2} \qquad (5.5.1a)$$

$$\frac{\partial}{\partial x}(x^*u) + \frac{\partial}{\partial y}(x^*v) = 0 \qquad (5.5.1b)$$

and these equations have to be solved subject to the boundary conditions (2.2.3) and to the momentum conservation equation (5.3.4), which as $x^* \longrightarrow \infty$ becomes

$$k = 4\pi\int_0^\infty u^2 x^*\, dy = \text{constant}. \qquad (5.5.2)$$

The new system of equations (5.5.1) is identical to the system of equations (5.3.1), i.e. at large distances from the flange of the exhaust the fluid behaviour in the radial free jet is identical to the flow which results from the uniform radial discharge of fluid

from a point source. A similarity solution of the equations of motion which govern the asymptotic behaviour of the radial jet is now sought for both laminar and turbulent flows.

5.5.1 The Laminar Radial Jet

Following Schlichting (1968) we seek a similarity solution of equations (5.5.1), where $\beta = \nu$, of the form

$$\psi = A(x^*)^p \, \hat{f}(\hat{\eta}) \quad , \quad \hat{\eta} = \frac{y}{B(x^*)^q} \, . \tag{5.5.3}$$

As $x^* \longrightarrow \infty$ the components of velocity (5.3.5) reduce to

$$u = \frac{1}{x^*} \frac{\partial \psi}{\partial y} \quad \text{and} \quad v = - \frac{1}{x^*} \frac{\partial \psi}{\partial x^*} \tag{5.5.4a,b}$$

and hence

$$u = \frac{A}{B} \, (x^*)^{p-q-1} \, \hat{f}' \tag{5.5.5a}$$

and

$$v = - A \, (x^*)^{p-2} \, (\, \hat{f}p - q\hat{\eta}\hat{f}' \,) \tag{5.5.5b}$$

where the prime now signifies differentiation with respect to $\hat{\eta}$. The usual boundary-layer assumptions result in

$$p = 1 \quad , \quad q = 1 \tag{5.5.6}$$

and

$$AB = \nu \, . \tag{5.5.7}$$

For convenience, we may choose

$$A = \nu \quad , \quad B = 1 \tag{5.5.8}$$

and hence

$$\psi = \nu \, x^* \, \hat{f}(\hat{\eta}) \quad , \quad \hat{\eta} = \frac{y}{x^*} \tag{5.5.9}$$

where $\hat{f}(\hat{\eta})$ satisfies the third-order ordinary differential equation

$$\hat{f}''' + \hat{f} \, \hat{f}'' + (\hat{f}')^2 = 0 \tag{5.5.10}$$

and which must be solved subject to the boundary conditions

$$\hat{f}'' = 0 \quad , \quad \hat{f} = 0 \quad \text{on} \quad \hat{\eta} = 0 \tag{5.5.11a,b}$$

$$\hat{f}' \longrightarrow 0 \quad \text{as} \quad \hat{\eta} \longrightarrow \infty \, . \tag{5.5.11c}$$

Equation (5.5.10) may be integrated three times to give

$$\hat{f} = 2\alpha \tanh(\alpha\hat{\eta}) \qquad (5.5.12)$$

where α is the constant of integration to be determined. From equation (5.5.2) we obtain the required expression for α, namely

$$\alpha = \left(\frac{3k}{32\pi\nu^2} \right)^{1/3} . \qquad (5.5.13)$$

Using equations (5.5.5a) and (5.5.9), the streamwise component of the velocity and stream function in the laminar radial free jet, as $x^* \longrightarrow \infty$, are then

$$u = 2\,\alpha^2\,\nu\,(x^*)^{-1}\,\mathrm{sech}^2(\alpha\hat{\eta}) \qquad (5.5.14)$$

and

$$\psi = 2\,\alpha\,\nu\,x^*\tanh(\alpha\hat{\eta}) , \qquad (5.5.15)$$

respectively.

5.5.2 The Turbulent Radial Jet

A solution of the equations of motion (5.5.1), where $\beta = \varepsilon$, which govern the flow of the turbulent radial jet in the limit as $x^* \longrightarrow \infty$ is now sought. The method adopted is analogous to that described by Schlichting (1968) for the two-dimensional plane jet and given by Tanaka and Tanaka (1976). Following Schlichting (1968) we shall assume that as $x^* \longrightarrow \infty$ the width of the jet, b, is proportional to x^*, i.e. $b \sim x^*$. The relationship between the centre-line velocity, $\tilde{u}$, of the turbulent radial free jet and x^* can then be determined from the momentum conservation equation (5.5.2) from which we obtain

$$k = \text{constant}\ \tilde{u}^2\,x^*\,b \qquad (5.5.16)$$

and hence

$$\tilde{u} = \text{constant}\ x^{*-1}\,k^{1/2}. \qquad (5.5.17)$$

From the Prandtl constant momentum transfer model for the apparent kinematic viscosity we have

$$\varepsilon = \chi \, b \, \tilde{u} \sim x^{*^0} = \text{constant} \qquad (5.5.18)$$

which implies that the apparent kinematic viscosity remains constant over the entire jet for sufficiently large values of x^*. Identifying values of the flow parameters $\tilde{u}$, b and ε at a fixed characteristic distance, s, from the jet orifice by the subscript s we may now write

$$\tilde{u} = \tilde{u}_s \left(\frac{x^*}{s}\right)^{-1} \quad , \quad b = b_s \left(\frac{x^*}{s}\right) \qquad (5.5.19a,b)$$

and hence

$$\varepsilon = \varepsilon_s \, . \qquad (5.5.19c)$$

The continuity equation (5.5.1b) is now satisfied by introducing the Stokes stream function, ψ, in the form

$$\psi = \sigma_\infty^{-1} \, \tilde{u}_s s \, x^* \, \hat{f}(\hat{\eta}) \quad , \quad \hat{\eta} = \sigma_\infty \frac{y}{x^*} \qquad (5.5.20)$$

where σ_∞ is an empirical constant which characterizes the asymptotic spreading rate of the jet such that $b = \sigma_\infty^{-1} x^*$ as $x^* \longrightarrow \infty$. The velocity components of the turbulent radial free jet, given by equations (5.5.4), are then

$$u = \tilde{u}_s s \, (x^*)^{-1} \, \hat{f}' \qquad (5.5.21)$$

and

$$v = \sigma_\infty^{-1} \, \tilde{u}_s s \, (x^*)^{-1} (\, \hat{\eta}\hat{f}' - \hat{f} \,) \, . \qquad (5.5.22)$$

Substitution of the velocity components (5.5.21) and (5.5.22) into equation (5.5.1a), where $\beta = \varepsilon$, leads to a third-order ordinary differential equation for $\hat{f}(\hat{\eta})$, namely

$$\hat{f}'^2 + \hat{f}\hat{f}'' + (\varepsilon_s \sigma_\infty^2 \, / \, \tilde{u}_s s) \, \hat{f}''' = 0 \qquad (5.5.23)$$

and the boundary conditions (2.2.3) become

$$\hat{f}'' = 0 \quad , \quad \hat{f} = 0 \quad \text{on} \quad \hat{\eta} = 0 \qquad (5.5.24a,b)$$

$$\hat{f}' \longrightarrow 0 \quad \text{as} \quad \hat{\eta} \longrightarrow \infty \, . \qquad (5.5.24c)$$

As ε_s contains the free constant χ we may simplify equation (5.5.23) by choosing

$$(\varepsilon_s \sigma_\infty^2 \,/\, \tilde{u}_s s) = \frac{1}{2} \,. \qquad (5.5.25)$$

After this simplification, equation (5.5.23) may now be integrated twice to give

$$\hat{f}' + \hat{f}^2 = 1 \qquad (5.5.26)$$

and whose solution is given by

$$\hat{f} = \tanh(\hat{\eta}) \,, \qquad (5.5.27)$$

and so the streamwise component of the velocity becomes $u = \tilde{u}_s \, (x^*/s)^{-1} \mathrm{sech}^2(\hat{\eta})$. The characteristic velocity $\tilde{u}_s$ can now be expressed in terms of the kinematic momentum flux, k, a known quantity. Thus from equation (5.5.2) we obtain

$$\tilde{u}_s s = \left(\frac{3k}{8\pi} \sigma_\infty \right)^{1/2} \qquad (5.5.28)$$

and hence the streamwise velocity component and the stream function of the turbulent radial free jet, as $x^* \longrightarrow \infty$, may be written as

$$u = \left(\frac{3k}{8\pi} \sigma_\infty\right)^{1/2} x^{*-1} \, \mathrm{sech}^2(\hat{\eta}) \qquad (5.5.29)$$

and

$$\psi = \left(\frac{3k}{8\pi\sigma_\infty}\right)^{1/2} x^* \tanh(\hat{\eta}) \,, \qquad (5.5.30)$$

respectively.

The apparent kinematic viscosity as $x^* \longrightarrow \infty$

From equations (5.5.19c), (5.5.25) and (5.5.28) the form of ε as $x^* \longrightarrow \infty$ is given by

$$\varepsilon = \frac{1}{2} \left(\frac{3k}{8\pi\sigma_\infty^3} \right)^{1/2} = \text{constant.} \qquad (5.5.31)$$

We now require a physically realistic value of the constant σ_∞ which governs the asymptotic spreading rate of the turbulent radial free jet. Although there have been very few published experimental studies on the turbulent radial free jet a survey of the available literature, see Table 5.1, shows that $\sigma_\infty = 8.21$ is an average of the

values determined by experiment.

Author	Value of σ_∞
Heskestad (1966)	7.86
Tanaka and Tanaka (1976)	8.99
Witze and Dwyer (1976)	8.31
Patel (1979)	7.66
Average	$\sigma_\infty = 8.21$

Table 5.1. Experimentally determined values of the spreading constant, σ_∞, for the turbulent radial free jet.

5.6 SOLUTION OF THE EQUATIONS OF MOTION GOVERNING THE FLOW IN A RADIAL FREE JET FOR $0 < x^* < \infty$

Solutions of the equations of motion (5.3.3), which govern the radial free jet flow of an Aaberg exhaust hood have now been determined for both laminar and turbulent flows in the two limiting cases, namely, at $x^* = 0$ and as $x^* \longrightarrow \infty$, and hence the initial and asymptotic behaviour of the radial free jet has been established. We now proceed to investigate the intermediate behaviour of the radial free jet, i.e. its behaviour for $0 < x^* < \infty$.

Non-dimensionalisation

At this stage it is convenient to rewrite the equations of motion (5.3.3) in their dimensionless form. All lengths in the model are referred to the radius of the exhaust flange:

$$X^* = x^*/a \quad , \quad Y = y/a \qquad (5.6.1)$$

and the components of the velocity, the stream function and the kinematic momentum flux of the jet are non-dimensionalised such that

$$U = \frac{u}{\beta_o/a}\ , \quad V = \frac{v}{\beta_o/a}\ , \quad \Psi = \frac{\psi}{\beta_o a}\ , \quad K = \frac{k}{4\pi\beta_o^2} \qquad (5.6.2)$$

where the scaling factor β_o is given by

$$\beta_o = \begin{cases} \nu & \text{for laminar flow,} \\ \varepsilon_o & \text{for turbulent flow} \end{cases}$$

and where $\varepsilon_o = b(0)\,u(0)$ is the 'initial' apparent kinematic viscosity.

Expressed in terms of the non-dimensional quantities (5.6.1) and (5.6.2) the governing equations of motion (5.3.3) become:

$$U\frac{\partial U}{\partial X^*} + V\frac{\partial U}{\partial Y} = \left(\frac{\beta}{\beta_o}\right)\frac{\partial^2 U}{\partial Y^2} \qquad (5.6.3a)$$

$$\frac{\partial}{\partial X^*}[(1+X^*)U] + \frac{\partial}{\partial Y}[(1+X^*)V] = 0 \qquad (5.6.3b)$$

and the boundary conditions (2.2.3) are

$$\frac{\partial U}{\partial Y} = 0\ , \quad V = 0 \quad \text{on} \quad Y = 0 \qquad (5.6.4a,b)$$

$$U \longrightarrow 0 \quad \text{as} \quad Y \longrightarrow \infty\ . \qquad (5.6.4c)$$

The continuity equation (5.6.3b) implies the existence of a dimensionless Stokes stream function, Ψ, where

$$U = \frac{1}{1+X^*}\frac{\partial \Psi}{\partial Y} \quad \text{and} \quad V = -\frac{1}{1+X^*}\frac{\partial \Psi}{\partial X^*}\ . \qquad (5.6.5a,b)$$

The method of solution of the equations (5.6.3) subject to boundary conditions (5.6.4) is now addressed.

5.6.1 The Laminar Radial Jet

The similarity solutions of the laminar radial free jet equations, i.e. equations (5.6.3) with $\beta/\beta_o = 1$, in the two limiting cases, illustrate that for $X^* \ll 1$ the behaviour of the Stokes stream

function is such that

$$\Psi \sim X^{*1/3}\, \bar{f}\left(\frac{Y}{X^{*2/3}} \right) \tag{5.6.6}$$

whilst for $X^* \gg 1$

$$\Psi \sim X^*\, \hat{f}\left(\frac{Y}{X^*} \right) . \tag{5.6.7}$$

Combining the similarity regimes (5.6.6) and (5.6.7) we will look for a single solution of equations (5.6.3), when $\beta/\beta_o = 1$, of the form

$$\Psi = X^{*1/3}(1 + X^{*2})^{1/3}\, f(X^*,\eta) \quad , \quad \eta = \frac{Y}{X^{*2/3}(1 + X^*)^{1/3}} \tag{5.6.8}$$

for $0 < X^* < \infty$. The single expression (5.6.8) exhibits both the properties of the two-dimensional laminar plane jet solution (5.4.15) for $X^* \ll 1$ and those of the asymptotic laminar radial free jet solution (5.5.15) for $X^* \gg 1$. From equations (5.6.5) and (5.6.8) the dimensionless components of velocity of the laminar flow may be expressed as

$$U = \frac{(1+X^{*2})^{1/3}}{(1+X^*)^{4/3}\, X^{*1/3}} \frac{\partial f}{\partial \eta} \tag{5.6.9a}$$

and

$$V = - \frac{1}{(1+X^*)} \left[\frac{(1+3X^{*2})}{3X^{*2/3}(1+X^{*2})^{2/3}}\, f + X^{*1/3}(1+X^{*2})^{1/3} \left(\frac{\partial f}{\partial X^*} + \frac{\partial f}{\partial \eta} \frac{\partial \eta}{\partial X^*} \right) \right] . \tag{5.6.9b}$$

5.6.2 The Turbulent Radial Jet

The similarity solutions of the turbulent radial free jet equations, i.e. equations (5.6.3) with $\beta/\beta_o = \varepsilon/\varepsilon_o$, in the two limiting cases, illustrate that for $X^* \ll 1$ the behaviour of the Stokes stream function is such that

$$\Psi \sim X^{*1/2}\, \bar{f}\left(\sigma_o \frac{Y}{X^*}\right) \tag{5.6.10}$$

whilst for $X^* \gg 1$

$$\Psi \sim X^*\, \hat{f}\left(\sigma_\infty \frac{Y}{X^*}\right) . \tag{5.6.11}$$

Combining the similarity regimes (5.6.10) and (5.6.11) we will look for a single solution of equations (5.6.3), when $\beta/\beta_o = \varepsilon/\varepsilon_o$, of the form

$$\Psi = X^{*1/2}(1+X^*)^{1/2}\, f(X^*,\eta) \quad , \quad \eta = \frac{Y}{X^*} \tag{5.6.12}$$

for $0 < X^* < \infty$. Although not unique, the single expression (5.6.12) exhibits both the properties of the similarity solution (5.4.30) for $X^* \ll 1$ and of the asymptotic similarity solution (5.5.30) for $X^* \gg 1$. From equations (5.6.5) and (5.6.12) the velocity components may be expressed as

$$U = X^{*-1/2}(1+X^*)^{-1/2} \frac{\partial f}{\partial \eta} \tag{5.6.13a}$$

and

$$V = -\frac{1}{(1+X^*)}\left[\frac{(1+2X^*)}{2X^{*1/2}(1+X^*)^{1/2}} f + X^{*1/2}(1+X^*)^{1/2}\left(\frac{\partial f}{\partial X^*} + \frac{\partial f}{\partial \eta}\frac{\partial \eta}{\partial X^*}\right)\right] . \tag{5.6.13b}$$

When substituted into equation (5.6.3a) the velocity components (5.6.9) and (5.6.13) for the laminar and turbulent flows, respectively, yield a third-order, non-linear parabolic partial differential equation in f; namely

$$\frac{\partial^3 f}{\partial \eta^3} + c_1(X^*)\, f \frac{\partial^2 f}{\partial \eta^2} + c_2(X^*)\left(\frac{\partial f}{\partial \eta}\right)^2 = c_3(X^*)\left(\frac{\partial f}{\partial \eta}\frac{\partial^2 f}{\partial X^* \partial \eta} - \frac{\partial f}{\partial X^*}\frac{\partial^2 f}{\partial \eta^2}\right) \tag{5.6.14}$$

whose coefficients $c_1(X^*)$, $c_2(X^*)$ and $c_3(X^*)$ are given by:

(i) for the laminar radial jet

$$c_1(X^*) = \frac{(1+3X^{*2})}{3(1+X^*)^{2/3}(1+X^{*2})^{2/3}} \qquad (5.6.15a)$$

$$c_2(X^*) = \frac{3X^{*3} - X^{*2} + 5X^* + 1}{3(1+X^*)^{5/3}(1+X^{*2})^{2/3}} \qquad (5.6.15b)$$

$$c_3(X^*) = \frac{X^*(1+X^{*2})^{1/3}}{(1+X^*)^{2/3}} \qquad (5.6.15c)$$

and (ii) for the turbulent radial jet

$$c_1(X^*) = \frac{(1+2X^*)X^{*1/2}}{2(1+X^*)^{3/2}}\left(\frac{\varepsilon}{\varepsilon_o}\right)^{-1} \qquad (5.6.16a)$$

$$c_2(X^*) = \frac{(1+2X^*)X^{*1/2}}{2(1+X^*)^{3/2}}\left(\frac{\varepsilon}{\varepsilon_o}\right)^{-1} \qquad (5.6.16b)$$

$$c_3(X^*) = \frac{X^{*3/2}}{(1+X^*)^{1/2}}\left(\frac{\varepsilon}{\varepsilon_o}\right)^{-1}. \qquad (5.6.16c)$$

Equation (5.6.14) has to be solved subject to the following boundary conditions:

$$\frac{\partial^2 f}{\partial \eta^2} = 0 \quad , \quad f = 0 \quad \text{on} \quad \eta = 0 \qquad (5.6.17a,b)$$

$$\frac{\partial f}{\partial \eta} \longrightarrow 0 \quad \text{as} \quad \eta \longrightarrow \infty \qquad (5.6.17c)$$

and subject to the initial condition which has

$$f = \bar{f} \quad \text{on} \quad X^* = 0 \,. \qquad (5.6.17d)$$

The apparent kinematic viscosity for $0 < X^* < \infty$

Before we can proceed to solve equation (5.6.14) in the turbulent case we must first postulate the behaviour of the apparent kinematic viscosity, ε, as the radial free jet develops in terms of the parameters in the flow.

Equation (5.4.31) which expresses the initial form of the apparent kinematic viscosity may be written

$$\frac{\varepsilon}{\varepsilon_o} = C_o \, X^{*1/2} \qquad \text{for } X^* \ll 1 \qquad (5.6.18)$$

where

$$C_o = \frac{1}{4}\left(\frac{3K}{2\sigma_o^3}\right)^{1/2} \qquad (5.6.19)$$

and on substitution of the Reichardt, see Schlichting (1968), value for the initial spreading constant, namely $\sigma_o = 7.67$, we obtain $C_o = 0.0144\ K^{1/2}$. The non-dimensional form of equation (5.5.31), which expresses the nature of the apparent kinematic viscosity for $X^* \gg 1$, is given by

$$\frac{\varepsilon}{\varepsilon_o} = C_\infty \qquad \text{for } X^* \gg 1 \qquad (5.6.20)$$

where

$$C_\infty = \frac{1}{2}\left(\frac{3K}{2\sigma_\infty^3}\right)^{1/2} . \qquad (5.6.21)$$

If we adopt the average experimental value of $\sigma_\infty = 8.21$, see Table 5.1, for the asymptotic spreading constant then we have $C_\infty = 0.0260\ K^{1/2}$.

Thus for $X^* \ll 1$ the apparent kinematic viscosity, $\varepsilon/\varepsilon_o$, is proportional to the square root of the distance from the orifice, whilst for $X^* \gg 1$ the value of $\varepsilon/\varepsilon_o$ remains constant over the whole jet and is independent of X^*. We now propose that the transition of the apparent kinematic viscosity from its initial to its asymptotic tendencies occurs smoothly as the jet develops, accordingly we shall write

$$\frac{\varepsilon}{\varepsilon_o} = \frac{C_o \, X^{*1/2}}{\left(1 + \left(\frac{C_o}{C_\infty}\right)^2 X^*\right)^{1/2}} \qquad (5.6.22a)$$

for $0 < X^* < \infty$. Expression (5.6.22a) does not uniquely describe the

transition of the apparent kinematic viscosity from initial to asymptotic behaviour and other expressions, for example

$$\frac{\varepsilon}{\varepsilon_o} = \frac{C_o X^{*1/2}}{\left(1 + \left(\frac{C_o}{C_\infty}\right)^4 X^{*2}\right)^{1/4}} \qquad (5.6.22b)$$

could equally have been chosen. The differences in the final solution which result from the different choices for the expression of $\varepsilon/\varepsilon_o$ will be examined in section 5.8.

5.7 NUMERICAL SOLUTION OF THE NON-LINEAR PARABOLIC PARTIAL DIFFERENTIAL EQUATION

In order to determine the function f and hence the form of the radial free jet a modified Crank-Nicolson, finite-difference technique as described by Merkin (1976) is employed to solve equation (5.6.14) subject to conditions (5.6.17). Following Merkin (1976) the new dependent variable q given by

$$q = \frac{\partial f}{\partial \eta} \qquad (5.7.1)$$

is introduced and then equation (5.6.14) becomes

$$\frac{\partial^2 q}{\partial \eta^2} + \frac{\partial q}{\partial \eta} \int_0^\eta \left(c_1(X^*) q + c_3(X^*) \frac{\partial q}{\partial X^*} \right) d\eta + c_2(X^*)\, q^2 - c_3(X^*)\, q \frac{\partial q}{\partial X^*} = 0. \qquad (5.7.2)$$

Equation (5.7.2) is then written in finite-difference form using $v = q_1 + q_2$ as a new dependent variable where $q_1 = q(X^*, Y)$, $q_2 = q(X^*+\delta X^*, Y)$ and δX^* is the step length in the X^* direction. The X^* derivatives are replaced by differences giving

$$\frac{\partial q}{\partial X^*} = \frac{v - 2q_1}{\delta X^*} + O(\delta X^*) \qquad (5.7.3)$$

and all other terms are averaged over the step from X^* to $X^*+\delta X^*$. For example, the second derivative with respect to η is given by

$$\frac{\partial^2 q}{\partial \eta^2} = \frac{1}{2}\left(\frac{q_{1j+1} - 2q_{1j} + q_{1j-1}}{h^2} + \frac{q_{2j+1} - 2q_{2j} + q_{2j-1}}{h^2}\right) \qquad (5.7.4a)$$

$$= \frac{1}{2h^2}(v_{j+1} - 2v_j + v_{j-1}) \qquad (5.7.4b)$$

where h is the step length in the η direction. The finite-difference equation at $\eta = jh$ is then

$$v_{j+1} - 2v_j + v_{j-1} + \frac{h^2}{4}(v_{j+1} - v_{j-1})(\lambda_1 V_j + \lambda_2 D_j) + \lambda_3 v_j h^2 (v_j - 2q_{1j}) + \lambda_4 h^2 v_j^2 = 0 \qquad (5.7.5)$$

for $j = 0(1)N$, where

$$V_j = \frac{1}{2}v_0 + v_1 + \ldots\ldots + v_{j-1} + \frac{1}{2}v_j \qquad (5.7.6a)$$

$$D_j = \frac{1}{2}q_{10} + q_{11} + \ldots\ldots + q_{1j-1} + \frac{1}{2}q_{1j} \qquad (5.7.6b)$$

$$\lambda_1 = \frac{1}{2}(c_1(X^*) + c_1(X^*+\delta X^*)) + \frac{1}{\delta X^*}(c_3(X^*) + c_3(X^*+\delta X^*)) \qquad (5.7.6c)$$

$$\lambda_2 = -\frac{2}{\delta X^*}(c_3(X^*) + c_3(X^*+\delta X^*)) \qquad (5.7.6d)$$

$$\lambda_3 = -\frac{1}{2\delta X^*}(c_3(X^*) + c_3(X^*+\delta X^*)) \qquad (5.7.6e)$$

$$\lambda_4 = \frac{1}{4}(c_2(X^*) + c_2(X^*+\delta X^*)) \; . \qquad (5.7.6f)$$

Boundary conditions (5.6.17a,c) are satisfied by taking

$$v_1 = v_{-1} \quad \text{and} \quad v_{N+1} = 0 \; , \qquad (5.7.7a,b)$$

respectively. The value of $(N+1)h$ is chosen to be sufficiently large so that condition (5.7.7b) is applied at a point at the outer edge of the shear-layer. The boundary condition (5.6.17b) is

automatically satisfied from choosing $q_{10} = 0$. Before equation (5.7.5) can be used to determine the form of the radial free jet an initial profile for q is required.

(i) Initial profile for the laminar radial jet

On substitution of $\partial f/\partial\eta$, from equation (5.7.1), into equation (5.6.9a) we can obtain the relationship

$$q = \frac{U\, X^{*1/3}(1+X^*)^{4/3}}{(1+X^{*2})^{1/3}} \quad . \tag{5.7.8}$$

The streamwise component of the velocity, U, in the laminar radial free jet at $X^* = 0$, i.e. the dimensionless form of equation (5.4.14), may be written

$$U = 6\,\alpha^2\, X^{*-1/3}\, \mathrm{sech}^2\left[\alpha\eta(1+X^*)^{1/3}\right] \tag{5.7.9a}$$

where $$\alpha = \left(\frac{K}{24}\right)^{1/3} \quad , \quad \eta = \frac{Y}{X^{*2/3}(1+X^*)^{1/3}} \tag{5.7.9b}$$

and hence substitution of equation (5.7.9a) into equation (5.7.8) yields the initial profile for the laminar radial jet, namely

$$q = 6\,\alpha^2\, \mathrm{sech}^2(\alpha\eta) \qquad \text{at } X^* = 0 \; . \tag{5.7.10}$$

(ii) Initial profile for the turbulent radial jet

On substitution of $\partial f/\partial\eta$, from equation (5.7.1), into equation (5.6.13a) we can obtain the relationship

$$q = U\, X^{*1/2}(1+X^*)^{1/2} \quad . \tag{5.7.11}$$

The streamwise component of the velocity, U, in the turbulent radial free jet at $X^* = 0$, i.e. the dimensionless form of equation (5.4.29), may be written

$$U = \left(\frac{3K}{2}\,\sigma_o\right)^{1/2} X^{*-1/2}\mathrm{sech}^2(\sigma_o\eta) \quad , \quad \eta = \frac{Y}{X^*} \tag{5.7.12}$$

and substitution of equation (5.7.12) into equation (5.7.11) yields

the initial profile for the turbulent radial jet, namely

$$q = \left(\frac{3K}{2}\,\sigma_o\right)^{1/2} \operatorname{sech}^2(\sigma_o \eta) \qquad \text{at } X^* = 0 \,. \quad (5.7.13)$$

The system of non-linear algebraic equations (5.7.5) is of the form

$$F_j(v_0,\, v_1, \ldots\ldots v_N) = 0 \qquad j = 0(1)N \quad (5.7.14)$$

and is solved iteratively using Newton's method, see Smith (1985). If we assume that $v_i^{(0)}$, for $i = 0(1)N$, is a known approximation to the exact solution v_i then by the Taylor series expansion

$$F_j(v_i) = F_j(v_i^{(0)}) + (v_i - v_i^{(0)})\left(\frac{\partial}{\partial v_i} F_j\right)_0 + \ldots = 0 \quad (5.7.15)$$

and hence to a first-order approximation

$$(v_i - v_i^{(0)})\left(\frac{\partial}{\partial v_i} F_j\right)_0 = - F_j(v_i^{(0)}) \,. \quad (5.7.16)$$

Equation (5.7.16) represents (N+1) linear equations for the (N+1) unknowns $(v_i - v_i^{(0)})$ and may be written in the matrix form

$$A\,\underline{l} = \underline{c} \quad (5.7.17)$$

where $l_j = v_j - v_j^{(0)}$, $c_j = - F_j(v_i^{(0)})$ and A is a matrix of the form

$$\begin{pmatrix}
AA_0 & 1+D_0 & 0 & \cdots & \cdots & \cdots & 0 \\
1+A_1/2-D_1 & AA_1 & 1+D_1 & \ddots & & & \vdots \\
A_2/2 & 1+A_2-D_2 & AA_2 & 1+D_2 & \ddots & & \vdots \\
A_3/2 & A_3 & 1+A_3-D_3 & AA_3 & \ddots & & \vdots \\
A_4/2 & A_4 & A_4 & 1+A_4-D_4 & AA_4 & \ddots & 0 \\
\vdots & \vdots & \ddots & \ddots & \ddots & \ddots & 1+D_{N-1} \\
A_N/2 & A_N & \cdots & \cdots & A_N & 1+A_N-D_N & AA_N
\end{pmatrix}$$

(5.7.18)

where

$$AA_j = \left(\frac{\partial}{\partial v_j} F_j \right)_0 \qquad j = 0(1)N \qquad (5.7.19a)$$

$$A_j = \left(\frac{\partial}{\partial v_i} F_j \right)_0 \qquad i = 1(1)j-1 \qquad (5.7.19b)$$

and

$$D_j = \frac{\partial}{\partial v_{j+1}}(F_j) - 1 \qquad j = 0(1)N. \qquad (5.7.19c)$$

From the finite-difference equation (5.7.5) we obtain the following expressions for the matrix elements

$$A_j = \lambda_1 \frac{h^2}{4} (v_{j+1} - v_{j-1}) \qquad j = 1(1)N \qquad (5.7.20a)$$

$$AA_j = -2 + \frac{1}{2}A_j + 2\lambda_3 h^2 (v_j - q_{1j}) + 2\lambda_4 h^2 v_j \qquad j = 1(1)N \qquad (5.7.20b)$$

$$D_j = \frac{h^2}{4} (\lambda_1 V_j + \lambda_2 D_j) \qquad j = 1(1)N. \qquad (5.7.20c)$$

Using the boundary condition (5.7.7a), the finite-difference equation at $j = 0$ reduces to

$$F_0 = 2(v_1 - v_0) + \lambda_3 v_0 h^2 (v_0 - 2q_{10}) + \lambda_4 h^2 v_0^2 = 0 \qquad (5.7.21)$$

and hence

$$AA_0 = -2 + 2\lambda_3 h^2 (v_0 - q_{10}) + 2\lambda_4 h^2 v_0 \qquad (5.7.22a)$$

$$D_0 = 1 \ . \qquad (5.7.22b)$$

The linear system of equations $A\,\underline{l} = \underline{c}$ are solved using the LU decomposition method proposed by Doolittle, see Burden and Faires (1989). This involves writing $A = L\,U$, where L is a lower triangular matrix whose diagonal elements are unity, i.e. $L_{ii} = 1$, and U is an upper triangular matrix. We first solve the equations $L\,\underline{w} = \underline{c}$ for $\underline{w}$ by forward substitution and then solve the equations $U\,\underline{l} = \underline{w}$ for $\underline{l}$ by backward substitution. The quantity $l_j + v_j^{(0)}$ is then used as the next guess and the procedure repeated until $(v_i - v_i^{(0)})$ is less than the specified tolerance, ε_1.

The initial solution at $X^* = 0$ was used to calculate the solution of equation (5.7.5) subject to the boundary conditions (5.7.7) at $X^* = \delta X^*$, until convergence to within the tolerance ε_1 had been achieved. The Newton procedure was repeated, solving equation (5.7.5) subject to conditions (5.7.7) at $X^* = \delta X^*/2$ using the results obtained at $X^* = 0$ and then using the results obtained at $X^* = \delta X^*/2$, equation (5.7.5) was then solved for each v_j, $j = 0(1)N$, at $X^* = \delta X^*$. Providing that the results obtained at $X^* = \delta X^*$ using the one step of length δX^* and the two steps of $\delta X^*/2$ differ by less than the tolerance ε_2 then the technique proceeds in the same manner to calculate v_j, $j = 0(1)N$, at $X^* = 2\delta X^*$. Once the v_j's have been determined in this manner the new q_j's are determined from $q_j = v_j - q_j$. The marching procedure was continued until the profile obtained approached the asymptotic similarity solution, i.e. until $f \longrightarrow \hat{f}$.

The initial profiles for q, i.e. equations (5.7.10) and (5.7.13), could have been determined numerically following the same method. However, in this case the first column of the matrix A will be slightly different due to the fact that the derivative boundary condition (5.7.7a) is no longer enforced and an analytic expression for q at $\eta = 0$ is enforced instead. This has to be done in order to avoid obtaining the trivial solution. Although an analytic expression for q is still required at $X^* = 0$, $\eta = 0$, calculating the initial profile in this manner does provide a useful means of checking the numerical procedure.

5.8 RESULTS AND DISCUSSION

Errors arising from the mesh size in the X^* direction were kept small by covering the step from X^* to $X^*+\delta X^*$ in first one and then two steps and insisting that the difference between the solutions, ε_2, be less than 5×10^{-5}. In the first few steps the solution was found to change very rapidly and it was necessary to take $\delta X^* = 10^{-7}$ for the first ten steps, then $\delta X^* = 10^{-6}$ for a further ten steps, etc.. Once the solution in the initial region of rapid changes had been determined the specified tolerance, ε_2, between the two solutions could be achieved with $\delta X^* = 0.05$. The value of the tolerance, ε_1 , in the Newton procedure, was taken to be 10^{-6}. This value of the tolerance was found to provide sufficient accuracy as choosing a smaller value for ε_1 had no significant effect on the solution obtained and results were graphically indistinguishable.

At each location X^* of the marching, after convergence had been achieved, the kinematic momentum flux, K, and the stream function, Ψ_∞, at the edge of the shear-layer were calculated from the expressions:

(i) for laminar flow

$$K = \frac{(1+X^{*2})^{2/3}}{(1+X^*)^{4/3}} \int_0^{(N+1)h} q_j^2 \, d\eta \qquad (5.8.1)$$

$$\Psi_\infty = X^{*1/3}(1 + X^{*2})^{1/3} \int_0^{(N+1)h} q_j \, d\eta \qquad (5.8.2)$$

(ii) for turbulent flow

$$K = \int_0^{(N+1)h} q_j^2 \, d\eta \qquad (5.8.3)$$

$$\Psi_{\infty} = X^{*1/2}(1 + X^{*})^{1/2} \int_{0}^{(N+1)h} q_j \, d\eta \qquad (5.8.4)$$

where the integration was performed numerically. The kinematic momentum flux, K, of the radial jet was evaluated at each location X^* to ensure that it was conserved as the jet developed; and hence provided a useful check of the accuracy of the numerical procedure.

From the injection operating conditions at which Fetcher and Saunders (1991,1993) ran an Aaberg exhaust hood we obtain the following approximate values of the physical quantities: $u(0) = 7.7\ ms^{-1}$, $b(0) = 7.5 \times 10^{-3}$ m and $a \simeq 0.15$ m. These operating conditions result in a Reynolds number, R_e, of approximately 3397 which implies that the flow in the radial free jet is almost certainly turbulent. The kinematic momentum flux, k, of the radial jet is given by

$$k = 2\pi\, a\, b(0)\, u(0)^2 \qquad (5.8.5)$$

and hence from Fletcher and Saunders (1991,1993) we obtain the approximate value of $k = 0.419\ m^4 s^{-2}$. Non-dimensionalising we obtain K to be $O(10^8)$ for the laminar radial jet and $K = O(10)$ for the turbulent radial jet.

As discussed in chapter 2, the flow induced by a radial jet is governed by the form of the stream function, Ψ_{∞}, at the edge of the shear-layer. Therefore it is reasonable to choose Ψ_{∞} as the quantity from which comparisons can be made between the solutions deduced from the current mathematical model and the available experimental and theoretical results of other authors. Comparisons are now made between Ψ_{∞} deduced from the model presented in this chapter with those deduced from the available empirical and semi-empirical

formulae.

5.8.1 The Laminar Radial Jet

Due to the very large magnitude of the dimensionless kinematic momentum flux of the laminar radial jet, i.e. K is $O(10^8)$, it was necessary to choose h = 0.00390625 and N = 300, i.e. Nh = 1.171875, in order for the value of K to be conserved to within 1% of its initial value. Increasing the position where the outer, infinity boundary was applied to Nh = 2.34375 had no significant effect on the overall solution obtained. The stream function, Ψ_∞, solution deduced from the laminar radial jet model is shown in Fig.5.2 as a function of X* for K = 10^8.

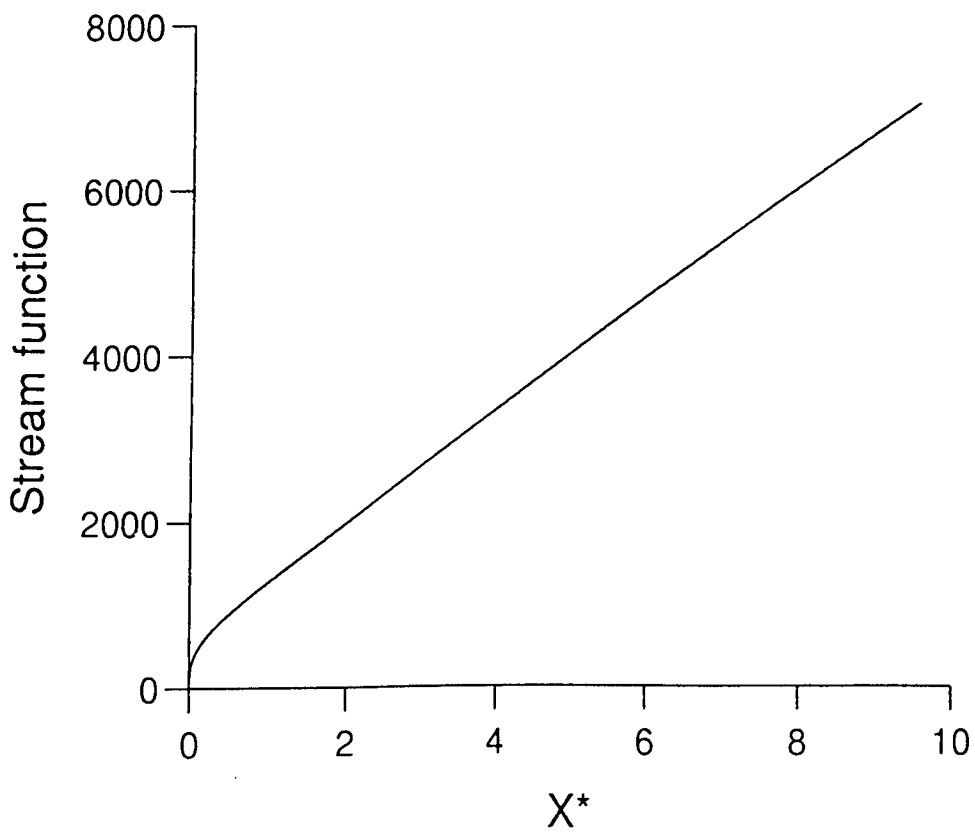

Fig.5.2 The stream function at the edge of the laminar radial jet as a function of X* for K = 10^8.

It has been observed that for a two-dimensional plane and a circular jet the transition to turbulence occurs at relatively low values of the Reynolds number, R_e, and there are no reasons to suggest why this should not also apply to a radial jet flow. Information regarding an experimental study of the laminar radial jet has not been found in the literature, this may be due to the fact that in most practical applications in which the radial jet is employed the value of the Reynolds number is relatively large and the flow is turbulent.

5.8.2 The Turbulent Radial Jet

With h = 0.00625 and N = 160, i.e. Nh = 1, the value of K was found to be conserved to within 1% of its initial value. Increasing the position where the outer, infinity boundary was applied to Nh = 2 had no significant effect on the overall solution obtained.

From equations (2.2.2), which describe the velocity distribution in a turbulent radial jet as derived by Tuve (1953), Squire (1955) and Heskestad (1966), Poreh and Cermak (1959) and Witze and Dwyer (1976), and Patel (1979), we can derive a general expression for the stream function at the edge of the turbulent radial jet. The general expression is arrived at after initially determining the centre-line velocity, $\tilde{u}$, from the momentum conservation equation (5.3.4), and then by integrating the resulting streamwise component of the velocity across the shear-layer. Non-dimensionalising we obtain the general expression for Ψ_∞, namely

$$\Psi_\infty = \gamma_e \, K^{1/2} \, X^{*1/2}(1 + X^*)^{1/2} \qquad (5.8.6)$$

where the values of the constant γ_e are given in Table 5.2.

Author	Value of γ_e
Tuve (1953)	0.494
Heskestad (1966)	0.437
Witze and Dwyer (1976)	0.425
Patel (1979)	0.416

Table 5.2 The coefficients, γ_e, of equation (5.8.6).

The Tuve (1953) and Patel (1979) expressions for the u component of the velocity in a turbulent radial jet, i.e. equations (2.2.2a) and (2.2.2d), are empirical formulae while the remaining expressions of Squire (1955) and Poreh and Cermak (1959), i.e. equations (2.2.2b) and (2.2.2c), are semi-empirical formulae. The expression (2.2.2b) was determined theoretically by Squire (1955) and the spreading rate of 7.86 was determined experimentally by Heskestad (1966). Similarly, expression (2.2.2c) was determined theoretically by Poreh and Cermak (1959) and the Witze and Dwyer (1976) experimentally determined expression for $b_{1/2}$, namely $b_{1/2} = 0.106\ x^*$, was used in order to derive expression (5.8.6). Tuve (1953) does not provide any information regarding the half width, $b_{1/2}$, of the jet and hence in order to determine the expression (5.8.6) for Tuve the half width was assumed to take the form $b_{1/2} = 0.107\ x^*$. The value of the constant chosen, i.e. 0.107, is an average of the experimentally determined values, see Table 5.1, where $b_{1/2}$ has been determined from the relationship: $b_{1/2} = 0.881\ b$.

The value of the stream function at the edge of the turbulent radial jet, as determined from the theory presented in this chapter,

is now illustrated in Fig.5.3 as a function of X* for each of the two expressions (5.6.22) which describe $\varepsilon/\varepsilon_o$. Also illustrated in Fig.5.3 are the expressions (5.8.6) for each of the authors given in Table 5.2.

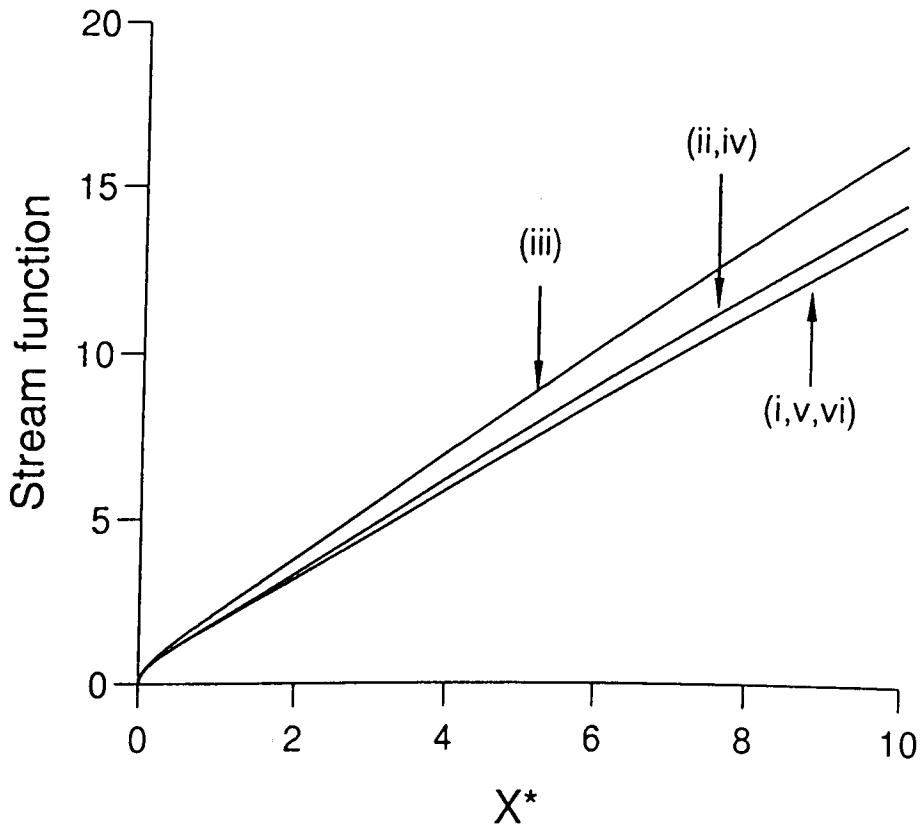

Fig.5.3 The stream function at the edge of the turbulent radial jet as a function of X* for K = 10, (i) $\varepsilon/\varepsilon_o$ as given by equation (5.6.22a), (ii) $\varepsilon/\varepsilon_o$ as given by equation (5.6.22b), (iii) Tuve (1953), (iv) Squire (1955) and Heskestad (1966), (v) Patel (1979), (vi) Poreh and Cermak (1959) and Witze and Dwyer (1976).

Curves (vi), (v) and (i) of Fig.5.3 illustrate that the stream functions at the edge of the turbulent radial jet as determined from Poreh and Cermak (1959), Patel (1979) and the current model, with $\varepsilon/\varepsilon_o$ as given by equation (5.6.22a), compare extremely well and are

graphically indistinguishable. Similarly, curves (ii) and (iv) which represent the current model, with $\varepsilon/\varepsilon_o$ as given by equation (5.6.22b), and the results of Squire (1955), respectively, are in very good agreement and the differences between the two solutions cannot be distinguished graphically. It should be noted that the Tuve expression for Ψ_∞, which is shown as curve (iii) of Fig.5.3, significantly overestimates the results obtained from the current model as well as those deduced from the velocity distribution of the authors considered. Tuve (1953) is believed to be one of the earliest documented pieces of experimental research on the turbulent radial jet and thus the observed differences between the measurement of Tuve and those of more recent experimentalists, e.g. Patel (1979), may be attributed to the development of more accurate flow analysing equipment.

Solutions arising when alternative expressions for the combined similarity regime (5.6.12), e.g. those arising when equation (5.6.12) is of the form $\Psi = X^{*1/2}(1 + X^{*n})^{1/2n} f(X^*,\eta)$, n = 2, 3 and 4, were found to be virtually graphically indistinguishable. However, curves (i) and (ii) of Fig.5.3 illustrate that the choice of the expression for $\varepsilon/\varepsilon_o$ has a more significant effect on the overall solution obtained. Equation (5.6.22a) is the most natural choice, based on Taylor series expansions, for the expression which models the transition of $\varepsilon/\varepsilon_o$ as a function of X^*, and the resulting solution for Ψ_∞, shown as curve (ii) of Fig.5.3, is in very close agreement with the theoretical results of Poreh and Cermak (1959) as well as the empirical results of Patel (1979). It is this expression that we shall adopt when modelling the radial jet produced by the Aaberg exhaust hood.

5.9 CONCLUSIONS

A numerical model for the fluid flow in a radial free jet has been developed for both laminar and turbulent flows. The model gives us a first approximation of the flow in a radial free jet and allows us to predict velocity profiles and stream function. The stream function, Ψ_∞, at the edge of the shear-layer provides us with a first-order estimate of the amount of fluid drawn into the radial free jet and thus the boundary condition for the outer, inviscid, jet-induced flow, which will be discussed in more detail later. The value of the stream function, Ψ_∞, at the edge of the shear-layer determined from the current turbulent model is in very close agreement with both available theoretical and experimental results. The full air flow pattern created by the three-dimensional axisymmetric Aaberg exhaust hood will now be presented in chapter 6.

CHAPTER SIX

A THREE-DIMENSIONAL AXISYMMETRIC MODEL OF THE FLUID FLOW PATTERN CREATED BY AN AABERG EXHAUST HOOD

6.1 INTRODUCTION

Now that the fluid flow behaviour in the radial free jet has been examined we proceed to consider the full air flow pattern generated by the three-dimensional axisymmetric Aaberg exhaust hood. The purpose of this chapter is to develop a mathematical model of the air flow pattern induced by such an exhaust hood, to identify the parameters which govern this flow and to predict how the air flow pattern and hence how the hood's performance is influenced by the governing parameters. The mathematical model is formulated in terms of the Stokes stream function, Ψ, and the governing equations of fluid motion are solved using finite-difference techniques. The injection flow of the exhaust hood is modelled as a turbulent radial jet and the entrained flow is assumed to be an inviscid potential flow. Sections through surfaces of constant air speed deduced from the model are used to examine what effect the turbulent radial jet flow has on the size and shape of the region in front of the hood from which we expect a neutrally-buoyant contaminant to be captured. Comparisons made between contours of constant air speed and centre-line air speeds deduced from the model and the available experimental data of Fletcher and Saunders (1993) and Pedersen and Nielsen (1991) show good quantitative agreement over a wide range of momentum ratios.

A three-dimensional axisymmetric investigation, analogous in its formulation to the two-dimensional model of Hunt and Ingham (1992), see chapter 3, is now presented.

6.2 THE MATHEMATICAL MODEL

Under ideal conditions, i.e without the effects of cross-flows or temperature gradients etc., the air flow pattern generated by the combination of the suction and injection flows of the original Aaberg exhaust hood is a three-dimensional axisymmetric flow. Hence, adopting the spherical polar coordinate system (r,θ,ϕ) we can assume that the solution is independent of the angular coordinate θ, see Fig.6.1. Using the symmetry of the flow the governing equations of fluid motion have only to be solved in the (r,ϕ) plane for $\theta = 0$, $r \geq 0$ and $0 \leq \phi \leq \pi/2$. The equations of motion and the boundary conditions used to model the axisymmetric flow of an Aaberg exhaust hood are now presented.

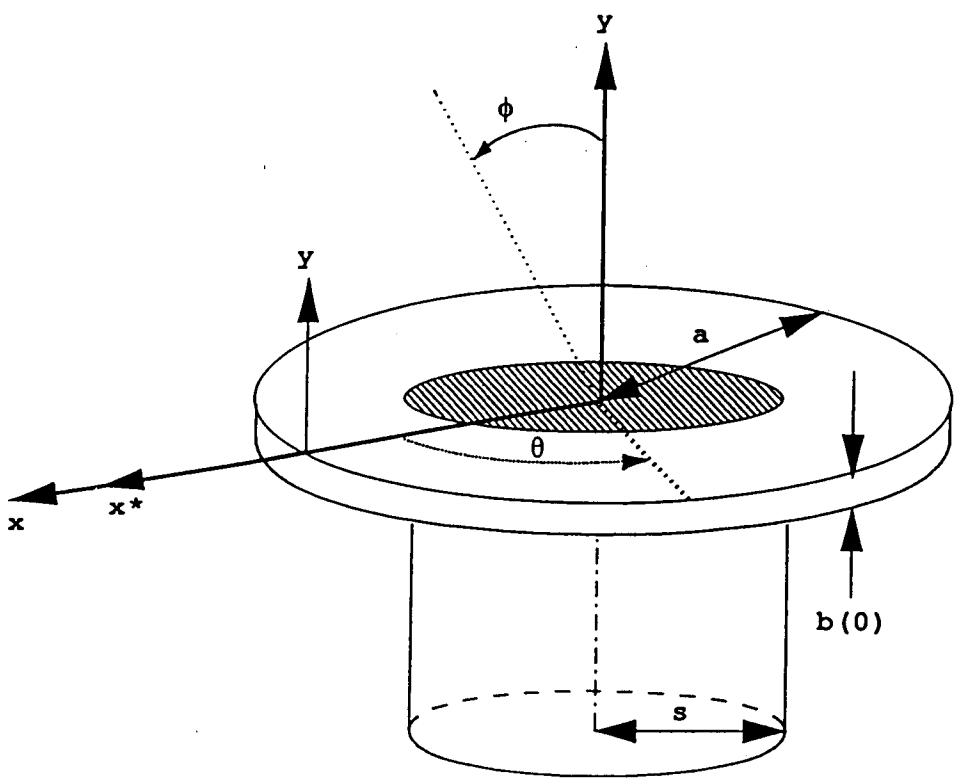

Fig.6.1 The geometry and coordinate system for the axisymmetric Aaberg exhaust hood.

6.2.1 The Axisymmetric Radial Jet Flow

A detailed analysis of the radial free jet, for both laminar and turbulent flows, has been presented in chapter 5. In chapter 5 it was established that the flow in a radial free jet is governed by its kinematic momentum flux, K, which may be thought of as a measure of the strength of the radial jet. The model of the turbulent radial jet developed in chapter 5, for which $\varepsilon/\varepsilon_o$ is given by equation (5.6.22a), is in very close agreement with both the experimental results of Patel (1979) and the theoretical results of Poreh and Cermak (1959). In practice the radial jet flow of the Aaberg hood is almost certainly turbulent and therefore it is this solution that we shall use in this chapter to model the injection flow of the axisymmetric Aaberg exhaust hood.

6.2.2 The Jet-induced Flow

The jet-induced flow is modelled by assuming that the flow induced by a slender, i.e. high Reynolds number, axisymmetric radial jet is an inviscid potential flow, i.e. it satisfies the conditions of incompressibility and irrotationality. Under these assumptions the fluid motion is governed by equation (2.2.23). Introducing the non-dimensional quantities as in expressions (5.6.2) the dimensionless form of the equation of motion (2.2.23) becomes

$$\frac{\partial^2\Psi}{\partial R^2} - \frac{\cot(\phi)}{R^2}\frac{\partial\Psi}{\partial\phi} + \frac{1}{R^2}\frac{\partial^2\Psi}{\partial\phi^2} = 0 \qquad (6.2.1)$$

where R = r/a. The value of the stream function at the edge of the jet shear-layer has been numerically determined at each location X, for X > 1, from equation (5.8.4). We are assuming that the jet is

slender and hence we shall enforce these values of the stream function along the X axis for X > 1, i.e.

$$\Psi(R,\pi/2) = \Psi_{\infty} \qquad R > 1. \qquad (6.2.2)$$

Thus, the boundary condition (6.2.2) governs the amount of fluid drawn into the turbulent radial jet and hence the jet-induced flow.

6.2.3 The Exhaust Flow

Modelling the suction inlet of the exhaust hood as a finite-sized circular opening of radius, s, into which a volume flux, m, of fluid per unit time passes and assuming that the fluid velocity across the face of the inlet is uniformly distributed we obtain the boundary condition

$$\psi(r,\pi/2) = \frac{mr^2}{2\pi s^2} \qquad 0 \le r \le s. \qquad (6.2.3)$$

Non-dimensionalising, see expressions (5.6.1) and (5.6.2), we obtain the inlet boundary condition

$$\Psi(R,\pi/2) = \frac{1}{2} R_{in} R^2 \qquad 0 \le R \le S \qquad (6.2.4)$$

where S = s/a is the dimensionless radius of the exhaust inlet and the Reynolds number, R_{in}, of the exhaust flow is defined to be

$$R_{in} = \frac{u_{in} a}{\beta_o} \qquad (6.2.5)$$

and where u_{in} is the fluid speed at the face of the exhaust inlet. Along the flange of the exhaust we therefore have the boundary condition

$$\Psi(R,\pi/2) = \frac{1}{2} R_{in} S^2 \qquad S < R \le 1. \qquad (6.2.6)$$

The axis of symmetry of the hood, i.e. the axis along which $\phi = 0$, represents a streamline of the flow and hence for convenience, when

determining boundary condition (6.2.4), we have chosen

$$\Psi(R,0) = 0 \qquad 0 \le R \le R_{\infty}. \quad (6.2.7)$$

6.2.4 The Upstream Boundary Condition

The boundary condition modelling the fluid flow at large distances from the Aaberg exhaust hood is enforced on $R = R_{\infty}$ for $0 \le \phi \le \pi/2$, where $R_{\infty} \gg 1$. This upstream boundary condition is taken to be the asymptotic solution of equation (6.2.1) subject to the appropriate boundary conditions which result from the shear-layer solutions on $\phi = \pi/2$ and to boundary condition (6.2.7) on $\phi = 0$, plus the radial flow contribution which results from the exhaust flow.

Initially, consider the component of the upstream boundary condition which results from the radial free jet flow. From equation (5.5.30), we have

$$\Psi(R,\pi/2) = G_{Axi}(R-1) \qquad \text{for } R \gg 1 \qquad (6.2.8)$$

where the dimensionless parameter G_{Axi} is defined to be

$$G_{Axi} = (3K/2\sigma_{\infty})^{1/2}. \qquad (6.2.9)$$

Thus, to a first-order approximation we have

$$\Psi = G_{Axi}R \qquad (6.2.10)$$

for $R \gg 1$ on $\phi = \pi/2$ and following the method of separation of variables we therefore seek a solution of equation (6.2.1) in the form

$$\Psi = R\,\Phi_1(\phi) \qquad (6.2.11)$$

where $\Phi_1(\phi)$ is a function of ϕ only. Substitution of expression (6.2.11) into equation (6.2.1) leads to the second-order ordinary differential equation

$$\Phi_1'' - \cot(\phi)\Phi_1' = 0 \qquad (6.2.12)$$

and the first-order solution, satisfying boundary conditions (6.2.10) and (6.2.7), is then

$$\Psi = G_{Axi} R(1 - \cos(\phi)) \ . \qquad (6.2.13)$$

To a second-order approximation

$$\Psi = G_{Axi} R - G_{Axi} \qquad (6.2.14)$$

for $R \gg 1$ on $\phi = \pi/2$, and hence we now seek a solution of equation (6.2.1) in the form

$$\Psi = G_{Axi} R(1 - \cos(\phi)) + \Phi_2(\phi) \qquad (6.2.15)$$

where $\Phi_2(\phi)$ is a function of ϕ only. Substitution of expression (6.2.15) into equation (6.2.1) then leads to the component of the upstream boundary condition which may be attributed to the influence of the radial jet flow, namely

$$\Psi = G_{Axi}(1 - \cos(\phi))(R - 1) \ . \qquad (6.2.16)$$

For sufficiently large distances upstream of the Aaberg exhaust hood the flow which results from the flux, m, of fluid into the suction opening may be modelled as a purely radial flow, and hence, for $r \gg 1$, the radial component of the velocity assumes the form

$$u_r = \frac{m}{2\pi r^2} \ . \qquad (6.2.17)$$

Using equation (2.2.21a), which relates the radial component of the velocity to the stream function, and insisting that $\psi = 0$ on $\phi = 0$, gives

$$\psi = \frac{m}{2\pi} (1 - \cos(\phi)) \qquad (6.2.18)$$

and non-dimensionalising equation (6.2.18) we obtain the condition which models the upstream influence of the exhaust flow, namely

$$\Psi = \frac{1}{2} R_{in} S^2(1 - \cos(\phi)) \ . \qquad (6.2.19)$$

The boundary condition to be enforced on $R = R_\infty$, for $0 \leq \phi \leq \pi/2$, which models the upstream flow generated by the axisymmetric Aaberg

exhaust hood then takes the form

$$\Psi(R,\phi) = G_{Axi}(1 - \cos(\phi))(R - 1) + \frac{1}{2} R_{in} S^2 (1 - \cos(\phi)) \quad . \qquad (6.2.20)$$

The effect of the exhaust's suction is to modify boundary condition (6.2.2) which now becomes

$$\Psi(R,\pi/2) = \Psi_{\infty} + \frac{1}{2} R_{in} S^2 \qquad R > 1 \quad . \qquad (6.2.21)$$

For clarity the geometry of the solution domain and the position of the boundary conditions used to model the axisymmetric flow of the Aaberg exhaust hood are shown schematically in Fig.6.2.

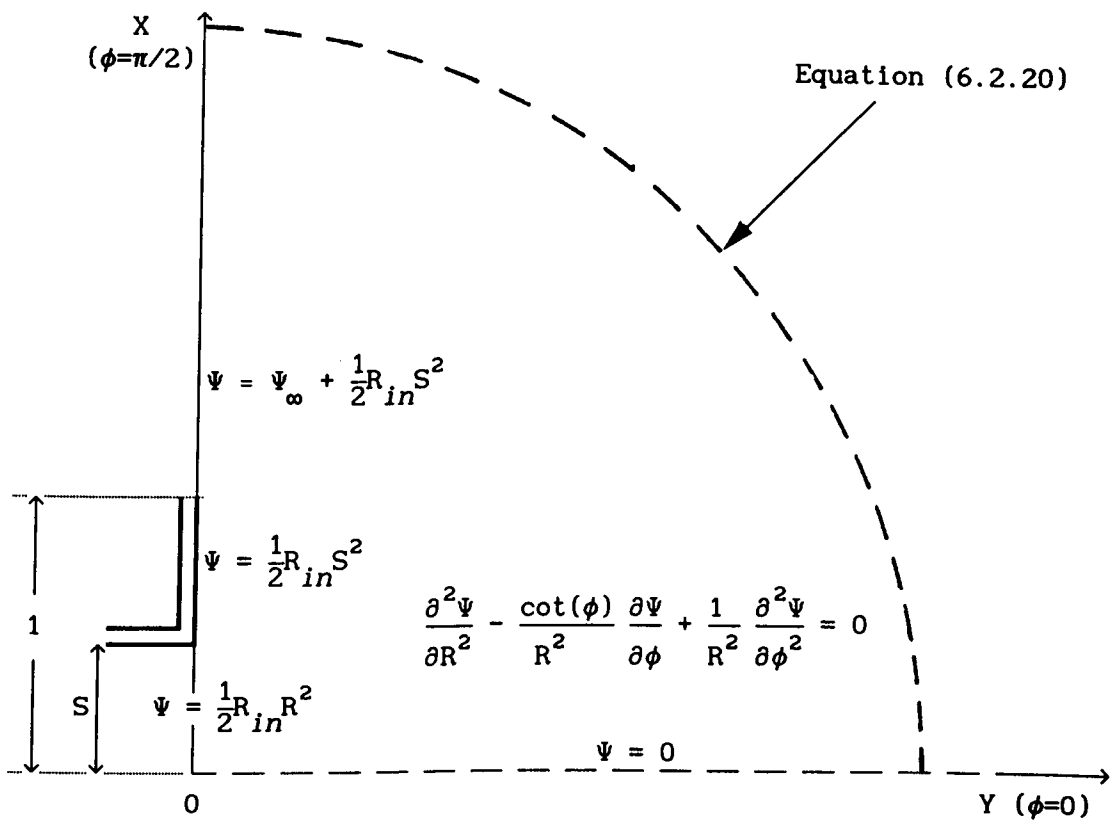

Fig.6.2 The solution domain and the boundary conditions used to model the axisymmetric Aaberg exhaust hood.

6.3 THE FINITE-DIFFERENCE SCHEME

A mesh was placed over the entire solution domain and all derivatives of the governing equations of fluid motion approximated by their usual central-difference approximations. The mesh generated was identical to the one described in chapter 4 and consisted of a fine mesh of constant step length for $0 \leq R \leq 1$ and a mesh of expanding step length for $R > 1$; this was achieved by a transformation of the radial coordinate such that $\xi = \ln R$. The governing equation of fluid motion for $0 \leq R \leq 1$, i.e. equation (6.2.1), was then approximated at the point (i,j) by the finite-difference equation

$$\Psi_{i,j} = \frac{1}{C4}\left(C3\ (\Psi_{i-1,j} + \Psi_{i+1,j}) + C1\ \Psi_{i,j-1} + C2\ \Psi_{i,j+1}\right) \qquad (6.3.1)$$

where the coefficients C1, C2, C3 and C4 are given by

$$C1 = \left(\frac{1}{R^2\delta\phi^2} + \frac{\cot(\phi)}{2R^2\delta\phi}\right) \qquad C2 = \left(\frac{1}{R^2\delta\phi^2} - \frac{\cot(\phi)}{2R^2\delta\phi}\right) \qquad (6.3.2a,b)$$

$$C3 = \frac{1}{\delta R^2} \qquad C4 = 2\left(\frac{1}{\delta R^2} + \frac{1}{R^2\delta\phi^2}\right). \qquad (6.3.2c,d)$$

For $R > 1$ equation (6.2.1) reduces to the equation

$$\frac{\partial^2\Psi}{\partial\xi^2} - \frac{\partial\Psi}{\partial\xi} - \cot(\phi)\,\frac{\partial\Psi}{\partial\phi} + \frac{\partial^2\Psi}{\partial\phi^2} = 0 \qquad (6.3.3)$$

which was approximated at the point (i,j) by the finite-difference equation

$$\Psi_{i,j} = \frac{1}{f5}\left(f1\ \Psi_{i-1,j} + f2\ \Psi_{i+1,j} + f4\ \Psi_{i,j-1} + f3\ \Psi_{i,j+1}\right) \qquad (6.3.4)$$

where

$$f1 = \left(\frac{1}{\delta\xi^2} + \frac{1}{2\delta\xi}\right) \qquad f2 = \left(\frac{1}{\delta\xi^2} - \frac{1}{2\delta\xi}\right) \qquad (6.3.5a,b)$$

$$f3 = \left(\frac{1}{\delta\theta^2} - \frac{\cot(\phi)}{2\delta\phi} \right) \qquad f4 = \left(\frac{1}{\delta\theta^2} + \frac{\cot(\phi)}{2\delta\phi} \right) \qquad (6.3.5c,d)$$

$$f5 = 2 \left(\frac{1}{\delta\xi^2} + \frac{1}{\delta\theta^2} \right) . \qquad (6.3.5e)$$

In order to ensure that the meshes match at R = 1 the step length $\delta\xi$ was chosen such that $\delta\xi = \ln(1+\delta R)$. The centre-line velocity is given by

$$u_r = \lim_{\phi \to 0} \left(- \frac{1}{r^2 \sin(\phi)} \frac{\partial\psi}{\partial\phi} \right) = - \frac{1}{r^2} \frac{\partial^2\psi}{\partial\phi^2} \qquad (6.3.6)$$

on $\phi = 0$.

6.4 THE OPERATING PARAMETERS

The mathematical model developed predicts that the air flow induced by the axisymmetric Aaberg exhaust hood is governed by three dimensionless parameters, namely S, K and R_{in}. It is interesting to note that these three parameters are encompassed in the single parameter considered by the experimentalists, namely, the ratio of the momentum flows, I, which may be expressed as

$$I = \frac{4\,K}{S^2 R_{in}^2} . \qquad (6.4.1)$$

The three operating parameters S, K and R_{in} are now examined.

Using equation (5.8.5), the non-dimensional expression for K, see equation (5.6.2), reduces to

$$K = \frac{a}{2b(0)} \qquad (6.4.2)$$

and hence the turbulent radial jet flow of the Aaberg exhaust hood is governed by the ratio of the radius of the exhaust flange to the jet nozzle width. The parameter K is thus a geometric ratio and is

directly proportional to the constraint ratio, C_R, defined by Witze and Dwyer (1976), namely,

$$K = \frac{1}{4} C_R \ . \qquad (6.4.3)$$

Witze and Dwyer (1976) characterize the general structure and behaviour of a wide range of radial jets according to the ratio C_R. Through their experiments they concluded that for constraint ratios greater than approximately 40 the nozzle walls constrain the flow leaving the jet orifice to be parallel, the spreading rate is approximately constant, and they classify the resulting flow as a *constrained* radial jet. A small constraint ratio is representative of two opposing free axisymmetric jets, the collision of which produces an *impinged* radial jet for which the spreading rate is almost three times that of the constrained jet. The findings of Witze and Dwyer would therefore imply that the present model is valid only for geometries in which K is greater than approximately 10.

The second parameter, S, is the ratio of the radius of the exhaust inlet to the radius of the exhaust flange and hence the geometry of the particular hood under consideration is characterized by the parameters K and S.

The third parameter R_{in} is a Reynolds number which reduces to

$$R_{in} = 2K \left(\frac{u_{in}}{u(0)} \right) \qquad (6.4.4)$$

when the flow in the radial jet is turbulent. For a hood of fixed dimensions the parameter R_{in} is therefore directly proportional to the ratio between the exhaust inlet speed and the jet exit speed and inversely proportional to the square root of the momentum ratio I.

6.5 RESULTS AND DISCUSSION

In this section comparisons are made between the air flow patterns predicted by the present model and the independent experimental observations of Fletcher and Saunders (1993) and Pedersen and Nielsen (1991). The characteristic dimensions a, b(0) and s of the Aaberg exhaust hoods used in these studies are shown in Table 6.1 together with the corresponding approximate model parameter values.

	Fletcher and Saunders (1993)	Pedersen and Nielsen (1991)
a	0.1515 m	0.1115 m
b(0)	0.0075 m	0.0025 m
s	0.0370 m	0.0515 m
K	10.1	22.3
S	0.244	0.445
R_{in}	$20.2(u_{in}/u(0))$	$44.6(u_{in}/u(0))$

Table 6.1 The characteristic dimensions of the axisymmetric Aaberg exhaust hoods of Fletcher and Saunders (1993) and Pedersen and Nielsen (1991) and the resulting model operating parameter values.

Figure 6.3(a) illustrates lines of constant air speed, in metres per second, in front of the exhaust hood as obtained by Fletcher and Saunders (1993) for a hood operating under suction alone and $u_{in} = 15.5\ ms^{-1}$. The air flow pattern deduced from the model for the corresponding operating conditions, namely K = 0, S = 0.244 and $R_{in} = 138132$, is shown in Fig.6.3(b). From the results shown in Fig.6.3 it is clear that the predictions of the model are

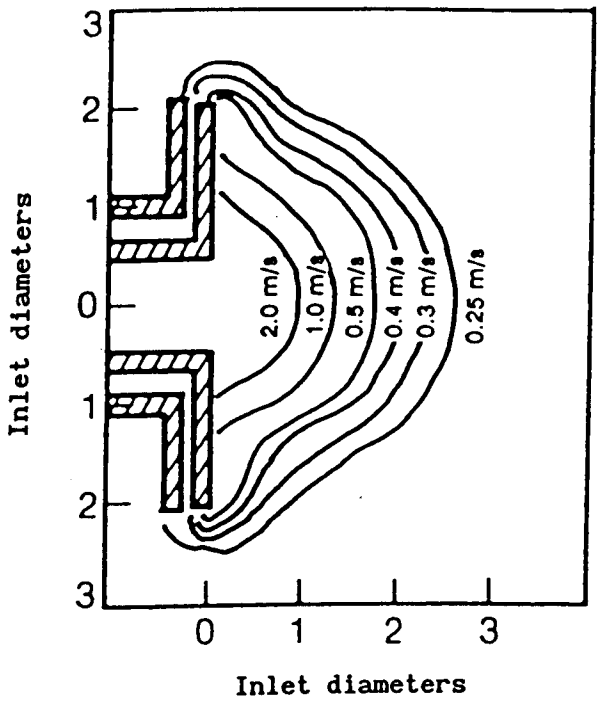

Fig.6.3(a) Lines of constant air speed in front of an axisymmetric flanged exhaust hood operating under suction alone; a = 0.1515 m, s = 0.037 m, u_{in} = 15.5 ms^{-1}, Fletcher and Saunders (1993).

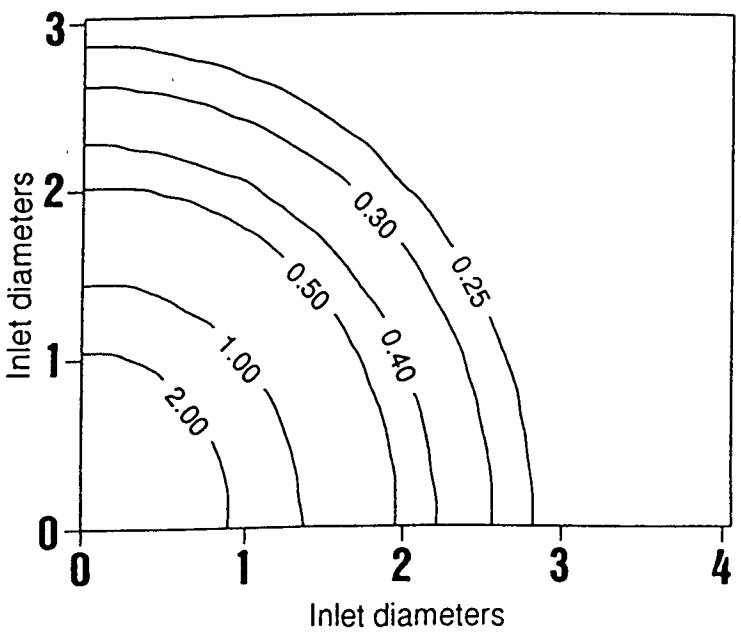

Fig.6.3(b) Lines of constant air speed deduced from the model for an axisymmetric flanged exhaust hood operating under suction alone, K = 0, S = 0.244, R_{in} = 138132.

in very close agreement with the experimental results of Fletcher and Saunders (1993) and illustrate that for a hood operating under suction alone the air speed in front of the exhaust inlet decays inversely proportional to the square of the distance from the inlet. In the typical working environments in which LEV systems are commonly used the level of background air disturbance, due for example to temperature gradients or the small movement of the occupants, etc., may be regarded as being of the order of 0.25 ms^{-1}. Thus, operating under suction alone and for the given inlet conditions, the effective capture region of the hood occupies a relatively small hemispherical region which has a radius of approximately 5s.

We now proceed to examine what effect the addition of a turbulent radial jet of fluid has on the air flow pattern created by the hood whilst maintaining the original conditions of exhaustion. Figure 6.4(a) illustrates lines of constant speed, determined experimentally by Fletcher and Saunders (1993), in front of a hood operating at a momentum ratio of $I \simeq 0.4$ and with u_{in} = 15.5 ms^{-1} and u(0) = 7.7 ms^{-1}. Lines of constant speed deduced from the model for the corresponding operating conditions, i.e. K = 10.1, S = 0.244 and R_{in} = 40.7 are shown in Fig.6.4(b). On comparing Fig.6.3 with Fig.6.4 the dramatic effect on the air speeds developed in front of the hood which is achieved by the combination of suction and injection is immediately apparent. As a result of the entrainment of air into the radial jet the air speed predicted in front of the hood has increased significantly and the line of constant speed which corresponds to the level of background air disturbance, i.e. q_c = 0.25 ms^{-1}, now intersects the longitudinal axis of the hood at a

distance of the order of 10s from the face of the exhaust inlet. Thus for the given conditions of exhaustion and injection the model predicts that the effective working range of the hood can be approximately doubled by increasing the momentum ratio from I = 0 to I = 0.4. From Fig.6.4 it is evident that the air speeds predicted by the model underestimate those observed by Fletcher and Saunders (1993) who predict that the line of constant speed $q_c = 0.25\ ms^{-1}$ intersects the longitudinal axis of the hood at a distance of the order of 18s from the inlet. However, for air speeds of greater than $0.4\ ms^{-1}$ the lines of constant speed predicted by the model are in favourable agreement with those observed by Fletcher and Saunders (1993). Furthermore, Fletcher and Saunders (1993) observed that, under the given operating conditions, the line of constant speed for which $q \simeq 0.5\ ms^{-1}$ bifurcates in a region where the flow divides with one part drawn towards the exhaust inlet and the other towards the blowing jet. The air speed at which the experimentally observed bifurcation occurs is in very close agreement with that predicted by the theory. Figure 6.4(a) shows that the lines of constant air speed observed by Fletcher and Saunders are not symmetrical about the centre-line of the hood which suggests that their measurements may have been subject to background air disturbances. The discrepancy between the experimental and theoretical results may also be attributed to the ratio between the flange radius and jet nozzle width which, for the hood considered by Fletcher and Saunders, is approximately 10. This suggests that the radial jet produced by the hood may not be constrained and not accurately modelled by the present theory.

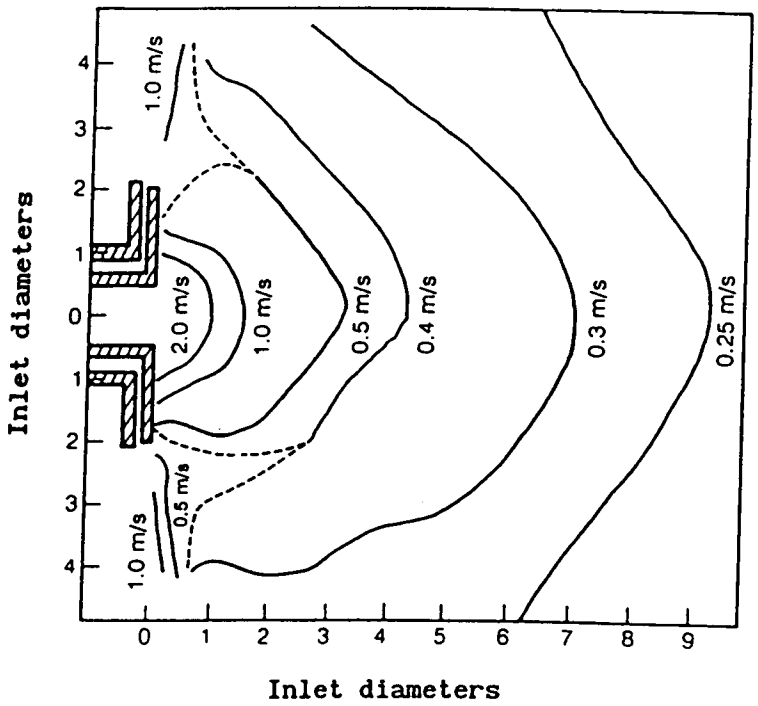

Fig.6.4(a) Lines of constant air speed in front of an axisymmetric flanged exhaust hood reinforced by a radial jet flow; a = 0.1515 m, s = 0.037 m, u_{in} = 15.5 ms^{-1}, b(0) = 0.0075 m, u(0) = 7.7 ms^{-1}, Fletcher and Saunders (1993).

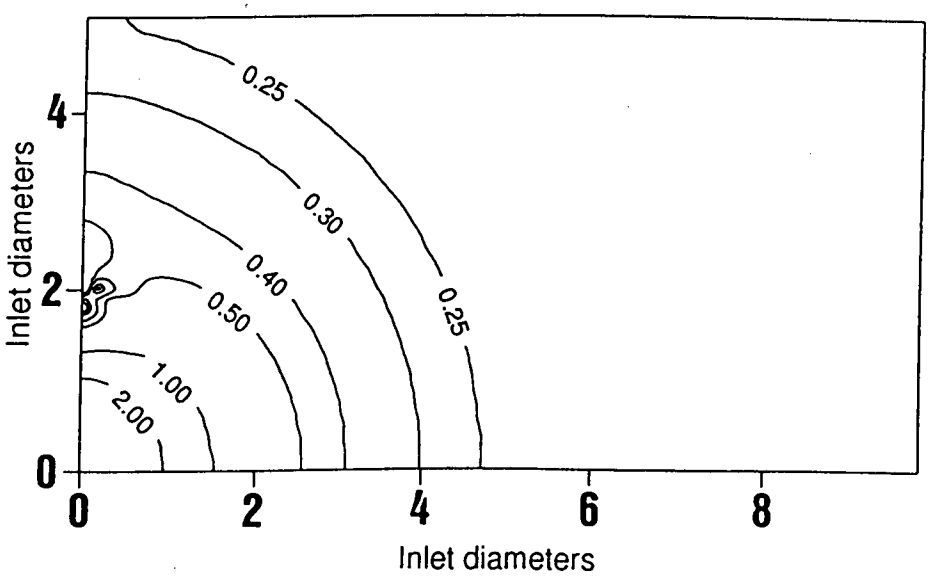

Fig:6.4(b) Lines of constant air speed deduced from the model for an axisymmetric flanged exhaust hood reinforced by a turbulent radial jet; K = 10.1, S = 0.244, R_{in} = 40.7.

Further comparisons between the model and the available experimental data are illustrated in Fig.6.5 which depicts the variation in the resultant air speed, u/u_{in}, along the centre-line of the hood as a function of the distance, y/a, along the centre-line. The experimental results shown are those recorded by Pedersen and Nielsen (1991) and made available by Pedersen (1993), for the hood described in the second column of Table 6.1 and operating with constant conditions of exhaustion given by u_{in} = 20 ms^{-1}. Four values of the momentum ratio are considered, namely I = 0.0, 0.5, 0.9 and 1.95, which were achieved during experiment with jet nozzle velocities of u(0) = 0.0 ms^{-1}, 30.8 ms^{-1}, 41.4 ms^{-1} and 60.9 ms^{-1}, respectively. These operating conditions result in R_{in} = 131176, 29.0, 21.6 and 14.7, respectively. Figure 6.5 shows that agreement between the air speeds predicted by the model and those observed experimentally by Pedersen and Nielsen (1991) are good for each momentum ratio considered.

The air speeds observed by Pedersen and Nielsen (1991) were more accurately reproduced by the model than were those observed by Fletcher and Saunders (1993). The constraint ratio for the Pedersen and Nielsen hood is approximately 90 and for their chosen operating conditions the Reynolds number of the jet, R_e, is greater than that based on Fletcher and Saunders experiments. Consequently, of the two experimental studies we would expect the agreement between the theory and the results of Pedersen and Nielsen to be the closer.

Fletcher and Saunders (1991,1993) and Pedersen and Nielsen (1991) do not provide any information regarding the streamlines of the axisymmetric flow and for this reason streamline comparisons between the results of experiment and the model cannot be made.

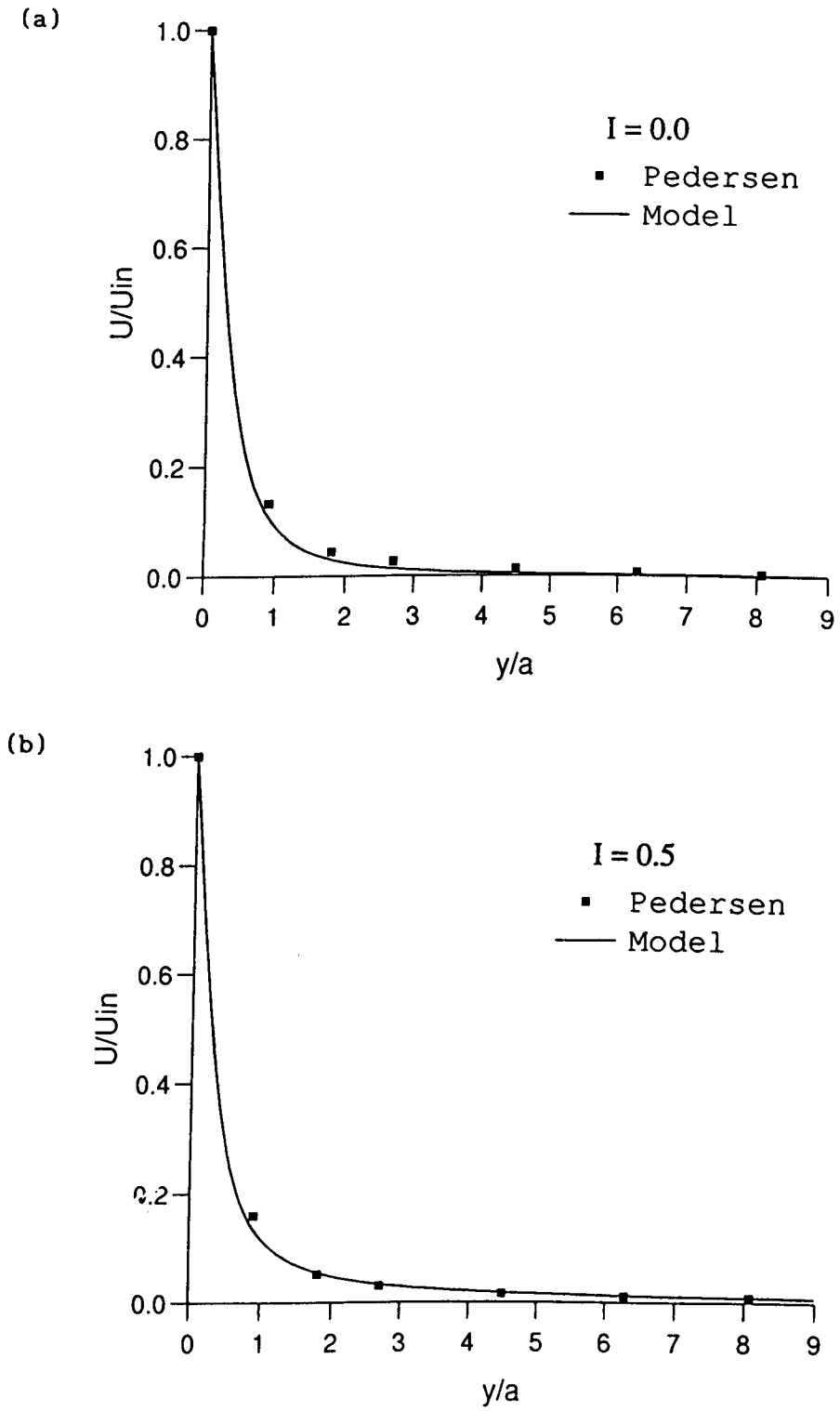

Fig.6.5 Variation in the centre-line air speed, u/u_{in}, as a function of the distance, y/a, along the hood's centre-line for (a) I = 0.0 and (b) I = 0.5. ■ Pedersen (1993), —— Model.

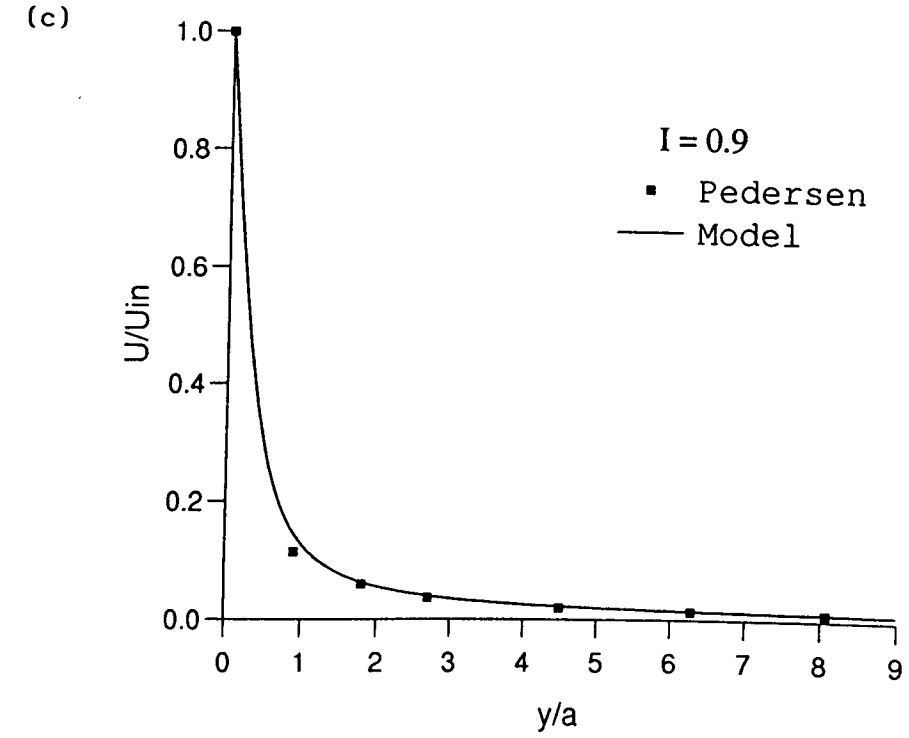

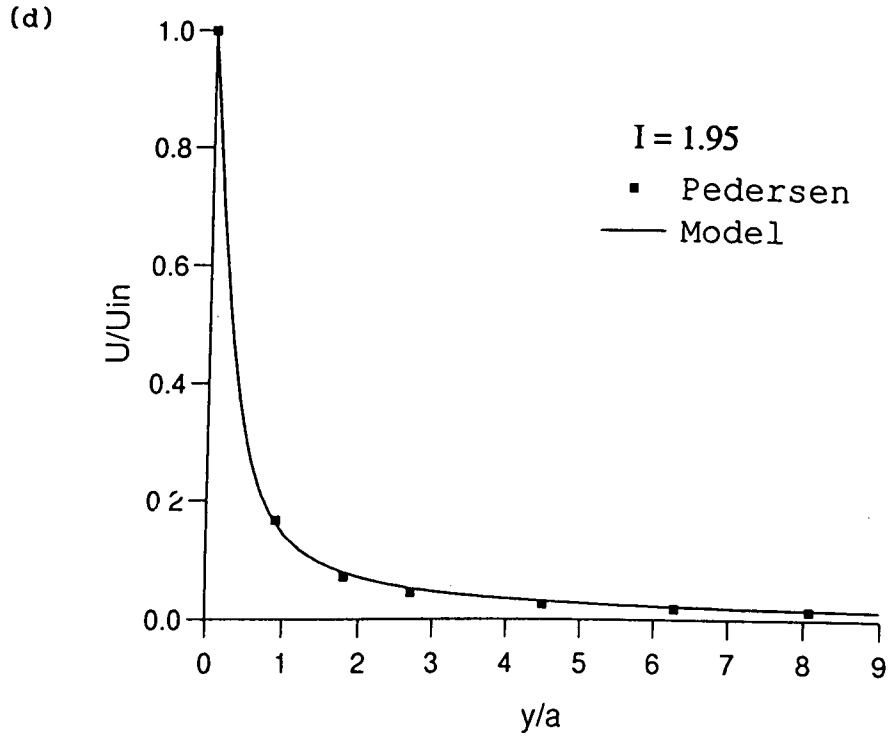

Fig.6.5 Variation in the centre-line air speed, u/u_{in}, as a function of the distance, y/a, along the hood's centre-line for (c) I = 0.9 and (d) I = 1.95. ■ Pedersen (1993), —— Model.

However, the results of the present axisymmetric model are in qualitative agreement with the two-dimensional models presented in chapters 3 and 4 and predict that the width of the efficient flow region decreases and the air speeds in this region increase as the momentum ratio I is increased.

6.6 CONCLUSIONS

A three-dimensional axisymmetric mathematical model for the fluid mechanics of an Aaberg exhaust hood has been developed and the three parameters which characterize the flow, namely K, S and R_{in}, have been identified. The model developed shows good agreement, both quantitatively and qualitatively, with the recent experimental observations of both Fletcher and Saunders (1993) and Pedersen and Nielsen (1991). The model developed is very versatile and can be easily adapted to consider a variety of other exhaust geometries or operating situations, e.g. the region of the workplace from which we expect air to be drawn into the exhaust inlet and successfully sampled may be determined as a function of the momentum ratio I or the parameter S.

CHAPTER SEVEN

APPLICATION OF THE AABERG PRINCIPLE TO THE SLOT EXHAUST HOOD

7.1 INTRODUCTION

Originally the Aaberg exhaust hood was three-dimensional and axisymmetric in design (circular exhaust opening) but a two-dimensional bench version with a slot exhaust opening, termed the Aaberg slot exhaust (ASE), has been experimentally studied by Pedersen (1991a). The principles of operation for the two- and three-dimensional Aaberg exhaust hoods are the same. The ASE studied by Pedersen (1991a), which is illustrated schematically in Fig.7.1, consists of a horizontal bench to which a vertical flange is attached. The flange houses a rectangular exhaust slot and jet nozzle. The distance between the bench surface and the centre of the exhaust slot, h_s, may be varied as may the width of the slot, 2s. The width of the jet nozzle, b(0), through which the jet of air issues vertically upwards along the exhaust flange may be varied, although the distance from the jet nozzle to the centre of the exhaust inlet, a, remains fixed. At the present time the ASE hood is still in an experimental form but the results of some preliminary tests carried out on the hood by Pedersen have been extremely encouraging.

The aim of this chapter is to develop a mathematical model of the air flow pattern created by a slot exhaust hood reinforced by a two-dimensional jet flow. In this chapter the two-dimensional jet flow of the ASE is modelled as (i) a turbulent wall jet and (ii) a turbulent free jet of fluid and the two parameters which characterize the subsequent induced potential flow are identified. Streamlines and lines of constant speed are deduced from the model and predictions are given for the area in front of the slot exhaust

hood from which a neutrally-buoyant contaminant can be successfully exhausted. Comparisons made between the available experimental data and the turbulent wall jet model show excellent quantitative agreement. The chapter concludes by suggesting a simple modification to the hood's design, deduced from the theory, which will enhance its effectiveness in the control of airborne contaminants.

7.2 THE MATHEMATICAL MODEL

During his experimental studies, Pedersen (1991a) observed that the flow field generated by the ASE was approximately two-dimensional except at the extremities of the bench where the flow was fully three-dimensional. Therefore, provided the bench is sufficiently wide, the flow pattern generated by the ASE may be assumed to be two-dimensional and hence we can assume that the solution is independent of z. The geometry and coordinate system of the two-dimensional mathematical model are shown in Fig.7.2, where for convenience polar coordinates (r,θ) have been adopted. The solution procedure for determining the air flow pattern follows that presented in section 4.2 of chapter 4. The equations of motion and boundary conditions are now examined.

For convenience all lengths in the model are non-dimensionalised with respect to p, where $p = a + h_s$, and the stream function with respect to the volume flux exhausted per unit length of the slot, m. We therefore introduce the dimensionless quantities:

$$R = \frac{r}{p} , \quad X = \frac{x}{p} , \quad Y = \frac{y}{p} , \quad S = \frac{s}{p} , \quad H_s = \frac{h_s}{p} ,$$

$$\Psi = \frac{\psi}{m} , \quad U_\theta = u_\theta/(m/p) , \quad U_r = u_r/(m/p) . \qquad (7.2.1)$$

Initially, as the fluid leaves the rectangular jet nozzle the jet flow of the ASE is most appropriately modelled as a two-dimensional turbulent wall jet. However, as the fluid reaches the end of the exhaust flange the wall jet undergoes a transitional stage and develops into a two-dimensional turbulent free jet. By modelling the injection flow both as a two-dimensional turbulent wall and a free jet which issue from the end of the exhaust flange, i.e. from X = 1, then comparisons of the resulting induced flows can be made and the robustness of the model examined. The solutions for the two types of jet are now outlined.

7.2.1 The Two-dimensional Turbulent Wall Jet

The turbulent wall jet is a flow commonly encountered in engineering where it has been applied to many practical problems, e.g. those of heating, cooling and ventilation. There have been a number of experimental studies on the plane turbulent wall jet, the majority of which were undertaken during the 1960's using hot-wire anemometry and have been critically reviewed by Launder and Rodi (1981). One of the most recent publications is Wygnanski et al. (1992), in which the applicability of scaling laws to the turbulent wall jet is examined.

The two-dimensional turbulent wall jet is assumed to issue from a narrow rectangular nozzle of width b(0) with an initial speed equal to u(0) and the maximum fluid speed at any station x* is denoted $\tilde{u}$; the notation and coordinate system for the wall jet is

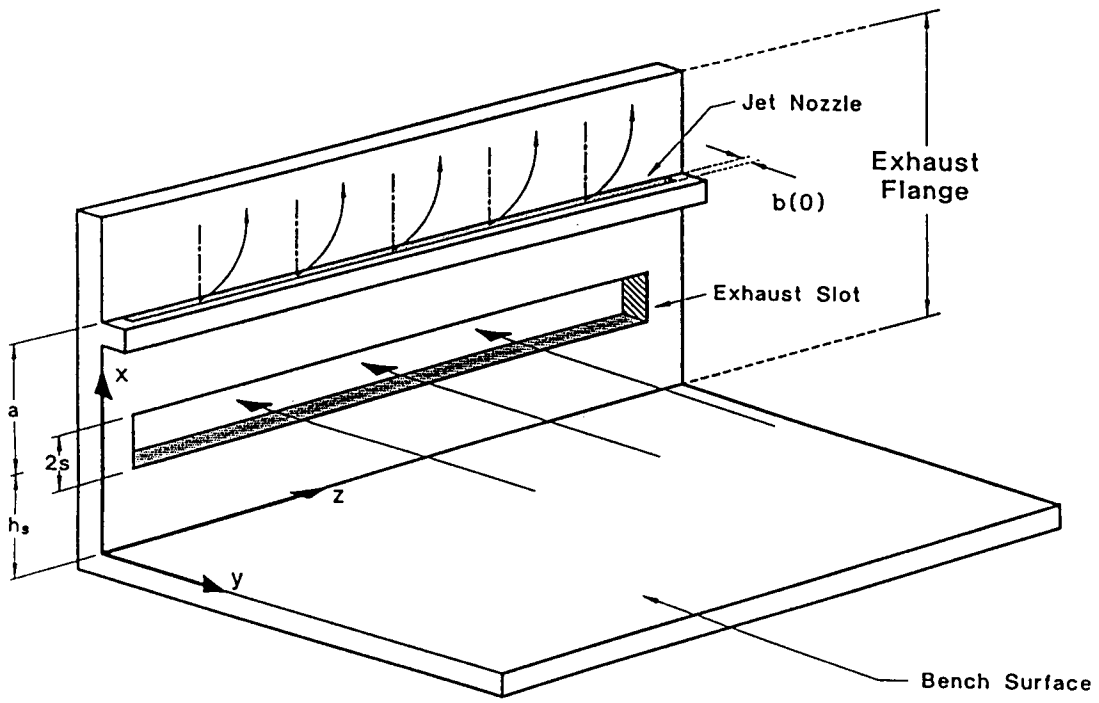

Fig.7.1 A schematic diagram of the Aaberg slot exhaust hood.

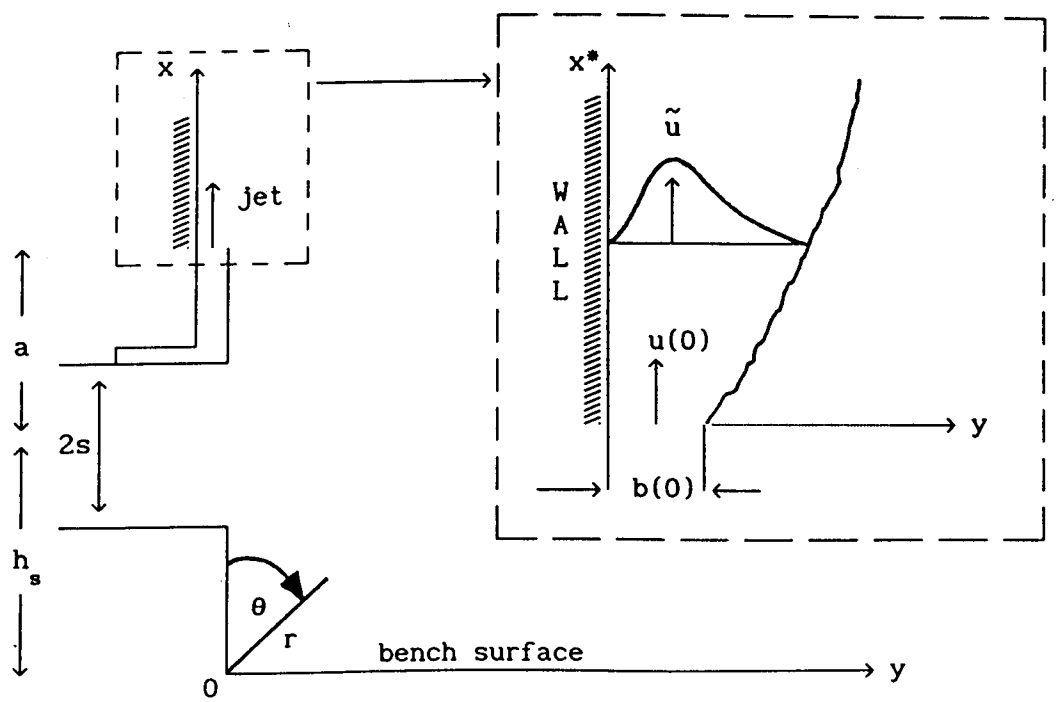

Fig.7.2 The geometry and coordinate system of the ASE model.

shown in Fig.7.2. The velocity distribution of the entire wall jet has been found to be similar for values of x^* greater than about 20 b(0) by a number of experimentalists, including Sigalla (1958b), Schwarz and Cosart (1961) and Myers et al. (1963) and in this chapter Verhoff's (1963) empirical equation describing the similarity solution, namely

$$\frac{u}{\tilde{u}} = 1.48\ \eta^{1/7}\ \mathrm{erfc}(0.68\eta) \quad ; \quad \eta = \frac{Y}{0.068X^*} \qquad (7.2.2)$$

where $X^* = x^*/p$, is used to model the two-dimensional wall jet flow. Verhoff's equation shows excellent agreement with the experimental observations of Myers over the range of values of $x^*/b(0)$ between 24 and 180. Other empirical expressions for the velocity profile have been considered, see Schwarz and Cosart (1961); however, these distributions do not compare as favourably with the experimental data as the Verhoff (1963) distribution. From an average of the available observations of the velocity decay in a two-dimensional turbulent wall jet for $1.9 \times 10^4 \leq R_e \leq 3.7 \times 10^4$, Rajaratnam (1976) describes the velocity decay as being well-represented by

$$\frac{\tilde{u}}{u(0)} = \frac{3.5}{\sqrt{x^*/b(0)}} \qquad (7.2.3)$$

for $x^*/b(0)$ at least up to 100. From equations (7.2.2) and (7.2.3) we obtain

$$\frac{u}{m/p} = G_w (X-1)^{-9/14}\ Y^{1/7}\,\mathrm{erfc}\left(\frac{10\ Y}{X-1}\right) \qquad (7.2.4)$$

where the dimensionless parameter G_w, referred to hereafter as the wall jet operating parameter, is defined to be

$$G_W = 7.61 \frac{u(0)}{m} \left(p\, b(0)\right)^{1/2} . \qquad (7.2.5)$$

The stream function for the turbulent wall jet may be deduced from equation (7.2.4) and hence by taking the limit as $Y \longrightarrow \infty$ the boundary condition for Ψ at the edge of the turbulent wall jet determined. The required boundary condition which will govern the flow induced by the turbulent wall jet is given by

$$\Psi \longrightarrow G_W (X-1)^{-9/14} \int_0^\infty Y^{1/7} \operatorname{erfc}\left(\frac{10\ Y}{X-1} \right) dY \qquad X > 1 \ . \qquad (7.2.6)$$

7.2.2 The Two-dimensional Turbulent Free Jet

The equations of motion modelling the steady, incompressible and turbulent flow in a two-dimensional free jet are the Prandtl shear-layer equations (3.2.30). Following Schlichting (1968) we find that $b \sim x^*$, $\tilde{u} \sim (x^*)^{-1/2}$ and the stream function, ψ, of the two-dimensional turbulent free jet is given by equation (3.2.39). In relation to the coordinate system (X,Y) the non-dimensional form of equation (3.2.39) may be written

$$\Psi = G_F (X-1)^{1/2} \tanh(\eta) \qquad X > 1 \qquad (7.2.7)$$

where $\eta = \sigma_o Y/(X-1)$ and the dimensionless parameter G_F, referred to hereafter as the free jet operating parameter, is defined to be

$$G_F = \frac{1}{2m} \left(\frac{3kp}{\sigma_o} \right)^{1/2} \qquad (7.2.8)$$

where $k = b(0)\, u(0)^2$. If we let $Y \longrightarrow \infty$ in equation (7.2.7) then we obtain the condition for Ψ at the edge of the free jet shear-layer, i.e.

$$\Psi \longrightarrow G_F (X-1)^{1/2} . \qquad (7.2.9)$$

The flow induced by the two-dimensional jet is governed by the potential equation (4.3.2) and in this model the boundary condition at large distances from the ASE is enforced on $R = R_\infty$, where $R_\infty \gg 1$, for $0 \le \theta \le \pi/2$. This boundary condition is taken to be the asymptotic solution of the Laplace equation (4.3.2) subject to the appropriate boundary condition for the jet-induced flow on $\theta = 0$, i.e. equation (7.2.6) or (7.2.9), and subject to $\Psi = 0$ on $\theta = \pi/2$ plus the radial flow contribution resulting from the exhaust flow. The surface of the bench represents a streamline of the flow and hence, for convenience, we have chosen

$$\Psi(R,\pi/2) = 0 \qquad 0 \le R \le R_\infty \,. \qquad (7.2.10)$$

To obtain an analytical asymptotic solution of the Laplace equation it is necessary to approximate equation (7.2.6) in the form

$$\Psi \propto A\,(X-1)^{\lambda} \qquad (7.2.11)$$

where the parameter A and the exponent λ depend upon the wall jet operating parameter G_W. Note that equation (7.2.9) is already in this form with $A = G_F$ and $\lambda = 1/2$. Following the method outlined in section 4.3.1 of chapter 4 the following upstream boundary condition is readily obtained

$$\Psi(R,\theta) = A\left\{\frac{R^{\lambda}}{\sin\lambda\frac{\pi}{2}}\sin\left[\lambda\left(\frac{\pi}{2}-\theta\right)\right] - \frac{\lambda R^{\lambda-1}}{\sin(\lambda-1)\frac{\pi}{2}}\sin\left[(\lambda-1)\left(\frac{\pi}{2}-\theta\right)\right]\right.$$

$$\left. + \frac{\lambda(\lambda-1)R^{\lambda-2}}{2!\sin(\lambda-2)\frac{\pi}{2}}\sin\left[(\lambda-2)\left(\frac{\pi}{2}-\theta\right)\right] - \ldots\right\} + \left(1 - \frac{2\,\theta}{\pi}\right) \qquad (7.2.12)$$

on $0 \le \theta \le \pi/2$, $R = R_\infty$.

The remaining boundary conditions are found by assuming that across the exhaust inlet the fluid velocity is uniformly

distributed. Modelling the suction inlet as a finite-sized slot of width 2S and positioned at a height H_s above the bench surface we obtain

$$\Psi(X,0) = \frac{1}{2S}\left(X - H_s + S\right) \qquad H_s - S \le X \le H_s + S \qquad (7.2.13)$$

and hence

$$\Psi(X,0) = 1 \qquad H_s + S < X \le 1 \qquad (7.2.14)$$

$$\Psi(X,0) = 0 \qquad 0 \le X < H_s - S. \qquad (7.2.15)$$

The effect of the exhaust's suction is to modify the boundary condition at the edge of the jet shear-layer which now becomes

$$\Psi(X,0) \longrightarrow 1 + G_W(X-1)^{-9/14} \int_0^{\infty} Y^{1/7}\,\mathrm{erfc}\left(\frac{10\,Y}{X-1}\right) dY \qquad X > 1 \qquad (7.2.16a)$$

and

$$\Psi(X,0) \longrightarrow 1 + G_F(X-1)^{1/2} \qquad X > 1 \qquad (7.2.16b)$$

for the wall and free jet cases, respectively. Due to the complexity of the problem an analytical solution is not possible and finite-difference techniques are employed to solve the problem numerically.

7.3 THE OPERATING PARAMETERS

From a knowledge of the physical quantities u(0), b(0), p and m obtained from the operating conditions at which Pedersen (1991a) ran an ASE, the operating parameters G_W and G_F which correspond to these conditions can be evaluated. Although the mathematical model developed may be used to examine many different aspects of the air

flow pattern induced by the ASE, in this study two main modes of ASE operation are considered.

The first mode of operation we consider, referred to as the HI-experiment by Pedersen, is one in which the suction inlet, of width $2s = 30 \times 10^{-3}$m, is flush with the bench surface and the ratio of the momentum flows, I, is varied. It should be noted that the hood's suction inlet is not always flush with the bench surface and in other experiments it may be raised above this datum level. The values of the physical quantities used by Pedersen in the HI-experiment were $b(0) = 2 \times 10^{-3}$m, $p = 0.23$ m and $m = 0.111$ m^3s^{-1} (i.e. per metre length of the slot) and these lead to the following approximate relationships:

$$G_W \propto 1.47\ u(0) \quad \text{and} \quad G_F \propto 0.0604\ u(0)\ . \qquad (7.3.1)$$

The second mode of operation we consider, referred to as the HHY-experiment by Pedersen, is one in which the momentum ratio is fixed at $I = 0.7$ and the height of the suction inlet, H_s, above the bench surface is allowed to vary. The exhaust inlet size is again $2s = 30 \times 10^{-3}$m. The values of the physical quantities used by Pedersen in the HHY-experiment were $u(0) = 12$ ms^{-1}, $b(0) = 2 \times 10^{-3}$m and $m = 0.111$ m^3s^{-1} (i.e. per metre length of the slot). These quantities lead to the following approximate relationships:

$$G_W \propto 36.8\ p^{1/2} \quad \text{and} \quad G_F \propto 1.51\ p^{1/2}. \qquad (7.3.2)$$

The values of H_s which we shall consider in the model are $H_s = 0.349$, 0.500 and 0.594; these values correspond to the values of h_s considered by Pedersen, namely $h_s = 0.115$ m, 0.215 m and 0.315 m, respectively.

7.4 RESULTS AND DISCUSSION

The parameter A and the exponent λ, defined in equation (7.2.11), may now be determined as functions of G_w and the boundary condition along $R = R_\infty$ deduced for the wall jet case. Approximating equation (7.2.6), as in the form of equation (7.2.11), we obtain the following approximate relationship

$$\Psi = 0.0342\ G_w(X-1)^{0.500}. \qquad (7.4.1)$$

The exponent λ was found to be independent of the operating parameter G_w for $0 \leq G_w \leq 33.4$, where the upper limit of $G_w = 33.4$ is the largest value of G_w arising from the experimental operating conditions considered by Pedersen. Comparisons are now made between Pedersen's experimental data and the results obtained from the theory in order to assess the ability of the mathematical model to predict the actual operating conditions of the ASE.

7.4.1 The HI-Experiments

In the HI-experiments Pedersen examines what effect the injection of fluid has on the air flow pattern by measuring the air speed induced by an ASE operating at different momentum ratios. The changes in the momentum ratios were achieved by Pedersen by varying the jet nozzle speed, u(0), whilst keeping all other quantities constant. Pedersen's air speed measurements were recorded along the length of the bench from y = 0 m to y = 1.2 m and at a vertical distance of 0.04 m above its surface, a vertical distance which corresponds to 0.174 dimensionless units. Pedersen (1991b) stated that these measurements of air speed were taken outside the

boundary-layer which forms along the bench surface and the boundary-layer observed by Pedersen during smoke experiments attained a maximum thickness of approximately 5×10^{-3}m. In the region where Pedersen's air speed measurements were recorded we expect the induced flow to be dominated by the flow into a wall jet and hence we expect the wall jet model to most accurately predict the true operating conditions of the ASE.

Figures 7.3(a)-(d) illustrate the variation of the dimensionless resultant air speed, Q, as a function of Y along X = 0.174 for the momentum ratios of I = 0.0, 0.5, 0.9 and 2.5, respectively. Each figure shows the air speeds predicted by the free and wall jet models together with Pedersen's experimental data. On comparing the graphs it is clear that increasing the momentum ratio, I, results in increasing the resultant air speeds along the line considered and this is most clearly illustrated by comparing Fig.7.3(a) with Fig.7.3(d). Figure 7.3 shows that the qualitative agreement between the predictions of the wall and free jet models and the experimental data is good. Quantitatively the agreement between the predictions of the wall jet model and the experimental data is very good for each momentum ratio, I, over the entire range of Y considered. However, the resultant air speeds along X = 0.174 predicted by the free jet model continually overestimate those observed experimentally. The significant quantitative differences between the wall jet and the free jet solutions can be explained in terms of the momentum fluxes of the two different jets. The momentum flux of the wall jet is not conserved but decreases with increasing distance from the jet orifice as the jet loses energy due to the contact with the wall. The presence of the wall is very significant

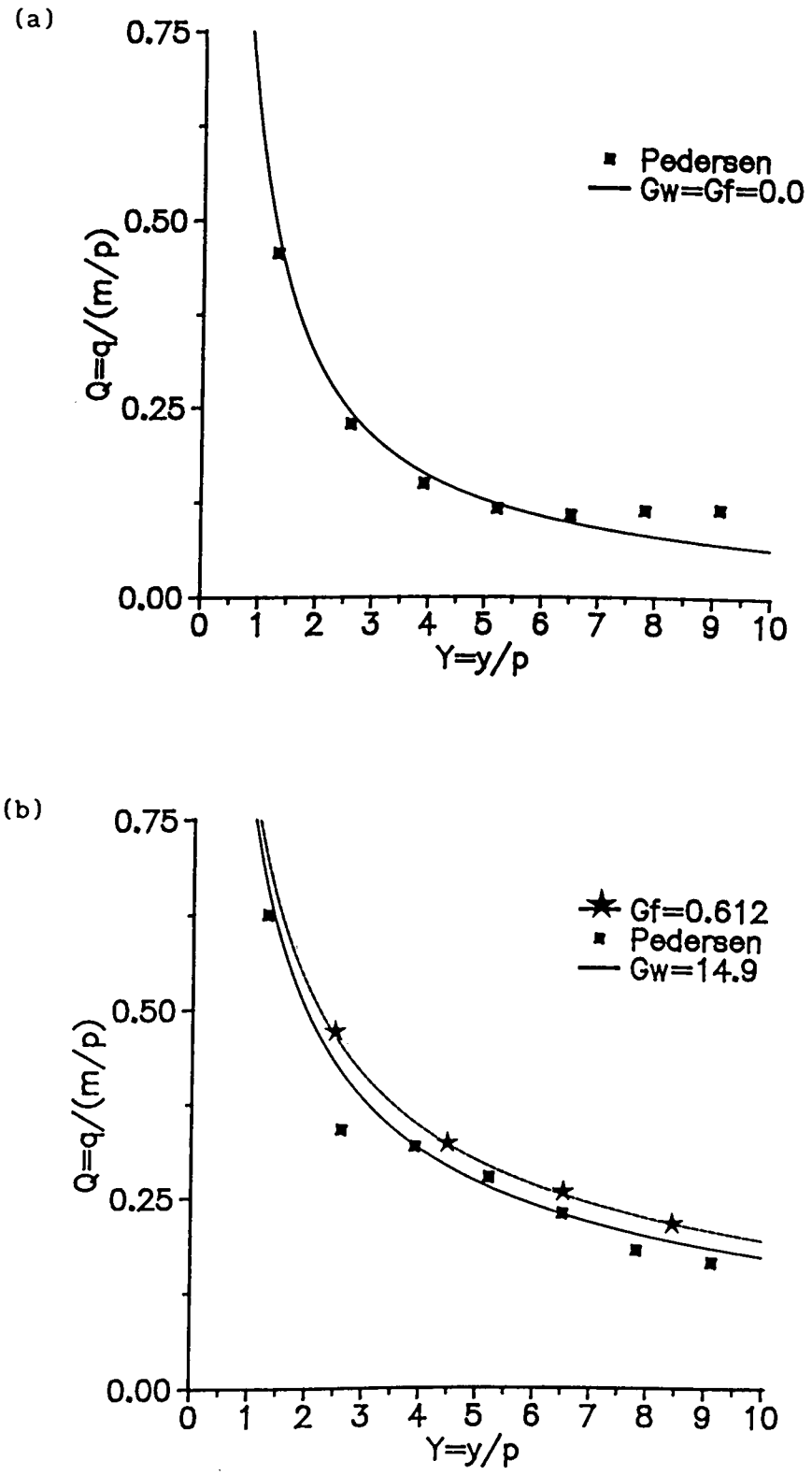

Fig.7.3 The variation in the dimensionless resultant air speed, Q, as a function of Y along X = 0.174, (a) I = 0.0 and (b) I = 0.5.

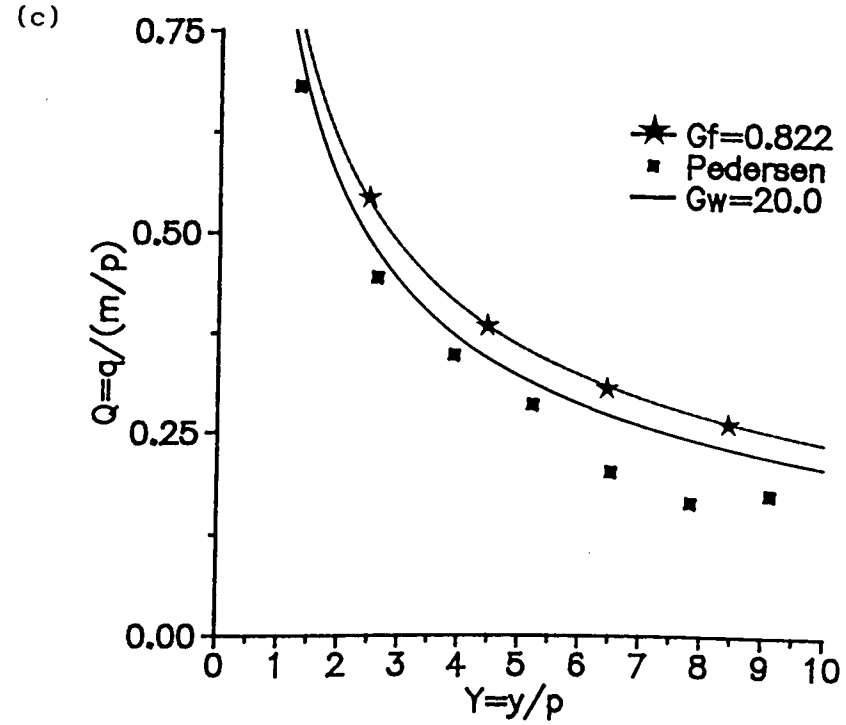

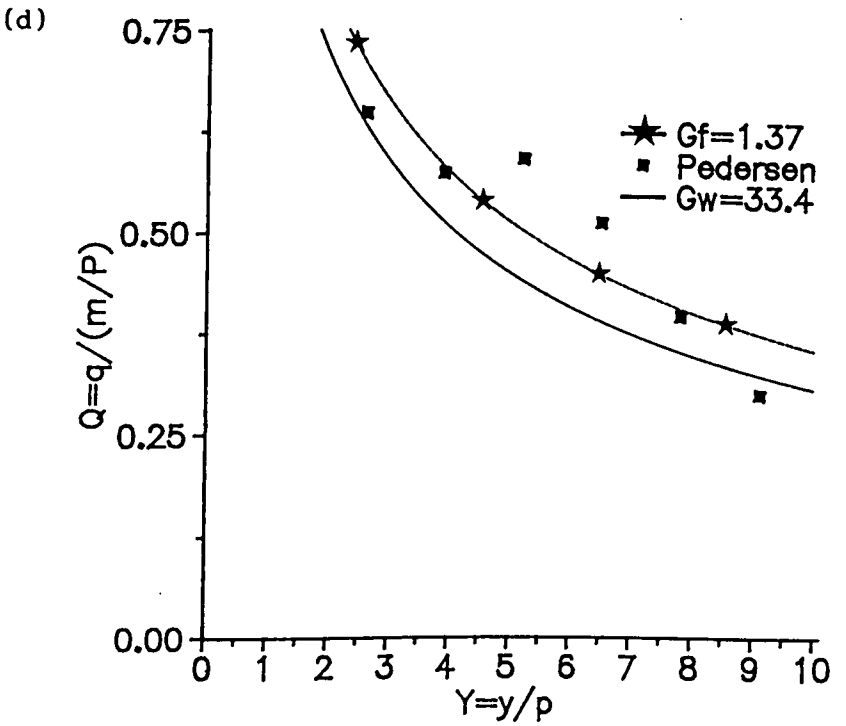

Fig.7.3 The variation in the dimensionless resultant air speed, Q, as a function of Y along X = 0.174, (c) I = 0.9 and (d) I = 2.5.

and for a rough wall the momentum flux of the jet may decrease by 50% in a longitudinal distance of 60b(0) from the jet orifice, see Rajaratnam (1965). However, as an assumption of the boundary-layer theory the momentum flux of the free jet is assumed to be constant and independent of X. Therefore, for a given momentum flux the free jet will entrain more fluid than the wall jet and expand more rapidly. In fact, from the Verhoff velocity distribution (7.2.2) the width of the wall jet is given by $b = (14.7)^{-1}x^*$, whereas the width of the two-dimensional free jet, as determined by Reichardt, is $b = (7.67)^{-1}x^*$. This implies that the free jet expands almost twice as rapidly as the wall jet. The greater flux of entrained fluid realized by the free jet, as compared with the wall jet, further concentrates the suction of the ASE and thus the resultant air speeds predicted by the free jet model are greater than those predicted by the wall jet model.

For values of the operating parameter G_F larger than those considered in this chapter the profiles of resultant air speed predicted by the model exhibit local minima and maxima air speeds. The presence of these turning points may be explained by considering how the air in front of the exhaust inlet is influenced by the effects of the exhaustion and injection. For large values of G_F the free jet solution predicts that for $Y < p/2$ the movement of air in front of the inlet is dominated by the exhaustion as the air speed falls rapidly with increasing distance from the inlet. At a distance of the order of $p/2$ from the inlet the free jet's entrainment of air influences the flow, raising its resultant speed until a maximum speed is reached at a distance of the order of $3p/2$ from the exhaust inlet. Thus, for the free jet the influence of the entrained air

flow is abruptly 'felt' after some minimum distance from the inlet is exceeded. Hence, the model predicts that when a hood employs the Aaberg principle the suction plays only a very small role in the movement of air in the workplace, as compared to the injection, and it is only needed to draw the contaminated air that final distance into the exhaust inlet over which the injection flow has no influence. Turning points are also present in the wall jet solutions for large values of G_w. However, the energy loss of the jet due to its contact with the exhaust flange results in the wall jet-induced flow more gradually affecting the overall air flow and the magnitudes of the air speed gradients are less than those predicted by the corresponding free jet solutions. The energy loss of the wall jet also accounts for the decreasing quantitative agreement between the free and wall jet solutions as the ratio of the momentum flows, I, increases.

The variation in the dimensionless resultant air speed, $Q = q/(m/p)$, as a function of X predicted by the wall and free jet models is shown in Fig.7.4 together with Pedersen's experimentally observed air speeds for an ASE operating at $I = 0.9$ and $I = 1.5$. The profiles of resultant air speed shown in Fig.7.4 are those predicted and observed vertically from $Y = 5.22$, the dimensionless distance corresponding to $y = 1.2$ m. Figure 7.4 shows that good agreement is achieved between the predictions of the wall jet model and the air speeds observed experimentally. Again it can be seen that the free jet solution overestimates the observed values and the wall jet solution. One notable feature of the ASE air flow which is both predicted by the wall jet model and which is observed experimentally is that the resultant air speed measured vertically from $Y = 5.22$ is

(a)

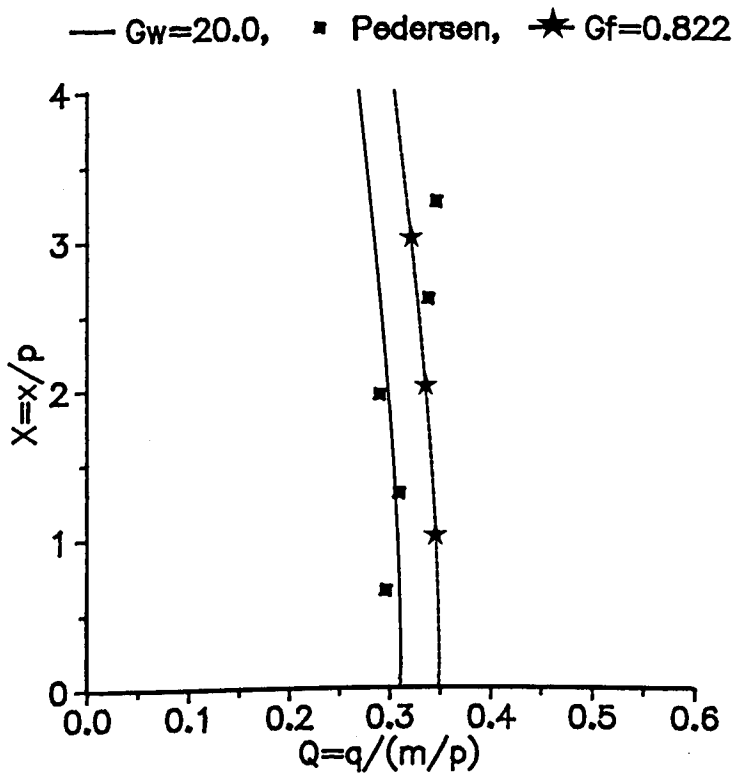

(b)

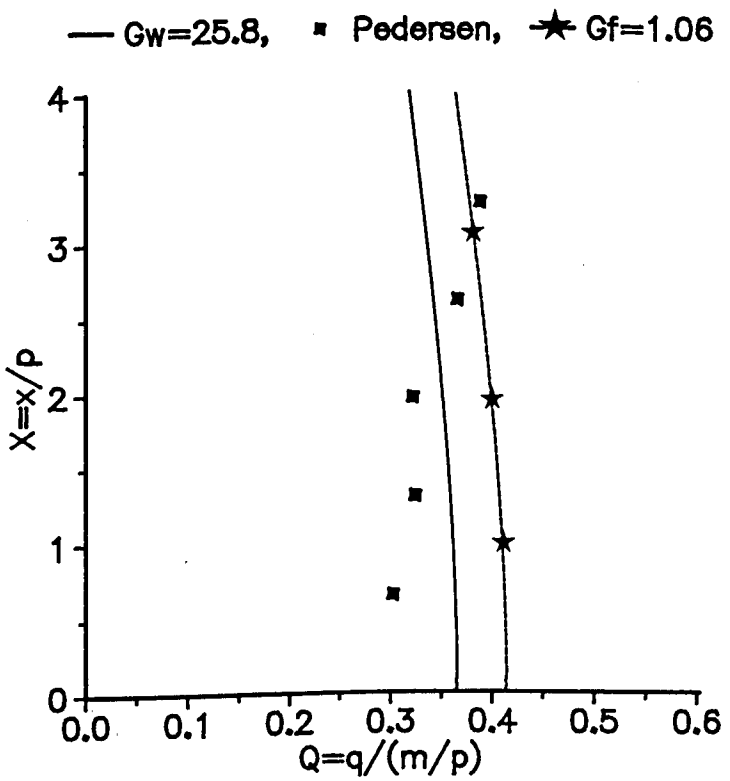

Fig.7.4 The variation in the dimensionless resultant air speed, Q, as a function of X from Y = 5.22, (a) I = 0.9 and (b) I = 1.5.

approximately constant and of the order of Q = 0.3 and Q = 0.35 for a hood operating at I = 0.9 and I = 1.5, respectively.

The slight deviation of the experimental observations of resultant air speed from the predictions of the wall jet model, most evident in Fig.7.3(d), may be as a result of inaccuracies encountered during Pedersen's experimental measurements. Pedersen's air speed measurements were recorded under laboratory conditions using a multi-channel DANTEC low velocity flow analyser and integrated over 300 s and background air disturbances were reportedly of the order of 0.02 ms^{-1}. However, the physical presence of the flow measuring apparatus would be enough to deflect the hood's air flow pattern and could alone account for the discrepancies. Furthermore, the ASE flow field may have been affected by other external influences during the experiments, e.g. temperature gradients.

We have seen from Figs.7.3 and 7.4 that the air flow predicted by the wall jet model gives a good representation of the observed flow in the regions considered. In order to examine further the effect of the injection on the overall air flow pattern created by the ASE we now examine streamlines deduced from the wall jet model. Sets of streamlines modelling the air flow pattern created by an ASE reinforced by a two-dimensional wall jet flow are shown in Figs.7.5(a)-(d) for the operating parameters G_W = 0.0, 14.9, 20.0 and 33.4, respectively. The four values of G_W considered correspond to I = 0.0, 0.5, 0.9 and 2.5, respectively. From the streamline plots the dramatic effect on the overall air flow pattern achieved by the introduction of the wall jet is clear. Figure 7.5 shows that as the value of the dimensionless operating parameter G_W is

(a)

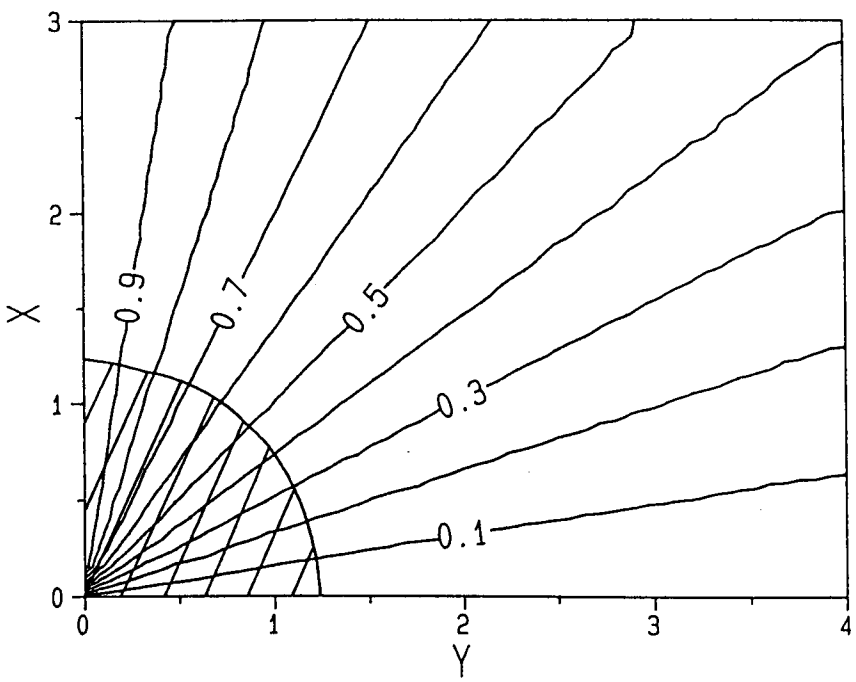

(b)

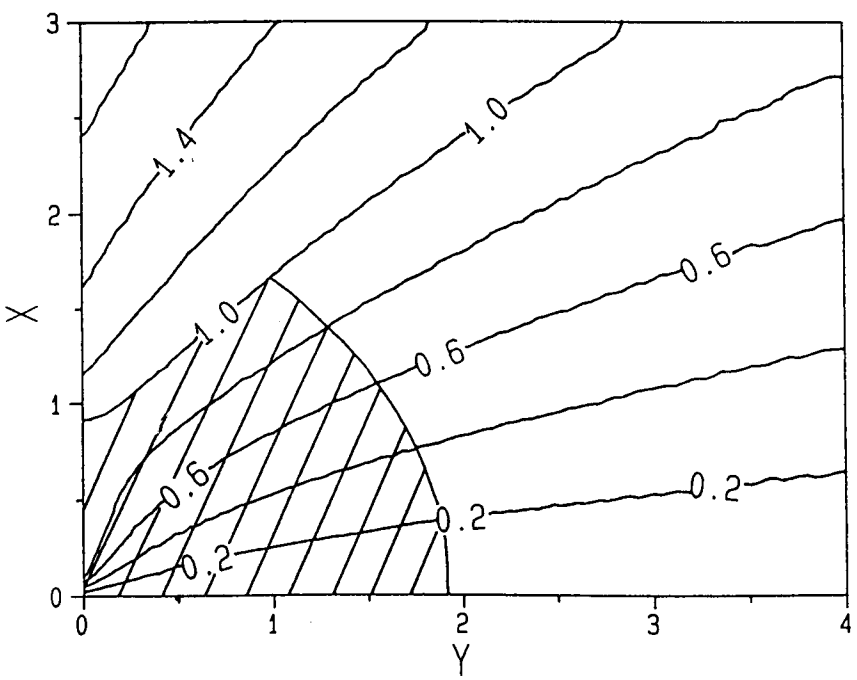

Fig.7.5 Sets of streamlines modelling the ASE flow pattern predicted by the wall jet model, (a) G_w = 0.0 and (b) G_w = 14.9. The shaded area represents the predicted effective capture region.

(c)

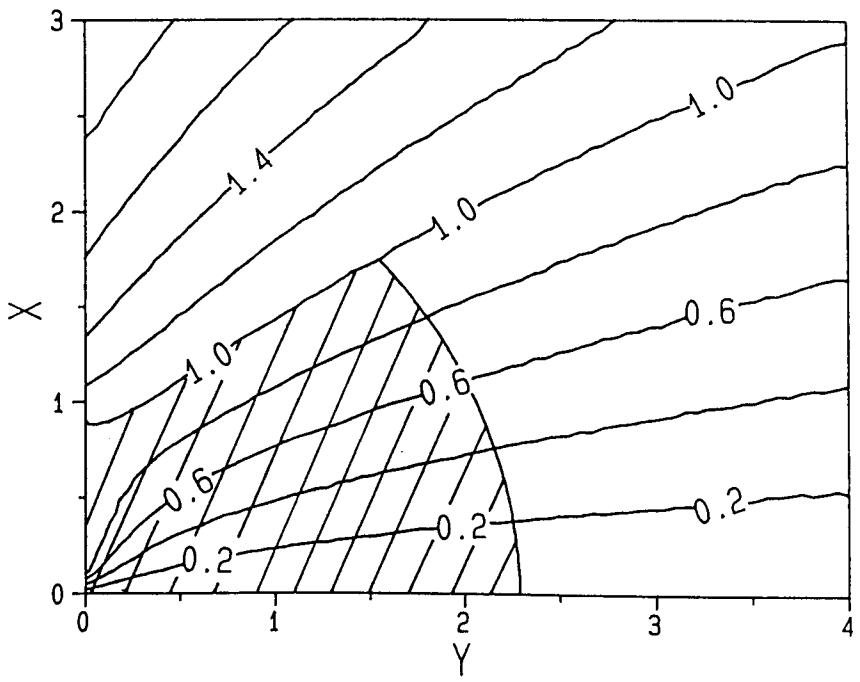

(d)

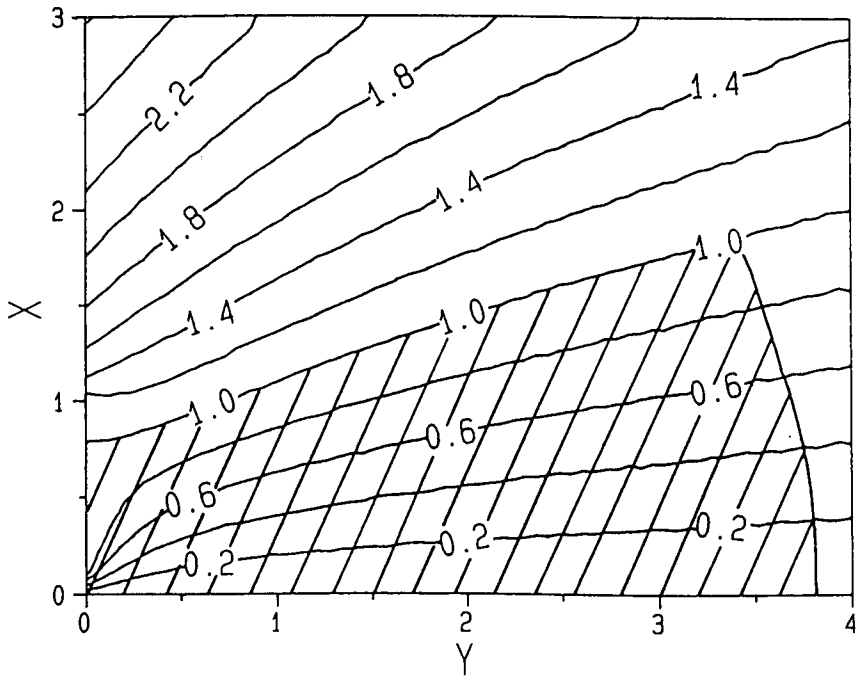

Fig.7.5 Sets of streamlines modelling the ASE flow pattern predicted by the wall jet model, (c) G_w = 20.0 and (d) G_w = 33.4. The shaded area represents the predicted effective capture region.

increased, the dividing streamline, $\Psi = 1$, which divides the flow travelling towards the exhaust inlet from that travelling towards the injection flow, is forced towards the bench surface. The displacement of the dividing streamline resulting from the introduction of the wall jet flow thus implies enhanced air speeds towards the inlet over the zero injection case. The selective nature of the reinforced exhaust, observed experimentally by Pedersen (1991a), is also illustrated in Fig.7.5. With $G_w = 0.0$, see Fig.7.5(a), air is drawn towards the inlet from all directions and under these conditions the ASE is non-selective and performs in the same way as a traditional flanged slot exhaust. However, as the value of G_w is increased, see Figs.7.5(b)-(d), air is now selected from a narrower and more well-defined region of the workplace. A capture speed of 0.25 ms^{-1} corresponds to a non-dimensional speed of $Q_c = 0.518$ for the operating conditions used by Pedersen (1991a) in his HI-experiments. Thus, we can define the effective capture region, i.e. the region from which the contaminated air will be drawn into the exhaust inlet and successfully removed from the workplace, to be the area bounded by the line of constant speed, $Q_c = 0.518$, and the dividing streamline $\Psi = 1$. The effective capture region is highlighted in Fig.7.5 by the use of shading and we can see how the shape of this region changes as the parameter G_w increases. On increasing the value of G_w we see that the maximum width of the effective capture region decreases as its length increases. Thus, increasing the value of G_w, and hence the momentum ratio, implies that the ASE can create controlled air movements over greater distances than possible when using traditional methods or in other words the injection creates long range exhaustion.

Pedersen (1991b) stated that the level of background air disturbances in the laboratory was of the order of 0.02 ms^{-1}. This would, however, lead to effective capture regions much larger than those predicted by the wall jet model and larger than one could possibly expect to achieve under practical circumstances.

7.4.2 The HHY-Experiments

Comparisons have also been made between Pedersen's observations taken during the HHY-experiments and the predictions of the mathematical model. Although these comparisons are not illustrated in this chapter the conclusions drawn from them are the same as those for the HI-experiments and again very good agreement is obtained between the predictions of the wall jet model and all the experimental observations.

7.5 CONCLUSIONS

A simple mathematical model for the fluid mechanics of an Aaberg slot exhaust hood has been developed and the parameters G_F and G_W, which characterize the subsequent free and wall jet-induced flows, identified. The wall jet model developed in this chapter shows good agreement, both quantitatively and qualitatively, with the experimental observations of Pedersen (1991a). The agreement gives us confidence in the theory and illustrates the mathematical modelling as a cost-effective means of confidently predicting the air flow field of the ASE. The simple mathematical model allows predictions to be made as to from what region of the workplace a

neutrally-buoyant contaminant can be successfully removed as a function of the governing parameters. The model also illustrates the directional flow pattern achieved when a traditional slot exhaust is reinforced by a jet flow and predicts that in all aspects a much improved air flow pattern is developed when using the Aaberg REEXS.

The resultant air speeds predicted by the free jet model imply that the air flow pattern of the ASE could be significantly enhanced through a simple modification to the hood's design. Namely, if the part of the exhaust flange along which the wall jet of the original ASE develops were moved 'backwards' then the emerging jet will issue as a free jet, see Fig.7.6. In this way the fluid entraining properties of the free jet can be utilized whilst still keeping the back wall to contain the technological process.

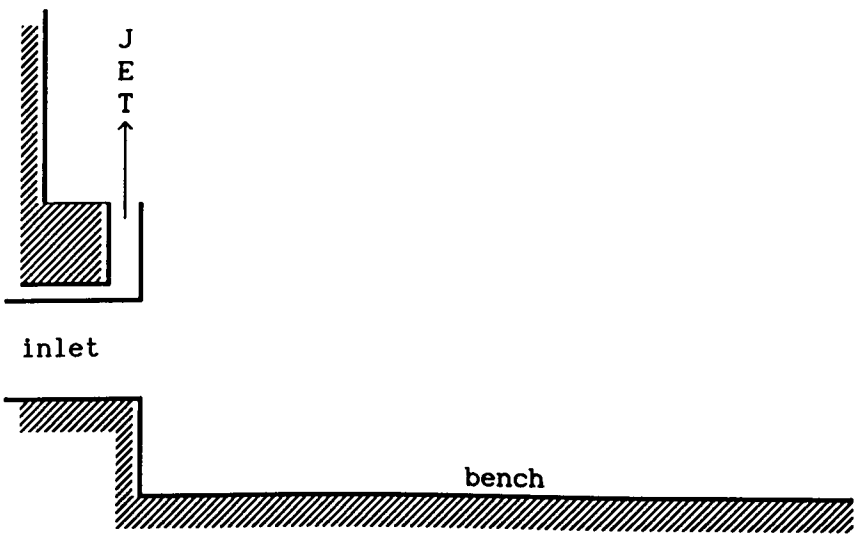

Fig.7.6 Cross-section through the Aaberg slot exhaust - illustrating the back wall design modification.

The implementation of the suggested design modification is only suitable when the ratio of the momentum flows is sufficiently large so that the jet is near vertical and relatively unaffected by the

exhaust flow. However, if the hood is to operate as a REEXS at low values of the momentum ratio then the back wall should be maintained. Pedersen and others have observed that the system is then able to operate as a REEXS for values of I lower than the corresponding free jet case due to the entrainment of fluid into the wall jet from the wall-side of the jet. This flow assists the jet to remain attached to the wall.

CHAPTER EIGHT

THE USE OF FLUENT

- A FULL TURBULENCE MODEL -

8.1 INTRODUCTION

The mathematical models presented in the previous chapters have been developed under the assumption that the flow induced by an Aaberg exhaust hood is inviscid and potential and that turbulent effects have been limited to the flow in the jet. As mentioned in earlier chapters, the typical experimental operating conditions of an Aaberg exhaust hood lead to Reynolds numbers which, based on the jet nozzle width, b(0), and initial jet velocity, u(0), imply that the fluid flow in the jet is turbulent. Similarly, the Reynolds numbers associated with the fluid flow into the exhaust inlet, for both (i) the axisymmetric Aaberg exhaust hood and (ii) the Aaberg slot exhaust hood, based on the radius or slot width, s , of the exhaust inlet and the face velocity, u_{in}, under typical operating conditions, are (i) $O(10^3)$ and (ii) $O(10^4)$. Thus, both the flow in the jet and in the region surrounding the exhaust inlet are very likely to be turbulent. However, in the region of practical interest, i.e. the region of the flow which leads into the exhaust inlet, the air flow created by the Aaberg exhaust hood is a convergent flow and therefore in this region we expect there to be a very low level of turbulence.

In this chapter the full, turbulent Navier-Stokes equations are solved using the control volume method and the k-ε model as developed by Launder and Spalding (1972) is employed in order to model the turbulent properties of the fluid flow. The quantities k and ε denote the turbulent kinetic energy and the turbulent energy dissipation of the turbulent motion, respectively. The widely used and commercially available CFD package FLUENT, which solves the full

turbulent equations using the aforementioned control volume technique, has been used to generate the results which are presented in this chapter. The air flows predicted by the full turbulent model for both the axisymmetric Aaberg exhaust hood and the two-dimensional Aaberg slot exhaust (ASE) are then compared with the air flows predicted by the inviscid flow models developed in chapters 6 and 7, respectively. The relative merits of the two different techniques for determining the flow field are also discussed.

The standard, full turbulent equations of motion are now introduced and a description of the control volume technique and the solution procedure SIMPLEC are given.

8.2 THE FULL TURBULENCE MODEL

The equations of motion which govern the flow of a steady, incompressible, turbulent viscous fluid are the time-averaged Navier-Stokes equations, namely the continuity equation (2.2.1a) and the momentum equation (2.2.1b).

8.2.1 The k-ε Model

In order to overcome the limitations of the Prandtl mixing length hypothesis, more sophisticated turbulence models, see for example Launder and Spalding (1972,1974), were developed which account for the transport of turbulent quantities by solving differential transport equations. The k-ε model is known as a two equation model, having transport equations for the kinetic energy,

k, and the dissipation rate, ε. A standard k-ε model, as developed by Launder and Spalding (1974), is now employed and the governing equations are as follows:

the turbulent kinetic energy equation

$$(\mathbf{u}.\nabla)k = \nabla.(\frac{\nu_e}{\sigma_k}\nabla k) + \Phi - \varepsilon \qquad (8.2.1a)$$

and the turbulent energy dissipation equation

$$(\mathbf{u}.\nabla)\varepsilon = \nabla.(\frac{\nu_e}{\sigma_\varepsilon}\nabla\varepsilon) + C_1\frac{\varepsilon}{k}\Phi - C_2\frac{\varepsilon^2}{k}. \qquad (8.2.1b)$$

The k-ε model uses equations (8.2.1) to calculate the distributions of k and ε, and the turbulent viscosity may be determined from the Prandtl-Kolmogorov formula:

$$\nu_t = C_\mu\frac{k^2}{\varepsilon}. \qquad (8.2.2)$$

In expressions (8.2.1) the quantity Φ is the generation of turbulent energy which is caused by turbulent stresses and the values of the coefficients C_1, C_2, C_μ, σ_k and σ_ε appearing in equations (8.2.1) and (8.2.2) are based on an extensive examination of free flows, see for example Launder and Spalding (1974), and in this thesis are taken to be $C_1 = 1.44$, $C_2 = 1.92$, $C_\mu = 0.09$, $\sigma_k = 1.0$ and $\sigma_\varepsilon = 1.3$. It is generally accepted that these values are applicable to any system in which the exponents of k and ε in equation (8.2.2) are 2 and 1, respectively.

8.2.2 The Boundary Conditions

All of the governing equations, namely equations (2.2.1) and (8.2.1), are elliptic in nature and therefore, in addition to the upstream boundary conditions, we must specify boundary conditions on the surface of the Aaberg exhaust hood and on the axis of symmetry.

The no-slip conditions of $u = v = 0$ are applied at boundaries representing stationary solid walls. Ideally the turbulent kinetic energy, k, is set to zero on the wall whilst the rate of dissipation, ε, is finite. However, there are two main difficulties encountered when imposing these boundary conditions, namely, (i) a fine grid is required in order to resolve the steep gradients that occur in the region close to the wall and this results in a very expensive computation, and (ii) the constants appearing in the k-ε equations are not applicable in the wall region.

The 'wall function' approach is often employed to overcome these difficulties and involves placing the first grid point P at a distance y from the wall. The 'boundary condition' for ε is then specified at the first grid point away from the boundary, thus avoiding the need to resolve the steep gradients across the boundary-layer. In the region of the turbulent flow where the fluid velocity is assumed to be governed by the wall function, namely

$$\frac{u}{u^+} = \frac{1}{\kappa} \ln(Ey^+) \qquad 35 < y^+ < 350, \qquad (8.2.3)$$

see White (1991), it is convenient to assume that the generation, Φ, and dissipation, ε, of turbulent energy are in equilibrium. Hence equation (8.2.1a), which governs the variation of k, has a constant solution and therefore the boundary condition

$$\frac{\partial k}{\partial n} = 0 \qquad (8.2.4)$$

should be enforced at the surface of the body. In equation (8.2.3), the von Karman constant $\kappa = 0.42$ for a smooth wall, the roughness parameter $E = 9.8$, $y^+ = yu^+/\nu$ is the dimensionless friction length, where y is the distance from the wall, and the shear velocity u^+ is defined as $u^+ = (\tau_w/\rho)^{1/2}$ in which τ_w is the shear stress on the

wall. The boundary condition for the dissipation rate at the point P is calculated from the following expression

$$\varepsilon_p = \left(\frac{C_\mu^{3/4} k^{3/2}}{\kappa y} \right)_p . \qquad (8.2.5)$$

On any boundary where the fluid leaves the system, and on the axis of symmetry, the condition of a zero normal gradient, i.e. $\partial/\partial n \equiv 0$, for all the dependent variables is specified. Also enforced on the axis of symmetry is the condition of a zero normal component of the velocity, i.e. $v = 0$. For the flow upstream of the Aaberg exhaust hood, the values of k and ε are not experimentally known although they may be predicted from the formula used for internal flows, i.e. $k = (I_\infty U_\infty)^2$ and $\varepsilon = 0.09\ k^{1.5}/(0.3R_h)$ where I_∞ and U_∞ are the turbulent intensity and the air speed upstream of the exhaust hood, respectively, and R_h is the hydraulic radius, see Nallasamy (1987).

In order to model the jet flow of the Aaberg exhaust hood, constant velocity and turbulence intensity values have been specified at the opening of the jet, from which boundary conditions on k and ε may be determined. The turbulence intensity of a constrained radial jet has been investigated by Witze and Dwyer (1976) who found that the level of the turbulence varies considerably across the width of the jet, from approximately 30% along the jet centre-line to a maximum of approximately 60% when $y/b_{1/2} \propto 1.5$. For wall jet flows, the turbulence intensity has been taken to be 20%, a value which represents an average of the maximum turbulence intensity recorded experimentally in the turbulent wall jet, see Launder and Rodi (1981). The respective turbulence intensities of 60% and 20% for the radial and the wall jet flows may

be considered as reasonable approximations for the present geometry and operating conditions.

Operating under suction alone the flow patterns generated by both the two-dimensional slot exhaust and the three-dimensional axisymmetric exhaust converge radially towards the exhaust inlet. Consequently, specifying the normal derivative of the velocity to be zero across the upstream rectangular boundary is not a reasonable representation of the fluid motion in this region. Therefore, for $I = 0$ the boundary conditions upstream were specified in terms of the pressure which was deduced from the Bernoulli equation under the assumption that the suction acts as a simple sink.

8.3 THE NUMERICAL METHOD

A brief summary of the methods used to solve the full k-ε equations, namely the control volume method and the Semi-Implicit Method for Pressure Linked Equations Consistent (SIMPLEC) are now given. SIMPLEC is not a control volume scheme in its own right but rather an improvement made, by Van Doormaal and Raithby (1984), to the existing SIMPLE scheme which was developed by Patankar and Spalding (1972) and which has been extensively discussed by Patankar (1980). All the results presented are of a two-dimensional or axisymmetric nature and consequently the numerical method is described in terms of only two dimensions.

For steady flow the equations of conservation of mass, momentum, and transport of k and ε can all be written in the general form

$$\nabla.(\rho u\phi) = \nabla.(\Gamma\ \nabla\phi) + S_\phi \qquad (8.3.1)$$

where ϕ now represents the general variable under consideration, Γ is the transport coefficient and S_ϕ is the source term for any transport effects not included in the transport coefficient. For a two-dimensional flow, equation (8.3.1) may be written in cartesian form as

$$\rho u \frac{\partial\phi}{\partial x} + \rho v \frac{\partial\phi}{\partial y} = \frac{\partial}{\partial x}\left(\Gamma \frac{\partial\phi}{\partial x} \right) + \frac{\partial}{\partial y}\left(\Gamma \frac{\partial\phi}{\partial y} \right) + S_\phi \ . \qquad (8.3.2)$$

The basic idea of the control volume method is to divide the solution domain into a number of discrete, non-overlapping control volumes such that there is one control volume surrounding each grid point. The simplest two-dimensional control volume is rectangular and is shown schematically in Fig.8.1, where the grid points labelled N, S, E and W represent the grid locations to the north, south, east and west, respectively, of the grid point P under consideration. The differential equations are then integrated over each control volume and by expressing the variation of ϕ between the grid points as piecewise linear profiles the required integrals may be evaluated. The discretization of the domain and the dependent variables therefore makes it possible to replace the governing differential equations (8.3.2) by a system of algebraic equations of the form

$$a_P\phi_P = a_E\phi_E + a_W\phi_W + a_S\phi_S + a_N\phi_N + S_\phi \qquad (8.3.3)$$

where a_i, i = P, E, W, N and S, represents the coefficient of ϕ at the grid point i. Equation (8.3.3) represents the relationship between the value of the variable ϕ at the node P to the values at the neighbouring nodes. In this section we shall concentrate our attention on the treatment of the momentum equation and consequently

it is convenient to consider equation (8.3.3) as having the form

$$a_p \phi_p = \Sigma\, a_{nb} \phi_{nb} + b \qquad (8.3.4)$$

where the subscript nb denotes a neighbour and the summation is taken over all neighbours and b is the source term of the momentum equation, i.e. it is the discretized form of the pressure gradient term.

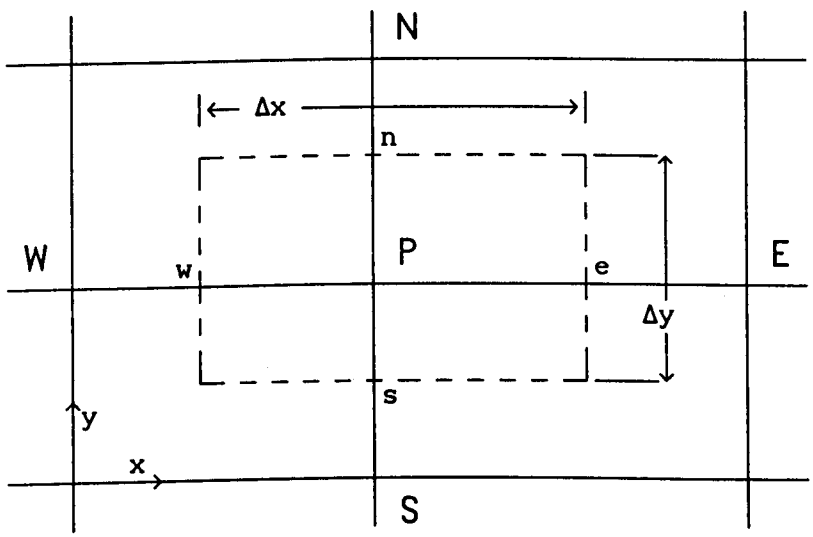

Fig.8.1 A two-dimensional rectangular control volume.

The variables k, ε and the pressure are calculated at the main grid points P, N, S, E and W, while the velocity components are calculated for the points which lie on the faces of the cell boundaries, see Fig.8.1, i.e. the staggered grid system has been employed. Using the main grid nodes such a discretization leads to a momentum equation which contains the pressure differences between two *alternate* grid points rather than between two *adjacent* ones. Not only does this affect the accuracy of the solution but it also results in a numerical method which would allow unrealistic

solutions, for example a zig-zag pressure field. Similar problems also arise in the treatment of the continuity equation when a staggered grid is not employed. Using a staggered grid the discretized x component of the momentum equation can be written as

$$a_e u_e = \Sigma a_{nb} u_{nb} + (p_P - p_E) A_e \qquad (8.3.5a)$$

where the pressure gradient dP/dx gives rise to the last term of equation (8.3.5a) and is the pressure acting on the u control volume, and A_e (= Δy in two dimensions) denotes the area on which the pressure difference acts. Similarly, for the y component of the momentum equation we obtain

$$a_n v_n = \Sigma a_{nb} v_{nb} + (p_P - p_N) A_n \, . \qquad (8.3.5b)$$

In most circumstances it is not possible to specify the correct pressure field and the velocity must be determined based on a guessed pressure field p*. The resulting velocity field, denoted by (u*, v*), will then not in general satisfy the continuity equation. The guessed pressure p* is improved by introducing a pressure correction term, p', such that

$$p = p^* + p' \qquad (8.3.6)$$

with the intention that the resulting approximate velocity components u* and v* become closer to satisfying the continuity equation. The velocity components will respond to this change in pressure and consequently the velocity corrections u' and v' are introduced such that $u = u^* + u'$ and $v = v^* + v'$. The velocity components u* and v* are then to be corrected in response to the pressure corrections via the velocity correction equations:

$$u_e = u_e^* + d_e (p'_P - p'_E) \quad , \quad v_n = v_n^* + d_n (p'_P - p'_N) \, . \qquad (8.3.7)$$

The only difference between the methods SIMPLE and SIMPLEC is in the choice of the coefficients d_e and d_n in equation (8.3.7) and in

SIMPLEC $d_e = A_e/(a_e - \Sigma a_{nb})$ and $d_n = A_n/(a_n - \Sigma a_{nb})$. On substituting expressions (8.3.7) for the velocity corrections into the continuity equation we obtain the pressure correction, p′, from

$$a_P p'_P = a_E p'_E + a_W p'_W + a_S p'_S + a_N p'_N + b \qquad (8.3.8)$$

where the term b and the coefficients a_P, a_E, a_W, a_S and a_N are now particular to the pressure correction equation (8.3.8). When solving the pressure correction equation (8.3.8), the condition of a zero normal gradient for the pressure correction is specified at all flow boundaries.

8.3.1 An Outline of the SIMPLEC Algorithm

The Semi-Implicit Method for Pressure Linked Equations is a sequential, rather than simultaneous, procedure for calculating the flow field and consists of the following steps:

(i) Guess the pressure field p*.

(ii) Solve the momentum equations (8.3.5) for u* and v*.

(iii) Solve the p′ equation (8.3.8) and update the pressure.

(iv) Update the velocity components u and v by using the velocity correction formulae (8.3.7).

(v) Solve the discretized form of equations (8.2.1) for k and ε.

(vi) Repeat steps (ii)-(v) until a converged solution has been obtained.

8.3.2 Solution of the Algebraic Equations and Convergence Criterion

The system of algebraic equations which results from the discretization of the governing equations is solved for one dependent variable at a time using the iterative line-by-line method, see Patankar (1980). With the line-by-line method a

relaxation factor, ω, is often employed and equation (8.3.4) may be written in the form

$$\frac{a_p}{\omega}\phi_p = \Sigma a_{nb}\phi_{nb} + b + (1 - \omega)\frac{a_p}{\omega}\phi_p^* \qquad (8.3.9)$$

where ϕ_p^* denotes the value taken by ϕ_p at the previous iteration. In the treatment of the non-linear momentum equation under-relaxation is necessary in order to avoid divergence of the iterative solution, whilst in contrast the pressure correction equation is linear, taking the form of a discretized Poisson equation, and over-relaxation may be used to speed up the convergence.

The convergence criterion used is usually referred to as the mass residual and is based on the reduction of the pressure correction term, p', to some small value. The mass residual of every control volume for the continuity equation is the constant term b in equation (8.3.8) and this may be written in the form

$$|R^k_{mass}| = C_e - C_w + C_n - C_s \qquad (8.3.10)$$

where C_e, C_w, C_n and C_s represent the mass flux through each face of the control volume surrounding the point P. The mass residual, R_{mass}, for the convergence criterion is the sum of the mass residuals over all the control volumes and is often normalized with respect to its value taken at the previous iteration. The mass residual serves as a useful indication of the rate of convergence of the iterative process as the continuity equation is exactly satisfied when $R_{mass} = 0$. This cannot of course be achieved using the numerical technique and convergence is taken to be when the mass residual is typically $O(10^{-3})$ or $O(10^{-4})$.

8.3.3 The Computational Grid

In order to produce solutions which are grid independent, solutions were obtained for increasingly fine grids and the results compared graphically. Grid independent solutions were taken to be those having no observable changes in the flow pattern on increasing the number of grid nodes. In addition to the grid independence test, the domain was doubled in size until graphically indistinguishable solutions were observed as for grid independent solutions.

In order to resolve the flow in the jets of the two exhaust hoods considered, a fine grid was necessary in these regions. The grid chosen in the direction parallel to the direction of the emerging jet was finest near the axis of the jet and expanded symmetrically outwards on either side of the jet. The grid chosen in the direction perpendicular to the direction of the emerging jet concentrated the grid cells in regions where rapid changes were expected, i.e. around the exhaust inlet and jet orifice.

Some difficulty was encountered in obtaining a smoothly varying flow in the jet but this was overcome by mesh refinement in the initial development region of the jet and a convergent solution was achieved when the mass residual was $O(10^{-3})$. Decreasing the mass residual to $O(10^{-4})$ resulted in no significant change to the solution obtained in all the cases considered in this thesis. With the standard meshing technique there is some uncertainty regarding adequate flow resolution in the jet and an alternative meshing technique which 'tracks' the progress of the jet, such as an adaptive meshing technique, would perhaps be more appropriate for this problem.

8.4 RESULTS AND DISCUSSION

The modelling techniques which have just been described are now applied to the problem of determining the air flow induced by the axisymmetric Aaberg exhaust hood and the Aaberg slot exhaust. Both cases have been studied in order to make comparisons between the simple mathematical models, developed in chapters 6 and 7, and the more sophisticated k-ε turbulence model as discussed in this chapter. Comparisons will also be made with the experimental results of Pedersen (1991a,1993) and Pedersen and Nielsen (1991).

8.4.1 The Axisymmetric Aaberg Exhaust Hood

The flow of the axisymmetric REEXS is assumed to be axisymmetrical, and the full Navier-Stokes equations are given in, for example, Anderson et al. (1988). All the numerical results presented in this chapter for the axisymmetric exhaust are based on the dimensions and inlet conditions given by Pedersen and Nielsen (1991), see Table 6.1, and in this study the effect of varying the momentum flux of the radial jet has been examined whilst all other parameters remain constant. The operating conditions now considered are I = 0.0, 0.5, 0.9 and 1.95, which correspond to jet exit speeds of u(0) = 0.0 ms^{-1}, 30.8 ms^{-1}, 41.4 ms^{-1} and 60.9 ms^{-1}, respectively.

The air flow pattern for the axisymmetric hood described is shown in Figs.8.2(a)-(d) for the momentum ratios I = 0.0, 0.5, 0.9 and 1.95, respectively. The variation in the resultant air speed, u/u_{in}, as a function of the distance, y/a, along the centre-line of the exhaust hood predicted by the CFD model is shown in Figs.8.3(a)-(d) for I = 0.0, 0.5, 0.9 and 1.95, respectively. Also

shown in Fig.8.3 are (i) the centre-line air speed predicted by the simple mathematical model presented in chapter 6 and (ii) the air speeds observed experimentally by Pedersen and Nielsen (1991).

Considering first the case I = 0.0, Fig.8.2(a) indicates that air is drawn into the exhaust inlet from all directions with a significant amount of fluid being sampled from behind the hood. The exhaust flow is inefficient and non-directional, as observed by Pedersen and Nielsen (1991), and the rapid decay in the centre-line air speed, which results in a limited range of contaminant capture, can be seen in Fig.8.3(a).

From the results shown in Fig.8.2 the effect of the turbulent radial jet on the hood's induced air flow, as a function of the momentum flux of the jet, is immediately apparent. For the largest momentum ratio considered, namely I = 1.95, the axis of the developing jet is almost perpendicular to the axis of symmetry of the hood and the jet-induced flow exhibits a degree of symmetry about the axis of the jet. However, as the ratio of the momentum flows, I, decreases, the axis of the jet deviates from the near vertical position and the curvature and thickness of the jet increases. As expected, the width of the efficient flow decreases and the air speed in the efficient flow increases as I increases. The dramatic changes in the spacing of adjacent streamlines shown in Fig.8.2 indicates that the air speeds increase significantly throughout the workplace as the momentum ratio increases.

A comparison of the results presented in Fig.8.3 shows that there is close agreement between the resultant centre-line air speed predicted by the CFD model and the simple mathematical model; both models accurately reproduce the air speeds observed experimentally

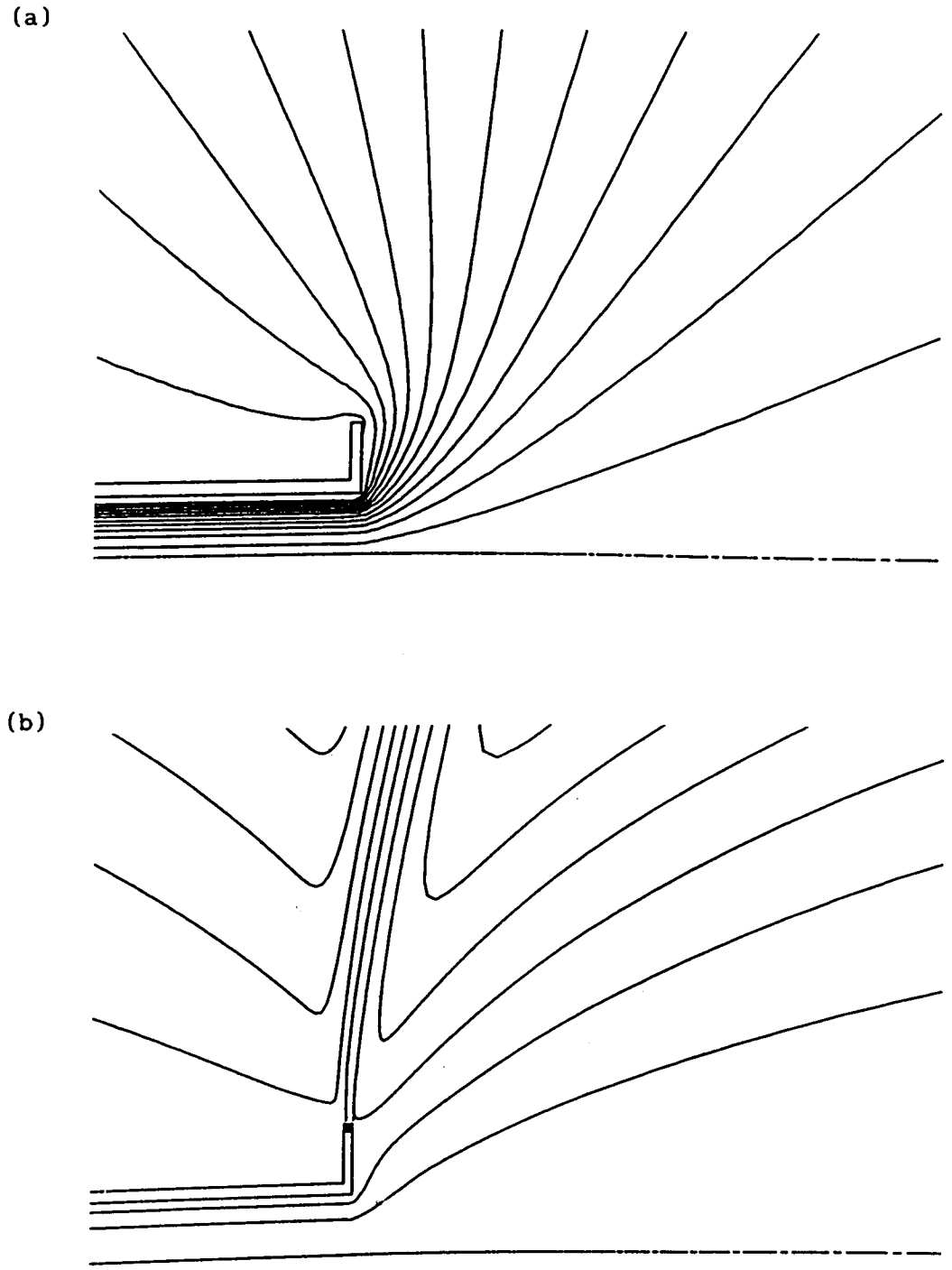

Fig.8.2 The streamlines for the flow around an axisymmetric Aaberg exhaust hood, the volume flux of air between adjacent streamlines is denoted by $\Delta\psi$, (a) I = 0.0, $\Delta\psi \propto 2.5\times10^{-3}m^3s^{-1}$, and (b) I = 0.5, $\Delta\psi \propto 1\times10^{-2}m^3s^{-1}$.

(c)

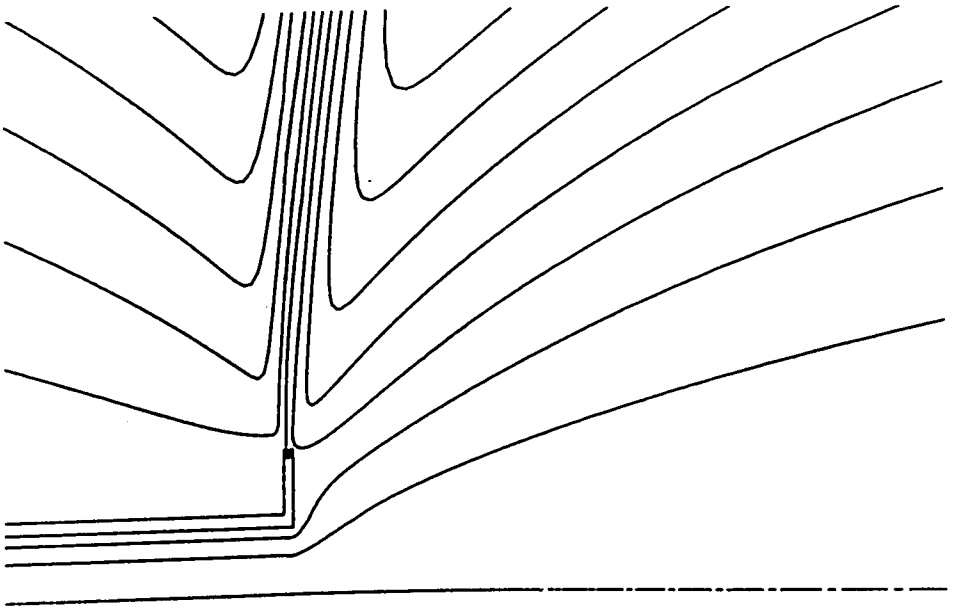

(d)

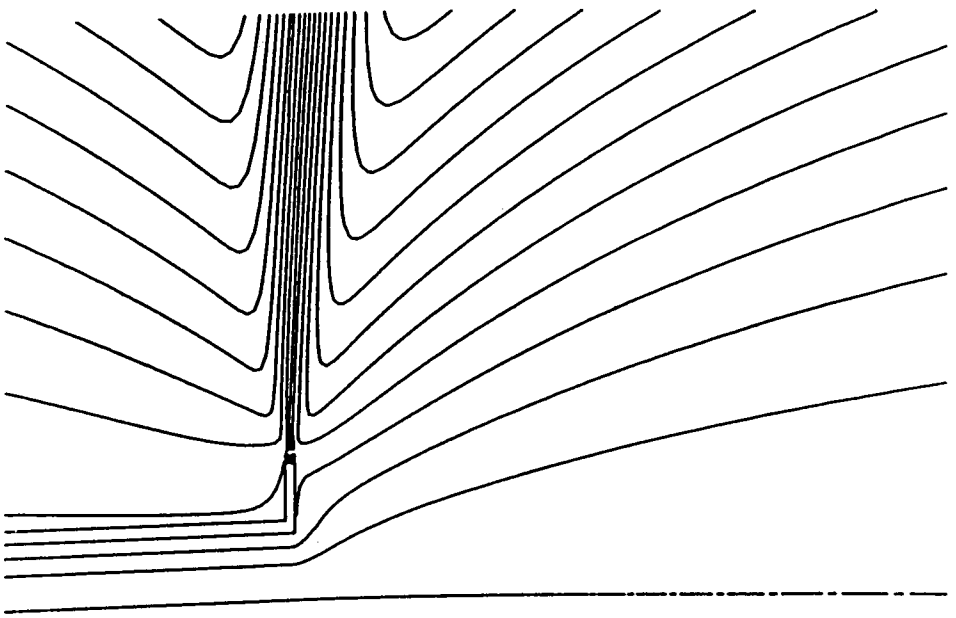

Fig.8.2 The streamlines for the flow around an axisymmetric Aaberg exhaust hood, the volume flux of air between adjacent streamlines $\Delta\psi \simeq 1\text{x}10^{-2}\text{m}^3\text{s}^{-1}$, (c) I = 0.9 and (d) I = 1.95.

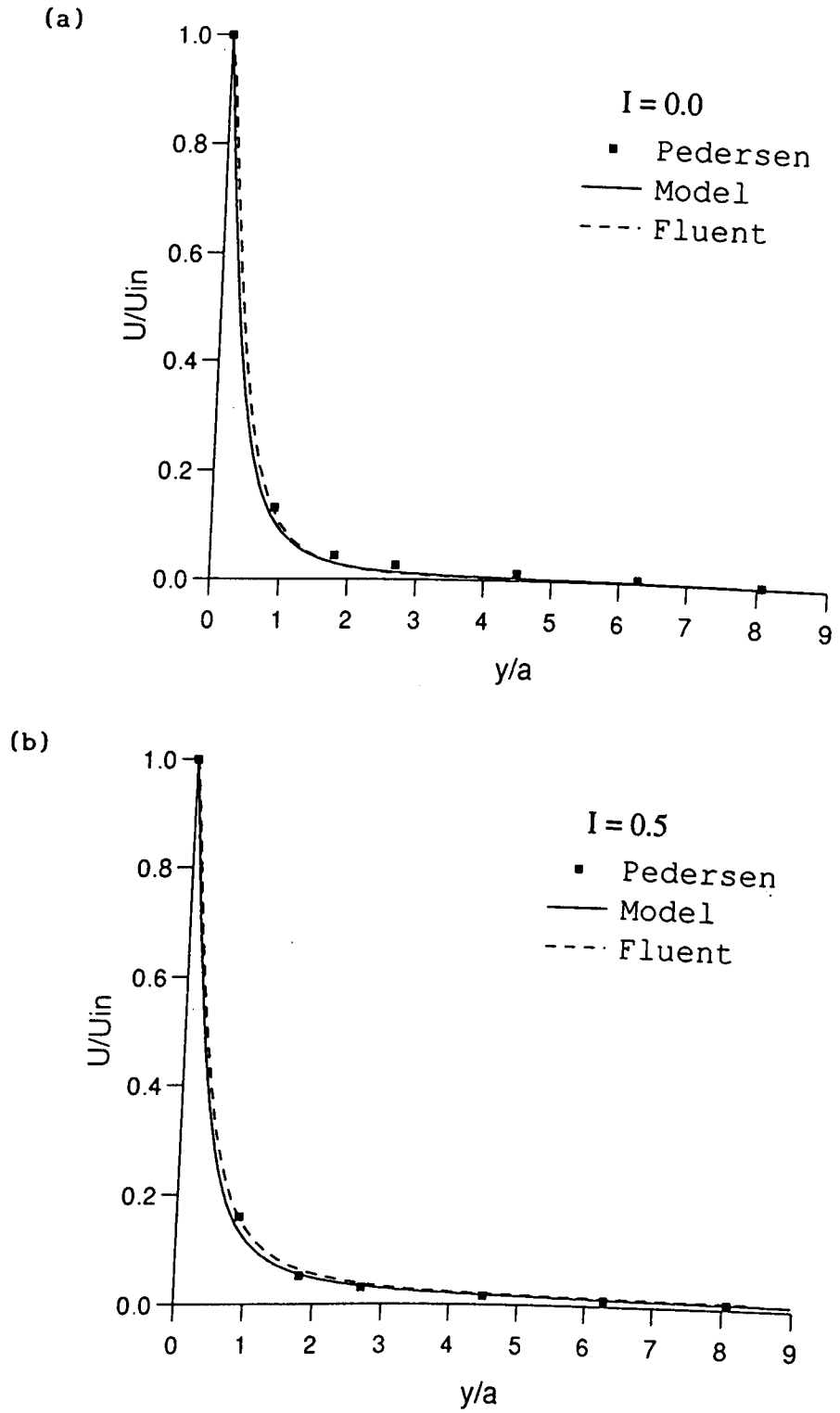

Fig.8.3 The variation in the resultant air speed, u/u_{in}, along the centre-line of the axisymmetric exhaust hood, showing the present CFD results (– – –), the model (——) and the experimental results of Pedersen (1993) (■), for (a) I = 0.0 and (b) I = 0.5.

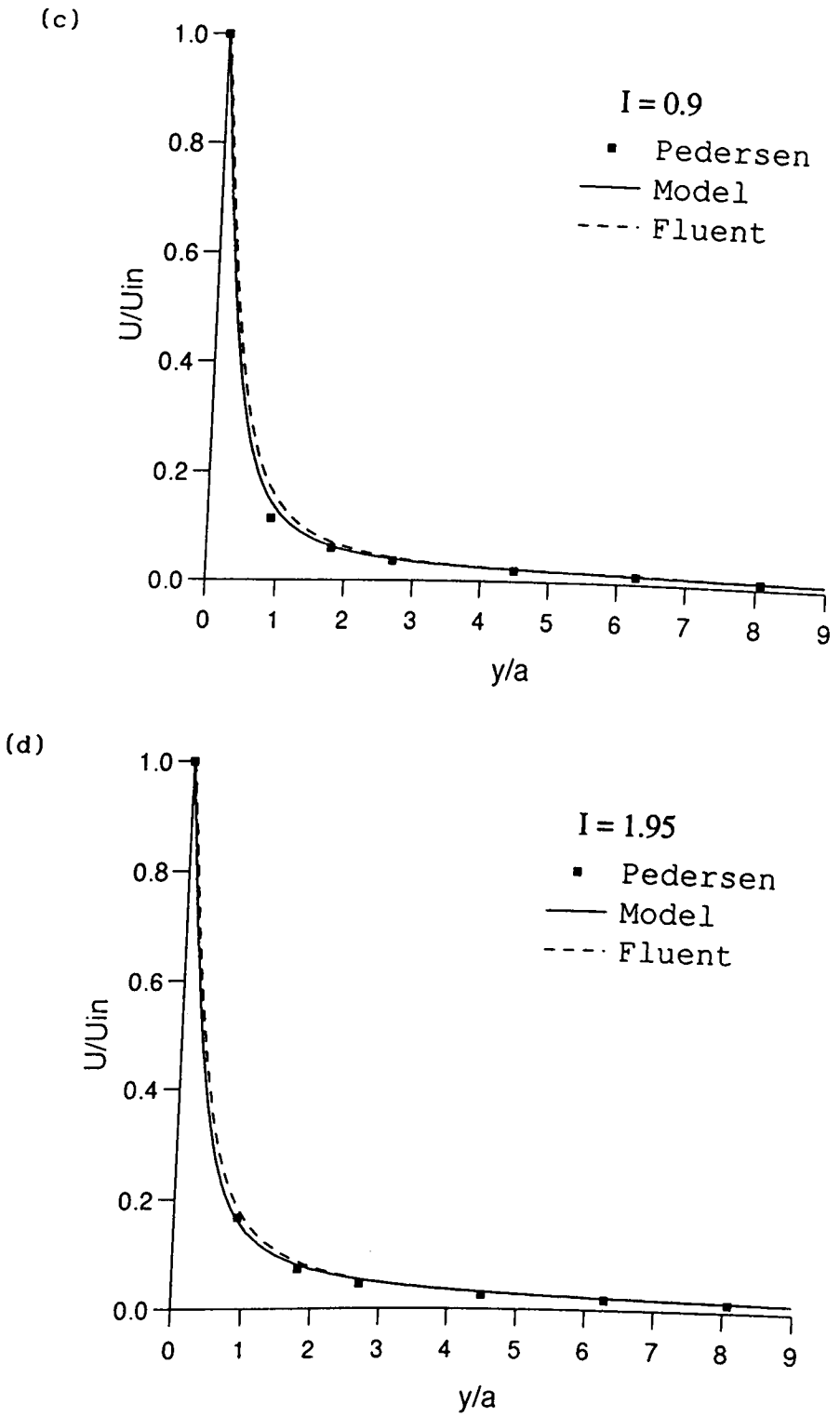

Fig.8.3 The variation in the resultant air speed, u/u_{in}, along the centre-line of the axisymmetric exhaust hood showing the present CFD results (– – –), the model (——) and the experimental results of Pedersen (1993) (■), for (c) I = 0.9 and (d) I = 1.95.

by Pedersen and Nielsen (1991). The close agreement, which is achieved over a wide range of momentum ratios, indicates that the simple mathematical model does provide an accurate means of predicting the centre-line air speed of the hood, even when the ratio of the momentum flows is small and the axis of the radial jet deviates significantly from the vertical. The good agreement may be due to the fact that the profile of the efficient flow region, and hence the air speeds in this region, is predominantly determined by the flow entrained into the initial development region of the radial jet, i.e. the region where the air speeds in the jet are still comparable with the jet exit speed. Further away from the jet orifice, where the air speed in the jet is relatively small compared with the jet exit speed, entrainment into the jet is expected to have no significant effect on the efficient flow region. In the initial development region of the jet, a slender jet with a vertical axis provides a good approximation to the flow predicted by the CFD model, see Fig.8.2. However, as the ratio I is further decreased, from I = 0.5, the jet is increasingly influenced by the exhaust flow and the simple mathematical model is expected to completely break down.

The CFD model has also been used to examine what effect the turbulence intensity in the radial jet has on the overall air flow produced by the exhaust hood. Three different values of turbulence intensity were considered, namely 40%, 60% and 80%, and the air flows produced by the hood operating at I = 1.95 were compared. The air speeds developed along the centre-line of the hood were found to be graphically indistinguishable, as were the streamlines in the entire flow region.

8.4.2 The Aaberg Slot Exhaust Hood

A series of investigations into the operation of an Aaberg slot exhaust have been performed by Pedersen (1991a). The present study assumes two-dimensional flow and concentrates on the flow behaviour with respect to changes in the momentum ratio, I, and consequently refers to Pedersen's HI-experiment, see chapter 7, in which all the operating parameters are kept constant, except for the jet exit speed and hence the momentum ratio. A broad range of momentum ratios have been investigated, namely I = 0.0, 0.5, 0.9 and 2.5, and comparisons made between the air flow predicted by the CFD model, the ASE model developed in chapter 7, see Hunt and Ingham (1993) and the experimental work of Pedersen.

Figures 8.4(a)-8.7(a) show the streamline patterns determined from the CFD model for a proportion of the domain close to the ASE for the operating conditions I = 0.0, 0.5, 0.9 and 2.5, respectively. The rectangular outline depicted in Figs.8.4(a)-8.7(a) represents the body of the exhaust system, which has a width of 0.2 m, a height of 0.4 m and an inlet width of 0.03 m. The small extrusion on the right hand side of the exhaust indicates the position of the jet nozzle, which has a width of 2×10^{-3}m. The corresponding non-dimensional streamline patterns predicted by the simple mathematical model for the ASE flow are shown in Figs.8.4(b)-8.7(b), where only the air flow in front of the exhaust is illustrated. By examining the profiles of the efficient flow region it is clear that the agreement between the CFD model and the simple mathematical ASE model is good over the range of momentum ratios considered. The streamlines illustrated in Figs.8.4(a)-8.7(a) show that the two-dimensional jet flow of the ASE is relatively

(a)

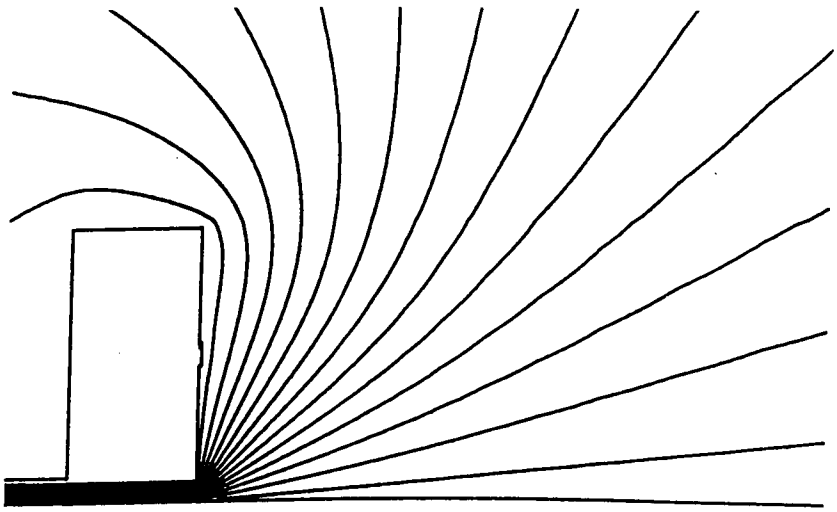

(b)

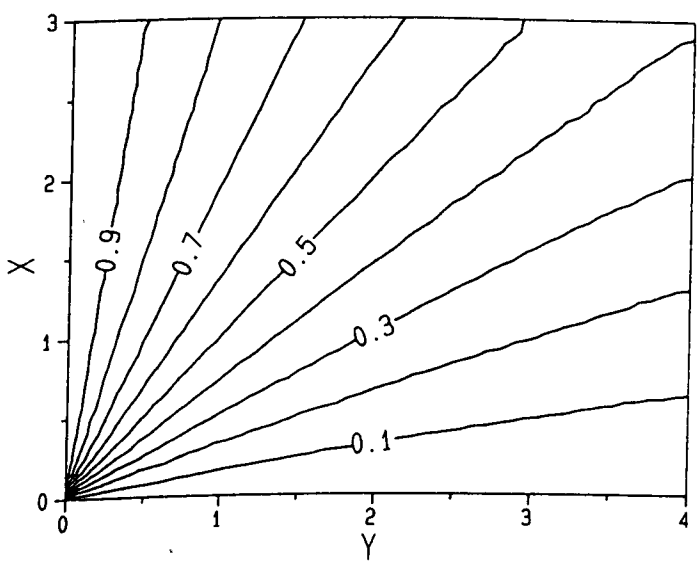

Fig.8.4 Streamlines for the flow around the ASE unit operating at $\dot{I}$ = 0.0, (a) the CFD model, the volume flux of air between adjacent streamlines $\Delta\psi \propto 8.75\times10^{-3} m^3 s^{-1}$ per metre length of the slot, (b) the simple mathematical ASE model, see chapter 7.

(a)

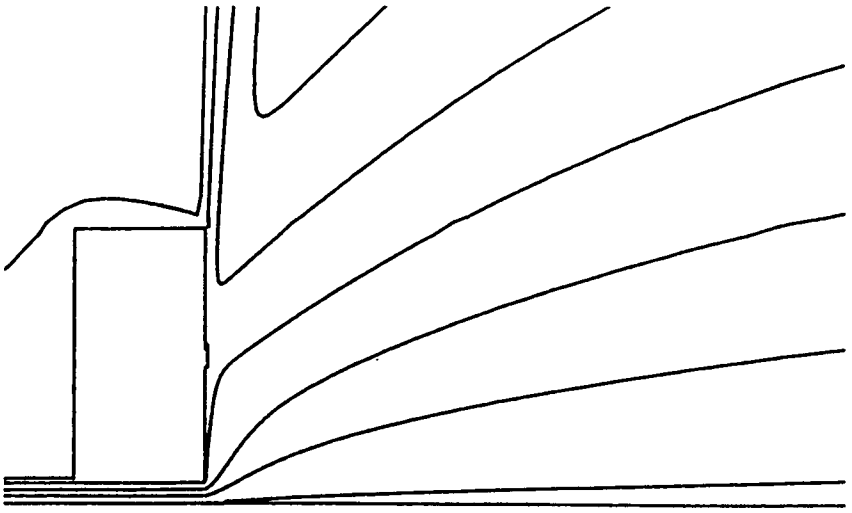

(b)

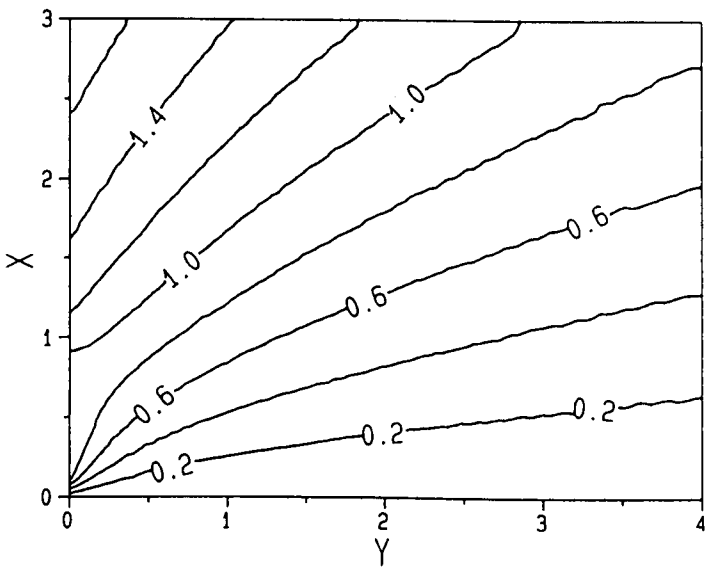

Fig.8.5 Streamlines for the flow around the ASE unit operating at I = 0.5, (a) the CFD model, the volume flux of air between adjacent streamlines $\Delta\psi \simeq 3.5\text{x}10^{-2}\text{m}^3\text{s}^{-1}$ per metre length of the slot, (b) the simple mathematical ASE model, see chapter 7.

(a)

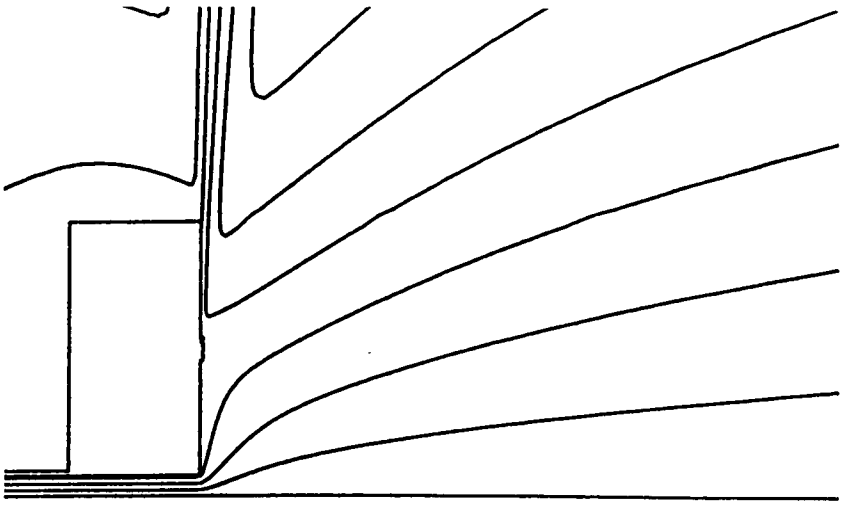

(b)

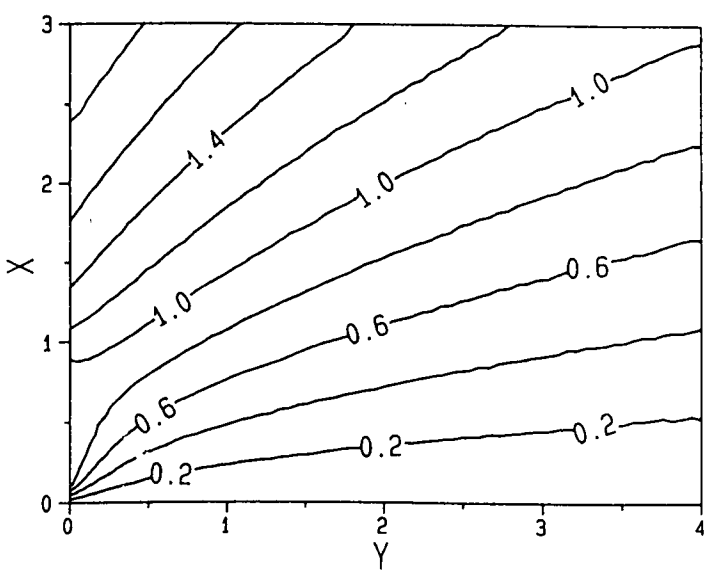

Fig.8.6 Streamlines for the flow around the ASE unit operating at I = 0.9, (a) the CFD model, the volume flux of air between adjacent streamlines $\Delta\psi \simeq 3.5\times10^{-2}m^3s^{-1}$ per metre length of the slot, (b) the simple mathematical ASE model, see chapter 7.

(a)

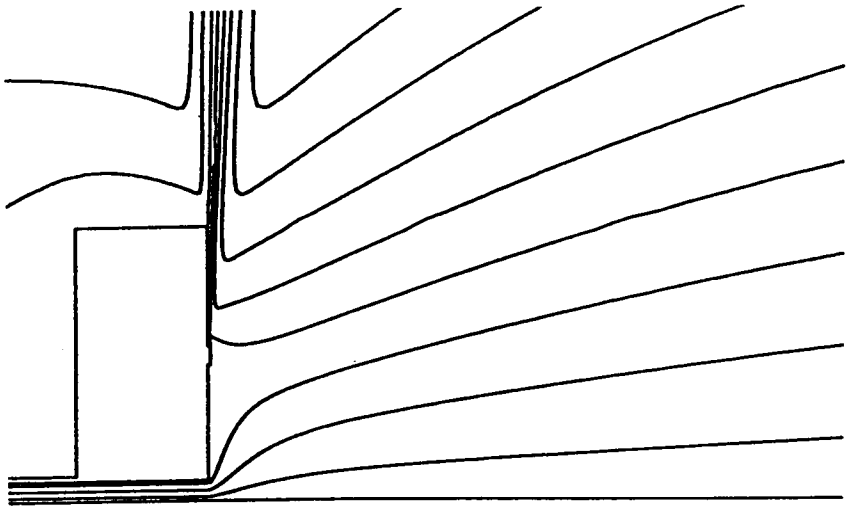

(b)

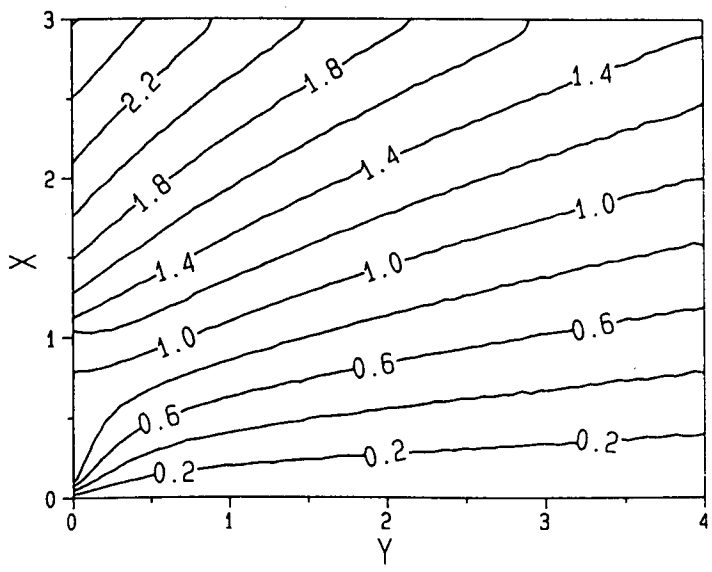

Fig.8.7 Streamlines for the flow around the ASE unit operating at I = 2.5, (a) the CFD model, the volume flux of air between adjacent streamlines $\Delta\psi \simeq 3.5\text{x}10^{-2}\text{m}^3\text{s}^{-1}$ per metre length of the slot, (b) the simple mathematical ASE model, see chapter 7.

unaffected by the suction flow as the axis of the jet remains approximately perpendicular to the bench surface for all the values of I considered. This result is in sharp contrast to the behaviour of the axisymmetric radial jet described in section **8.4.1** and indicates that the wall has a significant effect on the evolution of the two-dimensional jet flow for the ASE. This phenomena was also noted by Hyldgård (1987), who reported that the critical injection velocity for an axisymmetric hood with a back wall was lower than that for the standard hood.

The variation in the resultant air speed, q/(m/p), at a height of x/a = 0.174 above the surface of the bench, as a function of the distance, y/p, along the bench predicted by the CFD model is shown in Figs.8.8(a)-(d) for I = 0.0, 0.5, 0.9 and 2.5, respectively. Also shown are the air speeds predicted by the turbulent wall jet model of the ASE and those observed experimentally by Pedersen (1991a). In general the agreement between the CFD model and the simple mathematical ASE model is very good for each momentum ratio considered, although it is not clear which of the numerical techniques most accurately reproduces the experimental data. As expected, in both the CFD and simple mathematical model cases, a continuous decrease in the air speed is observed with increasing distance from the exhaust face, whereas Pedersen's observations exhibit some fluctuations in the air speed and this is most apparent when I = 2.5. As mentioned in chapter 7, the slight discrepancy between the experimental and numerical results could be explained in terms of background air movements in the experimental laboratory or by the presence of flow measuring equipment which could also disturb the flow.

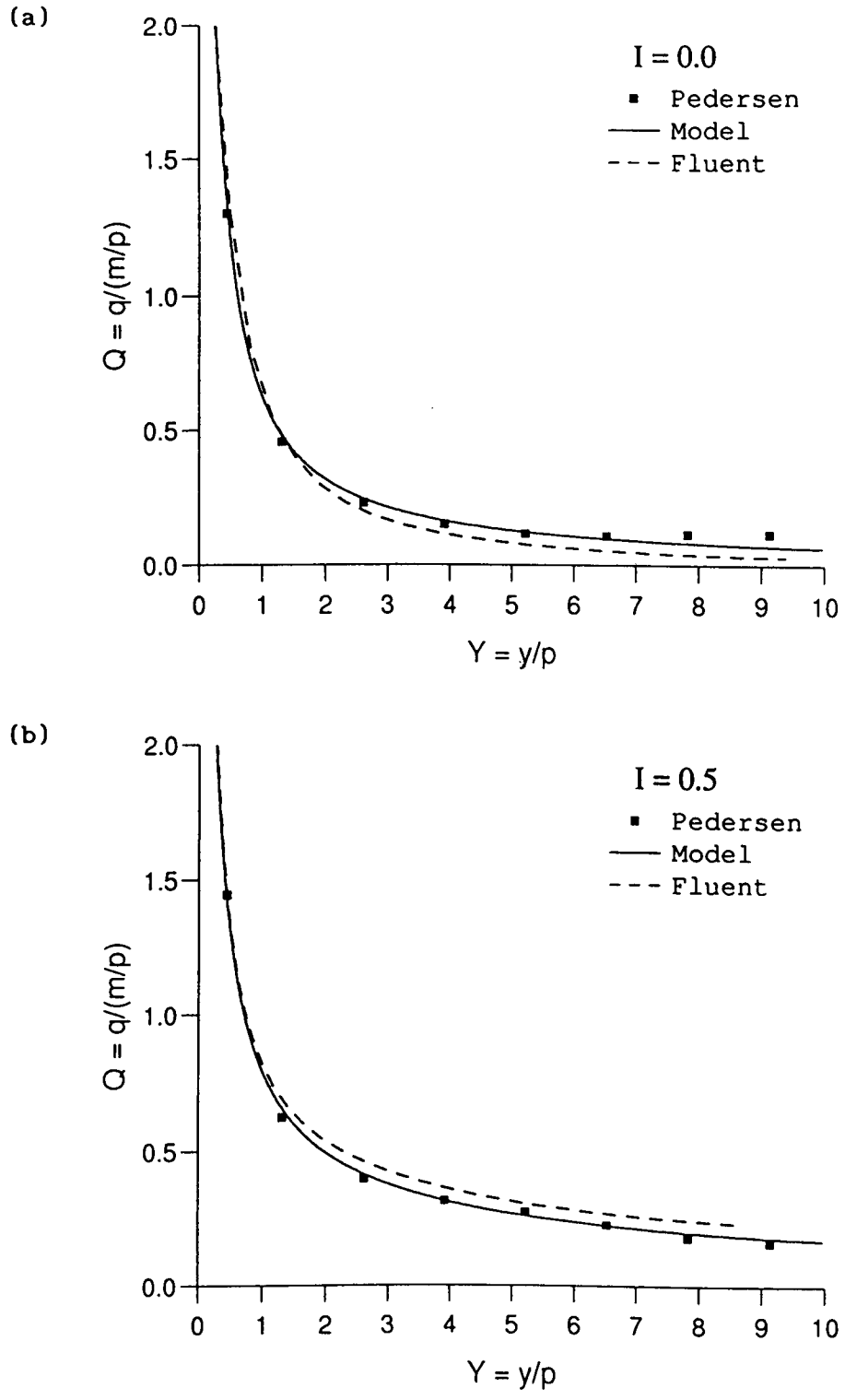

Fig.8.8 The variation in the resultant air speed, q/(m/p), at a height of x/a = 0.174 above the bench surface, showing the present CFD results (– – –), the ASE model (——) and the experimental results of Pedersen (1993) (■), for (a) I = 0.0 and (b) I = 0.5.

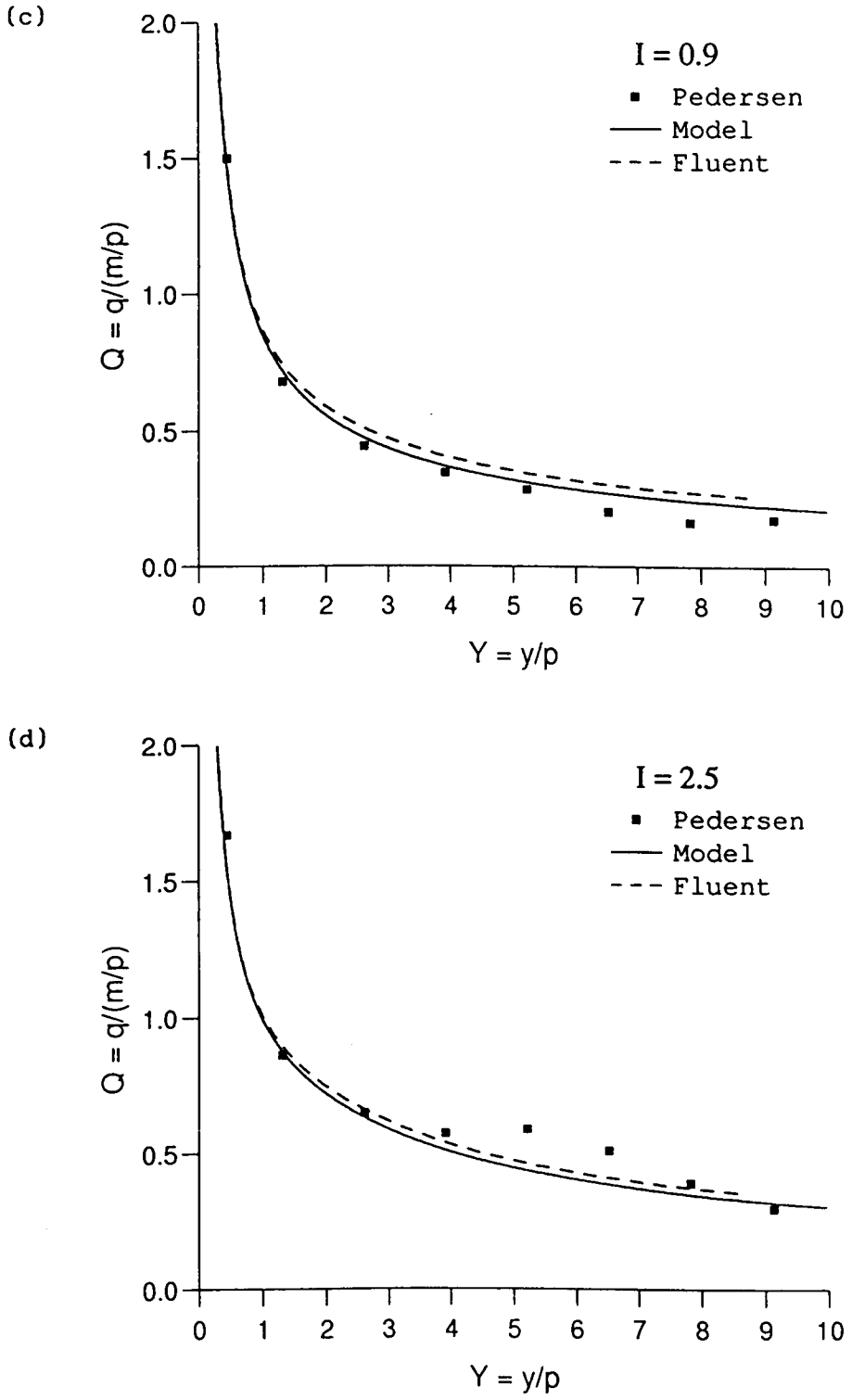

Fig.8.8 The variation in the resultant air speed, q/(m/p), at a height of x/a = 0.174 above the bench surface, showing the present CFD results (– – –), the ASE model (——) and the experimental results of Pedersen (1993) (■), for (c) I = 0.9 and (d) I = 2.5.

Figure 8.8(a) illustrates that for values of y/p greater than approximately 1.5, the CFD model underestimates the air speeds predicted by the simple mathematical model. This result was expected as the simple mathematical model assumes the exhaust flange has an infinite width and thus does not account for fluid being drawn from behind the exhaust system. From Figs.8.8(b)-(d) it is also evident that the air speeds predicted by the CFD model along x/a = 0.174 for I = 0.5, 0.9 and 2.5 slightly overestimate those predicted by the simple mathematical model. The differences between the two solutions are probably due to the different types of jet flow modelled. The simple mathematical model assumes a turbulent wall jet flowing along a flange of infinite length, whereas the jet flow modelled by the CFD model undergoes a transition from an initial turbulent wall jet phase to a turbulent free jet flow, where its momentum flux is then conserved. Consequently, we expect the latter of the two jets described to entrain more fluid and thus enhance the air speeds in the region of interest when compared with the infinite flange wall jet model.

8.5 CONCLUSIONS

In this chapter the axisymmetric REEXS and the two-dimensional ASE models presented in chapters 6 and 7, respectively, have been further validated by comparison with the results obtained from solving the full, turbulent Navier-Stokes equations using the CFD code FLUENT. In both the two-dimensional and three-dimensional axisymmetric cases the air speeds and flow fields predicted by the

CFD model and the simple mathematical models developed in this thesis are in good agreement. This gives us full confidence in the simple modelling techniques adopted.

The CFD package FLUENT was found to provide a convenient means of validating the models which have been developed earlier in this thesis and the determination of the full flow field using the CFD provides useful information regarding the interaction between the jet flow and exhaust flow regions. However, in comparison with the simple mathematical models, the parameters which govern the fluid flow of the Aaberg exhaust hood are less easily identifiable when using the CFD package as are the relationships between these parameters. Solving the full Navier-Stokes equations is computationally expensive in comparison with the modelling code; convergent results for the latter were achieved in a fraction of the computational time required by FLUENT. Clearly, both methods of determining the fluid flow have their advantages and disadvantages.

CHAPTER NINE

GENERAL CONCLUSIONS

The design of traditional exhaust hoods to give optimal flow and predictability of capture efficiencies under specific conditions of usage is a topic that has received a substantial amount of interest. However, until the start of the present work the many parameters which govern the fundamental fluid flow which is induced by jet-reinforced exhaust hoods, such as those employing the Aaberg principle, had not been identified and consequently the fluid flow produced by this type of hood was far from being well-understood. Experimental work has been performed with combined injection and exhaustion, mainly at the University of Aalborg, Denmark, and at the Health and Safety Executive, Sheffield, in order to obtain an improvement in the collection efficiency of the exhaust. However, as reported by Hyldgård (1987), and others, this has been "so far without success".

In the design, or in the selection of exhaust hoods for a particular application, the velocity profile in front of the exhaust hood determines its capture efficiency and, therefore, it is of prime importance. In some papers published in the early 1960's a simple linear approach to calculating the centre-line velocity was used in order to determine the exhaust hood design. Clearly this is not satisfactory and one of the main aims of this thesis was to develop simple fluid dynamics models of the Aaberg exhaust hood in order to predict the fluid velocity everywhere but in particular in front of the hood. This work has been very successful with both two-dimensional and three-dimensional axisymmetric models of the fluid flow induced by a jet-reinforced exhaust hood having been developed.

This thesis begins by considering the fluid flow which is induced by two-dimensional, jet-reinforced exhaust hoods which are of a simplistic design, see chapters 3 and 4. In chapter 3 the exhaust flow is idealized, and modelled as a line sink of fluid, in order to obtain analytical expressions for the components of the fluid velocity in front of the hood. In the following chapter this simple two-dimensional model was extended and the shape and size of the region of high capture efficiency was determined for a wide range of exhaust inlet sizes and for an exhaust hood which is suspended vertically above and facing the floor of the workplace. Although hoods of the simplistic nature modelled in chapters 3 and 4 of this thesis have not been studied experimentally, the simple models clearly identify the parameters which govern the flow induced by such exhaust hoods and give good qualitative agreement with all the available experimental data.

The remainder of this thesis has been devoted to the development and validation of mathematical models for the purposes of predicting the fluid flow produced by Aaberg exhaust hoods which exist in prototype form and whose fluid flows have been studied experimentally. Two types of hood have been investigated, namely the axisymmetrical reinforced exhaust system (REEXS) and the Aaberg slot exhaust (ASE). In the latter case the exhaust opening is in the form of a slot and is positioned above and perpendicular to a surface or 'bench', whereas in the former case the exhaust extends into a room and has an axisymmetrical geometry. Some of the parameters that have been varied in these two applications of the Aaberg principle are:

(a) The volumes of air injected and withdrawn.

(b) The shape of the exhaust hood.

(c) The size of the inlets and outlets.

(d) The orientation and position of the exhaust hoods.

A full description of the results obtained in each of the above investigations is given at the end of each appropriate chapter in the thesis and is therefore not repeated here. These models have now been fully developed and are very robust in their operations.

The formulation of the axisymmetric model for the REEXS involved a new approach to modelling the turbulent radial flow of a viscous fluid from a narrow annular orifice. The turbulent radial jet flow developed in chapter 5 of this thesis adopts the Prandtl constant momentum transfer model for the eddy viscosity and the resulting parabolic equations are solved numerically. These results are in very close agreement with both the empirical and theoretical results of numerous other authors who have investigated turbulent radial jet flows.

The mathematical models developed in this thesis for the axisymmetrical REEXS and the ASE systems have been extensively validated by comparing the numerically predicted results with the experimental data of Hyldgård (1987), Høgsted (1987), Pedersen and Nielsen (1991), Pedersen (1991a,1993) and Fletcher and Saunders (1991,1993). It is concluded that the results of the simple mathematical models give excellent agreement with all the available experimental data. Once a new design or operating procedure has been postulated by using the simple mathematical models then a more sophisticated model, i.e. a full computational fluid dynamics model, which is more expensive in both real time and CPU time, can be used to fine tune the design. Having done this then more experimental work can be performed in order to further optimize all the governing

parameters so that the efficiency of the Aaberg exhaust hood can be maximized.

There are many operating and geometrical design parameters which may be varied and in order to perform all the experiments needed to cover all parameter space it is both very costly and time-consuming. However, now that the basic fluid mechanics models have been developed they are very easy and cheap to use in order to test any suggested changes in the operating and/or geometric parameters for both the REEXS and the ASE systems. This approach therefore provides a cost-effective way of reducing the total number of experiments which have to be performed. It must, however, be stressed that both the simple mathematical models and the CFD models can be no substitute for performing experimental work in the industrial environment.

There is much scope for future investigation into both the design and the operating conditions of the Aaberg exhaust hood which will lead to an optimization of its fluid flow with respect to the energy consumption and capture efficiency. Preliminary investigations of possible hood design modifications performed by the author have indicated that the fluid speed induced by a two-dimensional Aaberg exhaust hood is significantly influenced by changes in the direction of the jet flow. The jet flow of the original design issues perpendicularly to the centre-line of the hood ($\phi = 90^{\circ}$). However, these investigations predict that the induced fluid speed in the region of interest can be significantly enhanced by orientating the jet flow such that $\phi < 90^{\circ}$. It is important that these design modifications, and others, should be addressed.

Finally, the work done in this thesis has focused on the fundamental fluid flow pattern induced by the Aaberg exhaust hood and for this reason the contaminant modelled has been assumed to be neutrally-buoyant and the effects of diffusion have been ignored. The models developed allow one to make confident predictions as to the fluid speeds induced by a hood of a specific geometry and operating under given conditions. However, the actual operating conditions of the exhaust must be tailored to fit the particular industrial application and they will depend upon the nature and location of the contaminant to be exhausted. The introduction into the fluid flow of a source of non-neutrally-buoyant contaminant is therefore the next logical progression in the mathematical and numerical study of the Aaberg exhaust hood.

REFERENCES

Abramovich, G.N. (1963) The Theory of Turbulent Jets. M.I.T.Press.

Anderson, D.A., Tannehill, J.C. and Pletcher, R.H. (1988) Computational Fluid Mechanics and Heat Transfer. Hemisphere, London.

Andrade, E.N. (1939) The velocity distribution in a liquid-into-liquid jet. The plane jet. *Proc. Phys. Soc.*, London, **51**, 784-793.

Bergstrom, D.J. (1992) A prediction of the pressure field in a plane turbulent jet using an algebraic stress model. *International Journal for Numerical Methods in Fluids*, **14**, 907-918.

Burden, R.L. and Faires, J.D. (1989) Numerical Analysis. 4th Edition, PSW-KENT Publishing Company, Boston.

Fletcher, B. (1977) Centre-line velocity characteristics of rectangular unflanged hoods and slots under suction. *The Annals of Occupational Hygiene*, **20**, 141-146.

Fletcher, B. (1978) Effects of flanges on the velocity in front of exhaust ventilation hoods. *The Annals of Occupational Hygiene*, **21**, 265-269.

Fletcher, B. and Saunders, C.J. (1991) Private communication. Health and Safety Executive, Research Division, Sheffield, England.

Fletcher, B. and Saunders, C.J. (1993) Jet enhanced local exhaust ventilation. *The Annals of Occupational Hygiene*, 37, 15-24.

Förthmann, E. (1936) Turbulent jet expansion. English translation N.A.C.A. Technical Memorandum No. 789. (Original paper in German, 1934. Ingenieur-Archiv, **5**, 42-54.)

Görtler, H. (1942) Berechnung von aufgaben der freien turbulenz auf grund eines neuen näherungsansatzes. *Z. angew. Math. Mech.*, **22**, 244-254.

Greenough, G.K. (1988) Industrial dust control - The problems and some suggestions for improvement. *The Annals of Occupational Hygiene*, **32**, 45-47.

Heskestad, G. (1966) Hot-wire measurements in a radial turbulent jet. *J. Appl. Mech.*, **33**, 417-424.

Høgsted, P. (1987) Air movements controlled by means of exhaustion. ROOMVENT'87. *International Conference On Air Distribution In Ventilated Spaces*, Stockholm.

Hunt, G.R. and Ingham, D.B. (1992) The fluid mechanics of a two-dimensional Aaberg exhaust hood. *The Annals of Occupational Hygiene*, **36**, 455-476.

Hunt, G.R. and Ingham, D.B. (1993) A mathematical model of the fluid-flow of a slot exhaust-hood reinforced by a two-dimensional jet-flow. *Journal of Mathematical Engineering in Industry*, **4**, 227-247.

Hyldgård, C.E. (1987) Aerodynamic control of exhaust. ROOMVENT'87. *International Conference On Air Distribution In Ventilated Spaces*, Stockholm.

Launder, B.E. and Rodi, W. (1981) The turbulent wall jet. *Prog. Aerospace Sci.*, **19**, 81-128.

Launder, B.E. and Spalding, D.B. (1972) Turbulence models and their application to the prediction of internal flow. *Heat and Fluid Flow*, **2**, 43-54.

Launder, B.E. and Spalding, D.B. (1974) The numerical computation of turbulent flows. *Comp. Methods in App. Mech. and Eng.*, **3**, 269-289.

Lippisch, A.M. (1958) Flow visualization. *Aeron. Eng. Rev.*, **17**, 24-36.

Malin, M.R. (1988) Prediction of radially spreading turbulent jets. *AIAA. J.*, **26**, 750-752.

Merkin, J.H. (1976) Free convection boundary layer on an isothermal horizontal cylinder. *A.S.M.E.-A.I.Ch.E. Heat Transfer Conf.*, St.Louis, Mo.

Myers, G.E., Schauer, J.J. and Eustis, R.H. (1963) Plane turbulent wall jet flow - development and friction factor. Trans. A.S.M.E., *J. Basic Eng.*, **85**, 47-54.

Nallasamy, M. (1987) Turbulence models and their applications to the prediction of internal flows: a review. *Computers and Fluids*, **15**, 151-194.

Patankar, S.V. and Spalding, D.B. (1972) A calculation procedure for heat, mass and momentum transfer in three dimensional parabolic flows. *Int. J. of Mass Transfer*, **15**, 1787-1806.

Patankar, S.V. (1980) Numerical heat transfer and fluid flow. Hemisphere Publishing Corporation, New York.

Patel, R.P. (1979) Some measurements in radial free jets. *AIAA. J.*, **17**, 657-659.

Pedersen, L.G. and Nielsen, P.V. (1991) Exhaust system reinforced by jet flow. VENTILATION'91. *International Conference On Ventilation*, Cincinnati.

Pedersen, L.G. (1991a) REEXS-Reinforced Exhaust System. Ph.D thesis, Danish Technological Institute, Arhus, Denmark.

Pedersen, L.G. (1991b) Private communication. Danish Technological Institute, Arhus, Denmark.

Pedersen, L.G. (1993) Private communication. Danish Technological Institute, Arhus, Denmark.

Poreh, M. and Cermak, J.E. (1959) Flow characteristics of a circular submerged jet impinging normally on a smooth boundary. Proceedings of the *Sixth Midwest Conference on Fluid Mechanics*, University of Texas, Austin, 198-212.

Rajaratnam, N. (1965) Plane turbulent wall jets on rough boundaries. Tech. Rep., Department of Civil Engineering, Univ. of Alberta, Edmonton.

Rajaratnam, N. (1976) Turbulent Jets. Developments in Water Science, no.5, chapter 10, 211-225. Elsevier Scientific Pub. Co., New York.

Rodi, W. (1972) The prediction of free turbulent boundary-layers by use of a two equation model of turbulence. Ph.D thesis, University of London.

Rubel, A. (1985) On the vortex stretching modification of the k-ε turbulence model: Radial jets. *AIAA. J.*, **23**, 1129-1130.

Rumer, Y.B. (1949) Turbulent source of free annular jet. *Dokl. Akad. Nauk S.S.S.R.*, **64**, 463-466.

Schlichting, H. (1968) Boundary-Layer Theory. 6th Edition, McGraw Hill Book Company, New York.

Schneider, W. (1981) Flows induced by jets and plumes. *J. Fluid Mech.*, **108**, 55-65.

Schneider, W. (1983) Asymptotic analysis of jet flows, *Fluid Dynamics Transactions*, 12. Proceedings of the XVIth Symposium on Advanced Problems and Methods in Fluid Mechanics, Spala.

Schwarz, W.H. and Cosart, W.P. (1961) The two-dimensional turbulent wall jet. *J. Fluid Mech.*, 10, 481-495.

Sigalla, A. (1958a) Experimental data on turbulent wall jets. *Aircraft Engineering*, 30, 131-134.

Sigalla, A. (1958b) Measurements of skin friction in a plane turbulent wall jet. *J. R. Aeronaut. Soc.*, 62, 873-877.

Smith, G.D. (1985) Numerical solution of partial differential equations: finite difference methods. 3rd Edition, Clarendon Press, Oxford.

Squire, H.B. (1955) Radial Jets. 50 years of boundary-layer research, edited by H.Görtler & W.Tollmein. Braunschweig: F.Vieweg & Son, 47-54.

Taliyev, V.N. (1954) Fundamental principles governing an annular turbulent source. *Dokl. Akad. Nauk S.S.S.R.*, 94, 405-408.

Tanaka, T. and Tanaka, E. (1976) Experimental study of a radial turbulent jet. *Bulletin of the J.S.M.E.*, 19, 792-799.

Tollmein, W. (1926) Calculation of turbulent expansion processes. Z. *angew. Math. Mech.*, 6, 468-478.

Tuve, G.L. (1953) Air velocities in ventilating jets. *Heat. Pip. Air Cond.*, 25, 181-191.

Van Doormaal, J.P. and Raithby, G.D. (1984) Enhancements of the SIMPLE method for predicting incompressible fluid flows. *Numerical Heat Transfer*, 7, 147-163.

Verhoff, A. (1963) The two-dimensional turbulent wall jet with and without an external stream. Rep. 626, Princeton Univ.

White, F.M. (1991) Viscous fluid flow. 2nd Edition, McGraw-Hill Series in Mechanical Engineering, McGraw-Hill, Inc., New York.

Witze, P.O. and Dwyer, H.A. (1976) The turbulent radial jet. *J. Fluid Mech.*, 75, 401-417.

Wood, P.E. and Chen, C.P. (1985) Turbulence model predictions of the radial jet - a comparison of k-ε models. *Canadian Journal of Chemical Engineering*, 63, 177-182.

Wygnanski, I., Katz, Y. and Horev, E. (1992) On the applicability of various scaling laws to the turbulent wall jet. *J. Fluid Mech.*, 234, 669-690.